Scuffing of Aluminum/Steel Contacts Under Dry Sliding Conditions

T. K. Sheiretov and C. Cusano

ACRC TR-131 August 1997

For additional information:

Air Conditioning and Refrigeration Center
University of Illinois
Mechanical & Industrial Engineering Dept.
1206 West Green Street
Urbana, IL 61801

(217) 333-3115

Prepared as part of ACRC Project 49
Compressor—Lubrication, Friction and Wear
C. Cusano, Principal Investigator

The Air Conditioning and Refrigeration Center was founded in 1988 with a grant from the estate of Richard W. Kritzer, the founder of Peerless of America Inc. A State of Illinois Technology Challenge Grant helped build the laboratory facilities. The ACRC receives continuing support from the Richard W. Kritzer Endowment and the National Science Foundation. The following organizations have also become sponsors of the Center.

Amana Refrigeration, Inc.
Brazeway, Inc.
Carrier Corporation
Caterpillar, Inc.
Copeland Corporation
Dayton Thermal Products
Delphi Harrison Thermal Systems
Eaton Corporation
Ford Motor Company
Frigidaire Company
General Electric Company
Hydro Aluminum Adrian, Inc.
Indiana Tube Corporation
Lennox International, Inc.
Modine Manufacturing Co.
Peerless of America, Inc.
Redwood Microsystems, Inc.
The Trane Company
Whirlpool Corporation
York International, Inc.

For additional information:

Air Conditioning & Refrigeration Center
Mechanical & Industrial Engineering Dept.
University of Illinois
1206 West Green Street
Urbana IL 61801

217 333 3115

ABSTRACT

Some typical applications where scuffing may occur are gear teeth, piston rings and cylinder pairs, cams and followers, splines, sleeve bearings, and parts of swash and wobble plate compressors. Unlike other tribology-related failures, scuffing occurs very fast, without any warning, and usually leads to the complete destruction of the sliding pair. Practical experience with steel has helped to outline safe ranges of operation for some components. Very little, however, is known about aluminum, which is the second most commonly used engineering metal. The aim of this study is to obtain a better understanding scuffing and seizure of aluminum/steel contacts.

The research includes an experimental study of scuffing of aluminum/steel contacts under dry sliding conditions, a study of the physics of the scuffing process, evaluation of various hypotheses for scuffing, and modeling of scuffing.

The experiments are conducted in a custom-designed tribometer, which provides accurate control of the environmental conditions. Special instrumentation, experimental procedures and software are developed as a part of the experimental program. These provide a reliable reproduction and identification of scuffing under laboratory conditions. The scuffing characteristics of five materials are obtained in air and refrigerant (R134a) environments. The effects of load, sliding velocity, mechanical strength, environmental temperature, specimen geometry, time, loading history, and type of environment are evaluated.

The mechanisms leading to scuffing are studied by examination of surfaces, subsurfaces and wear debris of specimens in the process of scuffing. Quantitative measurements of subsurface plastic strain are also obtained.

The theoretical part of the study includes the development of a finite element model for the contact of runned-in rough surfaces and several other models for subsurface stresses, temperatures, and strains. These models provide information about the local conditions in the subsurface

Based on the experimental observations and the scuffing models a new hypothesis for scuffing is proposed. According to this hypothesis, scuffing involves initiation of cracks due to subsurface plastic deformation, propagation of these cracks leading to the removal of the existing protective surface layers, and finally cold welding due to adhesion between bare metal surfaces.

TABLE OF CONTENTS

LIST OF TABLES

LIST OF FIGURES

LIST OF SYMBOLS AND ABBREVIATIONS

Symbols

A	area of contact, (m^2)
A_0	apparent area of contact, (m^2)
A_{ij}	elements of the influence matrix for the calculation of subsurface stresses
A_r	real area of contact, (m^2)
$\hat{A}$	unit area (of surface contact strip), (m^2)
a	half-width of a contact spot, (μm)
	crack length, (μm)
a_c	critical crack length, (μm)
$\Delta\bar{a}$	average crack extension per cycle, (μm)
b	half-length of a contact spot, (μm)
C	constant
$C_1 \ldots C_n$	thermal capacitance of the finite elements in the thermal model, (J/°K)
C_{kl}, C^*_{kl}	elements of the influence matrices for the Boussinesq solution
C_t	constant characterizing the thermal resistance and the dissipative characteristics of the system, (°C/W)
c_i	height of the isothermal semi-ellipsoids in the thermal model, (μm)
c_p	specific heat, (J/kg°K)
D	size of a subsurface void, (μm)
$\dot{D}$	growth rate of voids, (μm/s)
d	rigid body approach, (μm)
d1-d8	equidistant surface profiles of the disk
E	elastic modulus, (MPa)
E_{pin}	elastic modulus of the pin, (MPa)

E_{disk}	elastic modulus of the disk, (MPa)
E'	equivalent elastic modulus , (MPa) $E' = \left[\left(1-\nu_1^2\right)/E_1 + \left(1-\nu_2^2\right)/E_2\right]^{-1}$
$\mathbf{E}(r/a)$	complete elliptic integral of the second kind
E_f	activation energy characterizing the rate of oxide formation, (J)
E_r	activation energy characterizing the rate of oxide removal, (J)
$f_c(P,V)$	frequency of contact periods, (Hz)
$f_p(P,V)$	frequency of contact periods in which plastic flow occurs, (Hz)
$G(z)$	damage growth factor
H	hardness, (Pa)
h	wear depth, (μm)
$\bar{h}$	average wear depth of a single contact spot necessary for load transfer, (μm)
$\dot{h}$	wear rate, (μm/s)
h_{ave}	average wear depth on the disk specimen, (μm)
h_c	critical vertical displacement, (μm)
I_0, I_v, I_c	electric currents, (A)
i, j, k, l	indices
K	wear coefficient in Archard's law
k	thermal conductivity, (W/m°K)
L	length of contact used in the cylinder-on-flat model, (mm)
L_{arch}	length of the sliding arch, (mm)
l	half-width of the thermally or plastically affected zone, (μm)
Δl	distance between thermocouples, (mm)
M	number of finite elements over the apparent area of contact
m	constant in the empirical stress/strain relationship $\sigma_f = \sigma_s - (\sigma_s - \sigma_0)\exp(\chi\varepsilon^m)$
m,n,q	power factors in $P^n V^m T^q = const$
m_h	constant in Hertz's relationship between load and contact area

m_t ,n_t	coefficients characterizing the thermal distortion of a contact spot
N	number of unit contact strips
N_c	total number of loading cycles
N_w	number of loading cycles due to the discontinuity of wear
n	strain rate sensitivity factor $(\sigma_f/\sigma_0) = (\dot{\varepsilon}/\dot{\varepsilon}_0)^n$
	power factor in the $PV^n = C$ relationship
P	apparent contact pressure, (MPa)
PV	pressure - velocity factor (apparent pressure × sliding velocity), (MPa.m/s)
p	local contact pressure, (MPa)
$\overline{p}$	average local contact pressure, (MPa)
p1,p2	transverse surface profiles of the pins
p_{max}	maximum local contact pressure, (MPa)
p_{new}, p_{old}	successive values in the iteration process for the surface pressures, (MPa)
Q	frictional heat generated at the interface, (W)
Q_{pin}	heat flowing through the pin specimen, (W)
$\overline{q}$	average local heat flow, (W)
R	sliding radius, (m)
R_1,R_2,R_3,R_4	electric resistances of the contacting wires, (Ω)
R_0,R_c,R_v	electric resistances, (Ω)
R_1 ... R_n	thermal resistances of the finite elements of the thermal model, (°C/W)
R_A, R_B	curvatures of surfaces at the point of contact, (m)
R_a	average radius of curvature of surface asperities, (μm)
R_{ave}	average sliding radius, (mm)
R_{cyl}	radius of the cylinder used in the cylinder-on-flat model, (mm)
R_{pin}	radius of the pin specimen, (mm)
R_f, R_r	rates of oxide formation and oxide removal, (m^3/s)
R_t	thermal resistance, (°C/W)

R_{tip}	radius of the tip of the stylus, (μm)
$\Re$	the universal gas constant
r_t	coefficient for the heat partitioning at the interface
r	radial coordinate, (m)
r_c	correlation coefficient
S	distance slid, (m)
S_u	ultimate shear strength, (MPa)
s	spacing between the points in a digitized profile, (μm)
T	absolute temperature, (°K)
	torque resulting from the surface contact pressures, (Nm)
$T_1 \ldots T_n$	temperatures in the finite elements of the thermal model, (°C)
T_∞	temperature far from the contact spot, (°C)
ΔT	temperature difference, (°C)
T_0	environmental temperature, (°C)
T_2, T_4, T_6	thermocouple readings, (°C)
T_b	bulk temperature, (°C)
T_c	critical temperature, (°C)
T_f	flash temperature, (°C)
T_s	surface temperature, (°C)
t	time, (s)
t_a	time necessary to reach equilibrium in plastic strain accumulation, (s)
t_i	time necessary for crack initiation, (s)
t_p	time necessary for crack propagation, (s)
t_d	time to failure $t_d = t_i + t_p$, (s)
t_h	time spent within the zone of highest damage accumulation rate, s
$\bar{t}$	average duration of a contact period, (s)
$\bar{t}_0$	average time between contact periods, (s)

t_c	average duration of a loading cycle due to wear, (s)
t_w	duration of a loading cycle due to surface waviness, (s)
Δt	time step, (s)
$U(i)$, $Y(i)$	digitized surface profiles
u	horizontal displacement in the direction of sliding, (μm)
V	sliding velocity, (m/s)
V_0	volume worn, (m^3)
$V_1 \ldots V_n$	volumes of the finite elements of the thermal model, (m^3)
W	contact load, (N)
w	vertical displacement, (μm)
$(w_l)_{pin}$	vertical displacement of a point on the surface of the pin, (μm)
$(w_l)_{disk}$	vertical displacement of a point on the surface of the disk, (μm)
x	coordinate axis in the plane of contact, transverse to the sliding direction, (μm)
Δx, Δz	spacing of the nodes in a finite difference model, (μm)
x', y'	coordinate axes directions, (m)
x^*, z^*	coordinates of the surface profile, corrected for stylus tip errors, (μm)
y	coordinate axis coinciding with the sliding direction (μm)
z	coordinate axis perpendicular to the surface (μm)
z_c	critical depth, (μm)
$z_1(i)$, $z_2(i)$	undeformed surface profiles, (μm)
$z_1^*(i), z_2^*(i)$	deformed surface profiles, (μm)
α	angle of inclination between the datum lines of matching surface profiles
α_i	geometrical parameter of the elements in the thermal model
α_s	local slope of the surface profile
α_t	coefficient of thermal expansion
α_x, α_y	angles of inclination between the datum planes of two rough surfaces
β	coefficient characterizing the ratio of the real to the apparent areas of contact

$\gamma(\xi)$	cross correlation function for the alignment of surface profiles
γ	constant, $1.0 < \gamma < 2.0$
γ_c	critical shear strain
$\bar{\gamma}$	average shear strain
δ	thickness of the transformed layer, (μm)
δ_l	geometrical overlap of surface profiles, (μm)
$\delta(\xi)$	cross correlation function for the alignment of surface profiles
ε	equivalent plastic strain
$\bar{\varepsilon}_i$	average local equivalent plastic strain
$\dot{\varepsilon}$	equivalent strain rate
$\bar{\dot{\varepsilon}}$	average local plastic strain rate, (s^{-1})
$\dot{\varepsilon}_0$	quasi-static strain rate, (s^{-1})
$\dot{\varepsilon}_{xy}, \dot{\varepsilon}_{yz}, \dot{\varepsilon}_{zx}$	shear strain rates, (s^{-1})
$\dot{\varepsilon}_1$	curve fit parameter in the empirical stress/strain relationship $\frac{\sigma_f}{\sigma_0} = \exp\left(\frac{\dot{\varepsilon}}{\dot{\varepsilon}_1}\right)$
ζ	aspect ratio of the surface finite elements, *b/a*
η	constant of proportionality between load and number of contacts
Θ	angle of the brass/aluminum interface
θ_1, θ_2	angles determining the position of a point in the subsurface with respect to a contact strip
φ	ratio of the number of cycles due to wear to the total number of cycles $\varphi = N_w/N_c$
Λ	ratio between the lubricant film thickness and the composite surface roughness
μ	coefficient of friction
ν	Poisson's ratio
ν_{pin}, ν_{disk}	Poisson's ratios for the pin and disk materials
ν_f, ν_r	pre-exponential factors in Arrhenius-type relationship $R_f = \nu_f \exp(E_f/\Re T)$
ξ	horizontal misalignment of surface profiles

ρ	density, (kg/m^3)
σ	composite surface roughness, (μm)
σ_0	yield strength, (MPa)
σ_e	equivalent (Von Mises) stress, (MPa)
σ_f	flow stress of the material, (MPa)
σ_i	strength of the surface films, (MPa)
σ_m	hydrostatic stress, (MPa)
σ_r	normal stress across the faces of a crack, (MPa)
σ_s	saturation stress, (MPa)
σ_{ry}	shear stress driving the extension of a crack, (MPa)
$\sigma_{xx}, \sigma_{yy}, \sigma_{zz}$	local normal stresses, (MPa)
$\sigma_{xy}, \sigma_{yz}, \sigma_{zx}$	local shear stresses, (MPa)
τ_e	equivalent (von Mises) shear stress, (MPa)
τ_k	local shear surface traction, (MPa)
χ	constant in the empirical stress/strain relationship $\sigma_f = \sigma_s - (\sigma_s - \sigma_0)\exp(\chi\varepsilon^m)$
$\tan\phi$	slope of the $h_{ave} = f(P)$ curve
Ψ	plasticity index
Ψ_l	edge correction factor
ω	factor facilitating the numerical convergence in the Gauss-Seidel algorithm

Abbreviations

AES	Auger electron spectroscopy
DC	direct current
EHL	elastohydrodynamic lubrication
HPT	high pressure tribometer
LVDT	linear variable differential transformer

OECD	Organization for Economic Cooperation and Development
PTFE	polytetrafluoroethane
R12	dichlorofluoromethane
R134a	tetrafluoroethane
RMS	root mean square
RPM	revolutions per minute
SEM	scanning electron microscope
XPS	X-ray photoelectron spectroscopy

CHAPTER 1
INTRODUCTION

1.1 Definitions for Seizure and Scuffing

The study of a physical phenomenon should start with its proper definition. There is little agreement in the literature on what seizure or scuffing is, what causes it, or what its appearance is. This has resulted in a significant confusion because various researchers have lumped very different physical processes into the general heading of seizure or scuffing. Scuffing is described as a failure of lubricant films [1-3], desorption of active chemical species [4], destruction of oxides [5], large plastic deformation of the surface [6-9], unstable growth of contact junctions [10-13], accumulation of wear debris [14, 15] and bulk subsurface failure [16]. This is the reason why numerous definitions of scuffing and seizure have been proposed. It seems that there is agreement on only one characteristic feature of the scuffing process. This is the formation of macroscopically large areas of metal unprotected by surface films. The contact of these areas with the counterface material results in the formation of cold welds (Fig. 1.1) which may lead to the complete stopping of relative motion. This aspect of the scuffing process has led to the formulation of the most widely used definitions for seizure and scuffing. They are given by the Organization for Economic Cooperation and Development (OECD) [17]:

Seizure The stopping of relative motion as the result of interfacial friction.

Scuffing Localized damage caused by the occurrence of solid-phase welding between sliding surfaces without local surface melting.

In the definition for seizure, the stopping of relative motion is obviously dependent upon the power capabilities of the prime mover and cannot be used as a universal criterion. What the definition does require is an increase in the friction force. This increase can be caused by:

a. An increase in the normal load while the coefficient of friction remains constant.

The increase of the normal load may be caused by thermo-mechanical effects. The latter are often present in systems with geometric constraints, such as journal bearings. The thermo-mechanical seizures are very strongly system-dependent and their prevention in practice can benefit little from a fundamental study of films formation and destruction. The most effective way to avoid these seizures is by a better design based on a careful thermal and mechanical analysis of the system.

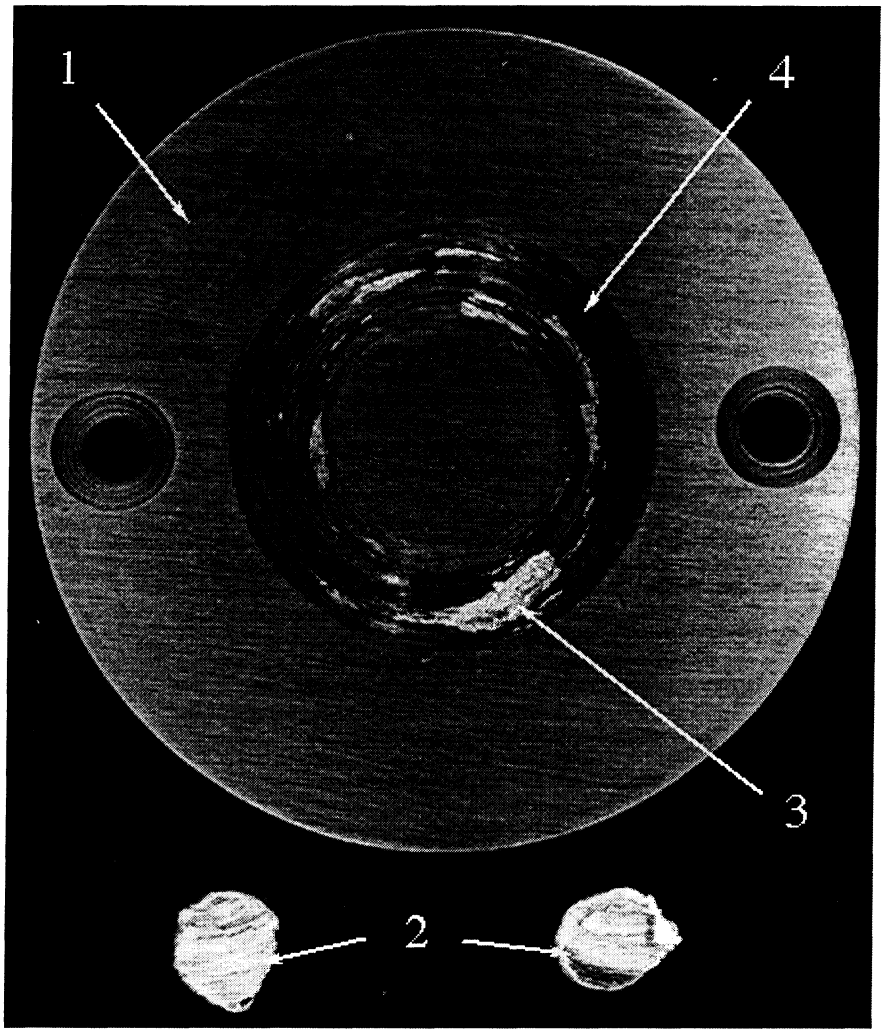

Fig. 1.1 - Typical scuffing failure of a two pins-on-disk area contact
Material of the disk: 1018 steel, Material of the pins: 390-T6 Al
The numbers in the photograph denote: (1) Virgin surface of the disk
(2) Top surfaces of the pins, (3) Large transfer particle, and (4) Wear scar

b. An increase in the coefficient of friction under constant normal load.

The seizures of this type are less system-dependent and can be expected to follow more general laws. They may be caused by formation of cold welds. These are the seizures of interest in the present study. They are characteristic of systems with no geometric constraints.

c. An increase in both normal load and friction coefficient.

The definition of scuffing requires the formation of welds between the sliding surfaces. As Ludema [9] points out, this definition is appropriate only for the final stage of the process, when macroscopically large areas of bare metal are generated and a strong adhesion between the sliding surfaces exists. The experimental data reported in the literature and the data obtained in the present study suggest that the scuffing process is far more complicated and can go through several stages and transitions. These have rarely been recognized as a part of the scuffing process.

Another problem of the above definition is that formation of cold welds occurs practically always when two metals are in contact, either moving, or stationary. The existence of microscopically small areas (known as A-spots) over which metal adhesion (cold welding) occurs is the reason for the ability of metals to conduct electric current through their surfaces, which are normally covered by oxides and other films [18]. Although other mechanisms for current conduction such as tunneling can also contribute to the electric conductivity, the major part is due to the contact of bare metal surfaces [18,19]. These areas are usually very small and can constitute only few parts per million of the real area of contact [19]. Another proof for the existence of microscopic cold welding is the mutual material transfer between bodies in sliding contact. Maps of chemical elements found on the surfaces of metals in sliding contacts have proven that traces of the counterface material are always detected [20-22]. The conclusion is that scuffing is not about whether cold welding occurs or not, but it is about the scale of this phenomenon. Clearly, there is a transition in the behavior of the materials which leads to an unstable growth of the microscopic A-spots to areas which may encompass the whole load-bearing surface. Based on this argument, it is necessary to add a transition condition in the definition for scuffing.

The two transitions which have been most widely used are the transitions in friction and wear. A sharp increase in friction is almost invariably observed at scuffing. This is the reason why the coefficient of friction is the most widely used indicator of scuffing in laboratory conditions. However, a transition in friction does not always indicate the formation of macroscopic cold welds. Other physical processes may also lead to a change in friction. A large increase in friction is often observed during the transition from a hydrodynamic or elasto-hydrodynamic lubrication, in which the surfaces are completely separated by a lubricant film, to a boundary lubrication, in which there is extensive contact between the surfaces. Similarly,

transitions in wear may be caused by a change in the dominant wear mechanism. As with the friction coefficient this change may not be associated with the formation of large-scale cold welds. In fact, most of the ambiguities in the literature have been caused by using these transitions as sufficient indicators for scuffing.

An alternative definition, given by Ludema [23], characterizes scuffing as "a roughening of surfaces by plastic flow whether or not there is material loss or transfer". However, the most important function of a definition is to distinguish with the least possible ambiguity between scuffing and no-scuffing conditions. The latter is not very helpful in that respect, because it lacks an appropriate reference. In addition, similar to friction and wear, transitions in surface roughness may not necessarily be caused by scuffing.

Transitions in the regime of lubrication (hydrodynamic or elasto-hydrodynamic to boundary) have often been described as scuffing [1-3]. It is obvious that a definition based on these criteria cannot be applied to dry sliding conditions. In addition, there are numerous examples of contacts capable of taking far higher loads, after such a transition has occurred. Therefore, these transitions represent only a necessary condition which makes their usefulness questionable.

It seems that the definition of the OECD is still the most convenient to use. Therefore, it was the definition used in this study. However, the scuffing condition was identified by several of the manifestations of this process, which are discussed in more detail in Section 1.2 below.

1.2 Phenomenological Manifestations of Scuffing

Scuffing can have various manifestations. In practice, the first obvious signs of scuffing are the increased noise and vibrations, followed by a progressive increase in the operating temperature. In the worst case scenario this leads to seizure - the complete stopping of motion. In a laboratory environment, scuffing can be detected by sharp transitions in various parameters. These are:

a. Transition (sudden increase) of the coefficient of friction.

b. Transition in the wear rate.

This transition is an indication of a change in the dominant wear mechanism. A nonlinear accumulation of wear is also often observed. This is very different from the "normal" wear mechanisms which lead to a stable and predictable material removal, usually described by a linear dependence on time. This non linearity indicates an unstable condition at the interface.

c. Sharp increase in surface and subsurface temperatures.

The increase in temperature is due to the higher coefficient of friction. The increased temperature may also cause large thermal expansion, thermo-mechanical loading, and thermal stresses. These in turn, may further deteriorate the conditions at the interface. This positive feedback can easily become unstable and lead to seizure.

d. Destruction of solid surface films.

The destruction of surface films is a very important feature of scuffing. In fact, it is the cause for scuffing. A run-time indicator for this process is the electric contact resistance. Scuffing is detectable by orders of magnitude drop in electric contact resistance.

e. Roughening of the surface.

The roughening of the surface is caused by the change in the wear mechanism. Large amount of plastic deformation is also associated with the surface roughening. Very large wear particles are also typical.

f. Gross material transfer.

Large amount of material transfer is observed. This is due to the strong adhesive bonds formed between bare metal surfaces, and facilitated by a weakening of the bulk material by various damage accumulation mechanisms, most notably formation of voids and cracks. Generally, the transfer is from the weaker to the stronger material.

g. Increased noise and vibrations.

This is caused by the increased surface roughness and by the presence of large transfer particles.

None of these features can be used solely as a reliable indicator of scuffing. As stated earlier, transitions in friction and wear may not necessarily be caused by scuffing. They can be due to changes in the regime of lubrication (if a lubricant is present), or changes in the wear mode (from corrosive to delamination for example). Large drops in the electric contact resistance can occur during transitions in the lubrication regime. Material transfer occurs continuously under boundary lubricated conditions and the distinction between micro and macro transfer is not clear. The most reliable proof that scuffing has occurred is the careful examination of the surface after the test. Unfortunately, this cannot be used for real-time monitoring and identification of scuff initiation. Typically, all the above manifestations are present at scuffing. There are, however, cases in which some of these may not be readily observed. Therefore, only the combined use of all of the above features can identify this process with the required degree of confidence.

1.3 Factors Affecting the Scuffing Process

Besides contact load, sliding velocity, environmental temperature, and loading history, which have always been recognized as important factors affecting scuffing, this process is strongly affected by additional factors which often make the study of scuffing very complex. These factors are:

a. Geometry of contact.

The geometry of contact often determines the lubrication regime. In addition it plays a major role in the distribution of local surface and subsurface contact stresses. The geometry of contact is also important for the ability of the contact to generate and dissipate thermal energy.

b. Surface roughness.

Together with the geometry of contact it determines the magnitudes of the real area of contact, the local contact pressures and temperatures. Surface roughness plays a major role in the establishment of hydrodynamic or elastohydrodynamic lubrication. It is also possible that it plays a role in the formation of transformed layers on the contacting surfaces.

c. Mechanical, thermal and chemical properties of the contacting bodies.

These factors are of primary importance. The mechanical properties determine whether the material can withstand the high local stresses and temperatures. The thermal properties affect the ability of the material to dissipate effectively the generated frictional heat. The chemical properties determine the ability of the material to react with the environment and to form protective films. However, the near surface properties of the bodies may differ significantly from the properties of the bulk material.

d. Chemical properties of the environment.

The ability of the environment to react with the surfaces of the contacting bodies and to form protective films is a major factor in the scuffing process.

e. Availability as well as the physical and chemical properties of the lubricant and the additives.

The ability of the lubricant and the additives to form protective films on the sliding surfaces is often critical. The destruction or thermal degradation of these films if considered by many researchers as the primary cause for scuffing.

f. Accumulation, agglomeration, and compaction of wear debris.

The role of debris in scuffing is controversial. Fine powder-like debris agglomerate in valleys of the surface, facilitating the formation of protective layers. On the other hand, large debris or fatigue wear particles may get jammed into the contact in systems with limited clearance. This may cause extensive plastic deformation and eventually cold welding.

g. Heat dissipation characteristics of the system.

The ability of the system to dissipate the generated frictional heat determines the bulk temperature of the contacting bodies. The temperature affects both the mechanical strength and the reactivity of the chemical species.

1.4 The Practical Importance of Understanding Scuffing

Some typical applications where seizure or scuffing may occur are gear teeth, piston rings and cylinder pairs, cams and followers, splines, sleeve bearings, and parts of swash and wobble plate compressors. Unlike other tribology-related failures, scuffing and its most severe manifestation, seizure, occur very fast, without any warning, and usually lead to the complete destruction of the sliding pair. This is the major reason why a large number of studies have been devoted to this phenomenon. However, scuffing is still not completely understood. The reason is that most of the studies on scuffing have been phenomenological in nature. Practical experience accumulated throughout the years with some widely used engineering materials and lubricants has helped to outline safe ranges of operation for some components. This practical knowledge cannot be used to predict the performance of the same components if they are made of other materials, or if they operate under different conditions. With the development of new materials and lubricants and the replacement of some conventional materials by lighter and cheaper substitutes, this problem becomes more apparent. Clearly, it is necessary to outline some more general criteria for materials selection based on a fundamental understanding of the scuffing process. As Ludema [23] and Dyson [24,25] point out, the slow progress in understanding scuffing and seizure is due to the lack of adequate analytical models and understanding of the details of protective film formation and destruction.

It is well known that scuffing is strongly dependent on the materials used in the sliding pair. Historically, most of the scuffing studies have been concerned with gears, cams and followers, and piston ring/cylinder pairs in internal combustion engines [24,25]. Therefore, steel is the material which has received most of the attention. Relatively little is known about aluminum, which is the second most commonly used engineering metal. This is in spite of the fact that aluminum and stainless steel are among the materials which scuff more easily [26]. As aluminum alloys become more common in tribological applications [27], the need for a better understanding of their scuffing behavior is increasing. The present study is an attempt to obtain a better understanding of the events leading to scuffing and seizure of aluminum.

The aluminum alloys used in tribological applications can be subdivided into two major groups [27]. In the first are the aluminum alloys used for bearing applications. The most common

use of these alloys is for journal bearings in internal combustion engines. These alloys typically contain soft metals, such as tin and lead, as alloying elements [27]. Graphite particle aluminum-matrix composites are another alternative meant for similar purposes [28]. The other major group of aluminum alloys designed for tribological applications are the silicon containing alloys. These are primarily designed for wear resistance and strength. Some of these alloys are used as replacements for cast iron, which often leads to weight and cost savings [29]. A typical example is the use of 390 aluminum instead of ductile cast iron in automotive air conditioning swash-plate compressors. A comprehensive review of the tribological behavior of various aluminum alloys is given in [27].

Scuffing studies on aluminum have been conducted for the first group of alloys [30-32]. The major concern of these studies is the optimization of the metallurgical composition, the microstructure, and method of fabrication of the alloys. Similarly, most of the studies on the silicon-containing alloys have been concerned with the optimal silicon content for wear resistance [33-38]. Few of these studies have addressed the scuffing behavior of the aluminum-silicon alloys, and the results presented in these papers are primarily phenomenological observations [39-40]. Since the popularity of the silicon-aluminum alloys is growing, there is a need for a better understanding of their scuffing behavior.

1.5 Progress in Understanding Scuffing

Serious studies on scuffing began approximately sixty years ago. In 1937, Block [41] postulated that scuffing occurs when a critical temperature of the surface is reached. His conclusions were primarily based on experimental work with gears. This work showed that gears, lubricated by straight mineral oils, scuffed when the temperature of the surface became approximately 150°C. This finding coincided with a major development in the field of tribology, which revealed the important role of adsorbed mono-molecular layers of lubricants in reducing friction and wear. It has been known for years that organic polar molecules such as fatty acids and alcohols adsorb on metallic surfaces and are not easily removed. Other lubricants such as mineral oils also posses this property, although the adsorption is weaker. This has led to the development of the adsorption model of lubrication which was first introduced by Hardy and Doubleday [42,43], and further developed in the classical work of Bowden and Tabor [44]. The effectiveness of the adsorbed layer as a lubricant is limited by the surface temperature. At high temperatures this layer desorbs or decomposes. It was natural to associate Block's postulate with the temperature of desorption of protective layers, which led to the formulation of the first and the best known hypothesis for scuffing. This hypothesis states that scuffing occurs when the surface temperature

reaches a critical value, at which desorption of the surface films occurs. This hypothesis has been evaluated in numerous studies, but the results are controversial [24]. It seems that it works well only for concentrated contacts between steel surfaces lubricated by straight mineral oils.

Extension of the above hypothesis have been proposed to account for the role of films which react chemically with metal surfaces [45]. These can be formed by additives or other chemically active species, most notably oxygen. The role that oxides and other chemical compounds play in the scuffing process is well known. Tests in vacuum have shown that even traces of oxygen can considerably increase the scuffing loads [44]. This has led to the hypothesis that scuffing is associated with the rate of oxide formation and destruction [5]. Both of these rates are viewed as functions of temperature. Thus, this hypothesis is also based on a critical surface temperature condition.

In the 1950's, another major development in the field of tribology was started. This was the recognition and understanding of elastohydrodynamic lubrication (EHL). The first notable breakthrough in this field occurred in 1949 when Grubin [46] managed to incorporate both the elastic deformation of the solids and the viscosity-pressure characteristics of the lubricant in analyzing the inlet region of lubricated non-conformal machine elements. Since then, the EHL has been an area of intensive research for more than thirty years. Therefore, it is not surprising that the EHL approach was used as a tool to study scuffing. Scuffing was explained as a collapse of the hydrodynamic and elastohydrodynamic films, which under normal operating conditions separate the sliding surfaces completely [47]. The common understanding is that a system is in danger of scuffing whenever the thickness of the fluid film between surfaces becomes less than the average height of asperities on the sliding surfaces. When this happens, some asperities come into contact with asperities from the counterface which results in high local temperatures. These temperatures may lead to reduction of the viscosity of the lubricant, more contact, and further increase in temperature. The final result is a total collapse of the lubricant film and severe adhesion. Thus, the collapse of the EHL film was explained as a thermally-driven phenomenon. This hypothesis was initially proposed in the work of Dyson [47], Tallian et al. [48], and Berthe et al. [49], and was developed further to account for the effects of a micro EHL on an asperity level by Cheng et al. [50,51] and Houpert et al. [3]. An alternative explanation for the collapse of the EHL was proposed by Enthoven and Spikes [15]. They suggested that accumulation of wear debris at the inlet of the contact is responsible for lubricant starvation and extensive asperity contact. The condition for scuffing is usually expressed in terms of the ratio Λ, which is defined as:

$$\Lambda = h/\sigma \tag{1.1}$$

where h is the fluid film thickness and σ is the composite surface roughness of the sliding pair. Extensive work suggests that there is some validity to the Λ criterion, but only in the rare case of minimum reactivity between chemically active species in the lubricant and the sliding surfaces [52]. Another difficulty of this approach is that, under isothermal conditions, hydrodynamics predicts that the lubricant film thickness increases with the sliding velocity. Hence, for the same load, the possibility of scuffing should be lower at higher velocities. However, the experimental studies of concentrated contacts (most notably the so-called IRG program [53-60]) show that the trend is exactly the opposite. Hence, the effect of decreasing film thickness due to high temperature must overpower the effect of increasing film thickness due to velocity. The conclusion is that, similar to Block's postulate, the EHL hypothesis gives good correlation with the experimental data in some cases, but generally scuffing can occur at very different values of Λ.

The major problem of the desorption and the hydrodynamic approaches is that the effect of the mechanical properties of the contacting surfaces is not taken into account. Both desorption of surface films and generation of hydrodynamic films are not functions of the strength or the metallurgical composition of the materials. This contradicts the results from numerous experimental studies. In an attempt to solve this problem the plasticity index has been proposed as a criterion for scuffing by Greenwood and Williamson [6]. The plasticity index is a measure of the amount of surface plastic deformation due to the contact between the asperities. It was postulated that scuffing will occur at some critical level (2%) of surface plastic deformation, which would lead to the destruction of the protective surface layers (thought to be mainly comprised of oxides). The parameters included in the estimation of the plasticity index are the hardness of the material, the equivalent modulus of elasticity, the composite surface roughness and the average radius of the asperities. Some experimental support of the plasticity index approach was provided in the work of Hirst and Hollander [7]. The most complete set of experiments for the validation of this hypothesis was conducted by Park and Ludema [61] Their results suggest that the correlation between scuffing and the plasticity index is weak. Similar to the Λ-ratio criterion, scuffing occurred in a wide range of plasticity index values. In addition, they found that the surface plastic deformation at scuffing was much higher than the postulated 2% level. Although the simple plasticity index approach does not correlate well with the experimental data, the concept of surface plastic deformation as the primary reason for scuffing seems to be valid in some cases. This concept was further developed in the work of several researchers [8,52].

A major break-through in the present understanding scuffing came from a recent study of the scuffing behavior of aluminum alloys by Somi Redy et al. [16]. Their results suggest that scuffing is due to a bulk subsurface failure. Another study by Kim and Ludema [62] correlates scuffing to low cycle subsurface fatigue. In general, following the introduction of the delamination

theory of wear by Suh and coworkers [63], the attention of many researchers has shifted from the surface to the subsurface. It seems that subsurface plastic deformation, bulk temperature, and bulk material properties may be more relevant to scuffing failures under dry sliding conditions than are the asperity-level interactions and the conditions at the surface.

The critical temperature, the EHL collapse and the critical surface and/or subsurface plastic deformation hypotheses represent the basis of the current understanding of scuffing. These hypotheses are based on very different physical processes which makes their generalization in a single theory of scuffing very difficult. The only common feature of these hypotheses is the destruction of protective films, although each hypothesis deals with films of very different physical and chemical nature. In general, it seems that the key to understanding scuffing is the dynamics of protective films formation and destruction. In some cases, films of various nature may be present at the sliding interface, building several lines of defense of the material against scuffing. Destruction of one of these lines of defense does not necessarily lead to scuffing. All of them should be removed for scuffing to occur. This view can be expressed in terms of necessary and sufficient conditions for scuffing, as suggested by Lee and Cheng [64]. The failure of EHL films and the destruction of adsorbed films represent only necessary conditions for scuffing. In the present study, it is suggested that the sufficient condition for scuffing is given by a subsurface failure due to extensive subsurface plastic deformation and subsurface fatigue.

1.6 Scope of Research

The present work is part of a joined study on scuffing by researchers at Northwestern University and the University of Illinois at Urbana-Champaign. This study is sponsored by the National Science Foundation UICRC program and is primarily focused on fundamental problems of scuffing of aluminum/steel contacts.

The present work is also part of a larger research project which addresses various tribological problems arising from the replacement of the currently used refrigerants by ozone-safe refrigerants. The project is sponsored by the Air Conditioning and Refrigeration Center (ACRC), an industry-university cooperative research center which performs studies on refrigerant and air conditioning systems.

In a series of previous studies [65-70], the tribological behavior of various materials and lubricants/refrigerant mixtures was investigated. The refrigerant which was studied in more detail was tetrafluoroethane (R134a). Tetrafluoroethane, a replacement for dichlorofluoromethane (R12), is primarily used in household refrigerators and mobile air conditioners. R134a is also a

major constituent in the refrigerant blends intended for use in household air conditioners. In these studies, it was found that the tribological properties of the R12/lubricant mixtures are generally not matched by the R134a/lubricant mixtures. The reason is that R12 reacts with metal surfaces to form metal fluorides and chlorides which are good solid lubricants. R134a did not seem to possess any lubricative properties. This lack of lubricative properties is thought to be one of the major reasons for the observed increased scuffing failures in some automotive swash plate compressors. The interest in the air conditioning and refrigeration industry for a better understanding of these failures was one of the reasons which led to the present study.

The materials pairs generally used in the refrigerant swash plate compressors are 52100 steel shoes sliding on a 390-T6 Al plate and Si-Pb brass shoes sliding on a hardened ductile cast iron plate. Scuffing problems, however, seem to be more prevalent with the aluminum/steel contact. Therefore, the major emphasis of this study was on these contacts.

The sliding contact in the swash plate compressor is lubricated by a lubricant/refrigerant mist. However, on rare occasions at compressor start-ups, the contact may run with very little or no lubrication for several seconds. Typically, this is the time when the scuffing failures occur. Therefore, understanding scuffing under dry sliding conditions may provide insights for the behavior of these machine components.

The scope of the research is not limited to the practical problem of scuffing in swash plate compressors. It is aimed at obtaining a more fundamental understanding of the physics of the scuffing process under dry sliding conditions. To this end, limited scuffing data are also obtained for steel/steel and brass/steel contacts. The geometry of contact used in the swash plate compressors is not suitable for a fundamental study because it is difficult to manufacture and instrument. For these reasons, it is replaced by a pin-on-disk contact which provides more repeatable experimental results. The 52100 steel is also replaced by 1018 carburized steel due to the availability of the 1018.

1.7 Objectives of Research

As stated in Section 1.3, scuffing is a very complex phenomenon. In order to understand its fundamentals, it is necessary to simplify the problem and to exclude the effect of some of the variables. In this study, scuffing under dry sliding conditions is examined. The effects of the lubricant and its possible interactions with the surfaces of the materials and the environment are excluded from consideration. It is expected that a better understanding of scuffing under dry sliding conditions will provide valuable information for the relative importance of the various

factors affecting scuffing in general. The results from the study under dry sliding conditions will also serve as a guideline for a more complex study of the general case of scuffing under lubricated conditions in the future.

The present research focuses on two major goals. The first is to obtain a set of experimental data for the scuffing behavior of several materials contact pairs. The second goal is to study the physics of the scuffing phenomenon, evaluate the existing hypotheses for scuffing and explore the possibilities for a theoretical description of scuffing. A more detailed description of these objectives is given below:

a. Objectives of the experimental studies

(1) Develop an experimental technique and its corresponding instrumentation, enabling the reliable identification and characterization of scuffing under laboratory conditions.

(2) Obtain experimental data for scuffing of various aluminum/steel contacts under dry sliding conditions in air and refrigerant (R134a) environments.

(3) Study the effects of the material, temperature, contact geometry, type of environment, loading history, and time on scuffing.

(4) Study the surfaces, subsurfaces and wear debris of failed specimens and specimens in the process of scuffing.

(5) Obtain quantitative data characterizing the subsurfaces of the test specimens. Obtain quantitative data for the accumulation of plastic deformation in the subsurfaces.

b. Objectives of the theoretical studies

(1) Based on the experimental observations, obtain a better understanding of the physical nature of scuffing.

(2) Model the surface interactions between the specimens under dry sliding conditions. Obtain estimates for the local states of stress, strain, and temperature on and below the surface.

(3) Evaluate the existing hypotheses for scuffing in the light of the experimental observations and the theoretical models.

(4) Develop a new hypothesis and criterion for scuffing.

1.8 Organization of the Thesis

The thesis is organized in nine chapters. Chapter 1 is the introduction to the problem and states the objectives of research. The experimental setup, instrumentation, and test procedures are described in Chapter 2. Chapter 3 presents the experimental results for the scuffing of various aluminum alloys in air and R134a environments. Limited data are also provided for steel/steel and brass/steel contacts. Chapter 4 describes the observations of subsurfaces, surfaces and wear debris. It also gives the method and the results from the quantitative measurements of subsurface plastic deformation. A finite element model for the contact of runned-in surfaces is developed in Chapter 5. The model gives estimates for the magnitude and the distribution of local surface pressures and areas of contact. Models for the state of stress, temperature and strain in the subsurface are discussed in Chapter 6. The existing hypotheses for scuffing are evaluated in Chapter 7. A new hypothesis for scuffing and its corresponding criterion are given in Chapter 8. The conclusions of this study and recommendations for future research are given in Chapter 9. The results obtained in each chapter are summarized at the end of the chapters. Contributions to the present state of knowledge in the field of scuffing due to original work conducted in this study are also summarized at the end of the chapters.

CHAPTER 2
EXPERIMENTAL SETUP

Scuffing is affected by numerous factors and can have various manifestations. A successful experimental study of scuffing must provide both accurate control of these factors and reliable means to identify the scuffing condition. In this study, the first of these tasks is achieved by conducting the tests in a specially designed high pressure tribometer (HPT) and by choosing suitable contact geometry, materials for the specimens, and operating conditions. The second task is achieved by the installation of special instrumentation.

2.1 Tribometer

As indicated in the previous chapter, the present study is part of a larger program, which addresses the tribological behavior of contacts operating in a refrigerant environment. The properties of the refrigerants and the properties of the lubricant/refrigerant mixtures are very strong functions of the environmental conditions. Therefore, the HPT, which was specifically built for the purposes of this research program, was designed with capabilities for accurate environmental control. The present study benefits from these capabilities, because scuffing is also a process which is strongly dependent on environmental factors. The environmental temperature and the type of the environment (air or R134a) are two of the factors, which effects were investigated in the present study.

In the HPT, the relative motion between the specimens is achieved by attaching one of the specimens to a rotating spindle, while keeping the other specimen stationary. The motion of the spindle can be either simple unidirectional (0-2000 rpm), or oscillatory with a variable amplitude (0-180°), frequency of up to 5 Hz, and a sinusoidal or a triangular wave form. The contact load on the specimen can be constant or oscillatory with the same frequency and wave characteristics of the spindle motion. It can be set to any value between 45 and 4450 N. For the purposes of this study, the HPT was equipped with a computer control of the axial load and the angular velocity of the spindle. The computer control is achieved through control boards and a set of solid-state relays. The corresponding software which was also developed as a part of this study allows for complicated loading and sliding velocity histories.

The major advantage of the HPT is that the test is conducted in a sealed chamber (Fig. 2.1). The pressure in the chamber can be set to values up to 1.72 MPa. The chamber is first purged to a vacuum of 0.1 Torr, after which the desired gaseous environment is introduced.

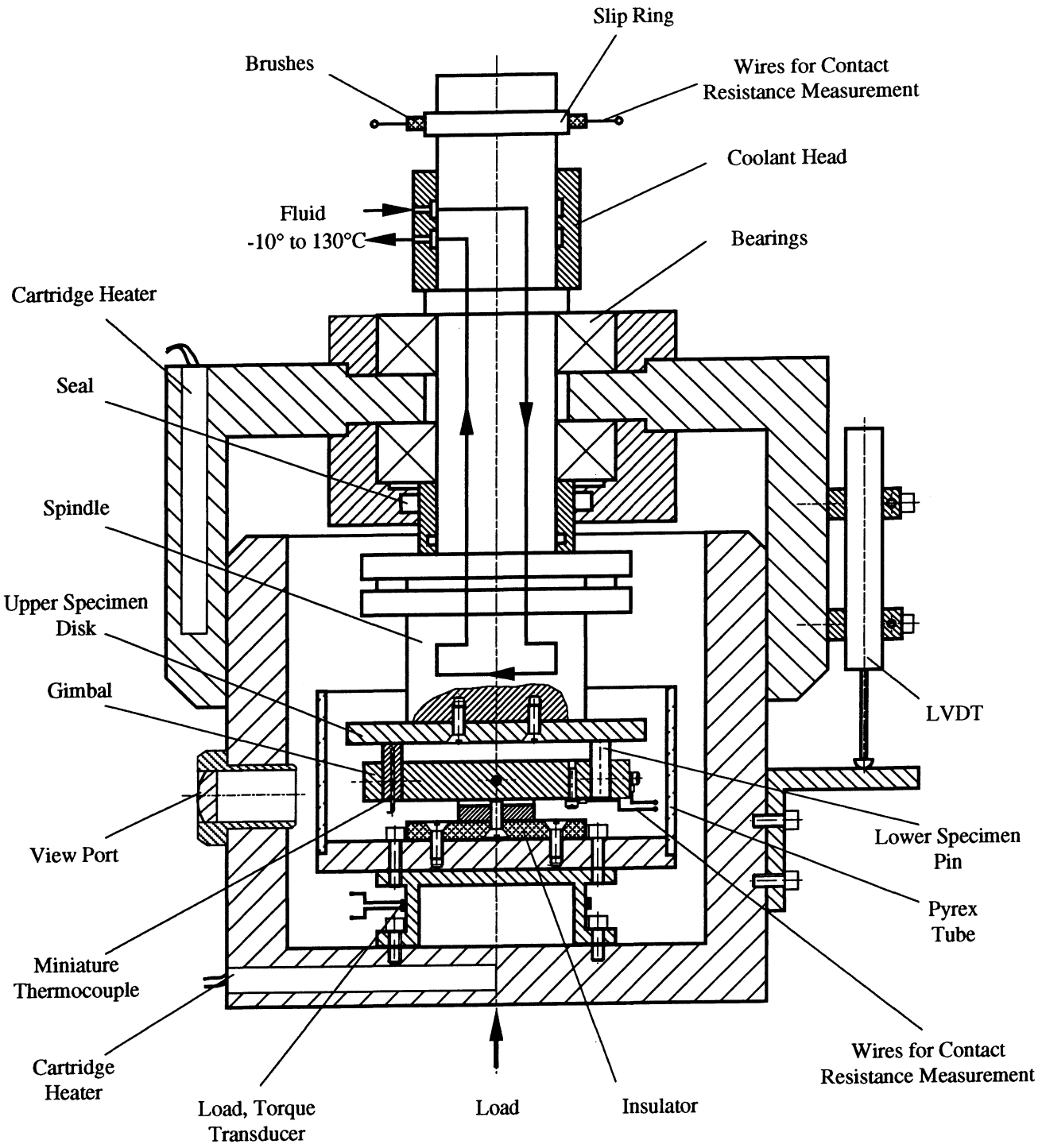

Fig. 2.1 - Schematic of the pressure chamber of the HPT

The environmental temperature in the chamber of the HPT can be raised to 120 °C by cartridge heaters. The desired temperature of the contact is obtained by pumping heat transfer fluid through the spindle. The temperature of the fluid is controlled within a 0.1 °C accuracy by an external unit which is capable of maintaining constant temperatures from -10 to 130 °C . The HPT is also outfitted with apparatus for purging, charging, sampling, and real time data acquisition and display of test data. A more detailed description of HPT's capabilities is provided in [65].

2.2 Geometry of Contact

A two pins-on-disk area contact was used in this study. A schematic of the geometry of contact is given in Fig. 2.2.

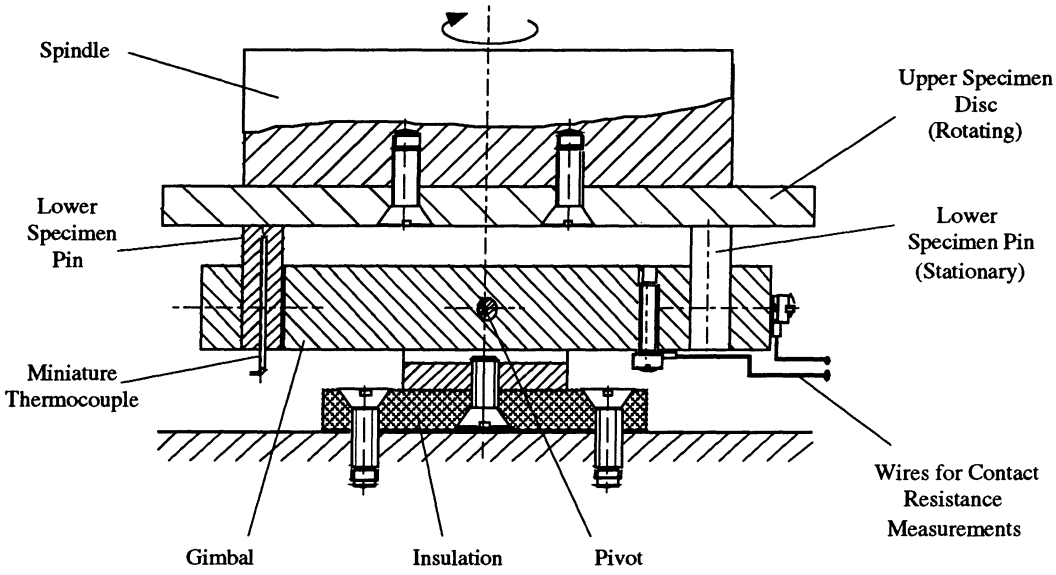

Fig. 2.2 - Two pins-on-disk geometry of contact

The reasons for the choice of this geometry of contact are:

a. This geometry is more easily instrumented.

b. There are no geometric constraints. The thermal expansion of the specimens and other parts of the test rig does not increase the load on the specimens.

c. The geometry of contact does not change with time. As the pins and the disk wear out the apparent area of contact remains the same.

d. The effect of debris accumulation can be excluded from the experiment. Since the disk is the upper specimen, most of the wear debris fall at the base of the pins.

e. Even load distribution due to the self-alignment of the pins/disk interface.

To cover a larger range of contact loads and sliding velocities, two sizes of pins and two sizes of disks were used. For the same purpose, the specimen holders were designed to provide three sliding radii. Data for the various geometries of contact are provided in Table 2.1.

Table 2.1 - Data for the various configurations of the geometry of contact

Designation	R12.7	R35.0	R44.5
Sliding radius	12.7 mm	35.0 mm	44.5 mm
Pin diameter	6.35 mm	6.35 mm	3.175 mm
Disk diameter	63.5 mm	63.5 mm	95.25 mm
Area of contact	63.3 mm^2	63.3 mm^2	15.8 mm^2
Max. sliding velocity	2.66 m/s	7.34 m/s	9.35 m/s
Max. frictional force†	1200 N	400 N	300 N
Max. contact pressure‡	57 MPa	20.5 MPa	63 MPa
†Based on torque limitation of the test rig; ‡Based on axial load limitation of the test rig			

2.3 Materials for the Tests

In all experiments the disk was made of 1018 carburized steel with an average hardness of 62 HRC and average surface roughness of 0.1 μm Ra. Five materials were used for the pins. The majority of the tests were conducted with 390-T6 aluminum (72 HRB), which in a previous study showed the best wear resistance of all aluminum alloys tested [70]. Commercially pure aluminum -1100 (28 HRB), and a Bi-containing aluminum alloy DHT-3 (46 HRB) were also tested. In addition, limited number of tests were conducted with 1018 steel (70 HRB) and Si-Pb brass (80 HRB). Data for the chemical composition of the aluminum alloys tested are provided in Table 2.2. Data for the Si-Pb brass are given in Table 2.3. Under the conditions of this study, the initial surface roughness of the pins is not an important parameter. The wear of the pins is relatively high and the initial surface features are destroyed within seconds after the initiation of the test.

Table 2.2 - Chemical composition of the aluminum alloys tested

Alloy	Alloying elements, % by weight								
	Al	Si	Fe	Cu	Mn	Mg	Zn	Bi	Ti
390	≈ 76.0	16-18.5	1.0	3.0-4.0	0.5	0.4-1.0	1.0	-	0.25
1100	99.0	< 0.9	0.05-0.2		0.05	-	0.1	-	-
DHT-3	≈ 83.0	6.5-12	0.2	2.0-5.0	0.15	-	0.15	3.0	0.2

Table 2.3 - Chemical composition of the Si-Pb brass specimens

Element	Cu	Zn	Mg	Si	Pb	Al	Fe
% by weight	61.5-63.0	30.5-36.0	1.5-3.5	0.5-1.5	0.4-0.8	0.5 max.	0.4 max.

Some data for the mechanical properties of 1100 and 390-T6 alloys are provided in the literature [27]. However, there are limited data for their shear strength at various temperatures and loading rates, a property relevant to this study. To obtain these data, the two alloys were tested according to the ASTM B 565-94 procedure. Typical load-displacement curves obtained with this procedure are given in Fig. 2.3. From the figure, it is evident that the failure mode for 390-T6 Al changes from brittle to ductile at about 250°C.

Figure 2.3 is used to obtain the shear strength of the two alloys as a function of temperature. These data are given in Fig. 2.4. From the figure it is evident that in the whole temperature range the 390-T6 alloy is approximately twice stronger than the 1100 alloy. The curve for the DHT-3 alloy is an estimation based on its room temperature hardness. The rationale behind such an estimation is that the relative decrease in strength with temperature for both the 1100 and 390-T6 alloys is about the same. This is illustrated in Fig. 2.5, where the data of Fig. 2.4 are represented in a non-dimensional form. The shear strength of both alloys increases with the shear displacement rate. These results are summarized in Table 2.4.

Table 2.4 - Shear Strength (MPa) of 390-T6 and 1100 Al
at various shear displacement rates and temperatures

	390-T6 Al			1100 Al		
Shear Rate	0.001 mm/s	0.05 mm/s	5.0 mm/s	0.001 mm/s	0.05 mm/s	5.0 mm/s
T = 150°C	154	170	171	72.5	78.9	83.7
T = 250°C	88.6	123	160	38.4	56.8	66.5
T = 350°C	34.4	52.7	81.3	--	20.7	--

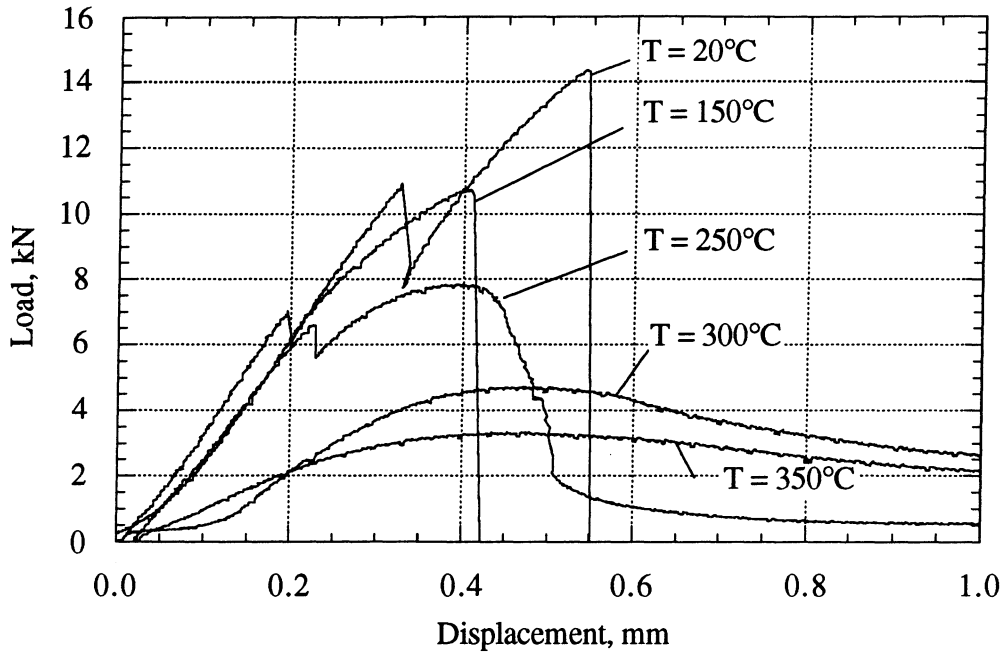

(a)

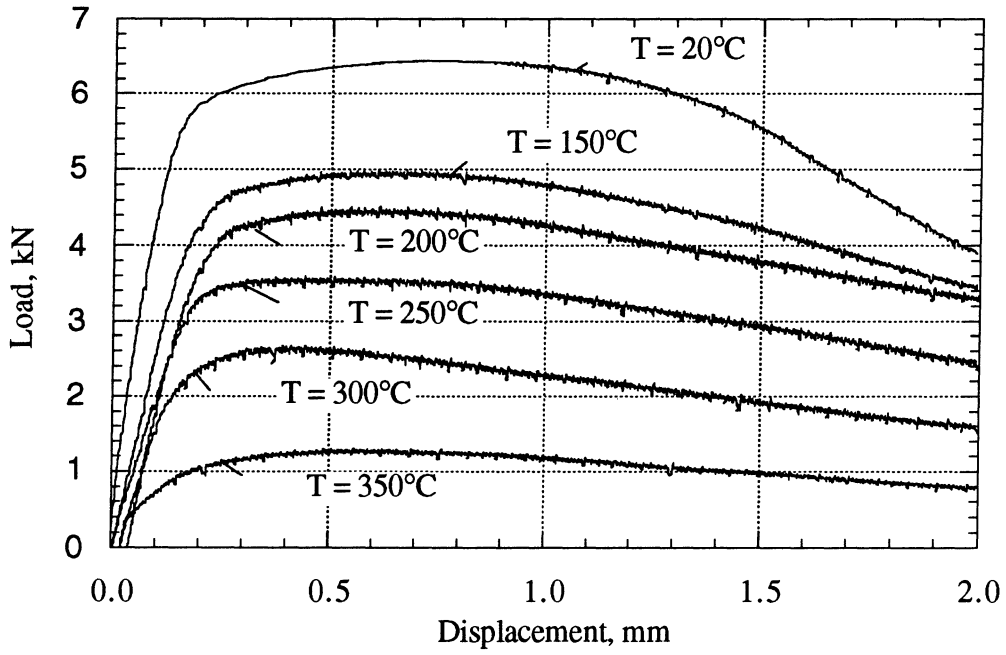

(b)

Fig. 2.3 - Typical load-displacement curves for (a) 390-T6 Al and (b) 1100 Al
Shear displacement rate = 0.05 mm/s.
Note the change from brittle to ductile failure for the 390-T6 alloy

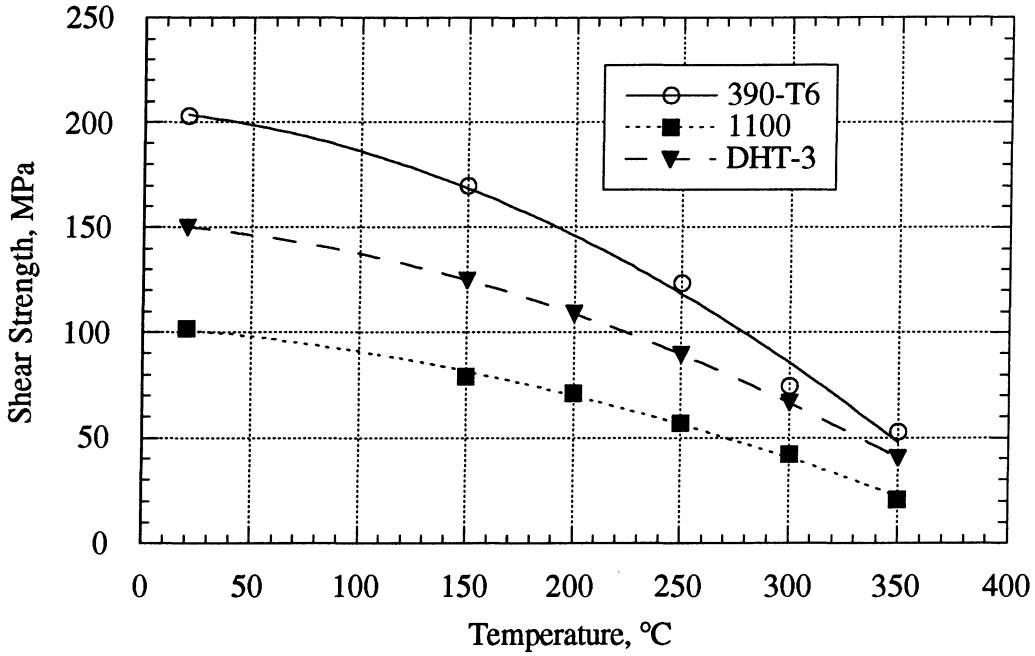

Fig. 2.4 - Shear strength of 390-T6, 1100, and DHT-3 Al as a function of temperature
Shear displacement rate = 0.05 mm/s. The data for DHT-3 are an estimate

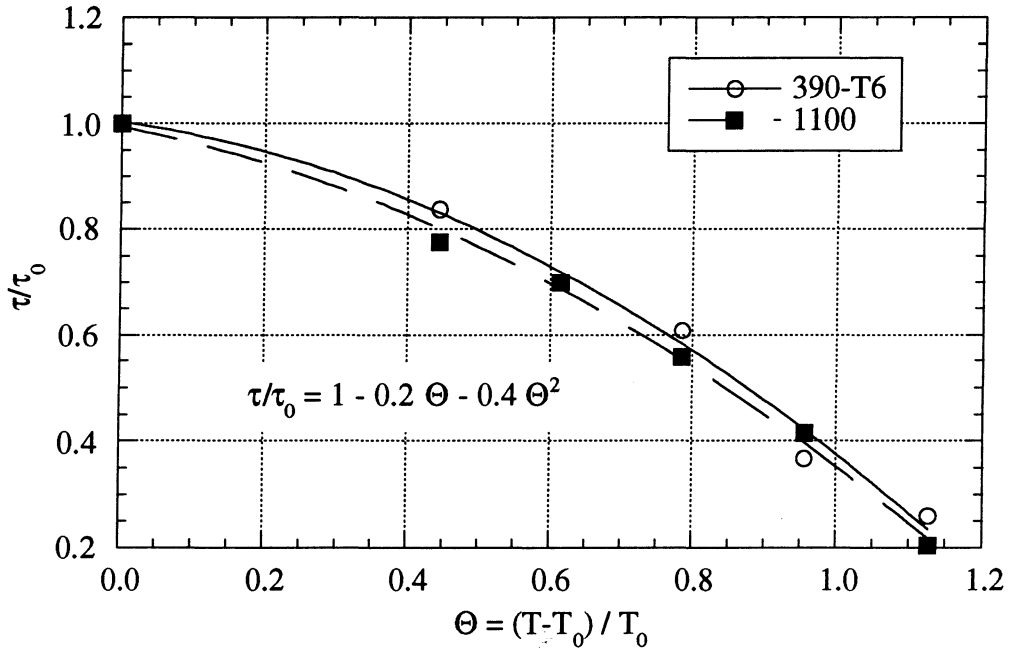

Fig. 2.5 - Relative shear strength of 390-T6 and 1100 Al as a function of temperature
Shear displacement rate = 0.05 mm/s. T_0 = 293°K

2.4 Test Procedure

The temperature and the sliding velocity were kept constant for each test. In most tests, the load was increased stepwise until scuffing occurred. Each time step was five minutes long. The duration of the step was chosen approximately twice the time necessary to reach thermal equilibrium at 2 mm under the surface. Constant load tests with an immediate loading and tests with longer steps were also conducted. Most of the tests were conducted at 30°C environmental temperature. Limited number of tests were conducted at 100°C. The environment for the tests was either air or R134a.

2.5 Instrumentation

The original instrumentation of the HPT included a real-time output for the axial and friction forces, the frictional torque, and the environmental temperature. As a part of the laboratory work reported here, the HPT was equipped with a data acquisition and real-time display systems. The software for these systems was developed specifically for the purposes of this study. To study the scuffing process, it is necessary to reproduce it and identify it reliably under laboratory conditions. This required the installation of special instrumentation. The scuffing condition is identified by transitions in friction, contact resistance, wear, and subsurface temperature. The instrumentation installed for the purposes of this study is described below:

a. Real-time wear monitor.

To monitor the wear continuously during the tests, the HPT was equipped with an LVDT position sensor which measures the relative displacements of the specimens during the test. The sensitivity of the LVDT is approximately 10 μm. The wear rate over several minute-long period of time can be determined with significantly higher accuracy by curve fitting. The lowest reliably identifiable wear rate is 10.0 nm/s. This is demonstrated in Fig. 2.6 showing two sets of position measurements corresponding to two consecutive load steps. The large displacement step between the two sets of data is due to the elastic response of the test rig.

The major advantage in real-time wear measurements compared to measurements after the test is the ability to observe transitions in wear rate which is indicative of transition in the wear mode. This is particularly useful when using complicated load histories or estimating the onset of scuffing.

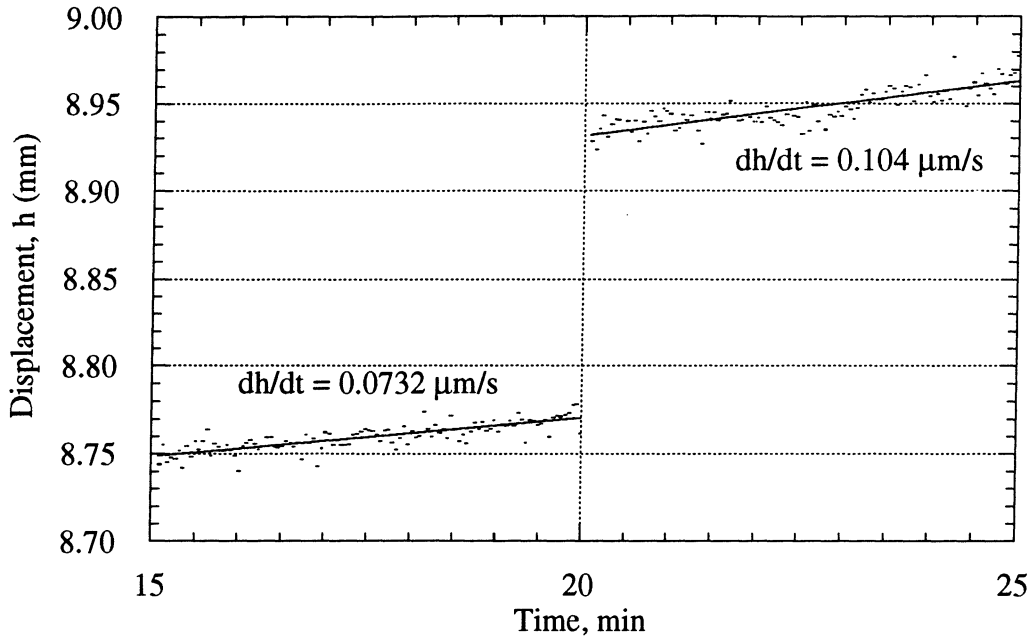

Fig. 2.6 - Typical output from the real-time wear monitor

b. Electric contact resistance measurement.

The electric contact resistance between the test specimens is commonly used as an indicator for transitions in the regime of lubrication [24,71]. However, its practical usefulness has often been limited by the large errors associated with connecting wires and fixtures. The most common arrangement of a contact resistance measurement circuit is given in Fig. 2.7a. Due to the low sensitivity of this circuit, it can be used only as an indicator for a transition from complete separation of the specimens by a lubricant film to a regime where asperity contact occurred. When the specimens are completely separated, the resistance is on the order of $10^6\ \Omega$ and the measured voltage is practically equal to the voltage of the power source. Conversely, when the surfaces are in contact, the output voltage becomes practically zero. The only useful information this circuit can provide is the percentage of time during which surface interactions occur [72]. In the present study, the transition of interest is from boundary lubrication to scuffing. Surface contact occurs all the time, which clearly makes the circuit shown in Fig. 2.7a inapplicable. The contact resistance under boundary lubricated conditions is typically of subohmic value, often dropping to $10^{-6}\ \Omega$ at scuffing. The measurement of such small resistances is not a trivial problem and requires the development of a special circuit, methods for noise suppression, and data processing software. A four-terminal circuit, schematically shown in Fig. 2.7b, was developed for this purpose.

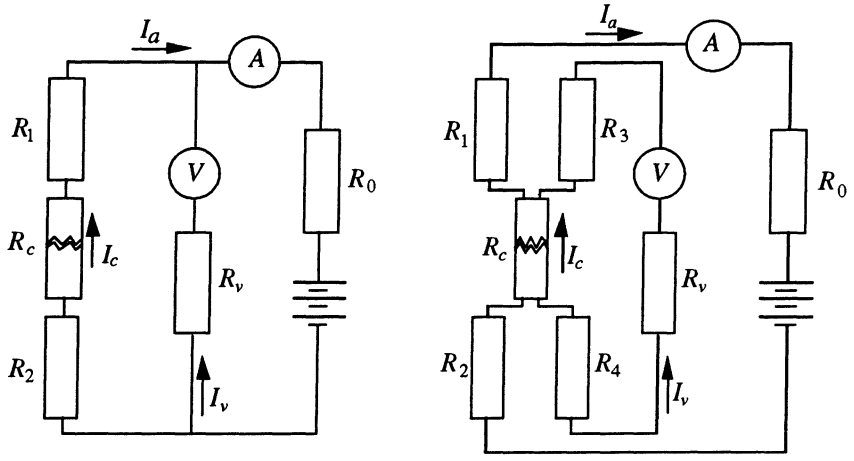

(a) (b)

Fig. 2.7 - DC circuits for contact resistance measurements
(a) Two-terminal and (b) Four-terminal

In the figure, R_c is the measured contact resistance, R_1, R_2, R_3, and R_4 are the resistances of the contacting wires, brushes and fixtures, R_v is the resistance of the voltmeter, and R_0 is a calibrated current-limiting resistance. The currents flowing through different parts of the circuits are denoted as I_a, I_v, and I_c. In both circuits the unknown contact resistance is assumed equal to the ratio of the readings of the voltmeter and the ammeter:

$$R_c \approx \frac{V}{A} = \frac{I_v R_v}{I_a} \tag{2.1}$$

The actual contact resistance for the two-terminal circuit is:

$$R_c = \frac{I_v R_v - I_c(R_1 + R_2)}{I_c} = \frac{I_v R_v}{I_a - I_v} - (R_1 + R_2) \tag{2.2}$$

Comparing equations (2.1) and (2.2), it is evident that there are two sources of error for the two-terminal circuit. The first is due to the assumption that I_a - $I_v \approx I_a$, and the second is due to the assumption that $[(I_v R_v)/(I_a - I_v)] >> (R_1 + R_2)$. The first assumption does not lead to any significant errors because $R_v >> (R_c + R_1 + R_2)$ and consequently $I_a >> I_v$. The second assumption, however, introduces error on the order of the resistance $R_1 + R_2$, which in a typical application is 10^{-3} Ω. This limits the sensitivity to an order of 10^{-2} Ω, which is insufficient for a scuffing study.

The actual contact resistance for the four-terminal circuit is given as:

$$R_c = \frac{I_v R_v + I_v(R_3 + R_4)}{I_c} = \frac{I_v R_v}{I_a - I_v} + \frac{I_v}{I_a - I_v}(R_3 + R_4) \tag{2.3}$$

In this case, the error introduced by the resistance of the wires and fixtures ($R_3 + R_4$) is multiplied by the factor $[I_v/(I_a - I_v)]$, which is a very small number, often on the order of 10^{-9}. Hence, the four-terminal circuit provides a much higher accuracy.

The very high sensitivity of the four-terminal circuit makes it susceptible to various noises. The electromagnetic fields of motors and instruments induce voltages which can sometimes be comparable to the voltage of the signal. In addition, temperature rise at the contact introduces Seebeck thermocouple voltages which can also be significant. In fact, the contact resistance measurement circuit, if properly calibrated, can provide information about the temperature at the contact. To eliminate these errors, the DC power source is continuously turned on and off by a computer controlled solid-state relay. The voltage measured when the power source is off is due to noise. The voltage measured when the power source is on is due both to noise and contact resistance. The difference of these two voltages is the true signal. In the circuit used in this study, this subtraction is conducted by the software. A schematic of the actual circuit used for the contact resistance measurements in this study is given in Fig. 2.8. The measurement range of this circuit is 10^{-6}-10^{+4} Ω. A large drop in the contact resistance is often a more sensitive indicator for scuffing than the coefficient of friction.

c. Subsurface temperature measurement.

The surface temperature is one of the most important tribological quantities. However, its direct measurement is difficult. There are two experimental techniques which can be used for this purpose. The first requires that one of the bodies be transparent. It utilizes an infrared sensor, positioned directly under the transparent specimen [73]. Clearly, this method has limited application. The second method utilizes the Seebeck effect. When two dissimilar metals touch each other a small voltage can be measured across the contact. This voltage is a function of the temperature at the junction. This is the effect utilized in all thermocouples. In a sliding system, the junction of interest is the sliding interface itself. Theoretically, with a proper calibration, the actual temperature at the interface can be obtained. However, the calibration is practically impossible to achieve. This is due to several reasons. These are the oxidation of the surfaces, strain hardening of the surface material, poor junction connection, and high thermal gradients. Each of these individually can compromise the accuracy of any thermocouple measurement, an effect known as decalibration. The combined effect of these factors limits this method to qualitative measurements. A more detailed discussion of the decalibration effects is given in [74].

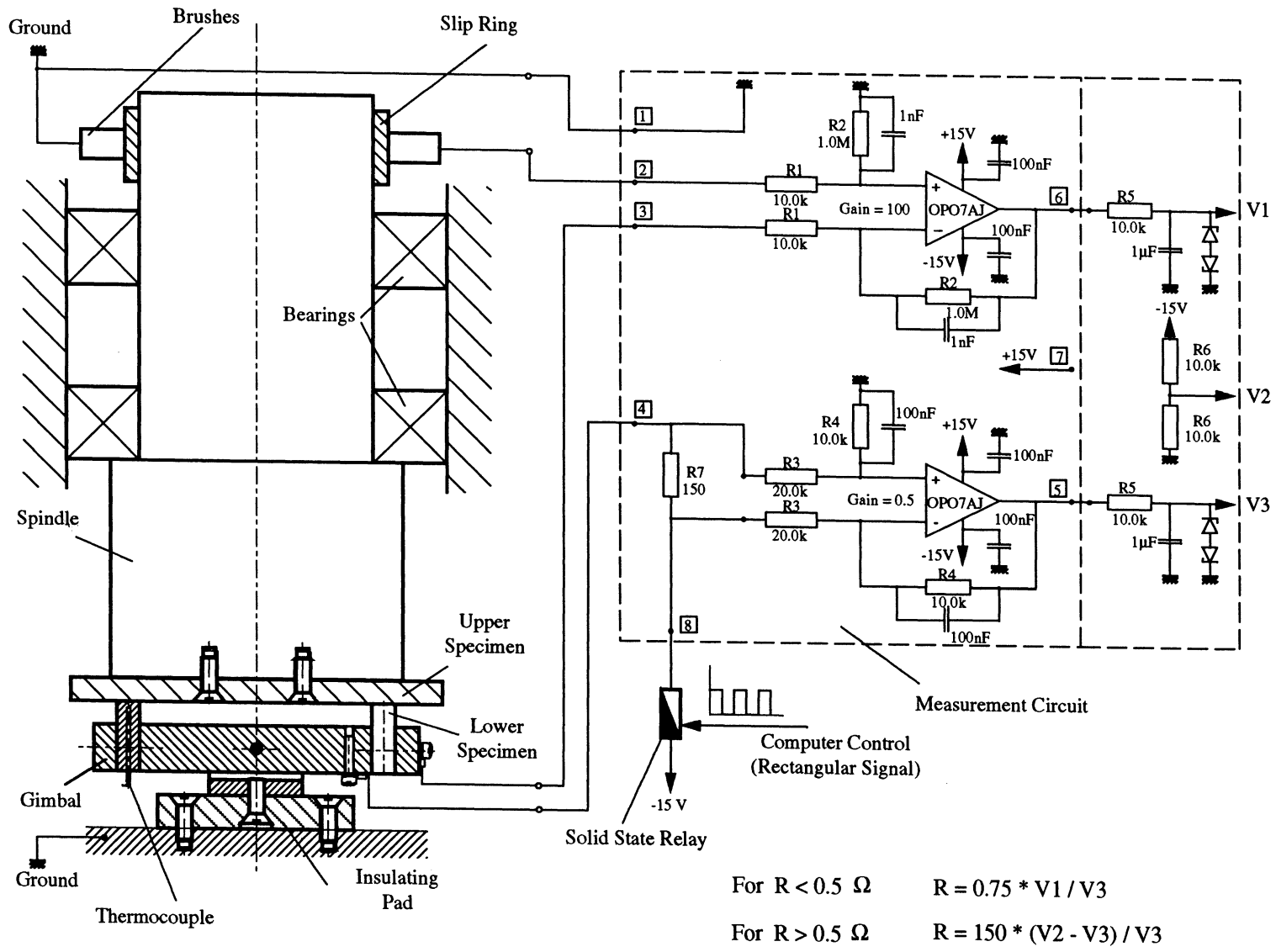

Fig. 2.8 - Schematic of the circuit for electric contact resistance measurements

Because of the above experimental difficulties, the temperature in the vicinity of the sliding interface is often estimated with the aid of thermal models and subsurface temperature measurements. The subsurface temperature in this study was measured by a miniature thermocouple implanted 2 mm below the surface of the pin. Steady-state thermal gradients were obtained by measuring the thermal differences between thermocouples implanted at various depths below the surface. The temperature at the surface and at several depths below the surface was estimated with a finite element model.

2.6 Summary

The experiments in this study are conducted in a specially designed tribometer, which allows accurate control of the environmental conditions. An area, two pins-on-disk geometry is used to study scuffing. Three combinations of pin sizes and sliding radii are tested. Five materials are used for the pins. These are: 1100 Al, 390-T6 Al, DHT-3 Al, 1018 steel, and Si-Pb brass. These materials are slid under dry sliding conditions against 1018 carburized steel disks. The environment for the tests is either air or R134a. Most of the tests are conducted in air at a constant sliding velocity, while the load is increased stepwise.

The instrumentation used to identify scuffing provides run-time records for the coefficient of friction, subsurface temperature, wear, electric contact resistance, and load history. Computer control of the test rig and specially developed software provide the desired load and velocity sequences.

2.7 Contributions

As stated earlier, the experimental data on scuffing reported in the literature is plagued by inconsistencies. These are partly due to the difficulties associated with the identification of scuffing under laboratory conditions. The contribution of this study in this respect is the development of a test setup in which the scuffing condition can be reproduced and identified reliably. This includes the development of a proper test procedure and the installation of special instrumentation. The major achievements in this respect are:

a. Simultaneous monitoring of friction, wear, temperature and electric contact resistance.

Combinations of these parameters have been used in many tribological studies. However, their simultaneous monitoring is applied for the first time as a run-time identification of scuffing.

b. Installation of a high-accuracy contact resistance measurement circuit

The four-terminal circuits for contact resistance measurements are fairly common in the field of electric measurements. However, a high accuracy circuit is applied for the first time to study scuffing.

c. Development of special software for control of the test rig, data acquisition, and data processing.

CHAPTER 3
EXPERIMENTAL RESULTS

The major difficulty in conducting experimental studies of scuffing is the reliable reproduction and identification of the scuffing condition. In this study, scuffing was identified by the sharp transitions in friction, contact resistance, wear rate, and temperature, as shown in Fig. 3.1. Increased vibrations, as the oscillations of the contact pressure at the end of the record indicate, are also typical. When this happens, the surface of the pin is often completely destroyed, while large amount of material is transferred from the pin to the disk.

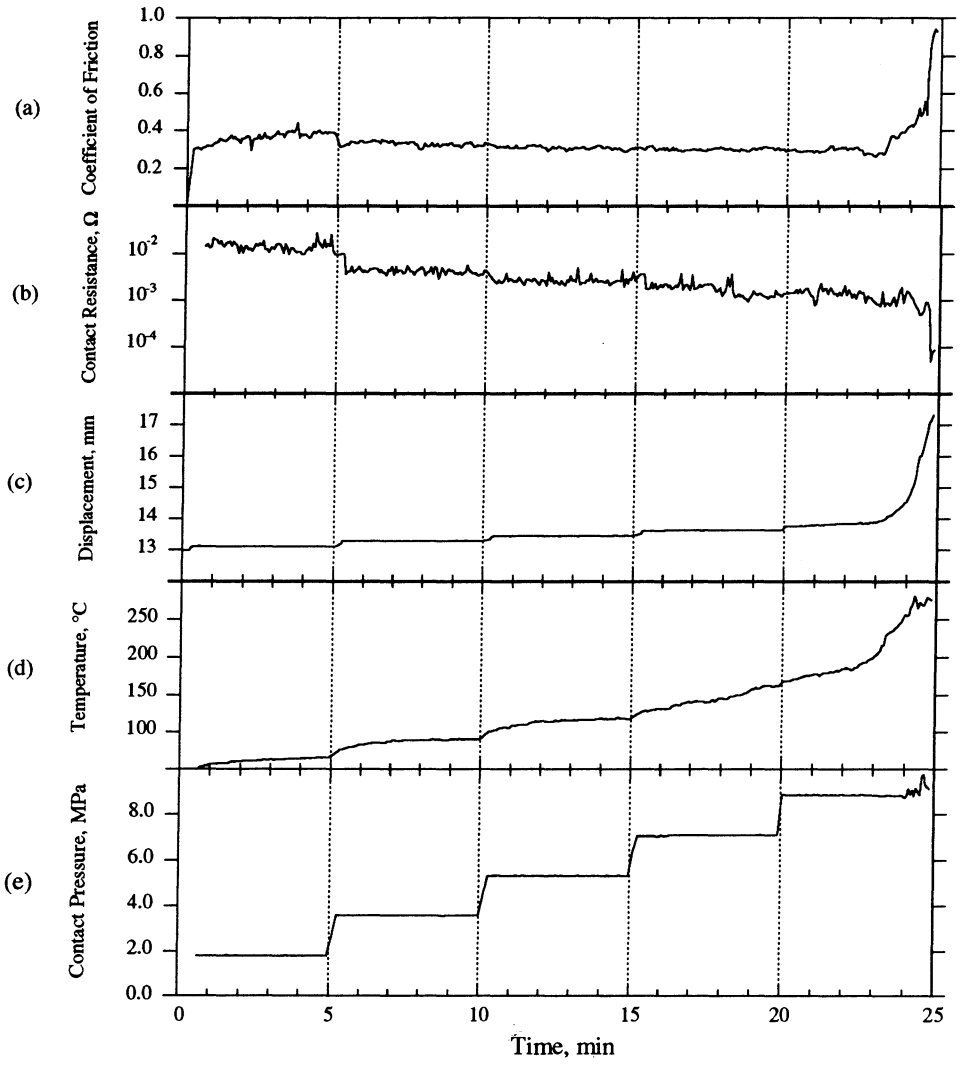

Fig. 3.1 - Typical test results. (a) Coefficient of friction, (b) Electric contact resistance, (c) Wear, (d) Subsurface temperature, and (e) Loading history

3.1 Effect of the Material

Scuffing is strongly influenced by the mechanical and chemical properties of the materials in contact. A comparison of the scuffing *PV*'s for 390-T6 Al, 1100 Al, DHT-3 Al, and 1018 steel is given in Fig. 3.2. From the figure, it is evident that 390-T6 had the best scuffing resistance among the aluminum alloys tested. This can be attributed to its higher mechanical strength, as shown in Fig. 2.4. The steel had the highest scuffing resistance. For all materials tested, the contact pressure at which scuffing occurred decreased with the sliding velocity. For the 390-T6 and 1100 aluminum alloys, the data points fall closely on lines given by $PV = const.$, where P is the contact pressure based on the apparent contact area and V is the sliding velocity. For these two materials, the subsurface temperature just before scuffing was approximately constant along the PV curve and was close to 240°C for the 390-T6 Al and close to 150°C for 1100 Al. The data points for DHT-3 Al and steel deviate from the $PV = const$ relationship and are better described by a power law $PV^n = const$ with $n > 1.0$. For these materials, the temperature just before scuffing was not constant and increased with the sliding velocity. The curve fit parameters, for the curves shown in Fig. 3.1, are summarized in Table 3.1. From the table, it is seen that the scuffing of steel deviates the most from the $PV = const$ behavior. Its scuffing is also characterized by the largest temperature differences: 302 °C at 0.33 m/s and 460°C at 2.66 m/s.

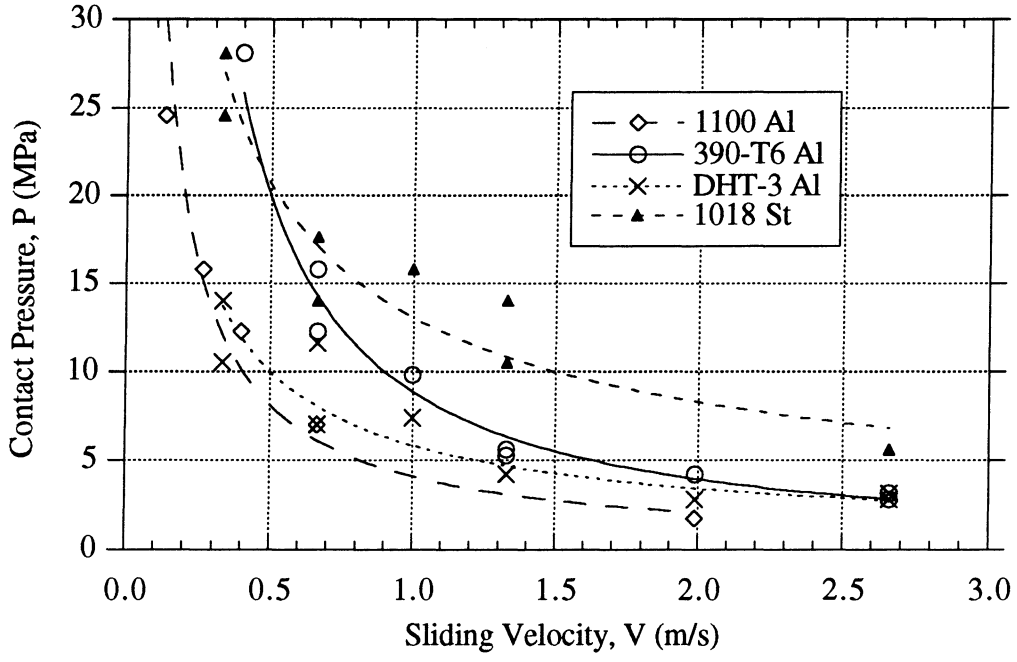

Fig. 3.2 - Scuffing results for 390-T6 Al, 1100 Al, DHT-3 Al and 1018 steel
T_0 = 30°C, Geometry: R12.7, Environment: air, Loading: stepwise with 5 minute-long steps

Table 3.1 - Parameters for a power law curve fit

Equation	$PV^n = C$		
Material	Coefficient, C	Power factor, n	Correlation Coeff., r_c
390-T6 Al	8.85	0.85	0.99
1100 Al	4.10	1.01	0.98
DHT-3 Al	5.85	1.28	0.91
1018 Steel	13.1	1.52	0.95

3.2 Effect of the Environmental Temperature for 390-T6 Al

The 390-T6 aluminum alloy was tested at environmental temperatures of 30°C and 100 °C. The results from these tests are given in Fig. 3.3. When the environmental temperature is increased, scuffing occurs at a much lower PV. The shape of the curve, however, remains the same and the effect of increased temperature is to shift the curve downward.

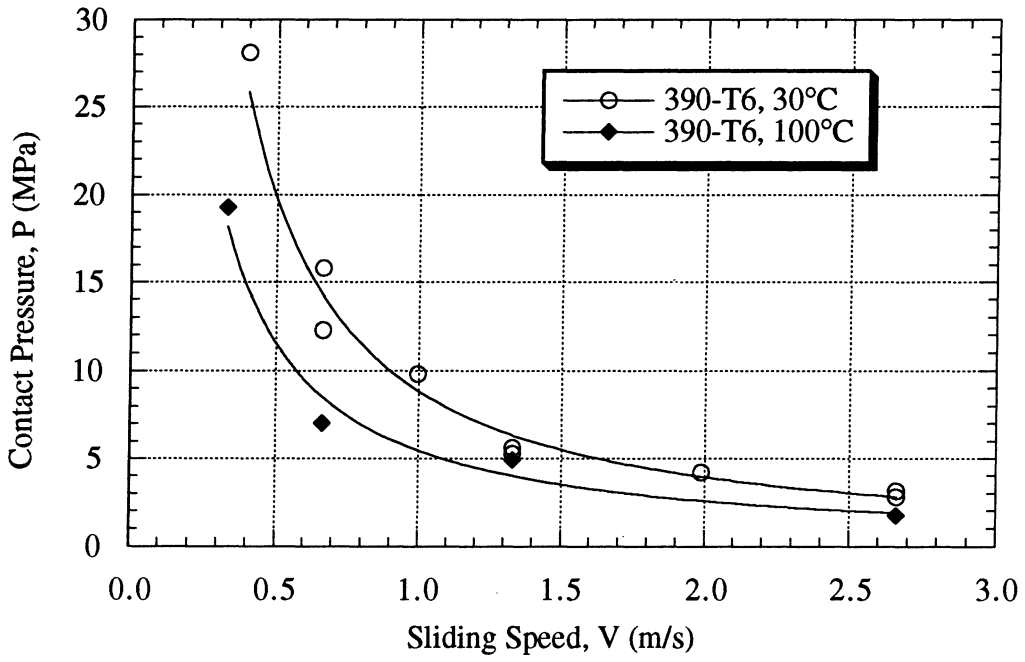

Fig. 3.3 - Effect of the environmental temperature on scuffing of 390-T6 Al alloy
Geometry: R12.7, Environment: air, Loading: stepwise with 5 minute-long steps

3.3 Size Effects for 390-T6 Al

The size of the specimens affects the scuffing *PV*. These results are shown in Fig. 3.4. In the figure, the data points for the smaller pins lie much higher than the data points for the larger pins. The shape of the *PV* curve is the same for both pin sizes, following closely the *PV* = *const* relationship. The temperature at scuffing for both pin sizes is approximately constant and equal to 240°C for the larger pins and 180°C for the smaller pins. The sliding radius does not seem to affect the scuffing *PV*. All the data points obtained with the ø6.35 mm pins can be fit with a single *PV* = *const* curve.

The size effects are in essence temperature effects. At the same *PV*, the contact between the smaller pins and the steel disk generates four times less heat than it is generated with the larger pins. The thermal dissipation characteristics of the specimen holders are also slightly different. As a result, the smaller pins run cooler and are capable to withstand almost double the *PV* of the larger pins. These results indicate that scuffing is strongly system-dependent.

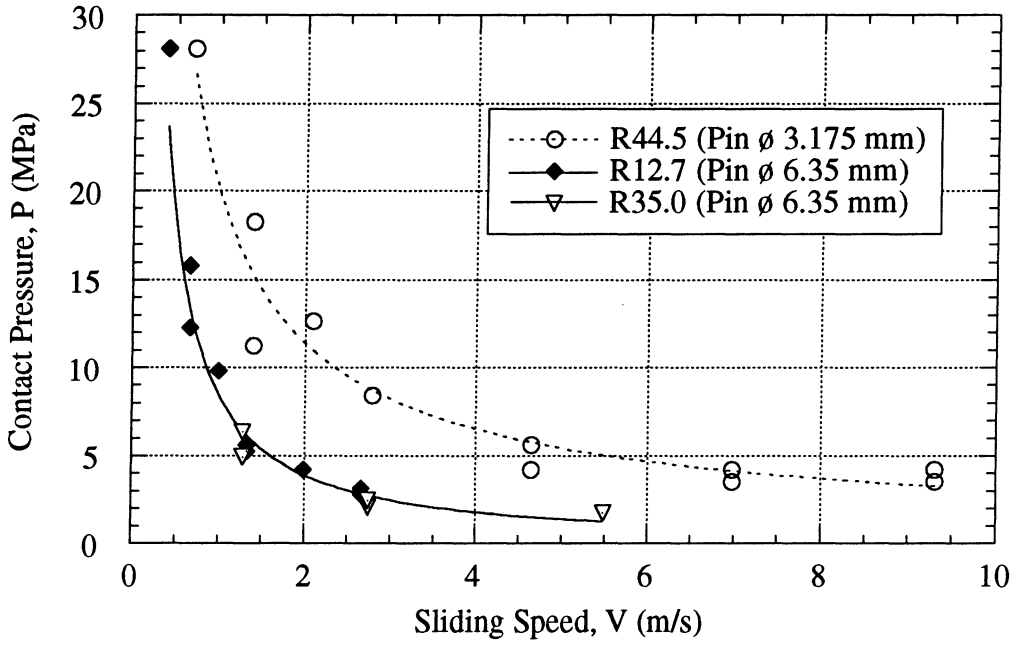

Fig. 3.4 - Scuffing results for 390-T6 Al for various test geometries
T_0 = 30°C, Environment: air, Loading: stepwise with 5 minute-long steps

3.4 Time and Loading History Effects for 390-T6 Al

Scuffing is a time-dependent phenomenon. Higher PV's shorten the time to scuffing, as shown in Fig. 3.5. This figure also suggests that scuffing does not occur within reasonably long test duration if the PV is below some critical value.

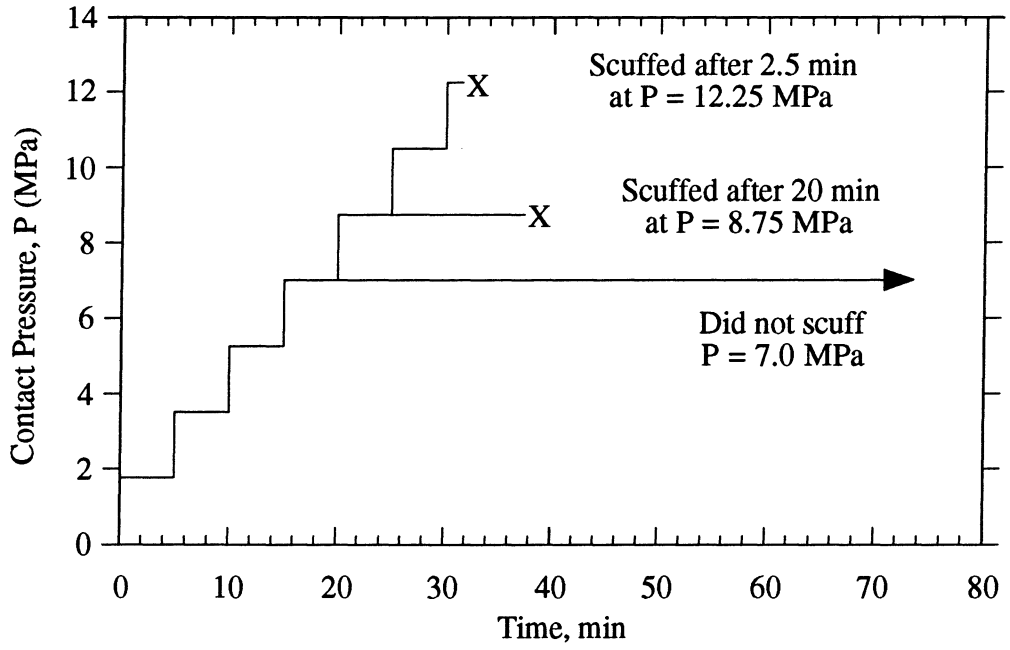

Fig. 3.5 - Time effects on scuffing for 390-T6 Al alloy
V = 0.66 m/s, T_0 = 30°C, Geometry: R12.7, Environment: air

The whole previous loading history may influence the conditions at which scuffing occurs. By changing the magnitude and the duration of the load steps, a whole family of curves can be constructed for a given temperature. Curves obtained with 5 minute-long and 30 minute-long steps, as well as a curve representing single step immediate loading are shown in Fig. 3.6. The two curves obtained with stepwise loading are very close to each other. Longer steps seem to be slightly more detrimental than short steps. The lowest scuffing PV's are obtained with the immediate loading, being only about 60% of the PV obtained from the stepwise loading with 5 minute-long steps. This result is the rationale behind running-in of machine components. The dependence on time and load history strongly suggests that a process of gradual accumulation of damage is responsible for scuffing in this alloy. Damage accumulation also can explain why the longer steps were more detrimental than the short steps.

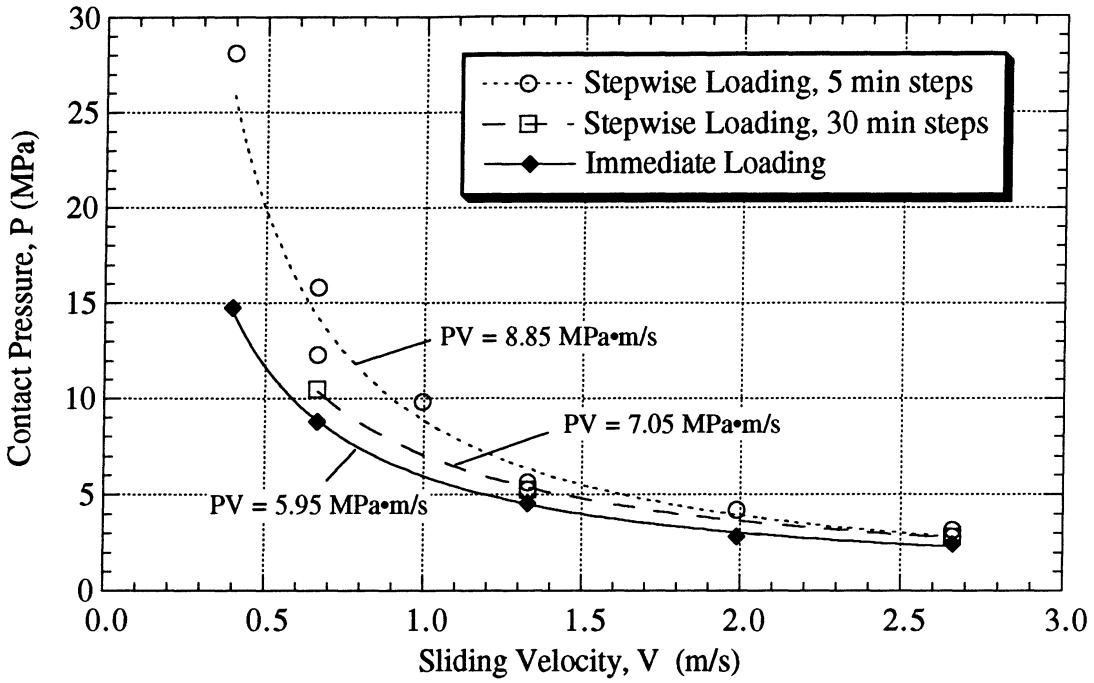

Fig. 3.6 - Effect of the loading history on scuffing of 390-T6 Al
T_0 = 30°C, Geometry: R12.7, Environment: air

3.5 Effect of the Environment for 390-T6 Al

As indicated in Chapter 1, the present study is part of a larger program for tribological evaluation of contacts operating under refrigerant environment. Tetrafluoroethane (R134a) is probably the most widely used ozone-safe refrigerant. This is the reason why it was chosen as one of the environments used in this study. Results from tests conducted in air and R134a environments are shown in Fig. 3.7. At higher loads and lower sliding velocities (V < 1.0 m/s), the data obtained in R134a follow closely the PV curve obtained in air. On the other hand, at higher velocities (V > 2.0 m/s), scuffing in R134a occurs at significantly higher PV's than in air. The region in between is characterized by a large scatter of data, with some data points following the curve in air and some lying much higher. These results suggest that a transition in scuffing behavior occurs in this velocity region, which is demonstrated by the curve drawn through the average values of the data obtained in R134a.

The appearance of the surfaces of the pins and disks which failed at higher PV's in R134a is very different from the specimens which failed at the lower PV's. These surfaces exhibit typical signs of chemical attack and corrosive wear. The chemical compounds found on the surface of the pins tested under R134a were identified with an XPS. The analysis revealed that large amounts of AlF_3 were present on the surface. In addition, a small amount of a fluorocarbon polymer with a

chemical structure similar to PTFE was detected. The aluminum fluoride is the result of a thermal degradation of the R134a molecule and the generation of free fluorine which attacks the aluminum surface. Since R134a and PTFE have very similar chemical structure, the polymer is probably the product of R134a polymerization. The generation of AlF_3 may promote a corrosive wear mechanism which leads to smaller wear particles, smoother sliding surfaces and less damage in the subsurface. The PTFE, on the other hand, is a very effective solid lubricant.

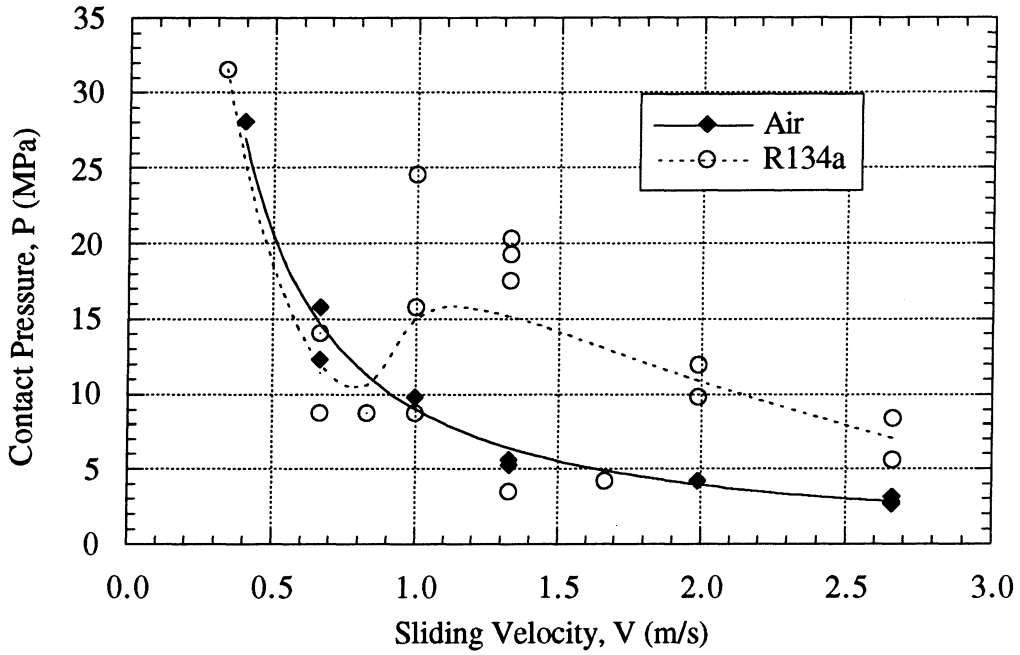

Fig. 3.7 - Scuffing results for 390-T6 Al tested in air and R134a
T_0 = 30°C, Geometry: R12.7, Loading: stepwise with 5 minute long steps

3.6 Thermal Gradients and Resistances for 390-T6 Al

Under dry sliding conditions, a significant amount of frictional heat is generated at the interface. Some of this heat is dissipated through convection and radiation and some is conducted away by the contacting bodies. The frictional heat generates thermal gradients in the specimens. The magnitude of the thermal gradients and the heat flow partitioning are important factors influencing the thermal and, therefore, the mechanical state of the subsurface material. The far subsurface (more than 2 mm away from the surface) thermal gradients and the amount of heat flowing through the pin specimens were measured by implanting thermocouples at depths of two (T_2), four (T_4), and six (T_6) mm below the surface. For these tests, thermocouples were installed

in both pins. The temperature difference between the two thermocouples was measured by a differential temperature controller. The results from these measurements are given in Fig. 3.8.

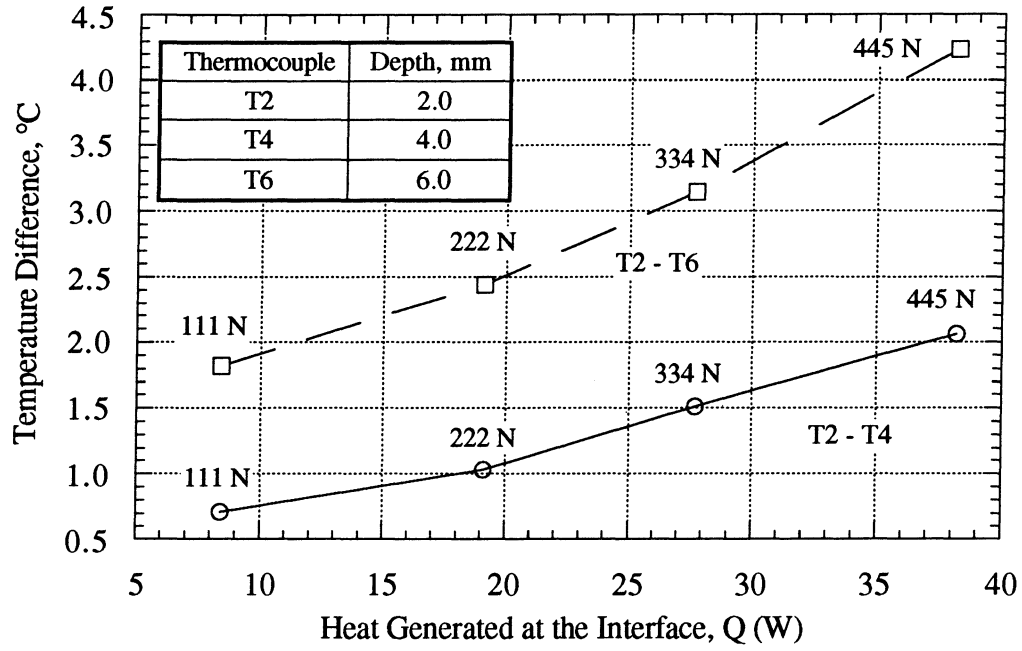

Fig. 3.8 - Temperature difference between thermocouples placed at different depths in the pins
Material: 390-T6 Al, Geometry: R12.7, $V = 0.66$ m/s, Environment: air
Contact loads: 111, 222, 334, and 445 N, Average coefficient of friction: 0.25

The results show that the temperature gradient in the far subsurface of the pins is relatively small. This is due to the large thermal resistance of the lower specimen holder (Fig. 2.2) which includes a gimbal and an insulating pad. The disk has lower thermal resistance and is attached to a surface, which is always kept at a constant temperature by a circulating coolant. In addition, the heat source on the surface of the disk is moving, while the heat source on the surface of the pin is stationary. Because of these factors, most of the heat flows into the disk.

Based on the measurements shown in Fig. 3.8 and assuming that conduction dominates, it is possible to calculate the amount of heat flowing into the pins and to estimate approximately the heat partitioning at the interface. The thermal resistance of the pin is given as:

$$R_t = \frac{1}{k}\frac{\Delta l}{A_0} \tag{3.1}$$

where k = 134 W/m°K is the thermal conductivity of 390 Al, Δl is the distance between the implanted thermocouples, and A_0 = 31.67 mm^2 is the cross section area of the ø6.35 mm pin. The amount of heat flowing through the pin is:

$$Q_{\text{pin}} = \frac{\Delta T}{R_t} \tag{3.2}$$

The results from these calculations are summarized in Tables 3.2 and 3.3. From the tables, it is evident that only a small percentage of the heat goes into the pin. This percentage decreases with the amount of heat generated. The differences between the values given in the last columns of Tables 3.2 and 3.3 are probably due to the fact that convection from the surface of the pins was neglected in the analysis.

Table 3.2 - Heat partitioning at the pin/disk interface based on the T_2 - T_4 measurement
V = 0.66 m/s, Geometry: R12.7, Environment: air, Average friction coefficient: 0.25

Load N	T_2 ℃	T_2 - T_4 ℃	$Q_{\text{pin}} = \Delta T / R_t$ W	$Q = \mu PVA_0$, W	Q_{pin} / Q %
111	67	0.7	1.52	9.9	15.4
222	95	1.0	2.21	18.0	12.3
334	120	1.5	3.24	25.8	12.6
445	152	2.0	4.42	33.1	13.3

Table 3.3 - Heat partitioning at the pin/disk interface based on the T_2 - T_6 measurement
V = 0.66 m/s, Geometry: R12.7, Environment: air, Average friction coefficient: 0.25

Load N	T_2 ℃	T_2 - T_6 ℃	$Q_{\text{pin}} = \Delta T / R_t$ W	$Q = \mu PVA_0$, W	Q_{pin} / Q %
111	65	1.8	1.95	8.44	23.1
222	98	2.4	2.62	18.9	13.7
334	125	3.1	3.37	27.7	12.2
445	157	4.2	4.54	38.2	11.9

The bulk temperature of the contacting bodies is the sum of the environmental temperature and the heat generated by friction. It can be expressed as:

$$T = T_0 + C_t \mu A_0 PV \tag{3.3}$$

where the constant C_t characterizes the thermal resistance and the dissipative capabilities of the system and has the heat partitioning incorporated in it. The constant C_t was determined experimentally for both the ø6.35 mm and the ø3.175 mm pins, as shown in Figs. 3.9 and 3.10. From the figure it is seen that the thermal characteristics of the R12.7 and the R44.5 geometries were different which explains the observed differences in scuffing PV's as shown in Fig. 3.4.

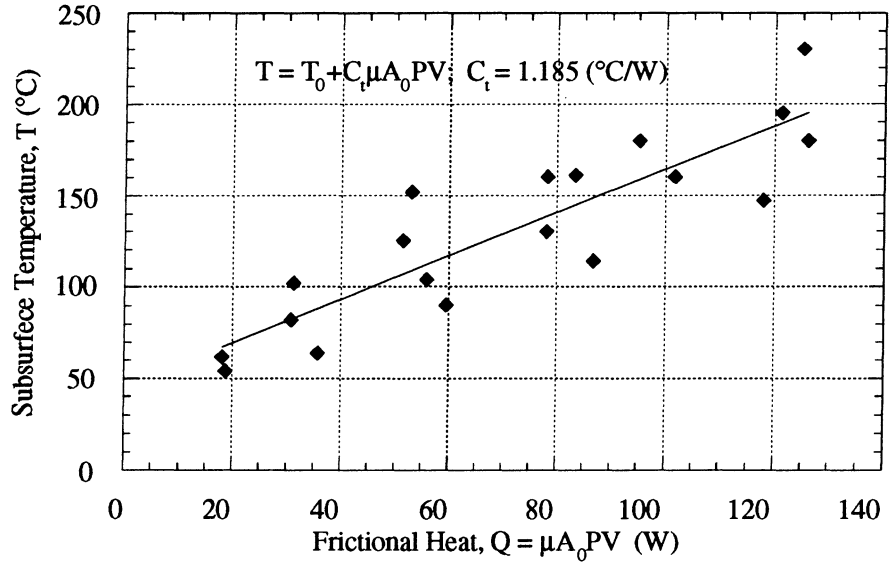

Fig. 3.9 - Determination of the thermal constant C_t for the ø6.35 mm pins. $T_0 = 30$ °C

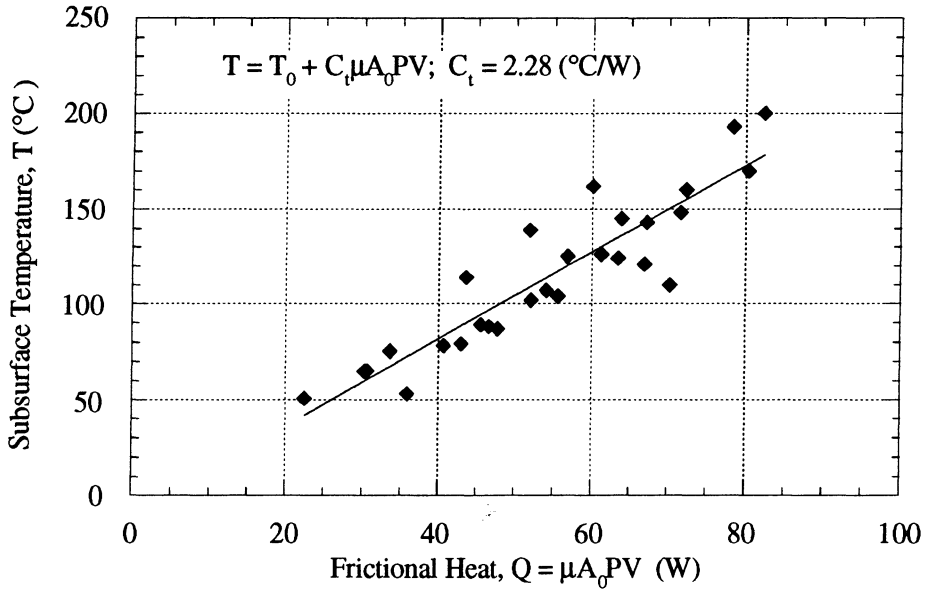

Fig. 3.10 - Determination of the thermal constant C_t for the ø3.175 mm pins. $T_0 = 30$ °C

3.7 Wear Rates of the Pin Specimens for 390-T6 Al

One of the most important characteristics of scuffing is the change in the dominant wear mechanism. Typically, several wear mechanisms are simultaneously active before scuffing. For the conditions of this study, the major wear mechanisms were corrosive, fatigue, and adhesive wear.

Corrosive wear is always present when a chemical reaction between the surface and the environment is possible. Oxide and other reaction films exist on the surfaces of most engineering metals. When the surfaces start rubbing against each other, the outermost parts of these films are removed by wear. However, due to the generated frictional heat, the reaction rate between the surface and the environment is accelerated. In addition, the films become more permeable to the molecules of the environment due to cracks and other damage done by the mechanical action. Finally, an equilibrium is reached between the rate of film removal by wear and the film formation by the chemical reaction. All the wear debris generated with this kind of wear are reaction products. High wear rates will result if the reaction rate is high and the reaction products are easily removed from the surface. On the other hand, some reaction products may act as solid lubricants which will reduce the wear rate. For the tests conducted in air, the reaction products were mainly aluminum and iron oxides. The wear debris generated from both specimens were small sub-micron sized particles. The wear rate under these conditions was low. This wear mechanism was dominant only at relatively low *PV*'s, typically less than 20% of the scuffing *PV*. In R134a, the products from the chemical reaction between the specimens and the environment were fluorides and PTFE-like polymers. This caused even lower wear rates, while the corrosive wear regime remained the dominant wear mode up to approximately 80% of the scuffing *PV*.

Fatigue wear is characterized by the initiation and propagation of subsurface cracks. The wear particles generated by this process are flat platelets which are partially surface reaction products and partially metallic. For the test conducted in this study, fatigue wear was the dominant wear mechanism just before scuffing.

Another wear mechanism which is present from the onset of sliding is the adhesive wear. Deformations of the surface, extrusion from cracks, or removal of parts of the surface by other wear mechanisms may generate areas of exposed bare metal. If these areas come into contact with the counterface, a strong adhesive junction may result. When this junction is broken, part of the junction material may be transferred to the counterface. The continuous formation of adhesive junctions enables the flow of electric current through metal/metal interfaces. Although other current conduction mechanisms like tunneling may be operable, the major part of the electrical current going through a metal/metal interface is due to adhesion spots [18,19]. Under the conditions of this study, small amounts of material were transferred to the counterface even at the

lowest PV's, suggesting the presence of adhesive wear. Under most sliding conditions, the adhesive junctions constitute a very small fraction of the whole area of contact, typically on the order of one part per million (1 ppm). However, at scuffing, large areas of bare metals can be formed and adhesive wear becomes the dominant wear mechanism. This leads to large amounts of material transfer, very high friction, and very low electric contact resistance. The wear rate is very high causing the destruction of the specimens.

Due to its importance in identifying scuffing, wear rate was monitored continuously during the test. Under all *PV*'s, with the exception of the periods right before scuffing, the wear remained approximately linear with time. Both the oxidative and the fatigue wear mechanisms obeyed this linear relationship. This relationship, also known as the Archard's law for wear, is expressed as:

$$V_0 = \frac{K}{H} WS, \quad \dot{h} = K\frac{PV}{H} \qquad \text{or} \qquad h = \frac{K}{H}(PVt) \tag{3.4}$$

where V_0 is the volume worn, S is the distance slid, W is the contact load, $\dot{h}$ is the linear wear rate (m/s), K is a wear coefficient, and H is the hardness of the material. According to the above relationship, for the same PV, the wear rate does not change if the ratio of P with respect to V changes. That this indeed was the case can be seen from Fig. 3.11.

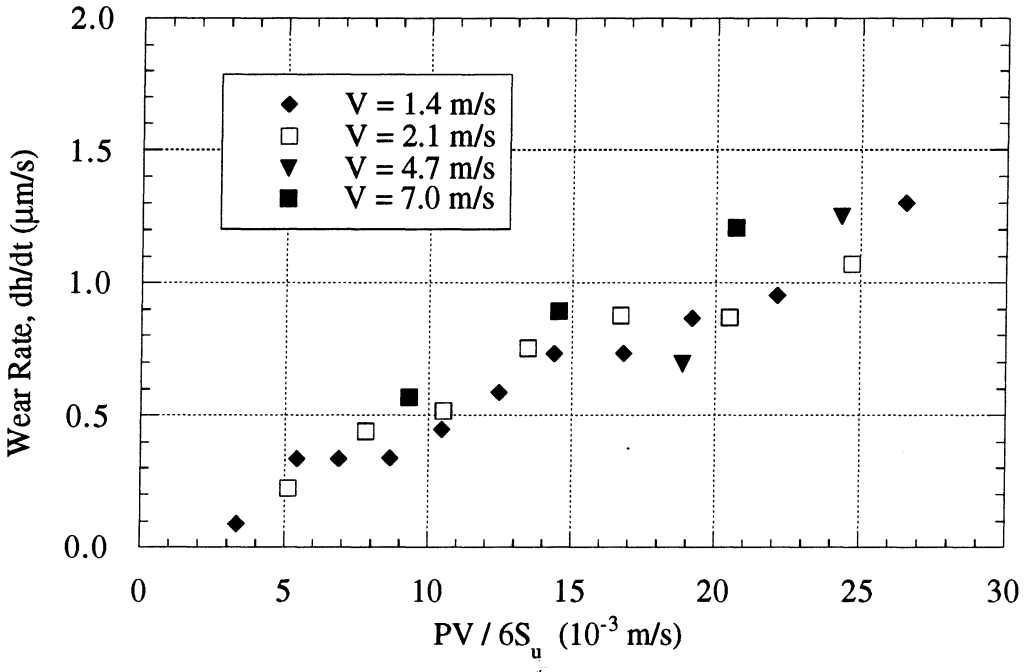

Fig. 3.11 - Wear rates as a function of $PV/6S_u$
Geometry: R44.5, Material: 390-T6 Al, Environment: air, T_0 = 30°C

Since data about the hardness of the 390-T6 alloy were not available for the test temperatures, the PV is normalized by $6S_u$, where S_u is the shear strength of the material obtained from Fig. 2.4. From the figure, it is evident that the wear rate increased linearly with $PV/6S_u$ which suggests that the wear factor K was constant This trend was typical for all the tests in this study. The wear rates for the R12.7 and R35.0 geometries were lower than the wear rates for the R44.5 geometry, but they also operated at lower PV's. However, for the same PV, the wear rate in R134a environment was significantly lower than the wear rate in air, which suggests a different wear mechanism. Various wear rates are compared in Fig. 3.12.

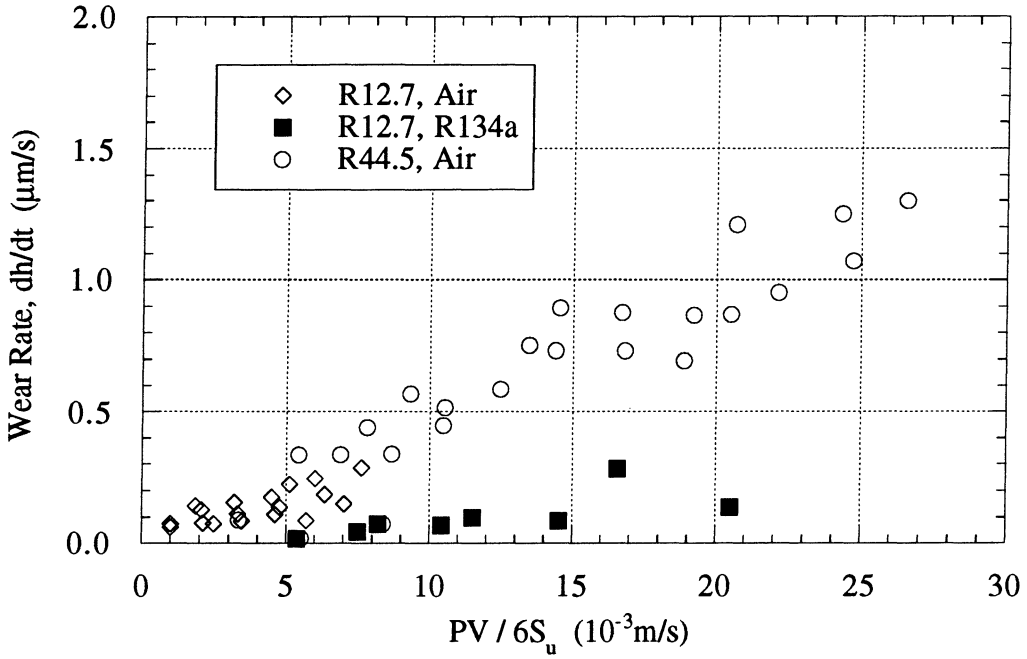

Fig. 3.12 - A comparison of various wear rates
Material: 390-T6 Al, T_0 = 30°C. Note that the V range for the R12.7 and R44.5 is different

3.8 Wear Rates of the Disk Specimens

The wear on the disk specimens provides important information about the pressure distribution over the contact area. Due to the high hardness of the disks, their wear rates were much smaller than the wear rates of the pin specimens. The wear on the disks was obtained by measuring the depth of the wear scars with a stylus surface profiler. Special one-hour-long tests, conducted at a constant load condition, were used to measure the wear rate. The results from these tests are shown in Fig. 3.13.

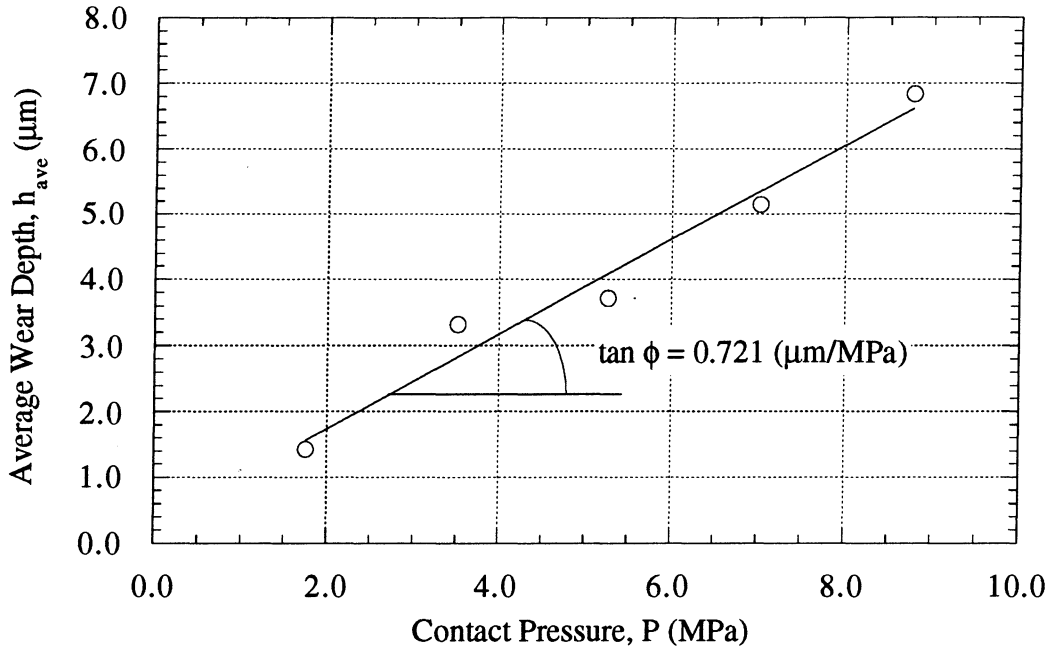

Fig. 3.13 - Average depth of the wear scar on the surface of the disk specimens
T_0 = 30°C, V = 0.67 m/s, Geometry: R12.7, Environment: air,
Loading history: constant load, Test duration: 1 hour

The pressure distribution over the contact area is important in defining the conditions for scuffing. Scuffing may be initiated preferentially at sites with surface pressure concentration. The shape of the wear scar on the disk specimens provides information on whether such sites of higher surface pressure form. The depth of the wear scar at such sites will be deeper than the depth calculated on the assumption of a uniform pressure distribution P. Assuming that Archard's law for wear holds, the factor K/H in Eq. (3.4)can be determined from Fig. 3.13:

$$\underbrace{4\pi R_{ave} R_{pin} h_{ave}}_{V_0} = \frac{K}{H} \underbrace{(2A_0 P)}_{W} \underbrace{(Vt)}_{S} \tag{3.5}$$

where R_{pin} is the radius of the pin and R_{ave} is the average sliding radius. Noting that $(h_{ave}/P) = \tan\phi$, the factor K/H can be obtained as:

$$\frac{K}{H} = (\tan\phi)\frac{4\pi R_{ave} R_{pin}}{2A_0 Vt} \qquad \text{or} \qquad \frac{K}{H} = 2.40\times10^{-9}\ \left(\text{MPa}^{-1}\right) \tag{3.6}$$

The wear depth at a particular sliding radius R can be expressed as:

$$h = 2\frac{K}{H}\frac{L_{arch}}{2\pi R}(PVt) \tag{3.7}$$

where L_{arch} is the length of the sliding arch (Fig. 3.14). The factor of two account for the two pins in contact. The factor ($L_{arch}/2\pi R$) reflects the fact that only part of the disk surface is loaded.

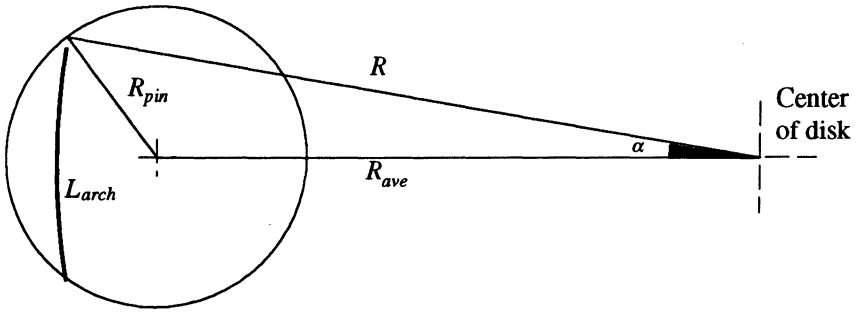

Fig. 3.14 - Geometry for calculating the arch length

The length of the arch can be expressed as:

$$L_{arch} = 2R\ \text{acos}\left[\left(R_{ave}^2 + R^2 - R_{pin}^2\right)/(2RR_{ave})\right] \tag{3.8}$$

Substituting equation (3.8) into (3.7) gives the analytical expression for the worn profile based on the uniform pressure assumption:

$$h = \frac{K}{H}(PVt)\frac{2}{\pi}\text{acos}\left[\left(R_{ave}^2 + R^2 - R_{pin}^2\right)/(2RR_{ave})\right] \tag{3.9}$$

The actual and the calculated profiles are compared in Fig. 3.15. From the figure, it is evident that the actual contact pressure was fairly uniform when averaged over the duration of the test. The small deviations of the actual profile from the calculated profile can probably be attributed to the fact that Archard's law is only an approximation of the wear process.

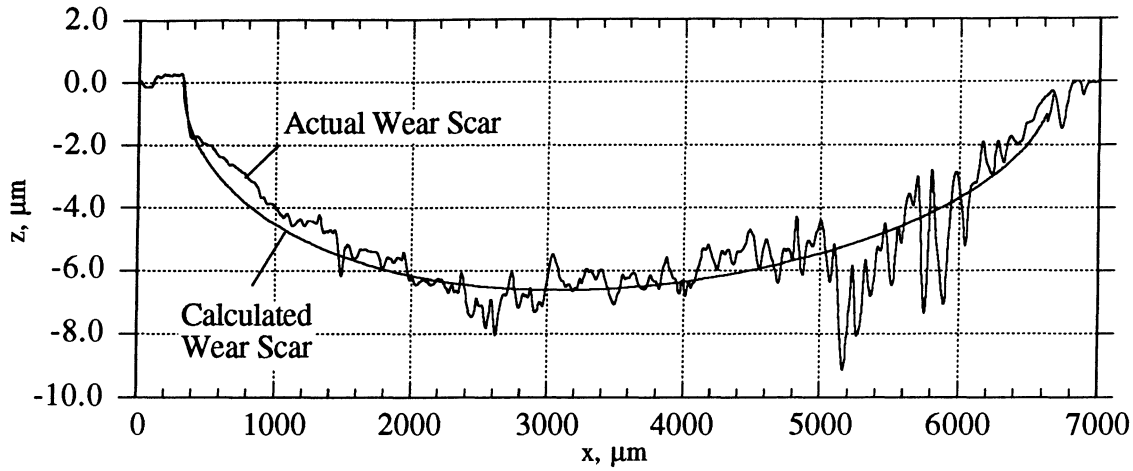

Fig. 3.15 - Typical comparison between the calculated and the actual shapes of the wear scar on the disk

3.9 Summary of the Experimental Results

The experimental results from the tests described in this chapter can be summarized as follows:

a. Scuffing is reliably reproduced and identified under laboratory conditions. This is achieved by the use of a specially designed tribometer, choice of suitable test geometry and test procedure, and the installation of special instrumentation.

b. For the tests conducted in air, at a given environmental temperature, specified contact geometry and loading history, the contact pressure at scuffing decreases with the sliding velocity. For the 1100 and 390-T6 aluminum alloys this relationship can be expressed as $PV = const.$ This curve also represents a constant subsurface temperature condition at scuffing. The PV curves for steel and DHT-3 aluminum deviate from this hyperbolic relationship. For these materials, the PV at scuffing increases with the sliding velocity.

c. From the aluminum alloys tested, the 390-T6 aluminum showed the highest scuffing resistance. This is also the material with the highest strength. Steel has the highest scuffing resistance of all the materials tested.

d. For 390-T6 Al, the scuffing PV decreases with the environmental temperature. The shape of the PV curve, however, remains the same. The effect of increasing the environmental temperature is to shift the curve downward in a PV map diagram.

e. Scuffing is strongly system-dependent. Changes in the size of the test specimens lead to shifting of the scuffing *PV* curve.

f. Scuffing is a time-dependent phenomenon. Above a certain critical *PV*, the time to scuffing decreases when the *PV* is increased. This suggests that scuffing occurs when a critical amount of damage is accumulated in the material.

g. The *PV* at which scuffing occurs depends on the previous loading history. The sudden application of the load is more detrimental than the stepwise loading. This is the rationale behind the practice of running-in of machine components.

h. The test environment affects scuffing. Chemical reactions between the environment and the surfaces of the specimens may change the dominant wear mechanism.. The scuffing *PV* of 390-T6 aluminum tested under R134a environment deviates significantly from the $PV = const$ curve. At low sliding velocities, scuffing occurs at approximately the same *PV* as in air. At high sliding velocities, scuffing occurs at considerably higher *PV*'s than in air. Aluminum fluoride and PTFE-like polymers are the products of the reaction between R134a and aluminum.

i. For the test geometry used, most (80-90%) of the frictional heat generated at the sliding interface goes to the disk. This heat partitioning is based on measured bulk temperature gradients.

j. The wear on both the pin and the disk specimens is approximately linear with load and sliding distance (obeyed Archard's law) for the whole range of test conditions. The wear rate in R134a environment is lower than the wear rate in air.

k. The time-average of the contact pressure is approximately uniform over the whole apparent area of contact. This conclusion is based on a comparison between calculated and measured wear scar profiles on the disk specimens.

3.10 Contributions

The present study is not the first investigation of scuffing resistance of aluminum. Results for the scuffing behavior of various aluminum alloys, including 1100 and 390 Al have been reported in the literature [16,34-40]. However, the major goal of these studies was to optimize the metallurgical composition and the method of fabrication of these alloys. Typically the scuffing resistance of alloys with varying amount of silicon and/or softer metals are compared to the scuffing resistance of pure aluminum. On the other hand, the major emphasis of this study is on the effects of the environment and the operating conditions. The present study also provides a more complete picture of the effect of various factors on the scuffing of aluminum. Some of these effects are investigated for the first time. In addition, data for the wear, bulk temperature, and heat partitioning at the interface are obtained. These can be used as an input to models for the

mechanical and thermal interactions at the surface, which can provide a better understanding of the local conditions at scuffing. A summary of the contributions of this study to the experimental database on scuffing of aluminum is given below:

a. The scuffing behavior of a Bi-containing aluminum alloy is studied for the first time.

The extruded DHT-3 alloy was introduced relatively recently as a possible substitute for the cast silicon alloys in various tribological applications. In a previous study [70], the wear resistance of this alloy was found to be similar to the wear resistance of 390 Al. It was expected that this alloy may also provide similar scuffing resistance. However, the results of this study indicate that this is not the case, especially at the high load end of the *PV* curve.

b. The effect of the size of the specimens is studied for the first time.

This set of experiments provides important information for the evaluation of various criteria for scuffing. It helps to distinguish between true material properties and system-dependent factors.

c. The time and loading history effects on scuffing are clearly demonstrated.

Time and load history effects are known to exist in general. Their strong influence on scuffing of aluminum is proven by the quantitative data obtained in this study. These data show that time and loading history effects must be included in the hypotheses for scuffing.

d. The effect of the refrigerant environment is studied for the first time.

The effect of a chemically active environment other than air contributes to a better understanding of scuffing. It shows that large deviations from a $PV = const$ curve can be expected in the presence of reaction films. The identification of the reaction films formed under dry sliding conditions and R134a environment is also reported for the first time.

e. A more complete set of data for the scuffing behavior of 390 Al.

Although, the scuffing resistance of 390 has been investigated, the data presented in the literature is not sufficient for the development of theoretical models and hypotheses. With the results from this study, a more complete data base is available for developing theoretical models.

CHAPTER 4
EXAMINATION OF SURFACES, SUBSURFACES AND WEAR DEBRIS

In the tribological community it is fairly common to treat scuffing as a surface-related phenomenon. Studies on the failure of lubricant films [1-3], desorption of active chemical species [4], formation and destruction of oxides [5], surface roughness [75-79], energy state of the surface [45], surface plasticity [6-9], surface temperature [41,80-84] and growth of contact junctions due to adhesion [10-13] have shaped most of the research in this area. The reason is that most of these studies are mainly concerned with lubricated contacts. Under dry sliding conditions, the surface interactions are more severe and their effect can be detected at significant depths below the surface. Therefore, the mechanisms leading to scuffing must also be related to processes in the subsurface. In addition, there are some indications that subsurface failure is the reason for some scuffing failures under starved lubrication conditions [85].

In this study, the major emphasis is on the behavior of the subsurface. The discussion below covers the structure of the subsurface, quantitative characterization of damage accumulation due to sliding, and the sequence of events leading to scuffing. Surfaces of worn specimens and wear debris are also examined.

The surface of the test specimens is studied with an optical microscope, a surface profilometer, and an XPS. The subsurfaces are studied by sectioning of specimens tested under scuffing and non-scuffing conditions and examining the sections with SEM and AES. Quantitative data for the chemical composition and the thickness of the surface layers are obtained. Quantitative results for the average plastic deformation at various depths under the surface are also obtained.

4.1 Structure of the Subsurface

The subsurfaces of all the materials tested, after being subjected to sliding under dry conditions, attained similar features. These subsurfaces can be subdivided into three characteristic regions:

a. A top layer of transformed material.

The layer is generated by oxidation, plastic deformation, material transfer, mechanical alloying and compaction of debris. It has very fine microstructure and hardness several times higher than the bulk. The thickness of this layer increases with the PV and, for the conditions of this study, was typically in the range of 3-30 μm. This is orders of magnitude larger than the thickness of the nascent films formed without any mechanical interaction (< 5 nm for Al) [86].

The transformed layer prevents bare metal-to-metal contact and severe adhesion at the interface. A micrograph of the transformed layer in a 390-T6 aluminum specimen is shown in Fig. 4.1. The chemical composition of this layer as a function of depth below the surface is given in Table 4.1. The chemical analysis was performed with an AES.

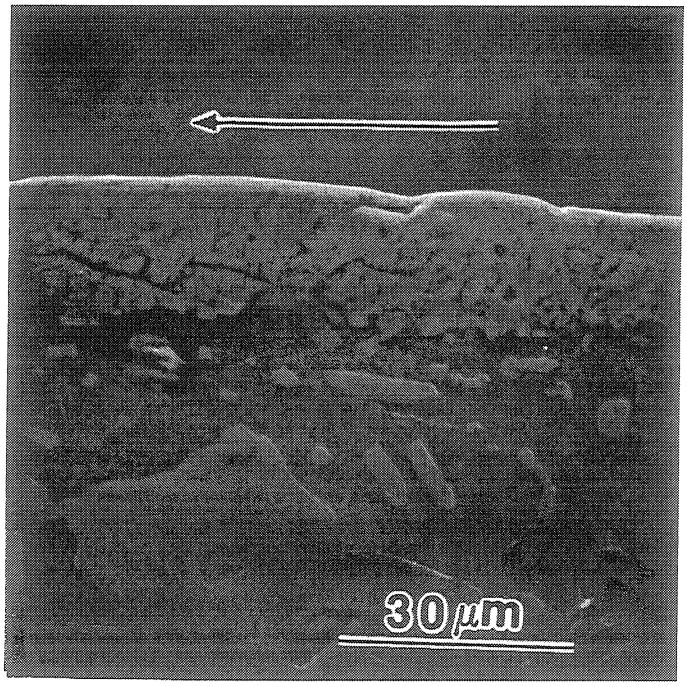

Fig. 4.1 - A layer of transformed material in a 390-T6 Al pin
The pin is sectioned parallel to the sliding direction, indicated by an arrow
P = 7 MPa, V = 0.67 m/s, T_0 = 30°C, Environment: air

Table 4.1 - Composition of the transformed layer of a 390-T6 Al specimen as a function of depth below the surface. P = 7MPa, V = 0.67 m/s, T_0 = 30°C, Environment: air

Element	Atomic concentration (%) at depth below the surface		
	10 μm	30 μm	50 μm
Aluminum	40.08	50.40	53.92
Silicon	17.52	18.79	17.21
Copper	4.73	4.62	4.02
Oxygen	16.87	12.44	10.58
Carbon	14.43	13.10	10.18
Iron	6.20	6.75	0.0

Oxidation is an important mechanism for the formation of the transformed layer. The large percentage of oxygen in its composition clearly reveals this. In fact, in a large number of literature sources, this is considered the only important mechanism for its formation [5,87,88]. It was argued that the rate of formation of such layers can be deduced from the static oxidational rates and frictional heating.

More resent research [22,89] points to another important mechanism - the compaction of wear debris and mechanical alloying. Evidence that this mechanism was also active for the generation of the layer in Fig. 4.1 can be found in Table 4.1. The large percentage of iron and carbon, which is not present in the bulk material, suggests that wear particles from the counterface steel disk were mixed into the layer. Since the surface of the disks is carburized, the wear particles from the disk probably contained large amount of carbon. The compaction of fine wear particles seems to be a necessary condition for the formation of the layer. This can be observed from tests conducted with brass specimens. A typical record of the applied load on the brass pin and the corresponding displacements, indicating the wear rates, are shown in Fig. 4.2.

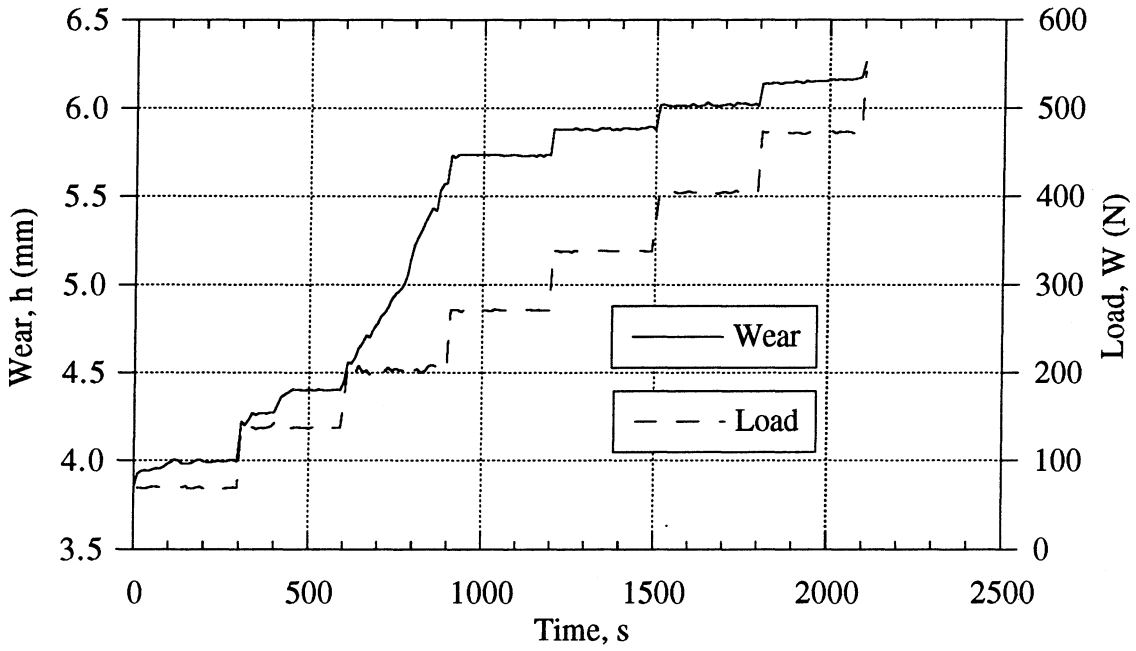

Fig. 4.2 - Records of the load and the wear for a brass pin specimen
V = 2.0 m/s, T_0 = 30°C, Environment: air

Brass is less reactive than aluminum and does not form oxidative wear particles readily. This slows down the formation of a transformed layer which leads to high wear rates even at relatively low loads. However, if the load is increased further, a transformed layer is finally formed. The wear rate decreases and the wear debris, which form under a wide range of loads afterwards, are powder-like particles, typical of oxidative wear. These particles were found to be magnetic, which indicates that their origin was from the steel disk. The conclusion is that the fine wear particles are essential for the formation of the transformed layer.

The third important mechanism for the formation of the transformed layer, which has often been overlooked, is the plastic deformation. Material from one location on the specimen is often displaced in the direction of motion by plastic flow, covering other surface features including oxides and wear debris. This material may in turn be covered by another layer of plastically deformed material coming from another location. In this way, a layered structure develops, which includes oxides, wear debris and strain hardened, severely deformed material. An illustration of this mechanism is given in Fig. 4.3, which shows the layered subsurface of a brass specimen. The transformed layer has a very different microstructure from the bulk material as seen from the micrograph given in Fig. 4.4. Within this layer, the presence of various defects is also typical.

The transformed layer is generated almost immediately after sliding begins. Results from measurements of the thickness of the transformed layer as a function of the sliding distance are given in Table 4.2. Note that this layer increases in thickness with the sliding distance. These results are obtained from sections of pins which slid under the same PV for different periods of time. The thickness of the measured transformed layer and the observed amount of plastic deformation in the subsurface follow similar trends. In the table the amount of plastic deformation is represented by the horizontal displacement in the sliding direction of a point in the subsurface 20 μm below the transformed layer. The measurements of subsurface plastic flow are discussed in more detail in Section 4.3 below.

Table 4.2 - Change in the thickness of the transformed layer as a function of sliding distance
$P = 7.01$ MPa, $V = 0.67$ m/s, $T_0 = 30°C$, $T_b = 180°C$, Environment: air, Material: 390-T6 Al

Sliding time, s	30	60	300	600
Sliding distance, m	20.1	40.2	201	402
Ave. thickness of the layer†, μm	13	17	25	25
Ave. subsurface displacement‡, μm	83	89	100	102
†Average of five measurements, ‡ Measured 20 μm below the surface				

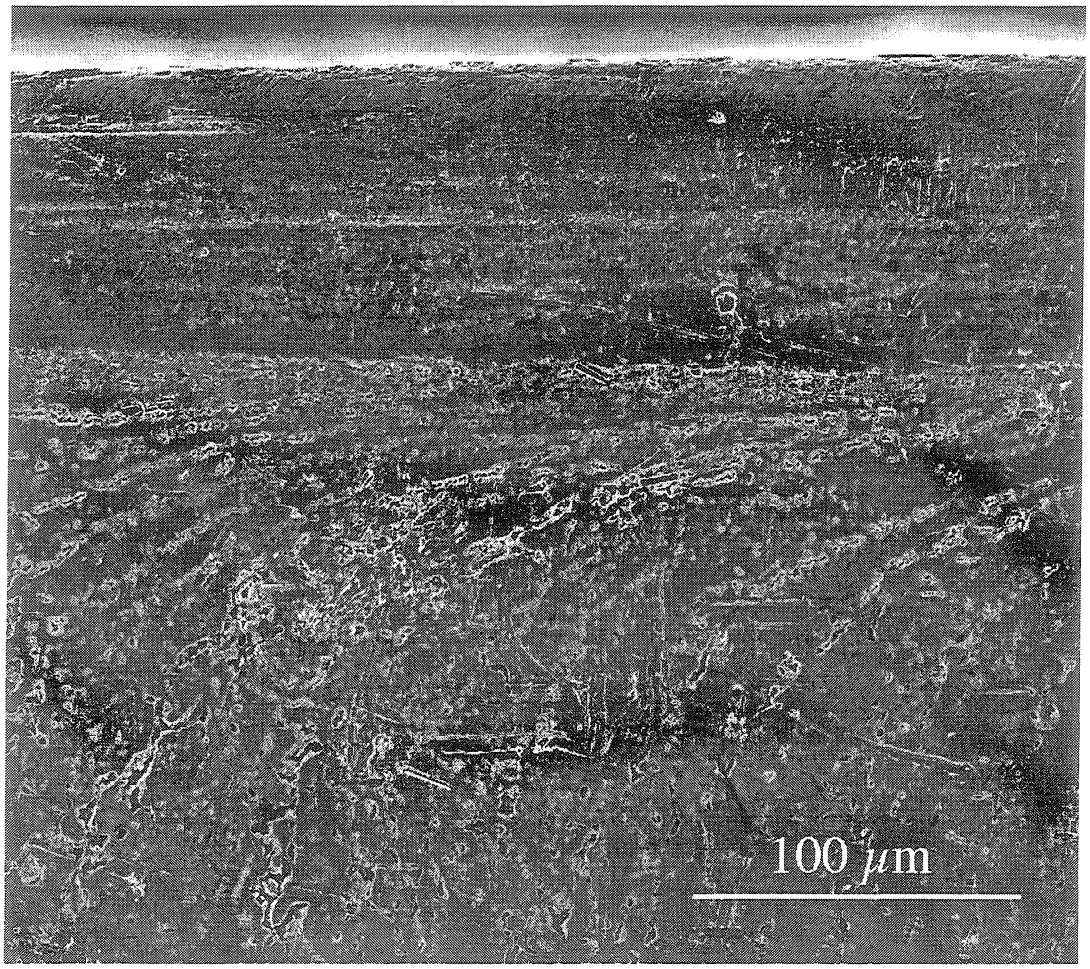

Fig. 4.3 -Layered structure of the transformed layer in a Si-Pb brass specimen
P = 6.4 MPa, V = 2.66 m/s. T_0 = 30°C, Environment: air

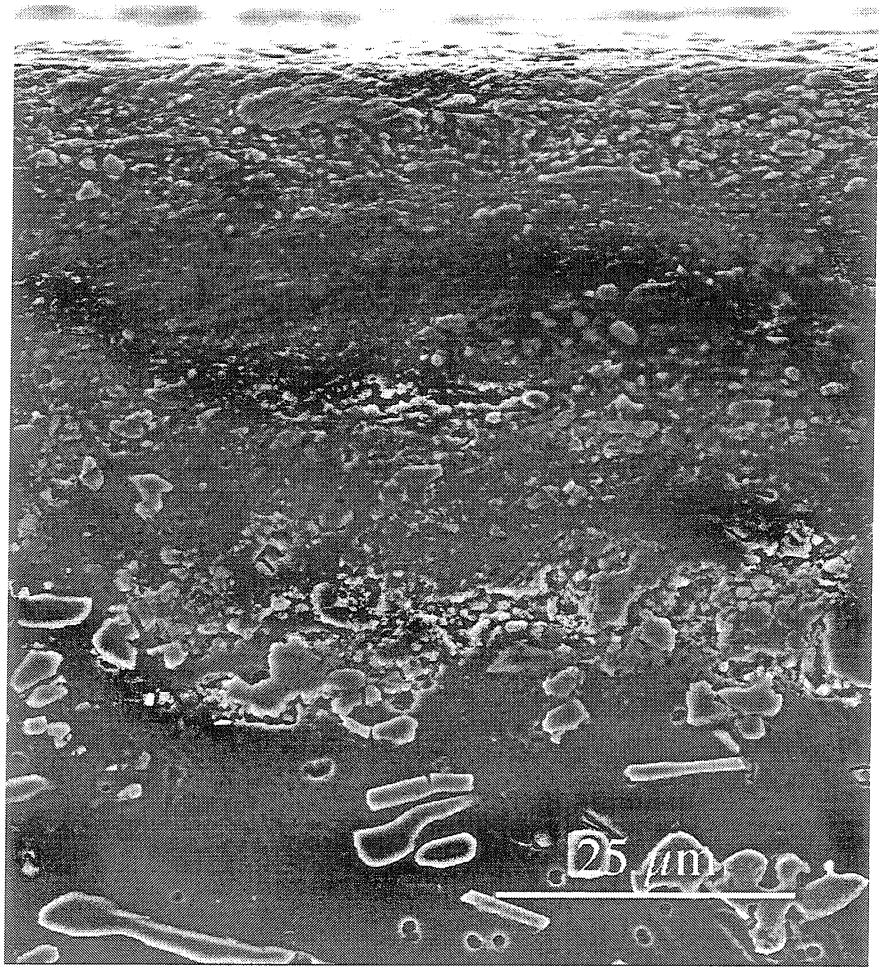

Fig. 4.4 - Various defects in the transformed layer of 390-T6 Al
P = 12.0 MPa, V = 0.67 m/s, T_0 = 30°C, Environment: air

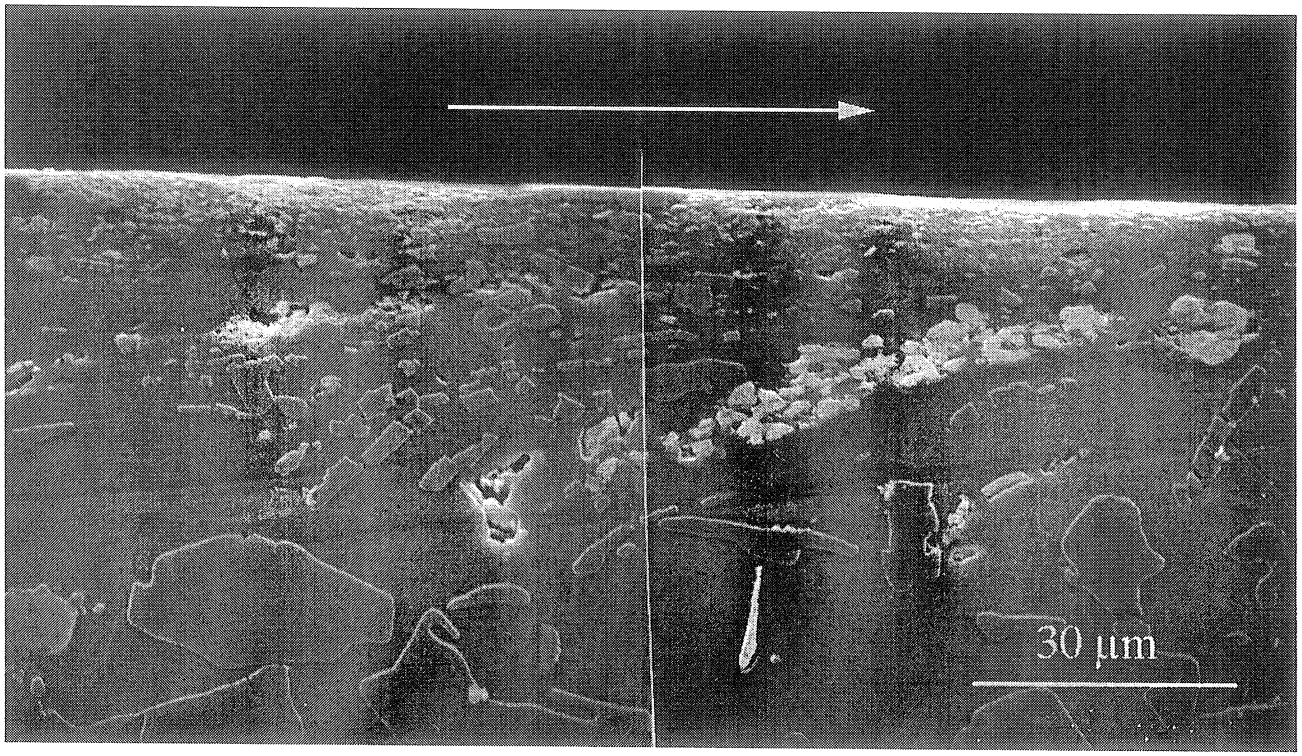

Fig. 4.5 - Plastic deformation in the subsurface of a 390-T6 aluminum pin
$P = 9.8$ MPa, $V = 0.67$ m/s, $T_0 = 30°C$, Environment: air
The arrow denotes the direction of sliding

b. A layer of plastically deformed material.

As stated earlier, under dry sliding conditions the material can be plastically deformed to a significant depth. The layer of plastically deformed material can reach depths of 100-150 μm depending on the *PV*. Characteristic of this layer is the orientation of all subsurface features in the direction of sliding. Other characteristics are the elongation of grains, the fracture of hard particles (silicon) and the formation of voids. Large plastic flow in the subsurfaces of brass and 390-T6 Al is shown in Figs. 4.3 and 4.5, respectively.

The boundary between the plastically deformed layer and the transformed layer is not always clear. Apart from the compositional changes these two layers can be usually distinguished by the angle of orientation of grains and other subsurface features with respect to the surface. Subsurface features almost parallel to the sliding direction outline the lower boundary of the transformed layer.

c. Elastically deformed material.

The three characteristic layers present in the subsurfaces of the materials tested are schematically shown in Fig. 4.6. This figure represents a typical subsurface of a 390-T6 aluminum pin.

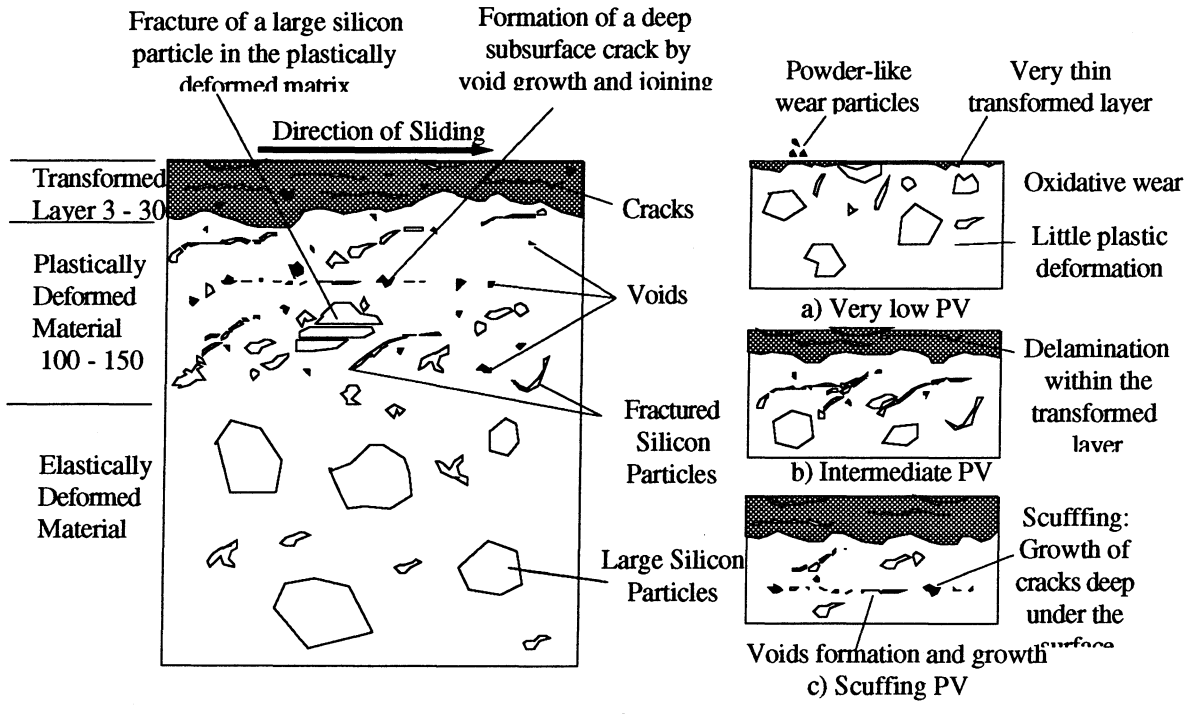

Fig. 4.6 - Schematic of the subsurface of the 390-T6 aluminum pins

4.2 Subsurfaces and Wear Debris at Various *PV*'s

Schematics of the subsurfaces of a 390-T6 pin at various *PV*'s is also shown in Fig. 4.6. At very low *PV*'s, the mechanism responsible for wear is the detachment of submicron-size, powder-like, particles (Fig. 4.7a) from the top of the transformed layer. The particles shown in Fig. 4.7a are, in fact, agglomerates of even smaller particles, as seen from Fig. 4.8a. Even at magnification of x100,000 (Fig. 4.8b), the particles seem to be composed of even smaller debris. The capability of the particles to agglomerate helps the formation of the transformed layer. At these very low *PV*'s there is almost no bulk plastic deformation and the thickness of the transformed layer is few microns.

At higher *PV*'s, cracks propagating within the transformed layer (Figs. 4.1, 4.4, 4.5) produce flake-like wear particles (Fig 4.7b). The wear rate under these conditions is higher, but the surface is still protected from scuffing. These wear particles reach fractions of a millimeter in length. Their thickness can be deduced from micrographs of sectioned specimens showing the depth of the craters generated after the removal of such a particle. This depth typically is 3-5 μm.

Finally, at the scuffing *PV*, voids may nucleate deep (over 50 μm) under the surface and grow with time and coalesce in cracks, which propagate parallel to the surface. Cracks formed under the surface of 390-T6 Al , DHT-3 Al, and 1018 steel are shown in Figs 4.9-4.11. When the cracks finally break to the surface, the whole transformed layer at this location is removed, resulting in very large wear particles (Fig. 4.7c,d). The top surface of the wear particle shown in Fig. 4.7c is characterized by fine grooves, indicative of "normal" sliding. Conversely, the bottom surface of the same wear particle (Fig.4.7d) shows cracks and signs of extensive plastic flow. The shear traction between the disk and this wear particle was not very high, because there are no obvious signs of adhesion on its top surface. Still the material failed at a significant depth. This could happen only because the material at this depth was already weakened by subsurface cracks. This wear particle also implies that deep subsurface cracks occur prior to any significant adhesion on the surface. The subsurfaces of the specimens shown in Figs. 4.9-4.11 also exhibit large amounts of plastic deformation and damage. Damage is accumulated and cracks are formed at several depths under the surface (Fig. 4.9) but it seems that there is critical depth where the damage accumulates the fastest. In the case of the 390-T6 and the DHT-3 alloys it is clear that the cracks originate next to the silicon particles.

No cracks could be observed in the subsurfaces of 1100 Al and brass specimens. These materials are very ductile and do not form cracks readily. However, cracks in the subsurface of pure aluminum have been observed by Sarkar and Clarke [90] under conditions similar to this study. Alpas et al. [91] have observed cracks in copper. They found that cleavage occurred at the transition boundary between the transformed layer and the bulk material.

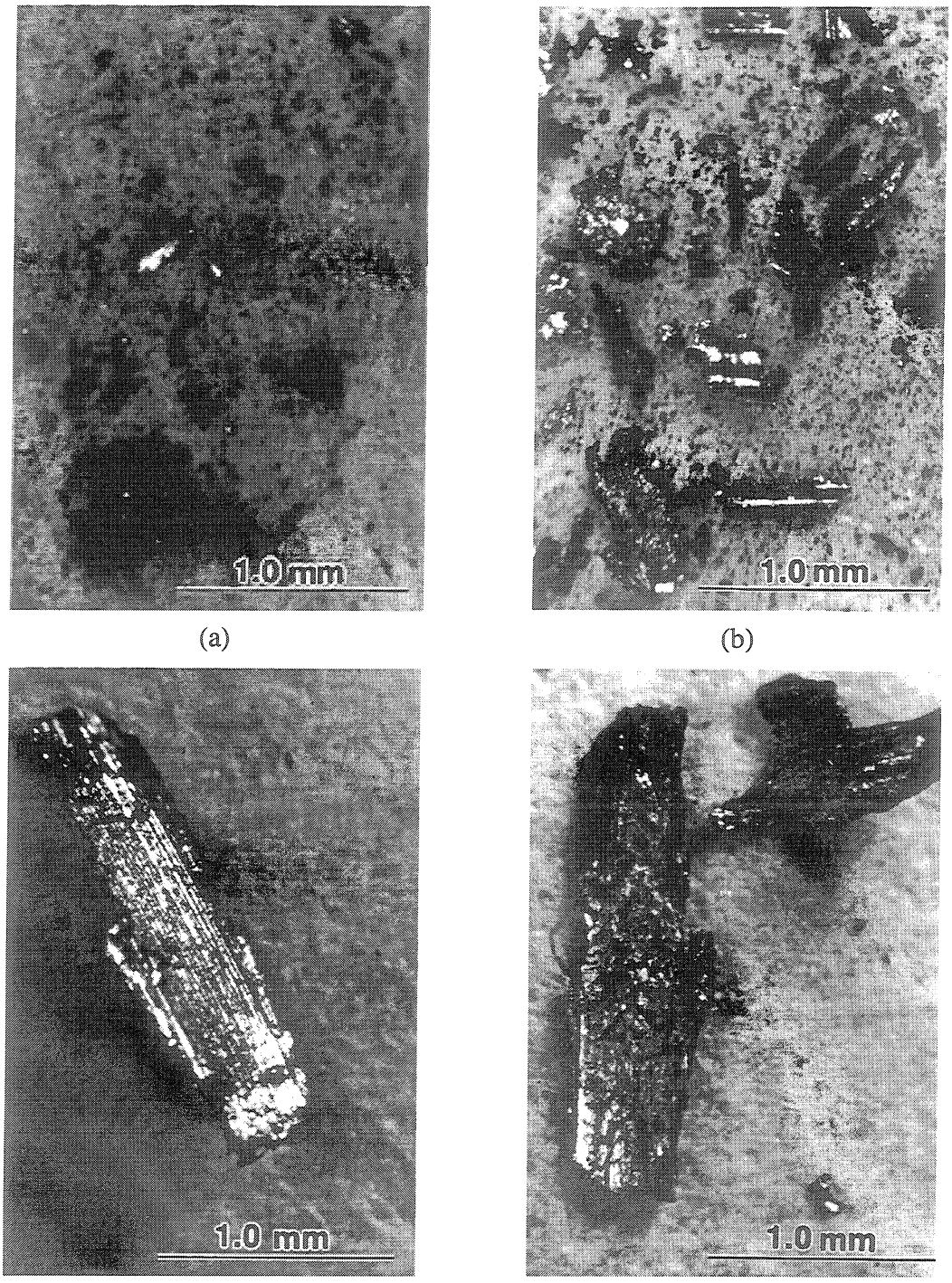

(a) (b)

(c) (d)

Fig. 4.7 - Optical micrographs of wear particles from tests conducted in air
(a) Powder-like wear particles typical of oxidative wear (P = 1.75 MPa, V = 0.67 m/s),
(b) Flake-like delamination wear particles (P = 7.0 MPa, V = 0.67 m/s),
(c) Top surface of a large wear particle generated just prior to scuffing (P = 12.0 Mpa, V = 0.67 m/s),
and (d) Bottom surface of the same wear particle

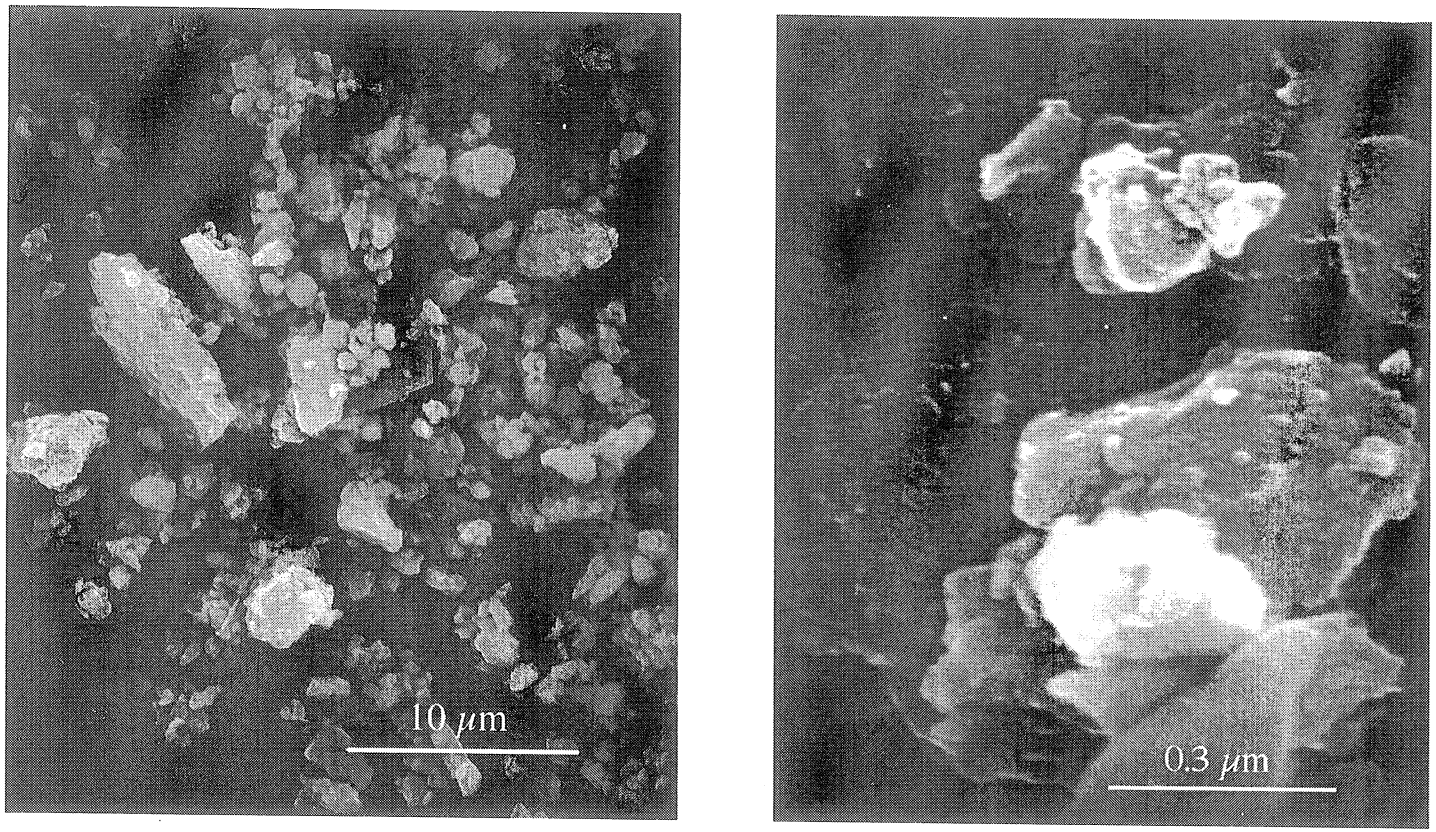

(a) (b)

Fig. 4.8 - Oxidative wear particles
(a) Magnification x3 000, and (b) Magnification x100 000

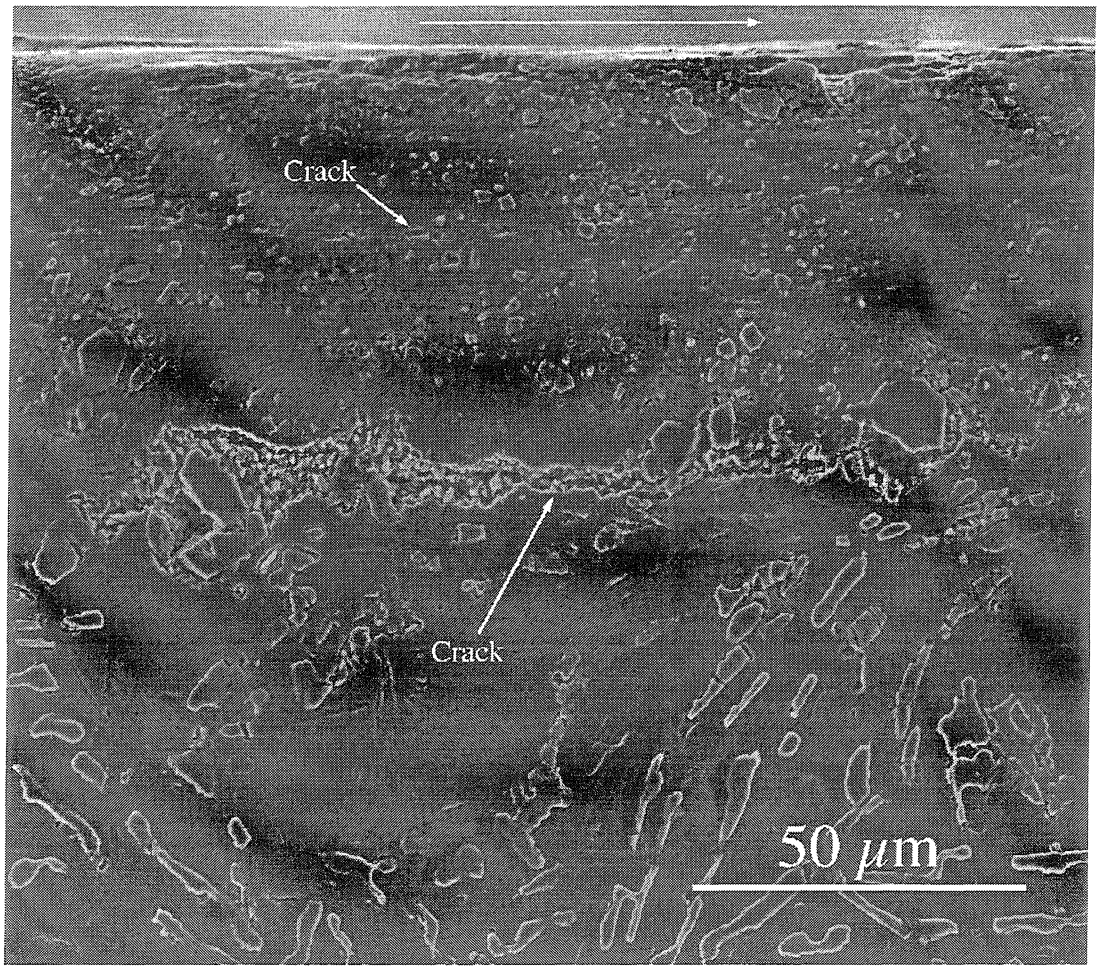

Fig. 4.9 - Formation of cracks in the subsurface of 390-T6 Al
V = 0.67 m/s, P = 12.0, MPa, T_o = 30°C, Environment: air
The arrow on top denotes the direction of sliding

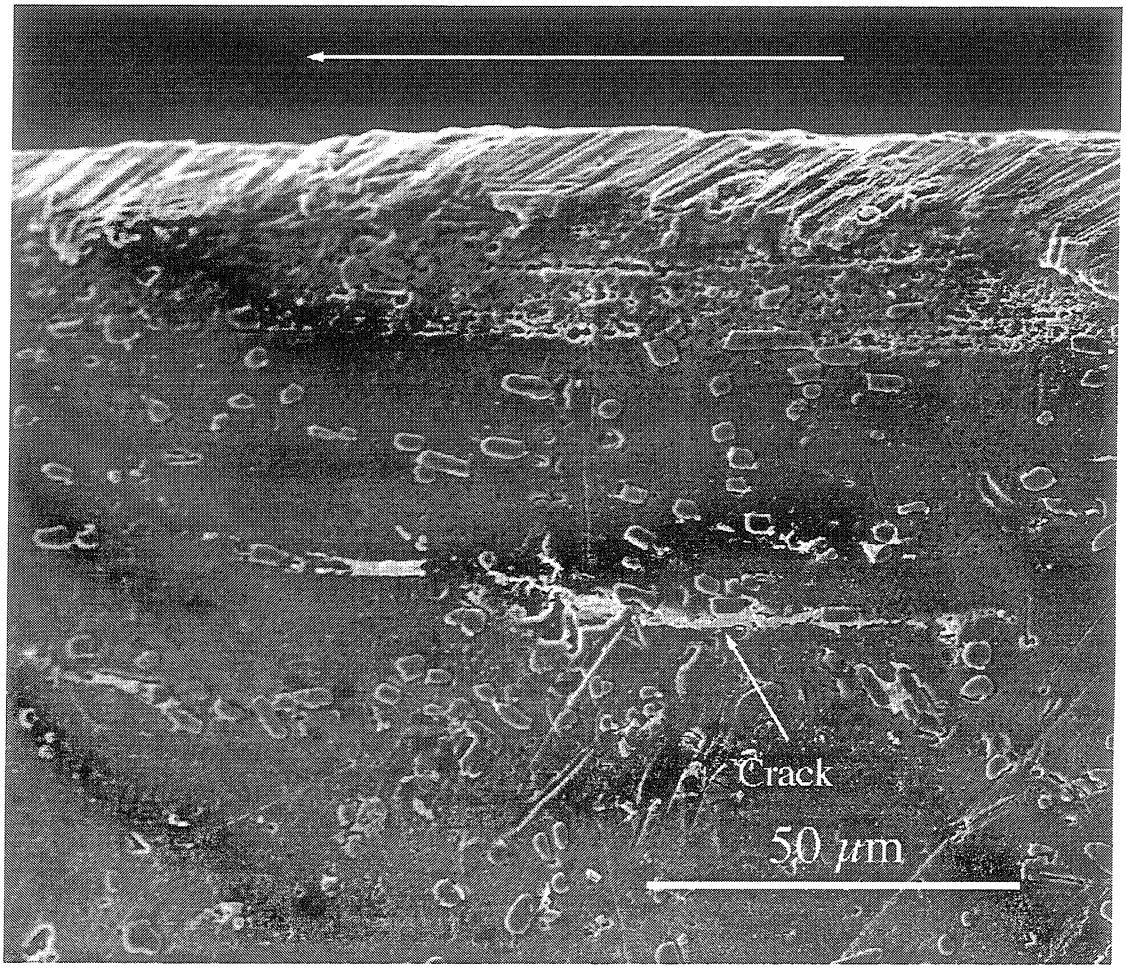

Fig. 4.10 - Formation of cracks in the subsurface of DHT-3 Al
V = 1.0 m/s, P = 7.02 MPa, T_0 = 30°C, Environment: air
The arrow on top indicates the direction of sliding

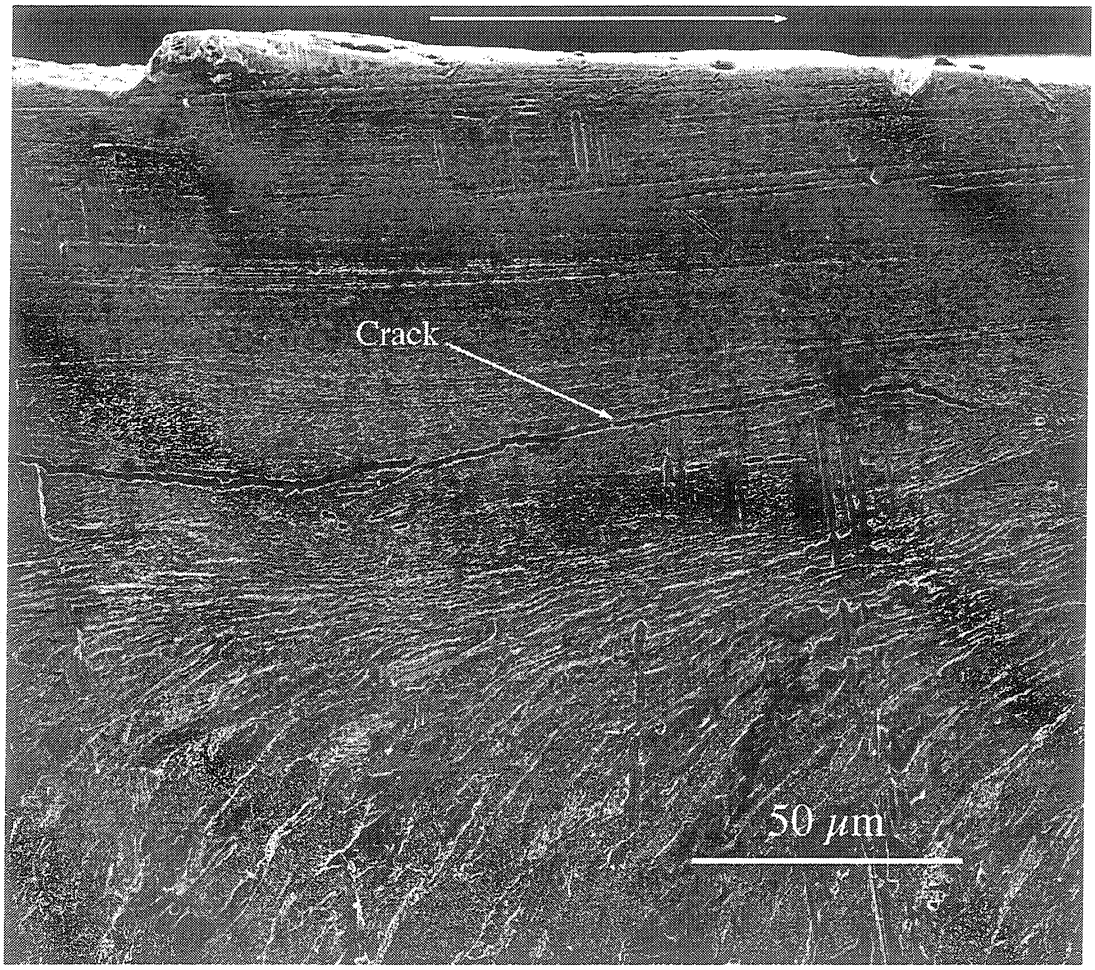

Fig. 4.11 - Formation of cracks in the subsurface 1018 steel
V = 0.33 m/s, P = 26.3, MPa, T_0 = 30°C, Environment: air
The arrow on top denotes the direction of sliding

The thickness of the transformed and the plastically deformed layers increase with the *PV*. These results are shown in Table 4.3. Based on the limited data given in table, it can be concluded that changing the ratio of *P* and *V* while keeping the *PV* constant does not seem to influence the thickness of the layers. The measured bulk temperature for these conditions is also shown. All the data in the table are from one hour long tests.

Table 4.3 - Thickness of the transformed and the plastically deformed layers at various *PV*'s
Environment: air

PV (MPa m/s)	1.18	2.35	3.53	4.70	5.88	5.88
V (m/s)	0.67	0.67	0.67	0.67	0.67	2.66
P (MPa)	1.76	3.51	5.27	7.02	8.78	2.19
T_b (°C)	57	83	110	136	162	165
Transformed layer (μm)	4-5	13-15	17-20	18-20	25-30	28-30
Deformed layer (μm)	-	80-100	100-125	120-130	150-160	130-150

4.3 Measurements of Subsurface Plastic Deformation

Both cracks and voids formation are due to excessive local plastic deformation. In general, the extent of damage accumulated in the subsurface can be related to the amount of plastic deformation. Therefore, it is important to obtain a quantitative measurements of its magnitude.

In this study the average plastic deformation in the subsurface was obtained from observations of sections of test specimens. Although the subsurface features often indicate the direction of plastic flow (Figs. 4.3 , 4.5, 4.11), its quantitative measurement is uncertain without a reference. To generate such a reference, brass inserts were placed in slots cut on the surfaces of the aluminum specimens. The inserts used in this study were 0.35 mm thick, 2 mm high, and 6.35 mm long. They were press-fitted in the slots and additionally bonded with an adhesive to prevent any relative slip during the test. After placing the inserts in their slots, the surfaces were machined to produce equal height of the insert and the rest of the surface. During the tests the inserts were positioned with their long side perpendicular to the direction of motion. The plastic

deformation occurring during the test bent the inserts in the direction of sliding. After the test the specimens were cut parallel to the direction of sliding to reveal the deformation of the brass/aluminum interface. The bending of the originally vertical interface was used as an indicator of the amount of plastic deformation. A typical section of a specimen from these tests is shown in Fig. 4.12. From the figure, it is seen that, in addition to the amount of plastic deformation, information about the thickness of the transformed layer can also be obtained. This information was already presented in Table 4.2. The method used to measure the displacements of the subsurface is shown in Fig. 4.13. The origin of the coordinate system was positioned at the interface between the transformed layer and the brass insert. The horizontal axis is parallel to the sliding direction and the vertical axis coincides with the original direction of the brass/aluminum interface.

All the tests used to measure subsurface plastic deformation were conducted with 390-T6 Al pins and R12.7 test geometry. Tests were conducted both in air and R134a environments at an environmental temperature of 30°C. These tests had various durations in order to obtain the changes of plastic deformation with time. To reduce the scatter of data due to differences in the initial surface conformity of the specimens, all the tests included a ten-minute run-in period at 20% of the test *PV*. This did not affect the results. Samples from the run-in period revealed that practically no plastic deformation was accumulated during this time. After the run-in period, the test *PV* was applied in a single load/velocity step. The tests with brass inserts were conducted at 80% of the scuffing *PV*, obtained from previous testing. Two combinations of *P* and *V* were used. The sliding velocities for these combinations were 2.66 m/s and 0.266 m/s, which covers a wide range along the $PV = const$ curve.

The results from the measurements of subsurface plastic deformation are summarized in Figs. 4.14-4.17. The horizontal displacement of points at various depths under the surface as a function of time is given in Fig. 4.14. Each data point is the average of four measurements. Data for test durations of 30 seconds, 1 minute, and 10 minutes are presented. Data were also obtained at 5 minutes, but are not shown, because they were virtually identical to the data obtained at 10 minutes.

The effect of the sliding velocity at a constant *PV* is shown in Fig. 4.15. From the figure, it is evident that for the tests conducted in air, the amount of plastic deformation is not sensitive to variations in *P* and *V* along the $PV = const$ curve. This is no longer true in R134a environment, as seen from Fig. 4.16. Although, the plastic deformation for both sliding velocities is smaller than the plastic deformation in air, the higher pressure curve is closer to the curve obtained in air. This is one possible explanation of the deviations from the $PV = const$ curve shown in Fig. 3.7.

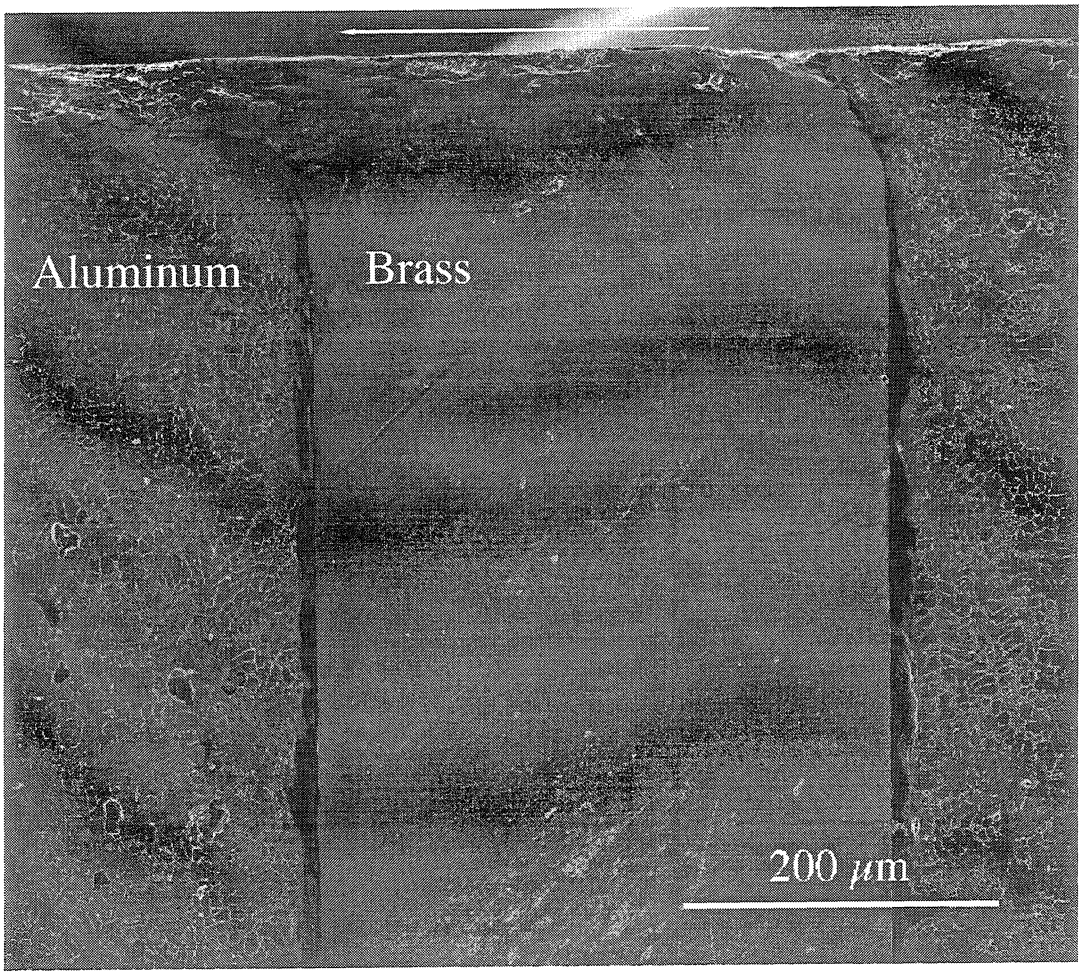

Fig. 4.12 - Measurement of the subsurface plastic deformation with a brass insert
P = 1.75 MPa, V = 2.67 m/s, T_0 = 30°C
Environment: air, Test duration: 10 min.

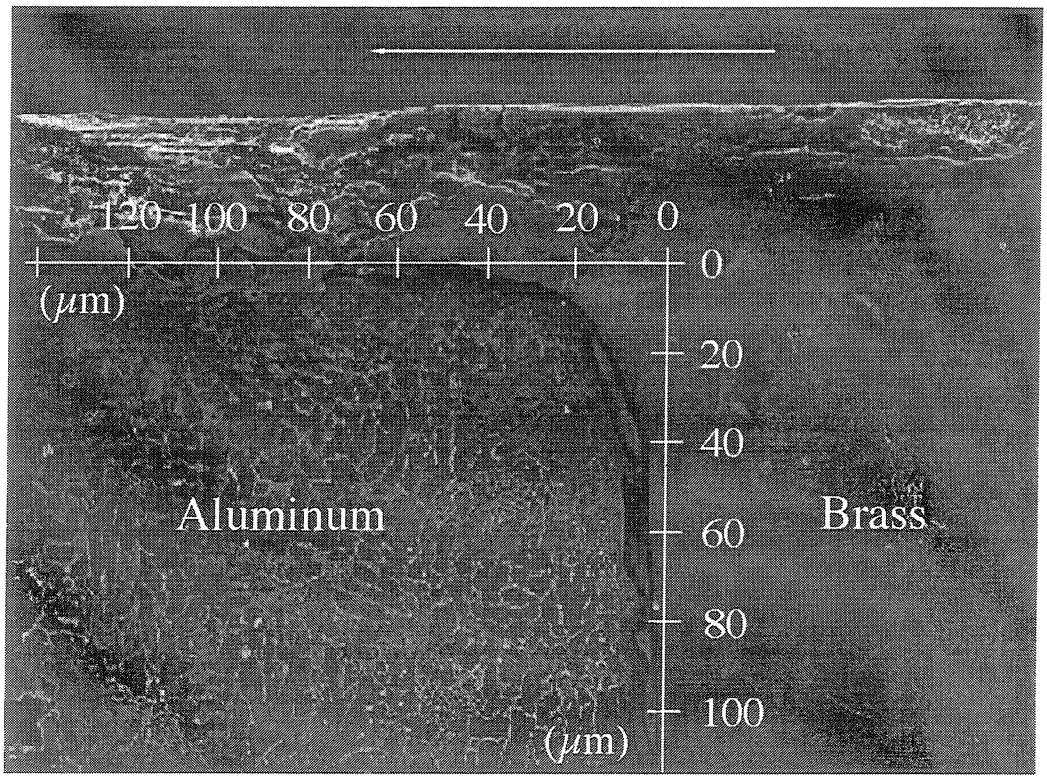

Fig. 4.13 - Coordinate system for measurement of subsurface plastic deformation
P = 1.75 MPa, V = 2.66 m/s, T_0 = 30°C
Environment: air, Test duration: 10 min.

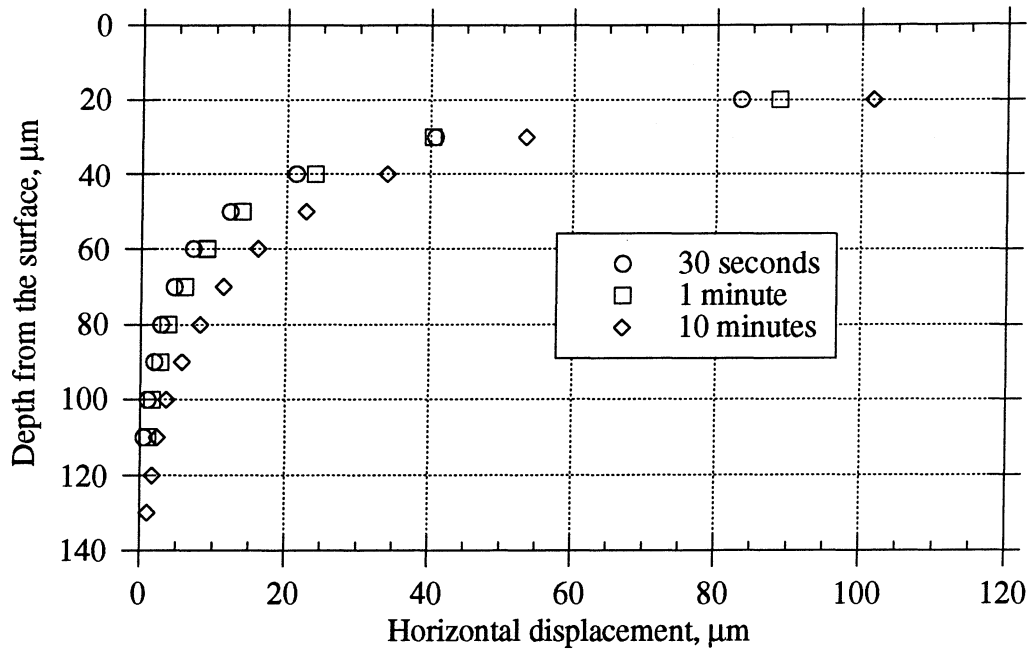

Fig. 4.14 - Subsurface horizontal displacements as a function of time
P = 17.5 MPa, V = 0.266 m/s, T_0 = 30°C, Environment: air

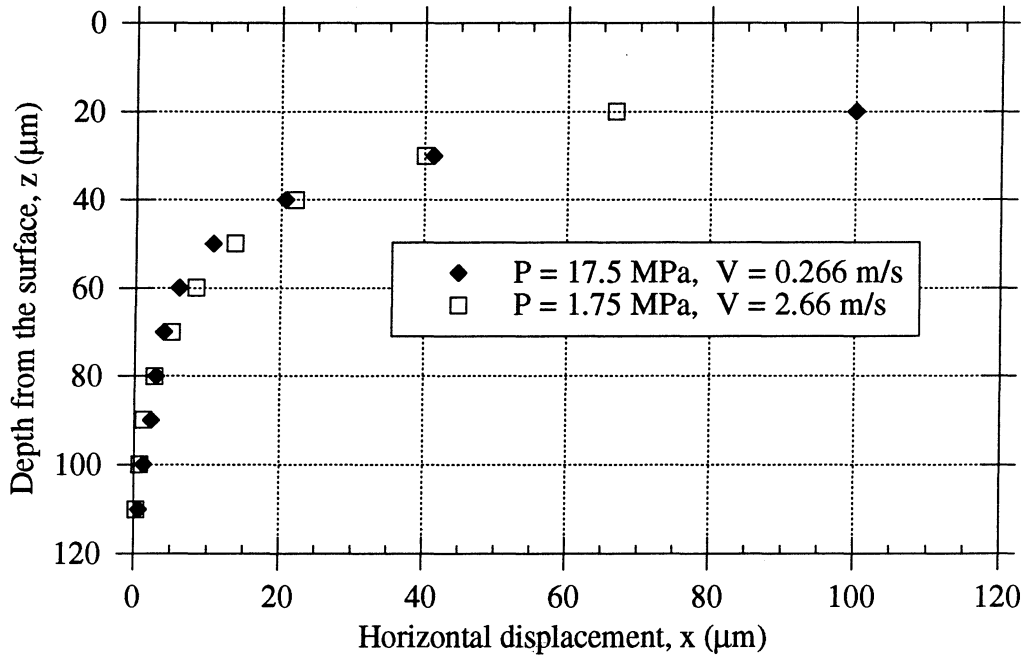

Fig. 4.15 - Subsurface plastic deformation for two PV = 4.66 (MPa.m/s) combinations
T_0 = 30°C, Environment: air, Test duration: 1 minute

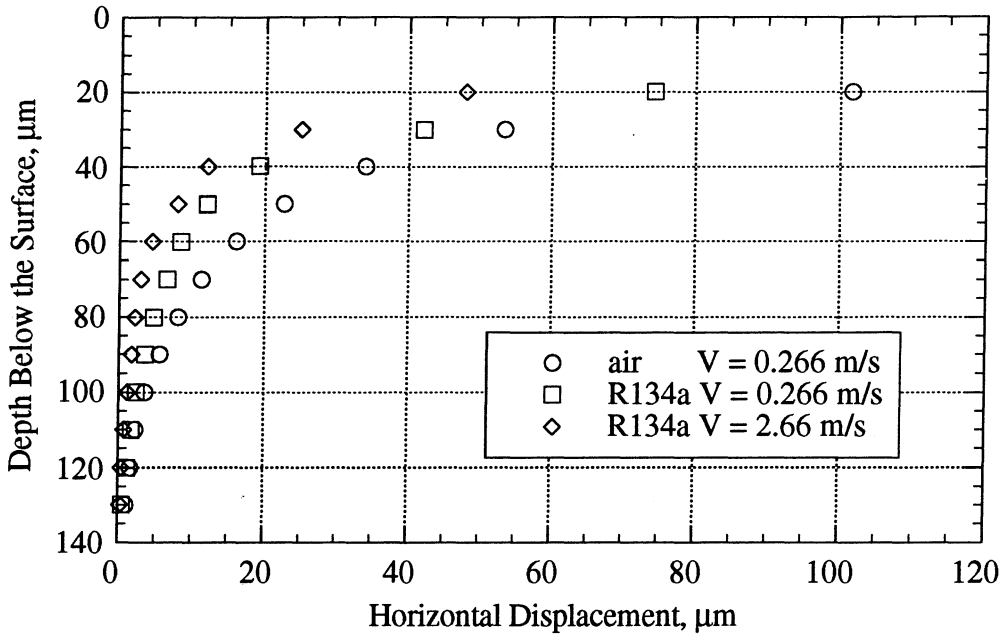

Fig. 4.16 - Comparison between the plastic deformation of subsurfaces tested in air and R134a PV = 4.66 MPa.m/s, T_0 = 30°C, Test duration: 10 min.

From the horizontal displacements of subsurface points it is possible to calculate the equivalent strain. Assuming that these displacements are the direct result of shear deformation parallel to the surface, neglecting the contributions from compression and rotation, the equivalent strain can be calculated as [91]:

$$\varepsilon = \frac{\sqrt{3}}{3}\tan\theta \tag{4.1}$$

where θ is the angle of the brass/aluminum interface and the normal to the sliding surface. Calculated equivalent strains for the displacement results given in Fig. 4.14 are shown in Fig. 4.17.

The results from the figure are similar to the data for subsurface strains of an eutectic Al-Si alloy, reported by Perrin et al. [92]. The results in Fig. 4.17 also indicate that, initially, most of the strain is concentrated closer to the surface. As the sliding proceeds, the strain closer to the surface decreases, while the strain further from the surface increases. The depth affected by plastic deformation also increases with time.

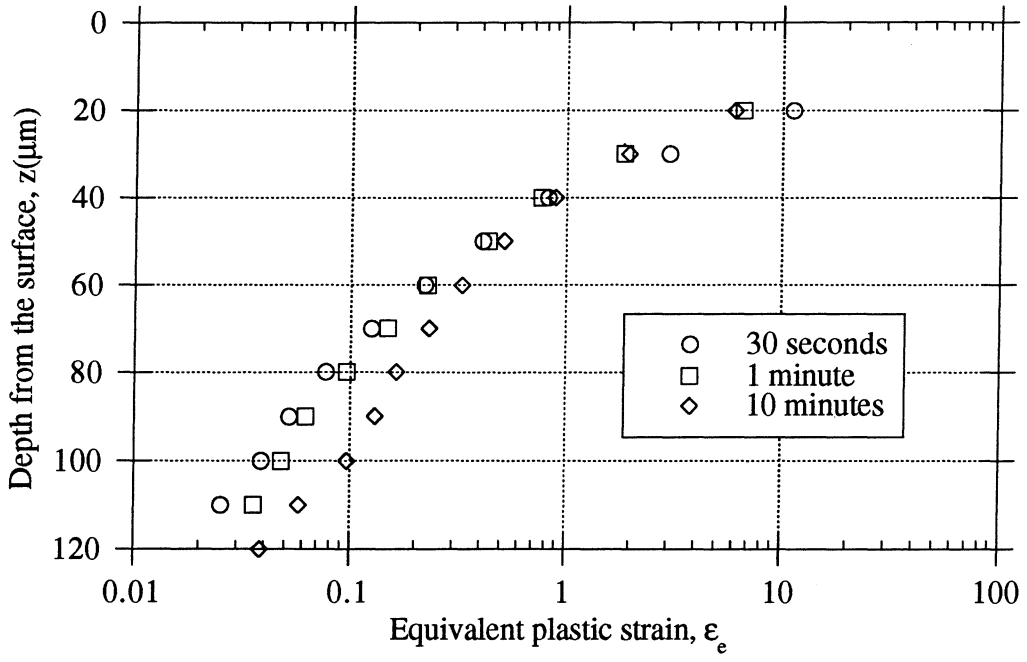

Fig. 4.17 - Equivalent strain in the subsurface as a function of depth and time
P = 17.5 MPa, V = 0.266 m/s, T_0 = 30°C, Environment: air

4.4 Progression of Scuffing

The progression of scuffing is demonstrated in Fig. 4.18, which shows photographs of the surface of a pin tested at a PV which led to scuffing after twenty minutes of sliding. The photographs were taken after five (Fig. 4.18a) and ten (Fig. 4.18c) minutes of sliding. In the figure, the dark color indicates the presence of surface films, while the light color is characteristic of sections of the surface removed by fatigue. This is proven by the surface profile (Fig. 4.18b) of the pin shown in Fig 4.18a. It indicates that the light-colored portions of the surface are deep valleys. In the second photograph, the parts of the surface removed by fatigue have significantly increased. Removal of sections of the load-bearing area increases the severity of loading over the remaining area. This process is unstable, self accelerates, and leads to fast removal of the protective film from most of the surface of the pin. The exposed bare metal adheres to the counterface and a cold weld is formed (Fig. 4.19). This is the final stage of scuffing.

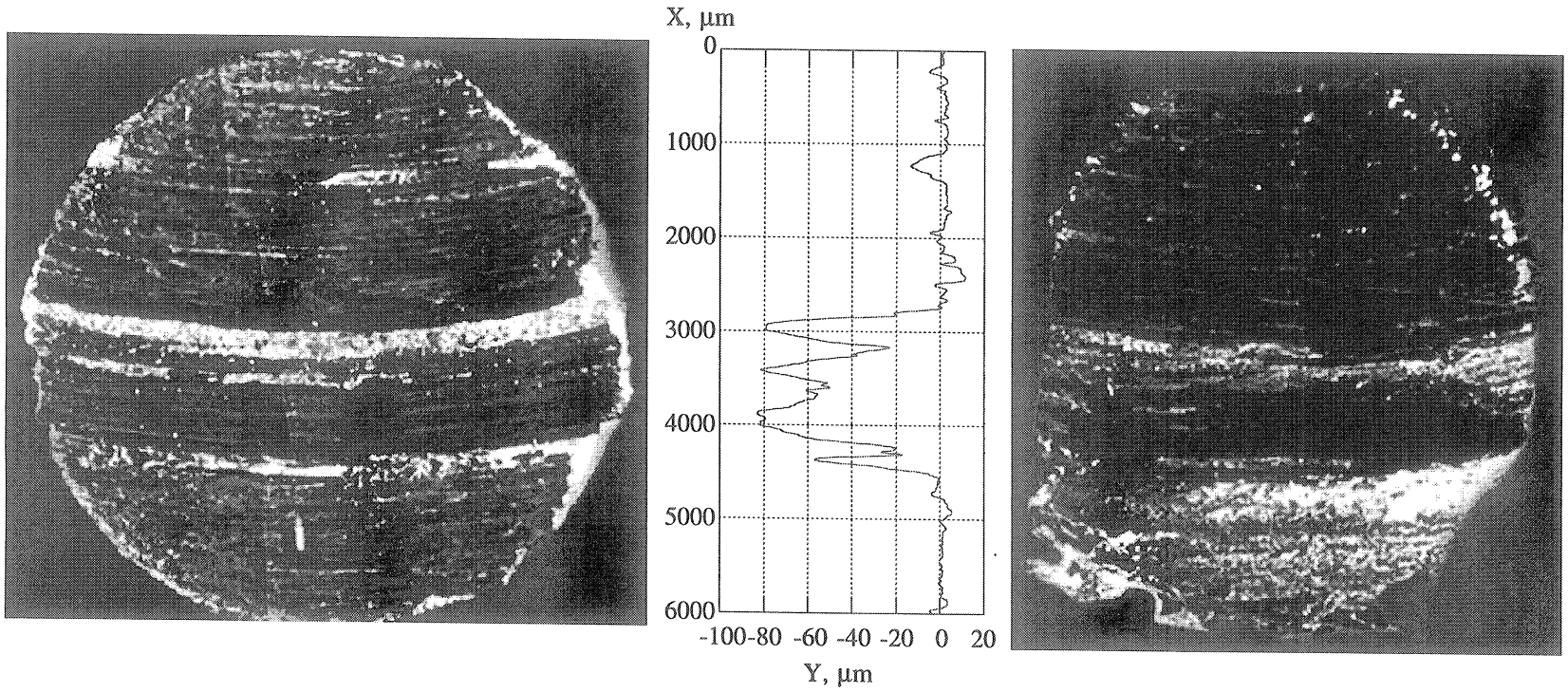

Fig. 4.18 - Progression of the scuffing process which caused scuffing after 20 minutes of sliding
$P = 8.76$ MPa, $V = 0.67$ m/s, $T_0 = 30°C$, Environment: air. (a) Top surface of the pin after five minutes of sliding,
(b) Profile of the same surface, and (c) Top surface of the same pin after ten minutes of sliding
The dark areas are covered by surface films, the light areas are metallic. Note that part of the deep valleys are covered by films

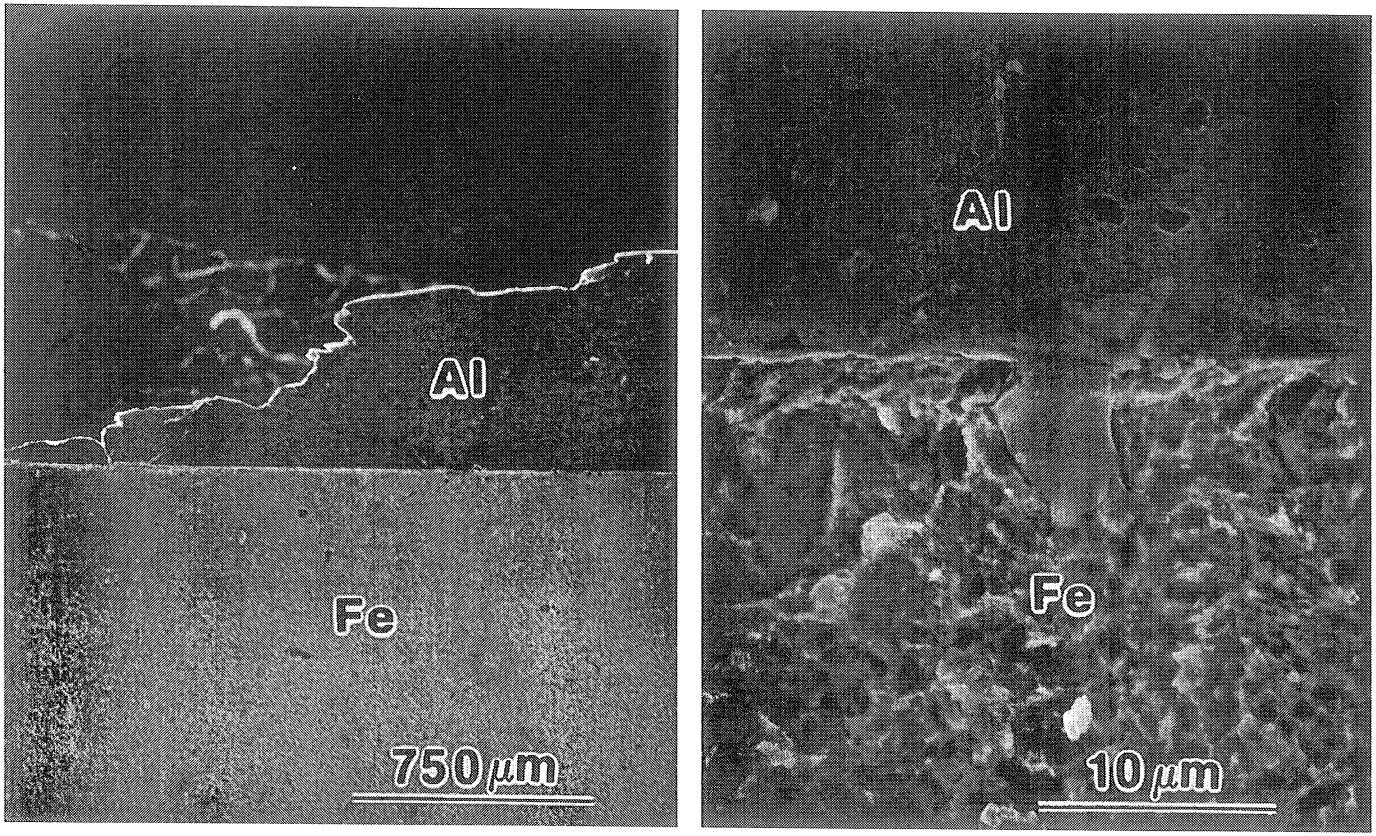

(a) (b)

Fig. 4.19 - Formation of cold welds: (a) Magnification x40 and (b) Magnification x3000
Geometry: R12.7, P = 12.3 MPa, V = 0.67 m/s, T_0 = 30°C, Environment: air
Loading: stepwise with 5 min-long steps

An important characteristic of this process is that sharp increase in friction and wear is not observed until the final stage of scuffing. For both surfaces shown in Fig. 18, the friction was below 0.25 at this moment of time. As Ludema [23] has indicated, this is typical for the scuffing process which can go through several stages. The more dramatic manifestations of scuffing appear only in the final stage with large adhesive wear. From the observations of the surfaces and the subsurfaces of the aluminum pins, it can be concluded that the preceding stages are characterized by gradual accumulation of plastic deformation, formation of voids and cracks, propagation of these cracks in the subsurface, which leads to the removal of whole portions of the load-bearing surface.

4.5 Summary

The mechanisms leading to scuffing under dry sliding conditions were studied by examination of surfaces, subsurfaces and wear debris and by quantitative measurements of average subsurface plastic deformation and surface layers thickness. Most of the observations listed below are based on the behavior of 390-T6 Al. However, the behavior of DHT-3 Al and steel indicates that this general behavior can be applied to other materials. The results of these studies can be summarized as follows:

a. Scuffing under dry sliding conditions is due to a subsurface failure. The processes leading to scuffing seem to involve the following events:

(1) Accumulation of plastic deformation
(2) Formation of voids and cracks in the subsurface
(3) Propagation of subsurface cracks and removal of sections of the surface
(4) Unstable decrease of the load bearing area
(5) Removal of protective layers from most of the surface
(6) Formation of cold welds

b. The subsurfaces of specimens tested under dry sliding conditions have three characteristic regions. These are a layer of transformed material, a layer of plastically deformed material, and a layer of undisturbed material.

c. The mechanisms for the formation of the transformed layer are oxidation, material transfer, compaction of fine wear particles, and plastic deformation.

d. At a constant PV, the thickness of the transformed layer increases with time until it reaches an equilibrium level. The thickness also increases with the PV.

e. For a given PV, the amount of subsurface plastic deformation increases with time until it reaches an equilibrium level. Most of the plastic deformation occurs at the beginning of the test.

f. For the tests conducted in air, the amount of accumulated plastic deformation increases with the PV. It is constant for a wide range of P and V combinations, provided that their product remains constant.

g. Under the same load and sliding velocity, the plastic deformation for the tests conducted in R134a environment is lower than the plastic deformation for the tests conducted in air.

h. Under R134a the plastic deformation is not constant along the $PV = const$ curve. It is a stronger function of the contact pressure.

4.6 Contributions

The general structure of the subsurface of materials in sliding contact has been known for years. The formation of transformed layers and the accumulation of plastic deformation are well documented in the literature [22,37,39,90,91]. However, in very few of the scuffing studies the subsurfaces of the test specimens have been studied. In even fewer, these studies are supported by quantitative measurements. One of the achievements of this study is that it provides a more complete picture of the scuffing process by combining the phenomenological experimental results with microscopic observations and measurements.

Cracks and other damage in the subsurfaces of test specimens are also often reported [16,37,39,91]. However, the existence of cracks at depths larger than the thickness of the transformed layer has not received much attention. The possibility that the formation of these cracks is the mechanism responsible for scuffing is suggested for the first time in the present study. There are several important findings related to these deep subsurface cracks. These are summarized below:

a. Deep subsurface cracks do not form at PV's lower than the scuffing condition.

Cracks propagating deeper than the thickness of the transformed layer were found only in the specimens which were in the process of scuffing. No such cracks were observed at lower PV's. This suggests a strong relationship between scuffing and deep subsurface fatigue. Although the idea of a relationship between scuffing and fatigue has been suggested in the literature [70], no definite mechanism or proof relating these events have been found so far. The present study provides the explanation for this relationship.

b. The formation of cracks occurs before the final stage of scuffing.

As stated earlier, the existence of subsurface cracks in scuffed specimens is well known. However, the cause and effect relationship between these two was unclear. These cracks could be caused by the large adhesive tractions after scuffing. The present study provides the proof that,

under dry sliding conditions, the generation of cracks precedes and actually causes the adhesive stage of the process.

c. The existence of several stages in the scuffing process can be explained.

It is generally known that scuffing goes through several stages. However, the physical events occurring in these stages have not been identified. The present study provides evidence that these stages are associated with the initiation and propagation of subsurface cracks.

d. The events in the final stage of scuffing are better understood.

The gradual removal of whole sections of the load-bearing surface before the final adhesive stage is also a new finding. This mechanism provides the explanation for the unstable and catastrophic growth of the areas of bare metal, leading to the final stage of scuffing.

CHAPTER 5
CALCULATION OF SURFACE PRESSURES AND REAL AREAS OF CONTACT

As evident from the discussion in the previous chapter, scuffing under dry sliding conditions is the result of subsurface material failure. At every particular location where the material fails, a critical combination of local stress, strain and temperature must be attained. Unfortunately, macroscopic parameters such as apparent contact pressure, apparent area of contact, and bulk temperature poorly correlate with the actual temperatures and stresses the material experiences. Therefore, the determination of the local stress and temperature distributions is very important in understanding the scuffing process.

The mechanical and thermal state of the subsurface is determined by the distribution of surface tractions, heat fluxes, and contact spots. These can be obtained by studying the problem of rough surfaces in contact. The major difficulty of this problem is that the real area of contact and the actual pressure distribution over the interface cannot be obtained experimentally. The only exception is the case when one of the bodies in contact is transparent. Hence, the determination of the above parameters has to rely on models for the contact of rough surfaces. There are two major approaches which can be taken to model the contact of rough surfaces. These are the stochastic approach and the deterministic approach.

In this study, the distribution of surface pressures and real contact areas was obtained by developing a model for the contact of runned-in surfaces. It combines a deterministic finite element model, statistical methods for surface alignment, and correction factors for deviations from the infinite half space approximation.

5.1 Stochastic Models for the Contact of Rough Surfaces

In most stochastic models, the shape of the asperities is assumed to be either hemispherical, or ellipsoidal. The features of the real surfaces are approximated by a set of such asperities with heights and sizes determined by probability density functions and their moments. The features of the two surfaces in contact are combined into a surface with "equivalent" roughness. This "equivalent" surface is then "pressed" against a rigid flat plane. The pressure distribution and the contact area of a single asperity is obtained by applying the analytical solutions of Hertz. The total area of contact is obtained from the solutions for a single asperity through statistical methods.

Greenwood and Williamson [6] developed the first and the best known stochastic model. In their model, hemispherical asperities with constant radius of curvature and Gaussian height distribution are pressed against a smooth, rigid plane. This model has seen numerous improvements, mainly to account for anisotropy in the shape of the asperities, variable radii of curvature and height distributions other than Gaussian [93-97]. These improvements lead to more realistic models, but the difficulty of their implementation often outweighs their advantages [98].

Fractals can be used instead of probability density functions to describe the features of a surface [99-102]. In this case, an assumption for the shape of the asperity is not required, but the surface is assumed to be self-similar at various scales. The contact mechanics part of the problem is also based on Hertz's theory.

The major advantage of the stochastic modes is that they are relatively easy to implement. However, with the increasing complexity of the most recent models this advantage becomes less apparent. These models may require complicated filtering of the experimentally obtained surface profiles, which leads to non-trivial problems in signal processing [95,98]

The stochastic models have many disadvantages which have limited their applicability and have always raised questions about the trustworthiness of their results [103-105]. The major disadvantages of these methods are:

a. All stochastic models require a decision for the asperity scale which is mechanically relevant. In fact, the very definition of an asperity requires an assumption for a dominant scale.

b. The stochastic models neglect the interactions between neighboring asperities. They do not take into account the deformation of the body as a whole. Therefore, there is no easy way to account for edge effects or variable stiffness of the specimens.

c. An assumption for the shape of the asperities or the self-similarity of the surface is required. Both of these assumptions are very limiting. In addition, a deviation from self-similarity can be expected for many engineering surfaces.

d. A statistical independence of the surface features of the contacting surfaces is assumed. Hence, the stochastic models cannot be applied to runned-in surfaces. This is a serious disadvantage, because it limits their application to virgin surfaces, or to surfaces with negligible wear.

For the conditions of this study, both assumptions (b) and (d) of the above are violated. Therefore, stochastic methods cannot be applied to determine the surface pressure and area of contact distributions under dry sliding conditions.

5.2 Deterministic Models

The deterministic models are often finite element models of various complexity [103-113]. The surfaces in contact are represented by digitizing the output of stylus profilers or other instrumentation for surface characterization. The major assumption of the deterministic models is that the contacting bodies can be approximated by elastic half-spaces, and that the point-load field solution of Boussinesq and Cerutti holds. This assumption is justified by the fact that the typical slopes of the surface features are small. The contact between the surfaces is assumed to be frictionless. Typically, the surface is subdivided into elements (rectangular in 2-D models and long strips in 1-D models) with only one degree of freedom - their vertical displacement. The pressure over each element is assumed to be either constant, or linearly varying.

A schematic of two rough surfaces in contact is given in Fig. 5.1. Note that the sliding between the surfaces occurs in the y-direction. The x-z plane is the plane of the transverse surface profiles. Also note that the datum planes of the two surfaces are inclined with respect to each other. This is an illustration of the angular misalignment, which can occur in the process of taking the surface profiles.

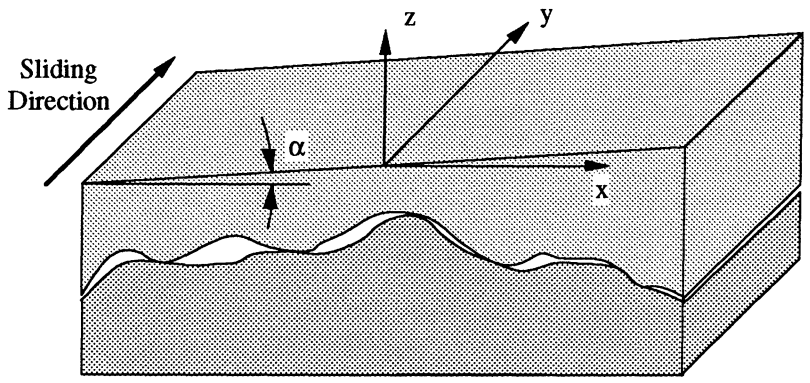

Fig. 5.1 - Schematic of the contact between two rough surfaces

According to the solution of Boussinesq, the vertical displacement w of an arbitrary point on the surface with coordinates (x, y) due to a point force $p(x',y')dx'dy'$ applied at (x',y') is given as:

$$w(x,y) = \frac{1-\nu^2}{\pi E} \iint_{A_0} \frac{p(x',y')dx'dy'}{\sqrt{(x-x')^2+(y-y')^2}} \tag{5.1}$$

If the apparent area of contact A_0 is divided into M elements of size $\hat{A}$, the above equation can be discretized in the form:

$$w_l = \frac{1-\nu^2}{\pi E}\sum_{k=1}^{N}\left\{\iint_{\hat{A}}\frac{dx'dy'}{\sqrt{(x-x')^2+(y-y')^2}}\right\}p_k \qquad \text{or} \qquad w_l = \frac{1-\nu^2}{\pi E}\sum_{k=1}^{N}C_{kl}p_k \quad (5.2)$$

where N is the number of elements in contact. Note that $N \leq M$, which indicates that not all of the elements over the apparent area are in contact. The influence matrix C_{kl} is easily calculated because the shape of each element is simple and the value of the integral depends only on the relative position of the points of load application and displacement calculation. The sum of the displacements $(w_1+w_2)_l$ of the two contacting bodies at every location must be equal to the geometrical overlap (δ_l) of the non-deformed profiles $z_1(l)$ and $z_2(l)$ resulting from any given rigid body approach (d) and rotations with respect to the x and y axes. For the simpler one-dimensional case (Fig. 5.2), the overlap is calculated as:

$$\delta_l = [z_1(l) - z_2(l)] + d + s(l - M/2)\tan(\alpha) \quad (5.3)$$

where s is the discretization step of the profile and α is the angle between the datum lines. This angle is measured with respect to the center of the surface profile which is located at $M/2$.

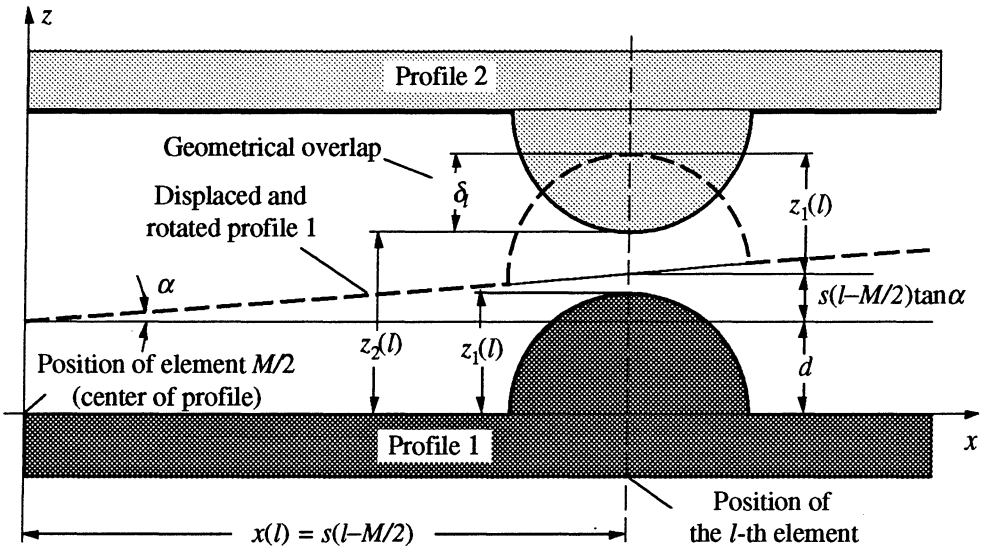

Fig. 5.2 - Illustration of the geometrical overlap between one-dimensional surface profiles. Each profile is shematically represented by a single cylindrical asperity. The asperities do not make contact initially. Profile 1 is displaced and rotated, resulting in overlap of the asperities.

Equation (5.3), generalized for the two-dimensional case gives:

$$\delta_l = [z_1(l) - z_2(l)] + d + x' \tan(\alpha_y) + y' \tan(\alpha_x) \tag{5.4}$$

where x' and y' are the coordinates of the l-th element with respect to the center of the apparent area of contact, and α_x and α_y are the rotations with respect to the x and y axes, respectively.

Making use of Eq. (5.2), the expression for the sum of the displacements $(w_1+w_2)_l$ is:

$$(w_1 + w_2)_l = \frac{1-\nu_1^2}{\pi E_1} \sum_{k=1}^{N} (C_{kl})_1 p_k + \frac{1-\nu_2^2}{\pi E_2} \sum_{k=1}^{N} (C_{kl})_2 p_k = \sum_{k=1}^{N} \underbrace{\left[\frac{1-\nu_1^2}{\pi E_1} (C_{kl})_1 + \frac{1-\nu_2^2}{\pi E_2} (C_{kl})_2 \right]}_{C_{kl}^*} p_k \tag{5.5}$$

where C_{kl}^* combines the influence coefficients for the two contacting bodies. Combining Eq. (5.5) for all the lements in the model leads to the set of equations:

$$\begin{Vmatrix} C_{11}^* & C_{12}^* & \cdots & C_{1N}^* \\ C_{21}^* & C_{22}^* & \cdots & C_{2N}^* \\ \vdots & \vdots & & \vdots \\ C_{N1}^* & C_{N2}^* & \cdots & C_{NN}^* \end{Vmatrix} \begin{Bmatrix} p_1 \\ p_2 \\ \vdots \\ p_N \end{Bmatrix} = \begin{Bmatrix} \delta_1 \\ \delta_2 \\ \vdots \\ \delta_N \end{Bmatrix} \tag{5.6}$$

Equation (5.6) is a matrix equation for the unknown pressures p_k. It can be solved by matrix inversion or some other method. A complication in the solution procedure arises from the fact that the pressures p_k cannot be tensile. Hence, the set of equations (5.4) is non-linear and requires an iterative solution. The general algorithm for the determination of the unknown pressures is as follows:

a. The surface profiles are made to approach each other such that contact occurs only at one point.

b. The surfaces are displaced vertically toward each other by an initial amount d.

c. Equation (5.6) is solved for the unknown pressures.

d. The sum of the local loads over the elements is compared to the applied load W.

e. If the sum is larger than W, d is decreased, if it is smaller d is increased. Iteration through steps (c)-(e) is continued until W and the sum become equal.

These models provide realistic pressure, subsurface stress, and area of contact distributions. The interactions of neighboring contacts is taken into account. In addition, it is possible to deal with high degrees of conformity, typical for run-in surfaces. Therefore, a

deterministic finite element method was chosen to determine the distributions of surface pressures and contact areas.

5.3 Contact of Runned-In Surfaces

Surfaces which have been rubbed against each other for some time attain surface features which are dependent on each other [114-117]. The surface profiles of such surfaces match (the peaks of one surface correspond to valleys on the other). This is schematically illustrated in Fig. 5.1. This increased conformity leads to a larger real area of contact and to lower local pressures. The conformity of surfaces is neglected in the stochastic models, because it requires a statistical covariance term which is generally unknown [118]. As stated earlier, this is one of the major disadvantages of these models, limiting their application to virgin surfaces. The deterministic models are not sensitive to this problem. It is , therefore, surprising that none of the deterministic models described in the literature takes the matching of runned-in surfaces into account, although, this is in principle possible.

The major difficulty in taking the surface conformity into account is to align the experimentally obtained surface profiles properly. The surfaces have to be matched with accuracy corresponding to the resolution of the experimental equipment, which typically is in the range 1-5 μm. This accuracy can be achieved only by statistical methods.

Aligning of surface profiles by statistical methods was used for the first time by Sigimura and Kimura [116] to quantify the topographical changes of surfaces during the run-in process. They introduced a cross-correlation coefficient which gives a quantitative expression for the similarity of profiles. Due to practical difficulties in locating a common starting point for the profiles during measurements, they may be displaced in the transverse x-direction. The cross correlation coefficient helps to identify this displacement. In the case when the profiles are digitized, they constitute sets of equally spaced points. Let $U(i)$ and $Y(i)$ denote two digitized profiles, where i determines the position of the point along the x-axis. Then the cross correlation coefficient is given as [116]:

$$\gamma(\xi) = \left(\sum_{i=1}^{n-\xi} U_i Y_{i+\xi}\right) \Big/ \left(\sum_{i=1}^{n-\xi} U_i^2 \sum_{i=1}^{n-\xi} Y_{i+\xi}^2\right)^{1/2} \tag{5.7}$$

where ξ s an integer number which, if multiplied by the sampling interval, gives the distance by which one of the surface profiles lags the other. The above function has a sharp maximum at some ξ_0 which corresponds to the most likely position (lag) of the second surface with respect to the first surface while they were in contact. A typical plot of $\gamma(\xi)$ for the alignment of a disk and pin

profiles is given in Fig. 5.3. Equation (5.7) works well only if all the ordinates in both profiles are positive. Hence, a vertical translation of one or both profiles prior to the application of the formula is necessary. In the case of pin/disk profiles matching, one of the profiles has to be inverted before the calculation.

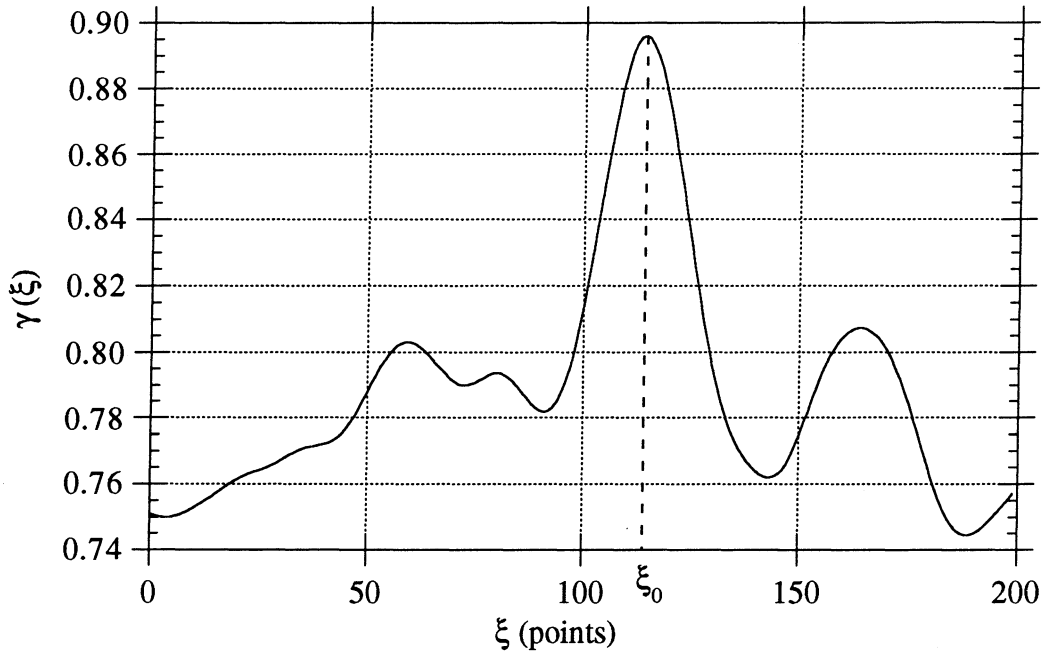

Fig. 5.3 - Determination of the lag between disk and pin surface profiles

To double-check the results predicted by equation (5.7), another statistical function was used. This function is the familiar least squares fit, which has a minimum at ξ_0 and is given by:

$$\delta(\xi) = \sum_{i=1}^{n} \left(U_i - Y_{i+\xi}\right)^2 \tag{5.8}$$

Equations (5.7) and (5.8) were tested on profiles with varying conformity. In all these tests, both statistical functions gave identical results. The equations were also checked by visual inspection of aligned surfaces with easily identified features. The alignment of eight surface profiles of the same disk, taken at equal angular increments of $\pi/4$ transverse to the direction of sliding is shown in Fig. 5.4.

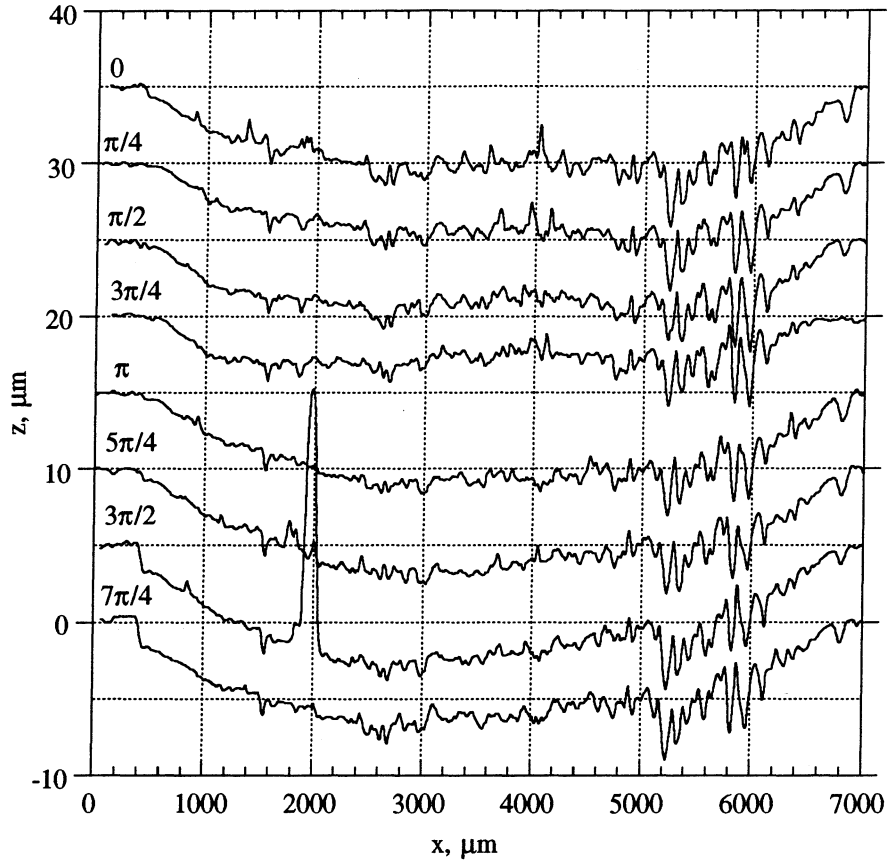

Fig. 5.4 - Alignment of surface profiles of the same disk
The profiles are taken transverse to the direction of sliding at eight equidistant locations
Geometry: R12.7, P = 7.02 MPa, V = 0.67 m/s, T_0 = 30°C,
Environment: air, Counterface: 390-T6 Al pins

The numerical results from the same alignment are given in Table 5.1. In the table, d1-d8 denote the disk profiles and p1 denotes a pin profile. The number of points (each point corresponds to 5 μm) by which the first profile lags the second profile is given in the second column of the Table 5.1. The same disk profiles are then aligned with a profile of a pin which was tested against this disk. These results are given in the fourth column of Table 5.1. Finally the results from a combined alignment, given by the differences in two consecutive disk-pin matches are shown in the sixth column. The proper alignment of the profiles has to meet two requirements. The first is that the sum of all lags over the circumference of the disk must add up to zero. This means that the sum of the numbers in both columns two and six must be zero. The second requirement is that columns two and six are the same. As seen from the table, both requirements

are satisfied fairly well keeping in mind that the accuracy of the analog-to-digital conversion of the profiles is one point. From these results, it can be concluded that equations (5.7) and (5.8), especially when used together, are a reliable tool for the alignment of conforming surfaces.

Table 5.1 - Results from the alignment of surface profiles
The disk profiles are taken transverse to the direction of sliding at eight equidistant locations
The pin profile is taken trough the center of the pin transverse to the direction of sliding

Disk-Disk	Lag (Points)	Disk-Pin	Lag (Points)	Combined	Lag (Points)
d1-d8	4	d1-p1	117	(d1-p1)-(d8-p1)	4
d2-d1	3	d2-p1	119	(d2-p1)-(d1-p1)	2
d3-d2	10	d3-p1	130	(d3-p1)-(d2-p1)	11
d4-d3	0	d4-p1	133	(d4-p1)-(d3-p1)	3
d5-d4	-29	d5-p1	103	(d5-p1)-(d4-p1)	-30
d6-d5	15	d6-p1	118	(d6-p1)-(d5-p1)	15
d7-d6	7	d7-p1	125	(d7-p1)-(d6-p1)	7
d8-d7	-11	d8-p1	113	(d8-p1)-(d7-p1)	-12
Total	-1				0

In addition to the x-axis misalignment, the profiles may also have angular misalignments, as shown in Fig. 5.1. These are corrected by requiring that the sum of the moments with respect to the center point of the profile of all forces resulting from the contact of the two surfaces is zero. Since this requires knowledge of the surface pressure distribution, this alignment is incorporated in the solution for the pressures and is discussed in more detail in Section 5.7 below.

5.4 One Dimensional Versus Two Dimensional Formulation of the Finite Element Model

The surface features on worn disks and pins are strongly anisotropic. The surface roughness perpendicular to the direction of sliding (transverse direction) is much larger than the surface roughness along the direction of sliding (longitudinal direction). In fact, the longitudinal surface roughness for the pins can be neglected. This follows from the observation that parallel

transverse surface profiles of the pins are practically identical. Even the transverse surface profiles of two different pins which slide against the same disk are very similar. This is demonstrated in Fig. 5.5. The reason for this similarity is that the features on the surfaces of the pins are produced through interactions with the same spots on the disk. Hence, the surface roughness of the pins can be assumed to be one-dimensional. Waviness of the surface of the pins is not important due to their small length in the direction of sliding. An optical photograph revealing the one-dimensional character of the surface of a 390-T6 Al pin is shown in Fig. 5.6.

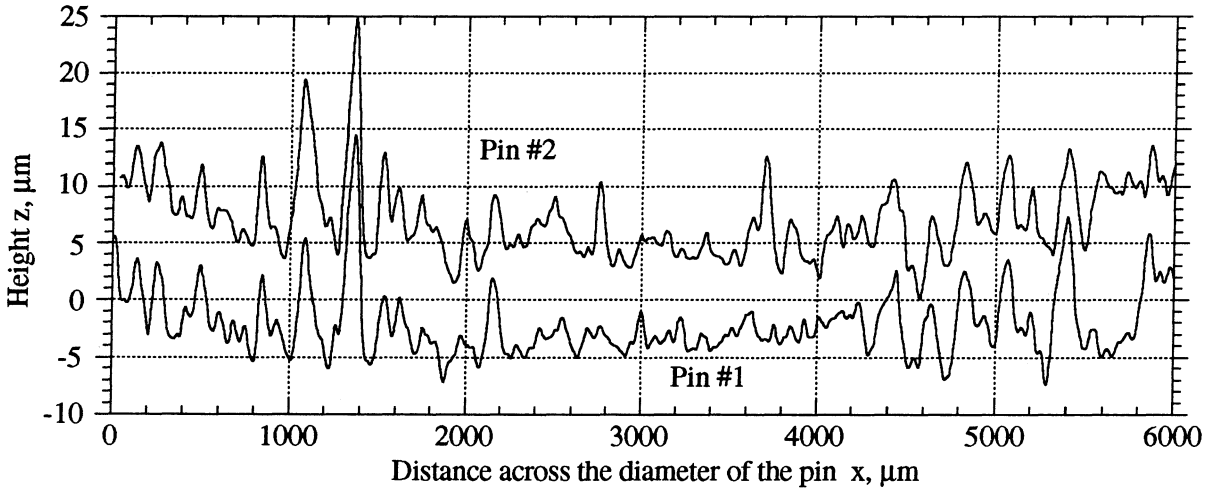

Fig. 5.5 - Transverse surface profiles of two pins which slide against the same disk
Geometry: R12.7, P = 7.02 MPa, V = 0.67 m/s, T_0 = 30°C, Environment: air, Material: 390-T6 Al

The surface of the disks, although anisotropic, is two-dimensional. Gradual changes in the profile of the disks in the direction of sliding does occur. This can be seen from the profiles shown in Fig. 5.4. From the figure, it is clear that although similar, the profiles have variations in depth. However, these variations involve distances much larger than the size of the pin. Therefore, the contact between the pin and the disk at every particular location on the disk can still be treated as one-dimensional. The variations of the pressure distribution in the direction of sliding can be obtained from several solutions of the finite element model corresponding to different locations on the disk.

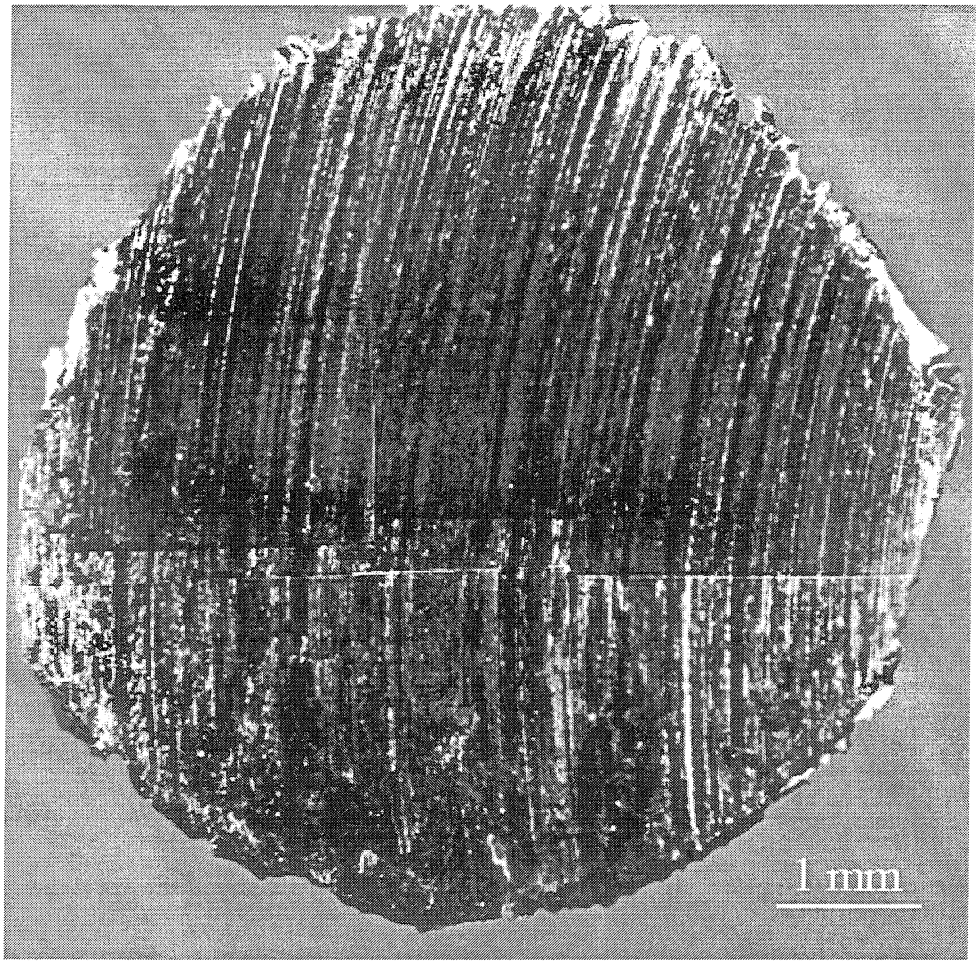

Fig. 5.6 - Top surface of a 390-T6 Al pin
The direction of sliding is from bottom to top
Geometry: R12.7, P = 7.02 MPa, V = 0.67 m/s, T_0 = 30°C, Environment: air

Another question, which must be addressed, is the accuracy of the one-dimensional models compared to the two-dimensional models of the same surface. This question has been studied by Francis [113]. The conclusion from his work is that the error in implementing one-dimensional models increases with decreasing anisotropy of the surface features. An aspect ratio (given as the length of the elements divided by their width) of over 3.0 is necessary for an error of less than one percent. The aspect ratio characteristic of the surfaces of this study are in the range 20 - 200. Therefore, the error due to the implementation of the simpler one-dimensional method is expected to be insignificant.

Additional error may result from the idealization of the shape of the contact area. Two possible representations of the contact surface by finite elements are schematically shown in Fig. 5.7. The representation given in Fig.5.7a is a true one-dimensional model. It has M identical finite elements. The length of the elements is determined by the requirement for the equality between the apparent contact areas of the model and the real surface. The elements of the influence matrix for this model depend only on the distance between the point where the displacement is calculated and the point of load application. The influence matrix is symmetric and the memory required for its storage is of size M. The question about the memory requirement is important because a true two-dimensional matrix may require storage on the order of 10^6 entries.

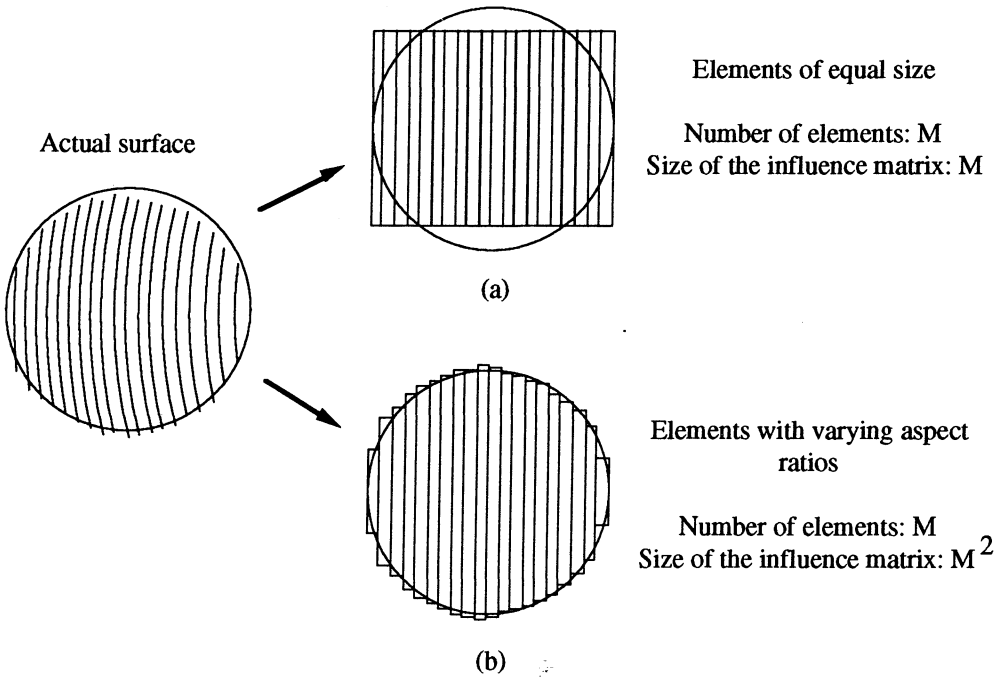

Fig. 5.7 - Representation of the surface of the pin by finite elements
(a) elements of equal size and (b) elements with varying aspect ratios

True one-dimensional models have been used successfully in various contact problems [104,105,111,112]. However, in all these problems, the actual contact area has also been rectangular in shape. The transformation from a circular to a rectangular contact area results in errors in the solution. The representation shown in Fig. 5.7b solves this problem. The length of the elements are different and equal to the actual length of the contact arch at the particular location on the contact area. This is a quasi two-dimensional model because the elements have various aspect ratios. It has a full influence matrix of M^2 elements. Solutions based on both of the above representations were compared for actual surface profiles and for specially generated trial surfaces. The discrepancies in the solutions were higher than five percent and were considered unacceptable. The second representation of the actual surface was chosen for the finite element model.

With the chosen representation of the contact surface, the elements are rectangles, $2a$ wide and $2b$ long. The surfaces of the pin and the disk are represented by their digitized profiles obtained with a stylus surface profiler. The number of elements in the representation of the surface is equal to the number of points in the digitized profile, typically (1200-1500). The width of each element is equal to the spacing between the data points in the digitized profile, s = 5 μm. The length $2b$ of each element is different and equal to the length of the contact arch (Eq. 3.8) at the particular location of the element. The contact pressure over each element is assumed to be constant. The elements of the influence matrix are calculated according to the formula given in [119] for the effect of a uniform pressure (p) acting on a rectangular area $2a$ x $2b$ on the vertical deflection w of a point (x, y):

$$\frac{\pi E}{1-\nu^2}\frac{w}{p} = (x+a)\ln\left[\frac{(y+b)+\sqrt{(y+b)^2+(x+a)^2}}{(y-b)+\sqrt{(y-b)^2+(x+a)^2}}\right] + (y+b)\ln\left[\frac{(x+a)+\sqrt{(y+b)^2+(x+a)^2}}{(x-a)+\sqrt{(y+b)^2+(x-a)^2}}\right] \tag{5.9}$$

$$+ (x-a)\ln\left[\frac{(y-b)+\sqrt{(y-b)^2+(x-a)^2}}{(y+b)+\sqrt{(y+b)^2+(x-a)^2}}\right] + (y-b)\ln\left[\frac{(x-a)+\sqrt{(y-b)^2+(x-a)^2}}{(x+a)+\sqrt{(y-b)^2+(x+a)^2}}\right]$$

Only the displacements at $y = 0$ are of interest. Setting $y = 0$ and making the substitutions:

$$2a = s, \qquad 2b = L_{arch}, \qquad \zeta = b/a, \qquad \text{and} \qquad x = |k - l| = is$$

gives the formula for the influence coefficients C_{kl}:

$$C_{kl} = \left\{ (2i+1)\ln\left[\frac{\zeta_k + \sqrt{\zeta_k^2 + (2i+1)^2}}{\zeta_k + \sqrt{\zeta_k^2 + (2i+1)^2}}\right] + \zeta_k \ln\left[\frac{(2i+1) + \sqrt{\zeta_k^2 + (2i+1)^2}}{(2i-1) + \sqrt{\zeta_k^2 + (2i-1)^2}}\right] \right.$$
$$\left. + (2i-1)\ln\left[\frac{\zeta_k + \sqrt{\zeta_k^2 + (2i-1)^2}}{\zeta_k + \sqrt{\zeta_k^2 + (2i-1)^2}}\right] + \zeta_k \ln\left[\frac{(2i-1) + \sqrt{\zeta_k^2 + (2i-1)^2}}{(2i+1) + \sqrt{\zeta_k^2 + (2i+1)^2}}\right] \right\} \tag{5.10}$$

where ζ is the aspect ratio of the elements. The vertical displacement then is:

$$w_l = \frac{s(1-\nu^2)}{2\pi E} \sum C_{kl} p_k \tag{5.11}$$

5.5 Edge Effects

As stated earlier, the major assumption of the deterministic models is that the infinite half-space approximation holds. This assumption is suitable for the surface of the disk which is large compared to the size of the contact area. However, it is violated for the surface of the pin, the whole of which is loaded. The stiffness of the pin close to the edge is lower than the stiffness in the center. In the solution for the pressures, this will result in stress concentration near the edge. From the experimental evidence presented in Fig. 3.15 it is clear that this does not happen. The reason is that any stress concentration accelerates the local wear rate, which leads to a better surface conformity and relieving of the higher stresses. To account for this effect, a correction in the infinite half space approximation is necessary.

The edge pressure concentration problem has been recognized and solved in the works of Francis [105] and Ren et al.[106]. Francis has proposed a profile bending technique which produces uniform average pressure distribution. It is based on the analytical solution of a rigid punch pressing on an elastic half-space. In this method, the actual surface profiles are divided into segments. A least squares straight line is fitted to the rough profile of each segment. Then the lines and their corresponding profile sections are rotated with respect to each other to an approximately parabolic shape, given from the punch-on-flat plane solution. This method is complicated and requires decisions about the size of the line segments, which brings additional uncertainties in the solution. The method used by Ren et. al.[106] involves the application of a constant uniform tensile pressure on the whole contact region. The actual solution is obtained by combining the displacements resulting from asperity interactions with the displacement resulting

from the tensile stresses. This method is easy to implement. Its major disadvantage is that their finite element method employs the concept of contact between an equivalent surface and a rigid plane. The equivalent surface is produced from the superposition of the surfaces of both bodies in contact. Thus, the correction for edge effects is applied to both surfaces. In the case of a pin-on-disk geometry, the correction must be applied only to the pin surface.

In this study, the correction for edge effects is based on the requirement that uniform pressure on the surface of the pin must produce uniform displacement. The solutions based on the infinite half-space approximation predict displacements which decrease in magnitude from the center of the loaded area towards the edges. Hence, the displacements over the whole loaded area must be multiplied by correction factors which will provide the necessary uniform displacement. These correction factors can be derived analytically. The expression for the displacements inside a uniformly loaded circular region is given in [119] as:

$$w = \frac{4(1-\nu^2)pa}{\pi E}\mathbf{E}(r/a), \qquad (r < a) \tag{5.12}$$

where $\mathbf{E}(r/a)$ is the complete elliptic integral of the second king with modulus (r/a), r specifies the position of the point within the circle and a is the radius of the circle. The correction factors are obtained as the ratio of the displacement in the center of the circle to the displacement given by Eq. (5.12). Since at the center $r = 0$ and $\mathbf{E}(0) = \pi/2$, the expression for the correction factors becomes:

$$\Psi = \frac{\pi}{2\mathbf{E}(r/a)} \tag{5.13}$$

This expression can be further modified to account for the discretization of the finite element problem:

$$\Psi_l = \frac{\pi}{2\mathbf{E}(|M/2 - l|/M)} \tag{5.14}$$

where l determines the position of the point on the digitized surface profile of the pin. A plot showing the variation of the correction coefficient over the surface of the pin is given in Fig. 5.8. Applying the correction coefficient to Eq. (5.11) gives the vertical displacement of the elements on the pin:

$$(w_l)_{pin} = \Psi_l \frac{s(1-\nu_{pin}^2)}{2\pi E_{pin}} \sum C_{kl} p_k \tag{5.15}$$

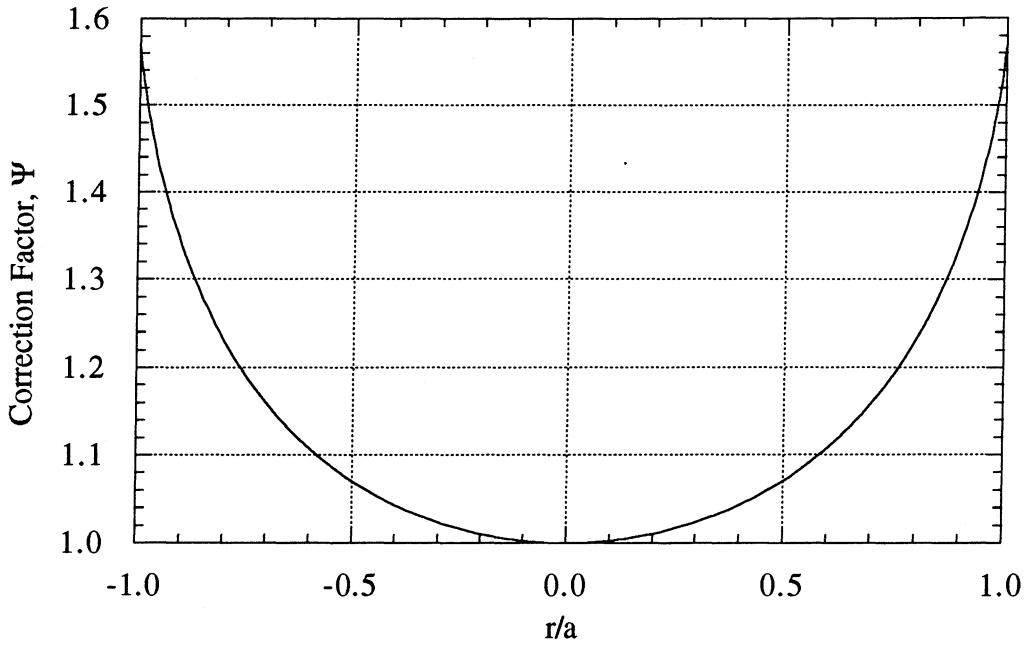

Fig. 5.8 - Correction factors for the displacements on the surface of the pin

The combined vertical displacement for both surfaces is:

$$w_l = (w_l)_{disk} + (w_l)_{pin} = \frac{s\left(1-\nu_{disk}^2\right)}{2\pi E_{disk}} \sum C_{kl} p_k + \Psi_l \frac{s\left(1-\nu_{pin}^2\right)}{2\pi E_{pin}} \sum C_{kl} p_k \tag{5.16}$$

or

$$w_l = \sum \underbrace{\left\{ C_{kl} \frac{s}{2\pi} \left[\frac{\left(1-\nu_{disk}^2\right)}{E_{disk}} + \Psi_l \frac{\left(1-\nu_{pin}^2\right)}{E_{pin}} \right] \right\}}_{C_{kl}^*} p_k \tag{5.17}$$

The final expression for the influence matrix accounting for both the pin and the disk surfaces is:

$$C_{kl}^* = C_{kl} \frac{s}{2\pi} \left(\frac{1-\nu_{disk}^2}{E_{disk}} + \Psi_l \frac{1-\nu_{pin}^2}{E_{pin}} \right) \tag{5.18}$$

5.6 Correction for the Stylus Tip Radius

Due to the finite radius of the tip of the stylus used for taking surface profiles, the valleys of the measured profile will become narrower and the peaks larger. This is schematically shown in Fig. 5.9. This effect can be corrected with a simple geometrical transformation:

$$z^* = z - R_{tip} \cos(\alpha_s)$$
$$x^* = x + R_{tip} \sin(\alpha_s) \qquad (5.19)$$

where R_{tip} is the radius of the tip of the stylus, α_s is the slope of the profile, x and z are the coordinates of a point on the experimentally obtained profile, and x^* and z^* are the coordinates of the corresponding point on the corrected profile. Since the points in the corrected profiles are no longer equidistant, interpolation between these was used to obtain equidistant points. This correction is necessary only for styluses with large radii and was applied to the profiles of one of the earlier tests of this study. These profiles were taken with a 12.5 μm stylus. The rest of the surface traces were taken with a stylus radius of 2.5 μm. For these profiles, no correction was made.

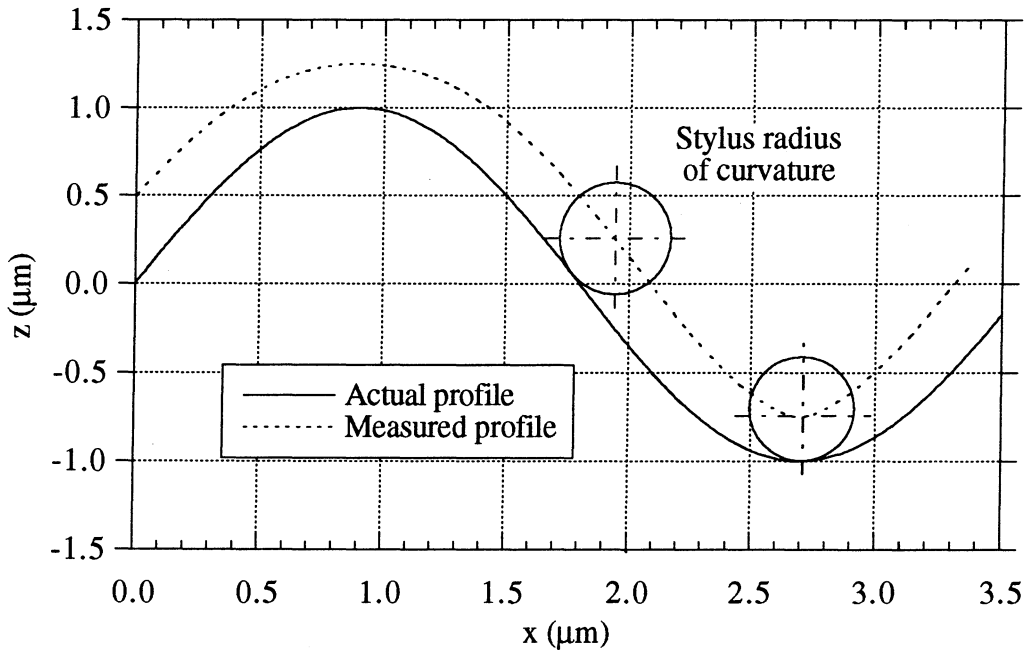

Fig. 5.9 - Errors associated with the finite radius of the stylus tip

5.7 Overall Solution Algorithm

The flowchart of the entire algorithm for calculation of the surface pressure and area of contact distribution is shown in Fig. 5.10. The input to the program are the load on one pin, the material properties at the test temperature, the digitized profiles of the disk and the pin, and data for the geometry of contact. Optional is the input of the yield stress of the softer material.

Steps (2) and (3) are separate algorithms for correction of the profiles, for their alignment and positioning. The arch lengths, the correction factors for the displacement of the pin, and the elements of the influence matrix are calculated in steps (4)-(6). As in any other iterative process, the solution must begin with an initial guess. A good initial guess is very important because it may significantly reduce the computational time. The initial approach is assumed to be equal to the displacement of the center of the pin profile which would result from a uniform pressure over the entire contact surface. This pressure is set equal to the applied apparent pressure P:

$$d_0 = P\sum_1^M C^*_{k(M/2)} \tag{5.20}$$

With the initial approach chosen, and with assumed zero initial inclination, the initial values of the overlap can be computed. The initial guess for the contact pressures assumes that they are proportional to the overlaps, with an average value equal to P.

The solution for the pressures follows a Gauss-Seidel iterative algorithm, as described in [102,104,119]. Other algorithms have also been successfully applied to the solution of Eqs. (5.6). The Gauss-Seidel algorithm was chosen because it offers several advantages. The first is that it is very robust and converges reliably. The second is that plastic behavior can easily be incorporated into the solution [102]. A simplified representation of the algorithm is given in Eq. (5.21) below:

$$(p_l)_{new} = (p_l)_{old} + \omega\left[\frac{\left(\delta_l - \sum_{k=0}^M C^*_{kl}p_k\right)}{C^*_{ll}}\right] \tag{5.21}$$

In the equation, $(p_k)_{\text{new}}$ and $(p_k)_{old}$ are the values of p_k in two successive iterations and ω is a factor facilitating the convergence. The values of p_k are continuously upgraded. If p_k becomes tensile, it is set to zero and the calculation proceeds with the new value. Similarly, if p_k exceeds some preset (yield) value, it can be set to this maximum value. More refined ways to deal with plasticity can also be incorporated. Strain hardening and constancy of volume are two of the possibilities.

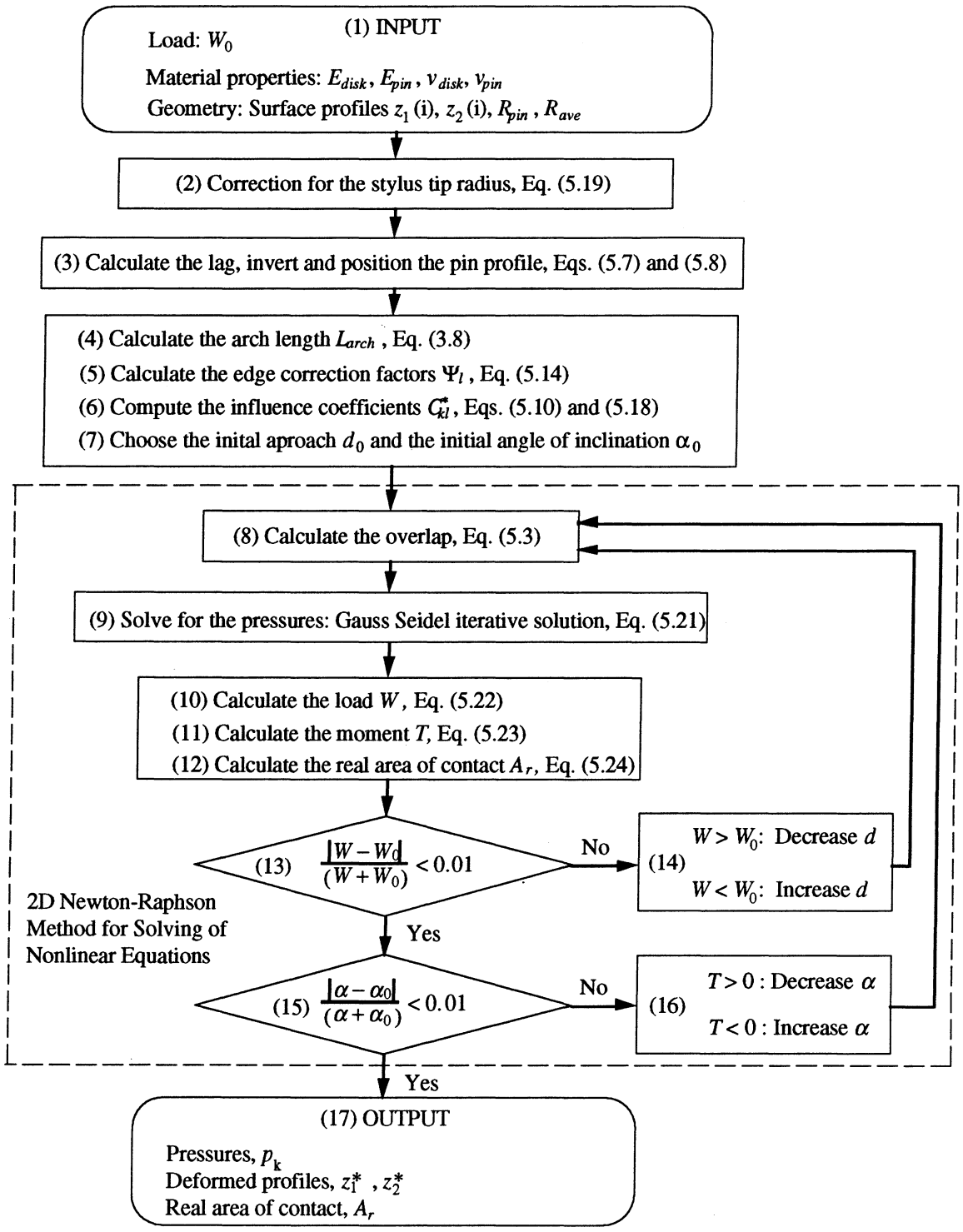

Fig. 5.10 - Flow chart of the overall finite element solution

The load, the moment with respect to he center of the surface profile and the real area of contact in steps (10-12) are calculated as follows:

$$W = s\sum_{k=0}^{M} L_{arch}(k)p_k \tag{5.22}$$

$$T = s^2\sum_{k=0}^{M} L_{arch}(k)p_k(M/2-k) \tag{5.23}$$

$$A_r = s\sum_{k=0}^{N} L_{arch}(k) \tag{5.24}$$

where N is the number of elements with non-zero pressures. The conditional statement (13) in Fig. 5.10 sets the maximum permissible error on the load (0.5%). Steps (15) and (16) perform the angular alignment of the profiles. Steps (8-16) represent a three-level imbedded iterative process. To speed up the solution, these steps are incorporated in a 2D globally convergent Newton-Raphson method [119].

The output of the program are the contact pressures, the deformed profiles and the real area of contact. These results are the input to other programs which calculate the subsurface stresses, temperatures and strains. These are discussed in more detail in the next chapter.

5.8 Verification of the Model

The model was verified by comparing its output to available analytical solutions. A cylinder-on-flat frictionless contact was chosen for the purpose. The results from the numerical solution with M = 200 are shown in Fig. 5.11. A comparison of these results to the analytical solution of Hertz is given in Table 5.2.

Table 5.2 - Comparison between the numerical and analytical solutions for cylinder-on-flat Hertzian contact. M = 200, R_{cyl} = 625 mm, $W/L = 5 \times 10^4$ N/m, $E_{1,2}$ = 70 GPa, $\nu_{1,2}$ = 0.3

Parameter	Analytical Solution	Numerical Solution	% Error
Max. Contact Pressure	44.26 MPa	45.15	1.97
Contact width	1.442 mm	1.435	0.485

The plots in Fig. 5.11 show that the results from the numerical solution are qualitatively correct. The error in the solution, as seen from Table 5.2, is within acceptable limits.

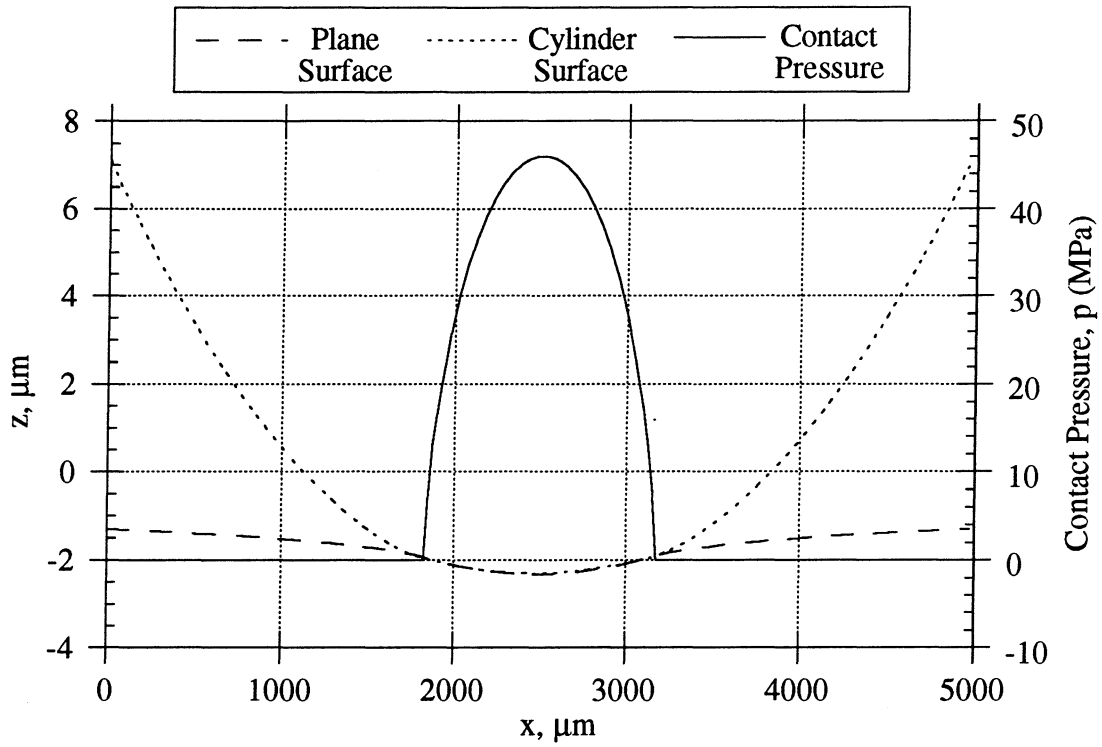

Fig. 5.11 - Verification of the model. Cylinder-on-flat frictionless Hertzian contact.

R_{cyl} = 625 mm, $W/L = 5 \times 10^4$ N/m, $E_1 = E_2 = 70$ GPa, $\nu_1 = \nu_2 = 0.3$

The ability of the model to handle edge effects was also tested. A fictitious circular (D = 5 mm) surface with five identical cylindrical asperities (Fig. 5.12), 5 µm high each, was "pressed" against a flat plane made of the same material (E = 70 GPa, ν = 0.3). The average contact pressure based on the apparent area A_0 was P = 10 MPa. Two solutions, with and without edge corrections, were obtained. These results are given in Figs. 5.13 and 5.14. The pressure distribution for the corrected solution is almost uniform. In addition, the deformed surface of the disk has the largest deformation under the central asperity, which is what should be expected. The solution without correction factors gives contact pressure concentrations close to the edges and fairly uniform deformation of the disk, both of which are wrong.

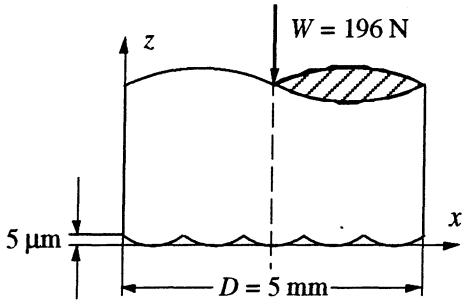

Fig. 5.12 - Schematic of the cylindrical surface used to test the edge corrections of the model

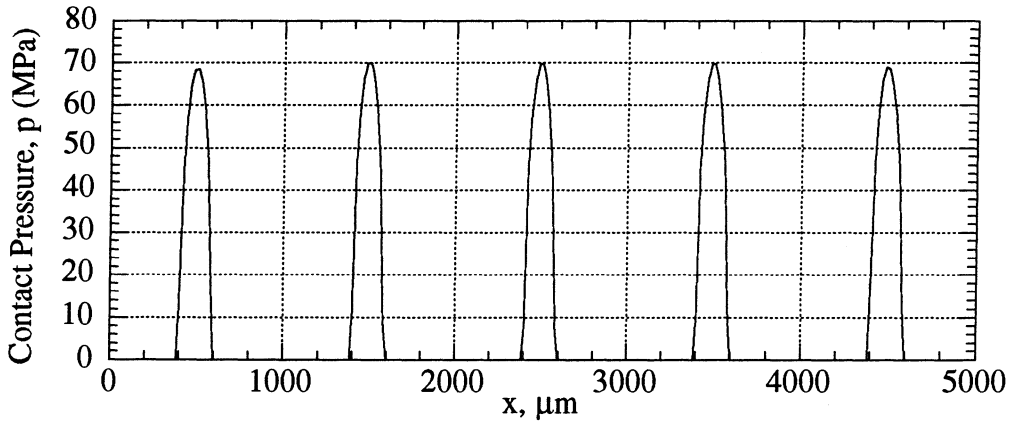

(a)

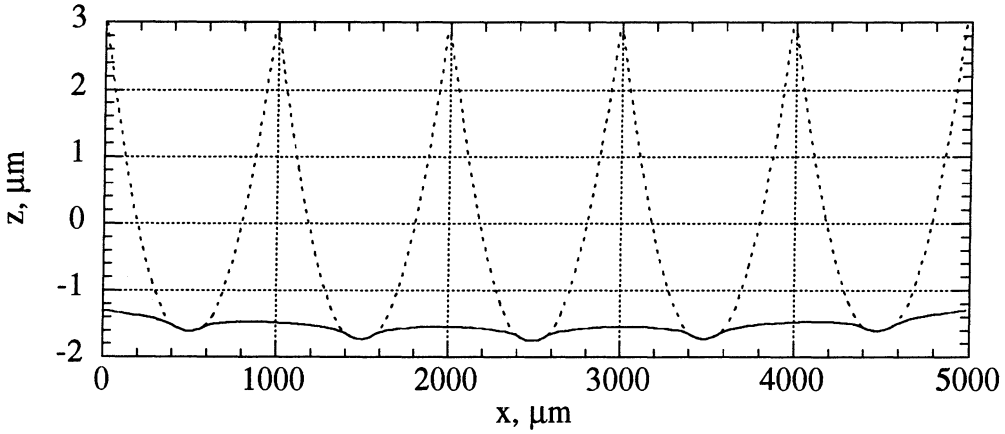

(b)

Fig. 5.13 - Solution for a circular surface with edge corrections

(a) Pressure distribution and (b) Deformed profiles

$E_1 = E_2 = 70$ GPa, $\nu_1 = \nu_2 = 0.3$, $P = 10$ MPa

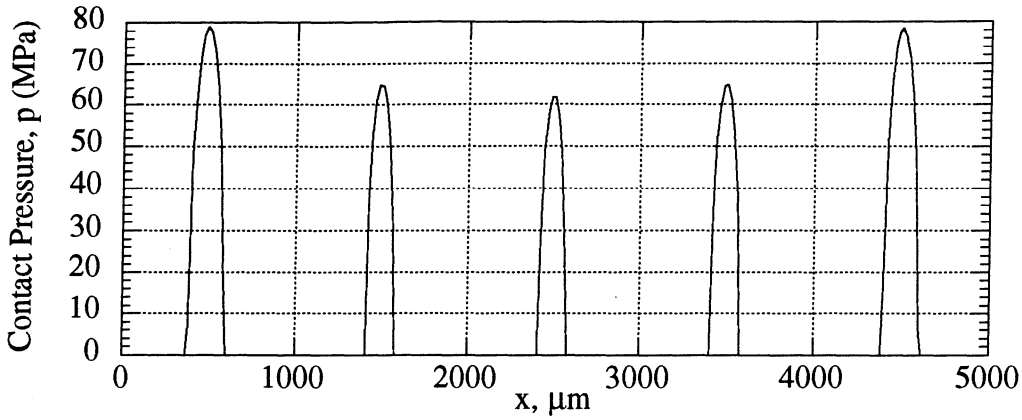

(a)

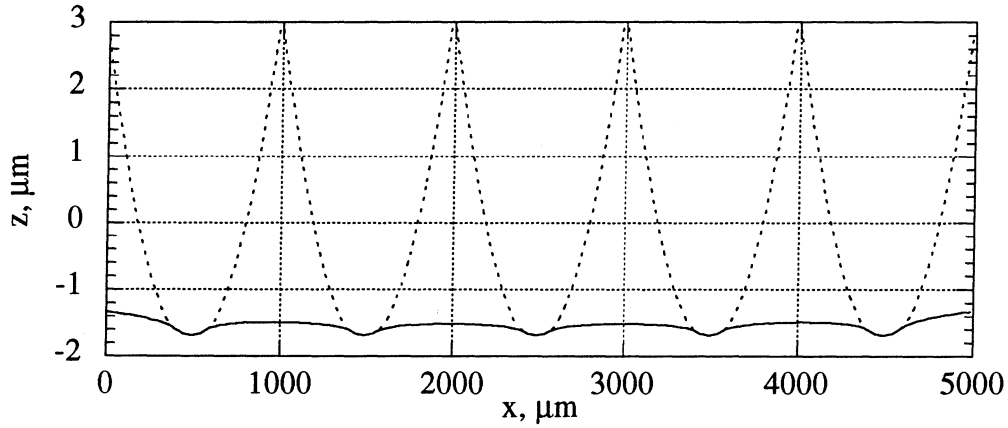

(b)

Fig. 5.14 - Solution for a circular surface without edge corrections
(a) Pressure distribution and (b) Deformed profiles
$E_1 = E_2 = 70$ GPa, $\nu_1 = \nu_2 = 0.3$, $P = 10$ MPa

5.9 Results for the Contact Pressure and Area of Contact Distributions

The surfaces which were studied with the finite element model were obtained from constant load tests. The tests were one hour long. To study the effect of the applied load on the real area of contact, the maximum contact pressure, and the average contact pressure, tests were conducted at 20%, 40%, 60%, 80%, and 95% of the scuffing *PV*, obtained with a single step load application. All tests were conducted at the same sliding velocity of 0.67 m/s. Thus, a separate test was used to obtain the input data for each finite element solution.

A typical solution for the contact pressures is given in Fig. 5.15. It was obtained at 80% of the scuffing load. The pressure distribution is characterized by spikes of very high pressure over small contact areas, which are far apart from each other.

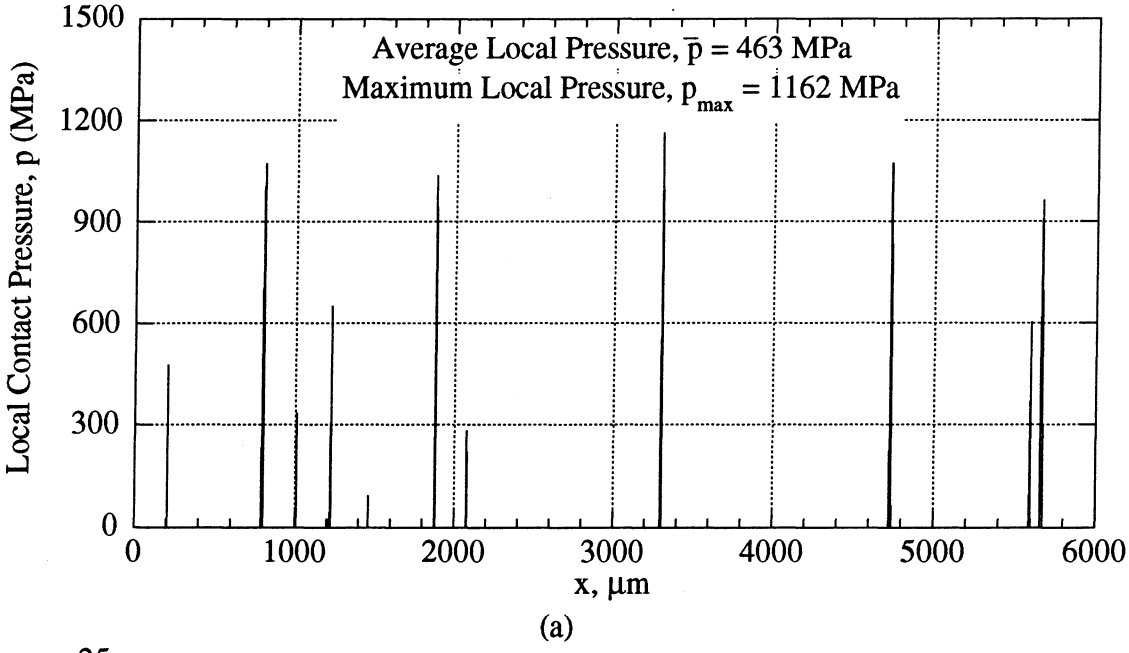

(a)

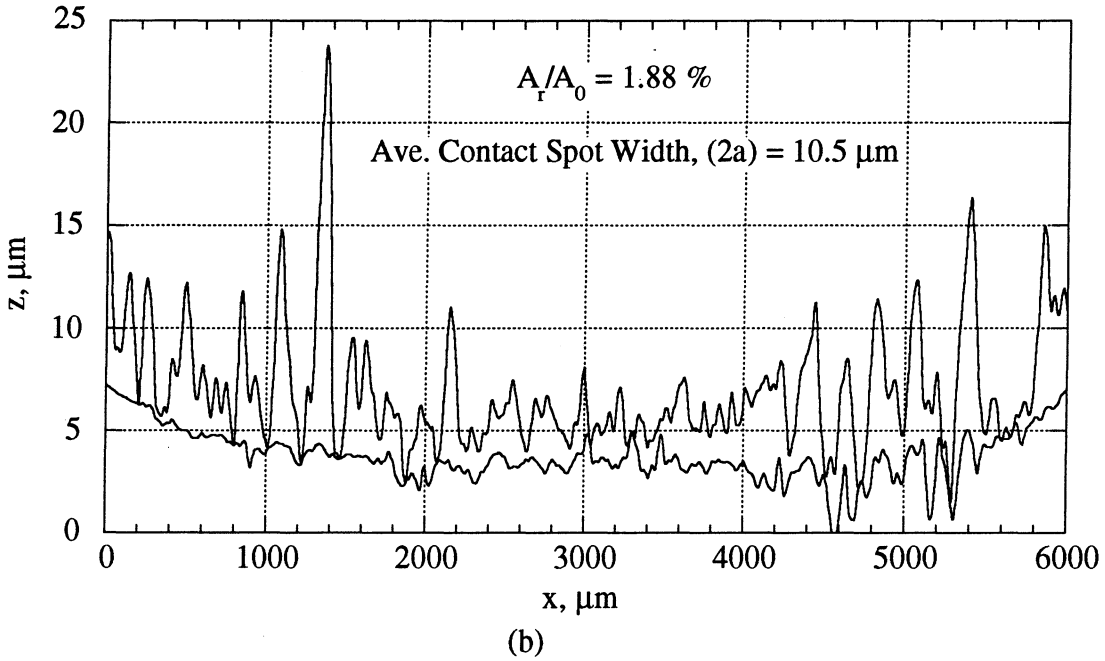

(b)

Fig. 5.15 - Typical results from the finite element solution

(a) Contact pressures and (b) Deformed profiles

PV = 4.72 MPa.m/s (80% of the scuffing PV), P = 7.04 MPa, V = 0.67 m/s, Environment: air

W = 222.0 N on one pin, T_b = 180°C, T_0 = 30°C, Material of the pin: 390-T6 Al

The solution given in Fig. 5.15 is based on a fully elastic response of the material. It can be expected that the modulus of elasticity of the materials in contact changes with temperature. This will couple the thermal and the mechanical effects and make the problem extremely difficult. Fortunately, the modulus of elasticity of both aluminum and steel is not a very strong function of temperature in the temperature range of interest (180-200°C), as shown in Fig. 5.16. Hence, the elastic response of the material is assumed independent of the temperature.

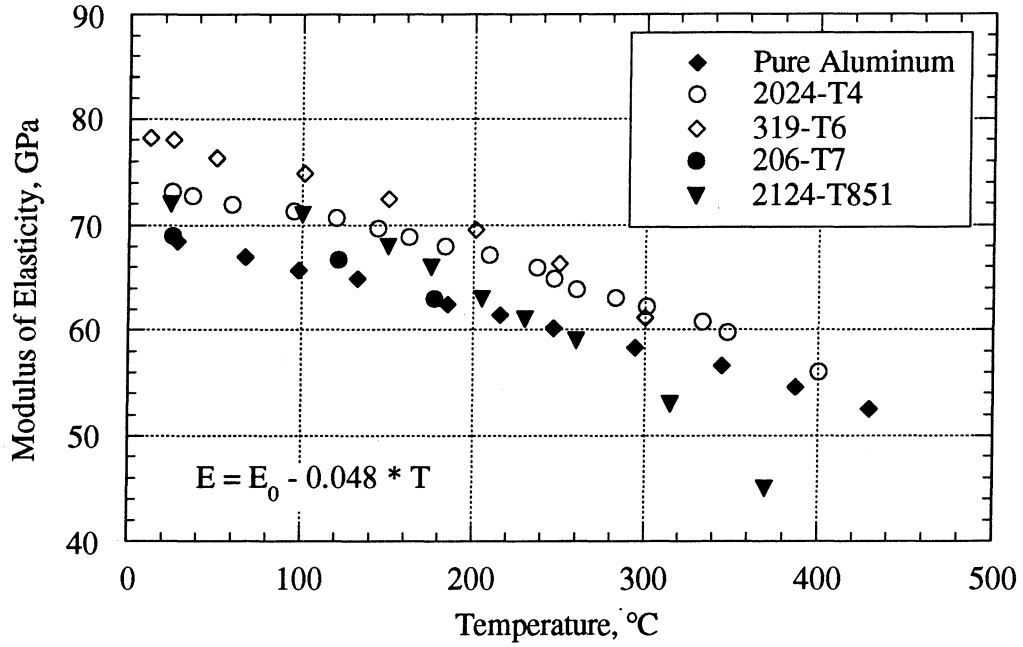

Fig. 5.16 - Change of the modulus of elasticity with temperature for several aluminum alloys
E_0 is the elestic modulus at room temperature

The changes of the real area of contact and the maximum and average contact pressures as a function of load are shown in Fig. 5.17. The change in the average contact spot width ($2a$), with load is shown in Fig. 5.18. Each of the data points in the figures is the average of eight solutions, corresponding to equidistant angular positions on the disk. As expected, the real area of contact increases linearly with the load. Both the average and the maximum pressures seem to be weak functions of the load. The maximum pressure shows a slight increasing trend at lower loads, but quickly levels-off at about 170 N. The initial lower values of the maximum pressure can be attributed to smoother surfaces caused by oxidative wear which dominates at these conditions (Fig. 4.6). The average pressure has an even weaker dependence on the load.

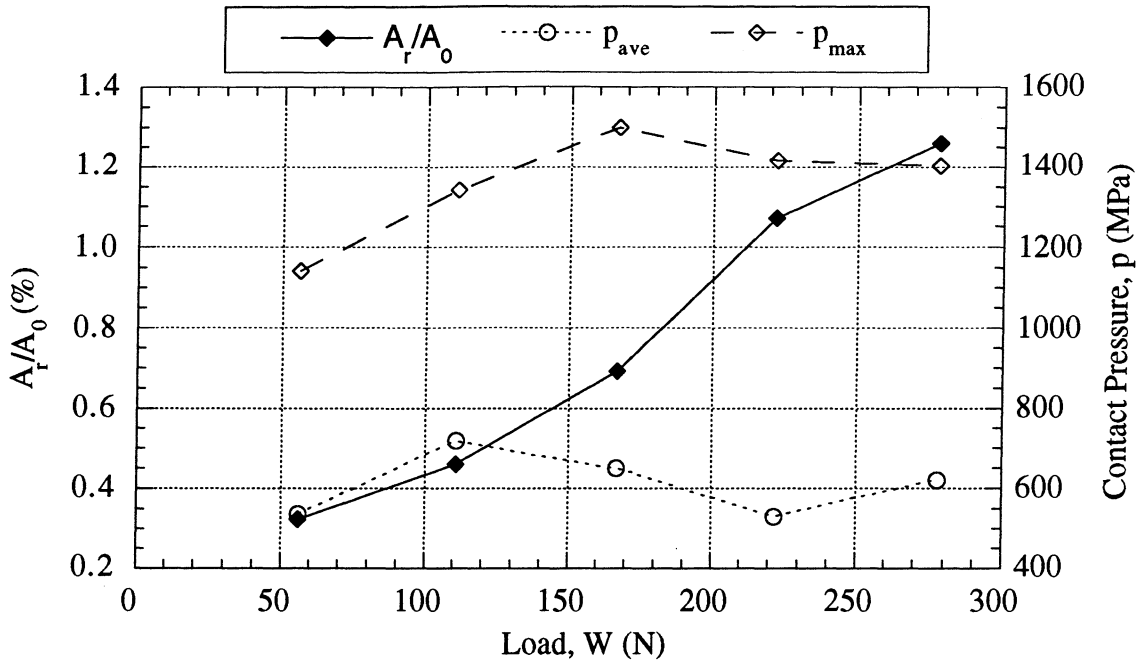

Fig. 5.17 - Changes in the real area of contact, the average and the maximum contact pressures with load. Each data point is the average of eight numerical solutions.
Geometry: R12.7, $V = 0.67$ m/s, $T_0 = 30°C$, Pin material: 390-T6 Al

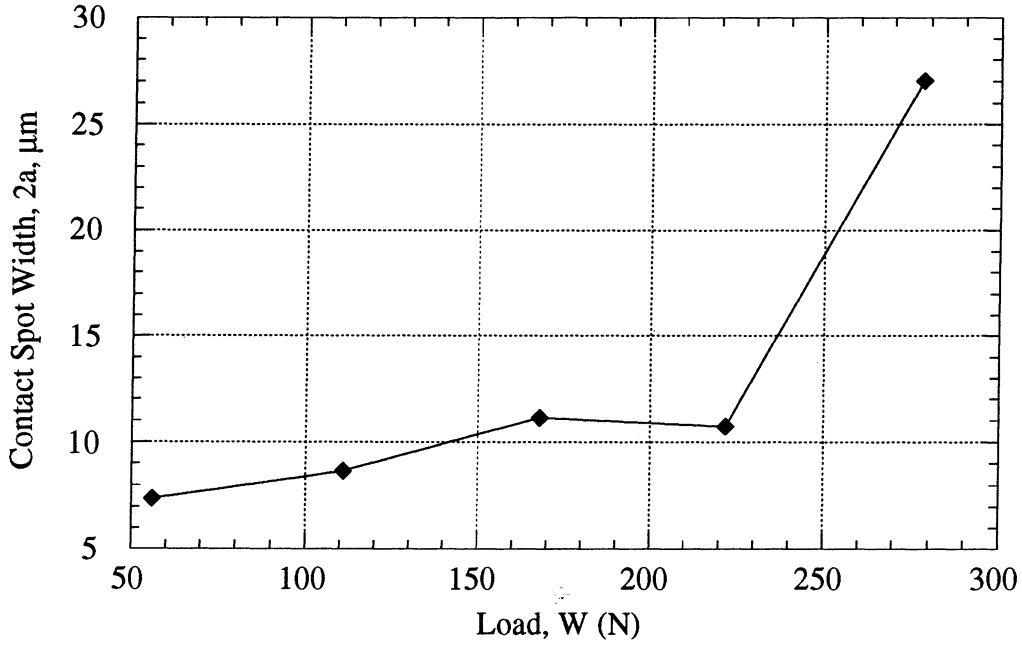

Fig. 5.18 - Average width of the contact spots as a function of load
Geometry: R12.7, $V = 0.67$ m/s, $T_0 = 30°C$, Pin material: 390-T6 Al

The constancy of the maximum pressure cannot be expected to be universally true. It seems that it will depend on the severity of the loading conditions. Lubricated contacts may show an increase of the maximum pressure with load, as reported by He [121].

The concept of a constant average pressure is common in various tribological models. It is based on the assumption that the increase of the real area of contact with load is due mainly to the increasing number of asperities coming in contact. It is also assumed that the average size of the contact spots does not change significantly. As seen from Fig. 5.18, the average size of the contact spots is not a strong function of the load for most of the load range. However, the size of the contact spots becomes much higher at a load of 278 N. This load corresponds to 95% of the scuffing load, which at the test velocity of 0.67 m/s was 295 N. Under these conditions, deep grooves are formed on the surface and the available load-bearing area becomes smaller. This leads to a sharp increase in the size of the contact spots. The last point in Fig. 5.18, corresponds to the surface shown in Fig. 4.18 a.

It can be expected that the highest maximum pressures will only be realized in few locations. The percentage of elements subjected to various ranges of pressures is shown in Fig. 5.19.

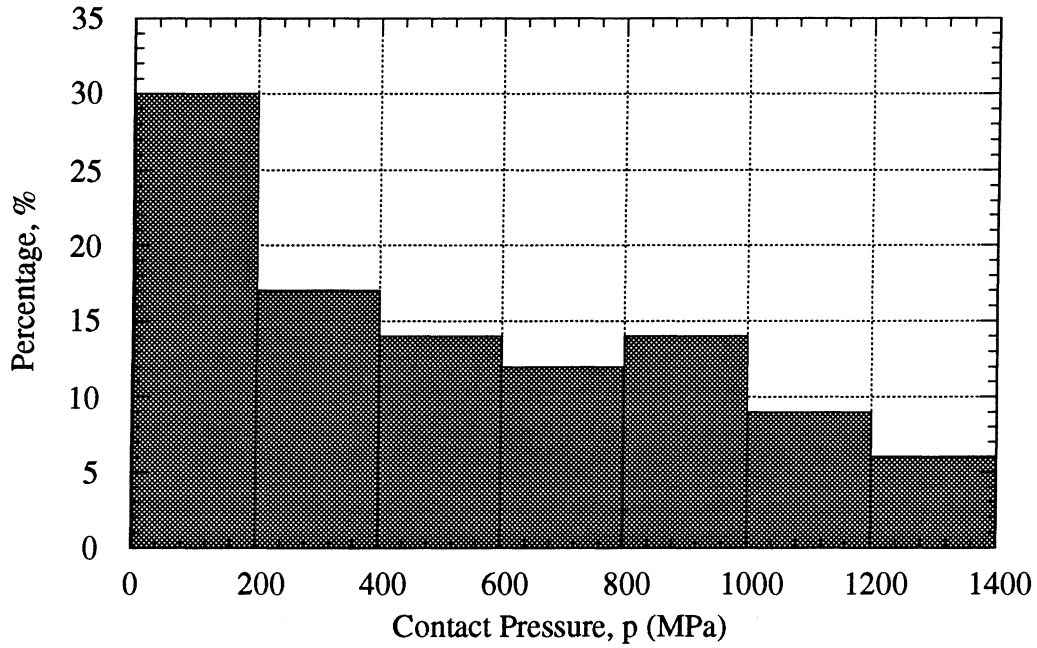

Fig. 5.19 - Percentage of elements subjected to a range of contact pressures
The calculation is based on a fully elastic response of the material
Geometry: R12.7, P = 7.04 MPa, V = 0.67 m/s, T_b = 180°C, Material of the pin: 390-T6 Al

As stated earlier, variations in the distribution of the contact pressures may occur due to disk waviness. This is demonstrated in Fig. 5.20, where the pressure distributions on eight locations on the same disk are shown. These pressure distributions correspond to the disk profiles given in Fig. 5.4.

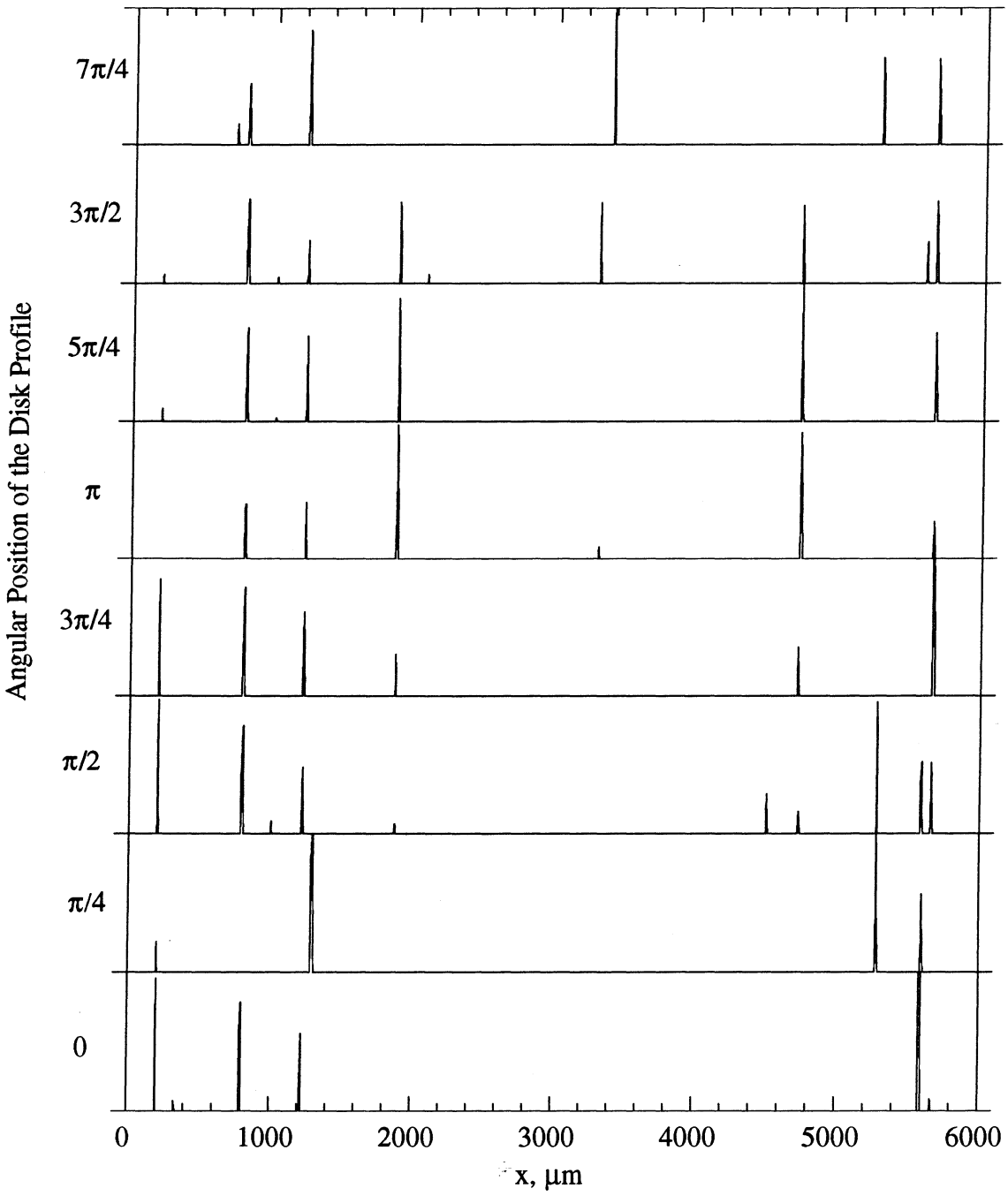

Fig. 5. 20 - Pressure distributions over eight locations on the same disk
Geometry: R12.7, P = 7.04 MPa, V = 0.67 m/s, T_b = 180°C, Material of the pin: 390-T6 Al

From the figure, it is seen that most of the pressure spikes occur at the same radial location on the disk. However, there are some pressure spikes which are characteristic only to one or two particular profiles. Others do not change location but increase or decrease in magnitude. This is an illustration of the local variability of the loading.

5.10 Summary

The problem of finding the local pressures and contact area distributions is solved by developing a model for the contact of runned-in surfaces. The model incorporates a finite element simulation of the contact of rough surfaces, statistical methods for the alignment of surface profiles and analytical correction factors for deviations from the infinite half-space approximation. The results obtained with the method can be summarized as follows:

a. A reliable alignment of surface profiles can be achieved. The alignment in essential for the correct calculation of the pressure and area of contact distributions.

b. Deviations from the half-space approximation can be successfully corrected by analytical expressions based on the principle that uniform pressure on the surface of the pins must produce uniform surface displacement.

c. For the conditions of this study, the pressure distributions are characterized by few high pressure spikes far apart from each other.

d. The real area of contact increases linearly with the applied load.

e. For the conditions of this study, the maximum and the average contact pressures are weak functions of the load.

f. The size of the contact spots increases slowly with the load. However, a sharp increase in the size of the contact spot occurs right before scuffing.

g. Most of the spikes characteristic for the pressure distribution persist for one revolution of the disk. However, some spikes may change magnitude, or have shorter duration. This illustrates the variability of the loading on a local basis and the presence of loading cycles.

5.11 Contributions

Finite elements methods for rough surfaces interactions and methods for statistical alignments of surface profiles are both well known and described in detail in the literature. However, there are no reports for the combined use of these methods. The contribution of this study is their simultaneous use, which opens the possibility to solve the problem for the contact of runned-in surfaces. Several minor improvements to the existing methods are also made. The most important among these is the simpler and better method for correcting edge effects.

CHAPTER 6
SUBSURFACE STRESSES, TEMPERATURES AND STRAINS

The subsurface stresses, temperatures and strains are needed to understand how the material fails on a local basis. Based on the solution for the surface pressure and contact area distributions, it is possible to obtain estimates for these parameters. The subsurface stresses are calculated by assuming a fully elastic response of the material and by applying the analytical solutions for an infinite elastic half-space. In this calculation it is assumed that the temperature does not influence the elastic constants of the material. The temperatures are calculated with the aid of a thermal finite element model. The magnitude of the local heat fluxes required as an input to the thermal model is calculated from the surface pressure distribution, the sliding velocity, the coefficient of friction, and the experimentally obtained heat partitioning at the interface. The time dependence of the heat fluxes is estimated from an analysis of wear debris and wear rates. With the subsurface stresses and temperatures known, the strains are calculated by applying constitutive laws taken from literature sources. The estimates for the local strains are compared to the experimentally observed average strains in the subsurface.

6.1 Subsurface Stresses

The major assumption made in this study for the calculation of the subsurface stresses is that the response of the material is fully elastic. The reasons for this assumption are:

a. The local state of stress is characterized by a large hydrostatic compressive component.

b. The material is subjected to pulses of high stress for very short periods of time. Under these conditions, the yield strength is higher due to strain rate effects.

c. The mechanical strength of the material close to the surface is higher due to strain hardening, oxidation, grain refinement and mechanical alloying.

d. A solution accounting for the plasticity effects is practically impossible to obtain. The major difficulties are related to the local material properties. There are additional uncertainties about the duration of a loading period

Assuming fully elastic response, and applying the principle of superposition, the subsurface stresses can be easily determined if the distribution of the surface tractions is known. The distribution of the surface contact pressures is obtained from the model for the contact of

runned-in surfaces, described in the previous chapter. It is assumed that each contact pressure p_k generates a tangential traction τ_k, which is related to p_k through a constant coefficient of friction μ:

$$\tau_k = \mu p_k \tag{6.1}$$

With all the surface tractions known, the stress components at every location under the surface can be calculated. The calculations are based on the formulas for the stresses generated by uniform normal pressure and shear tractions over an infinitely long strip of width $2a$ [119]. The coordinate system used for the calculation of the stresses is shown in Fig. 6.1. In the figure, the y-axis coincides with the direction of sliding.

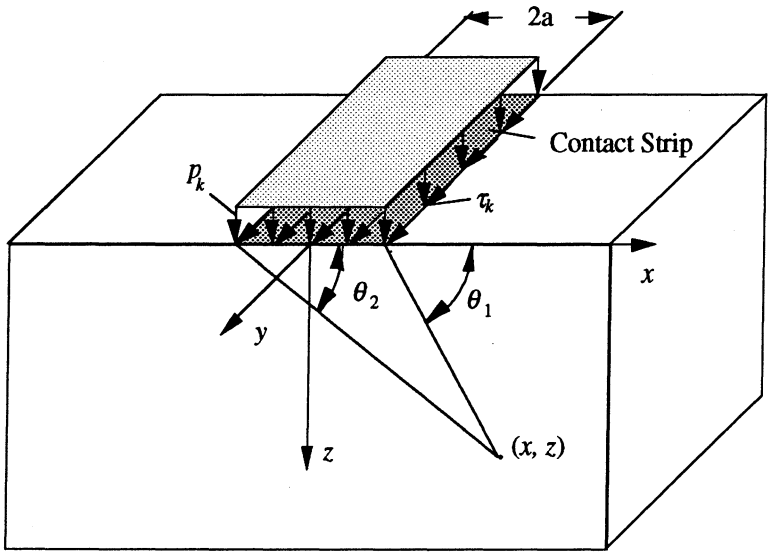

Fig. 6.1 - Coordinate system used for the calculation of the subsurface stresses

For a point located at (x, z) from the center of the strip, the subsurface stresses are:

$$\sigma_{xx} = -\frac{p}{2\pi}[2(\theta_1 - \theta_2) + (\sin 2\theta_1 - \sin 2\theta_2)] \tag{6.2}$$

$$\sigma_{zz} = -\frac{p}{2\pi}[2(\theta_1 - \theta_2) - (\sin 2\theta_1 - \sin 2\theta_2)] \tag{6.3}$$

$$\sigma_{xz} = \frac{p}{2\pi}(\cos 2\theta_1 - \cos 2\theta_2) \tag{6.4}$$

$$\sigma_{xy} = \frac{\mu p}{2\pi} \ln \frac{z^2 + (x^2 - a^2)}{z^2 + (x^2 + a^2)} \tag{6.5}$$

$$\sigma_{yz} = \frac{\mu p}{\pi} \left(\operatorname{atan} \frac{x - a}{z} - \operatorname{atan} \frac{x + a}{z} \right) \tag{6.6}$$

$$\theta_1 = \operatorname{atan} \frac{z}{x - a}, \qquad \theta_2 = \operatorname{atan} \frac{z}{x + a} \tag{6.7}$$

The normal stress in the y direction, σ_{yy} , is calculated based on the plane strain condition $\varepsilon_{yy} = 0$, which gives:

$$\sigma_{yy} = \nu(\sigma_{xx} + \sigma_{zz}) \tag{6.8}$$

It is convenient to perform the calculations for the stresses on a square grid of points using the same discretization step $s = 2a$, as in the finite element model for the surface pressures. Hence, $x = (k - l)s$ and $z = ms$, where k is the point of pressure application, l is the horizontal position of the point of interest, and m is the vertical position of the same point. Then the six components at each point can be expressed by relationships of the form:

$$(\sigma_{ij})_{ml} = \sum_{k=0}^{M} (A_{ij})_{klm} p_k \tag{6.9}$$

where $(A_{ij})_{klm}$ are elements of influence matrices calculated with formulas (6.2-6.8). Applying the von Mises formula

$$\tau_e = \frac{1}{\sqrt{6}} \sqrt{(\sigma_{xx} - \sigma_{yy})^2 + (\sigma_{yy} - \sigma_{zz})^2 + (\sigma_{zz} - \sigma_{xx})^2 + 6(\sigma_{xy}^2 + \sigma_{yz}^2 + \sigma_{zx}^2)} \tag{6.10}$$

the equivalent shear stress can be calculated at every location. The stress state of the subsurface, at the location where the surface pressures are applied, is characterized by a very large hydrostatic component. A typical set of results showing part of the subsurface in the vicinity of a contact spot, consisting of three loading elements, is given in Fig. 6.2. The calculation of the stresses corresponds to the solution for the surface pressures given in Fig. 5.15. The contact spot shown in Fig. 6.2 is located at $x = 4730$ μm in Fig. 5.15.

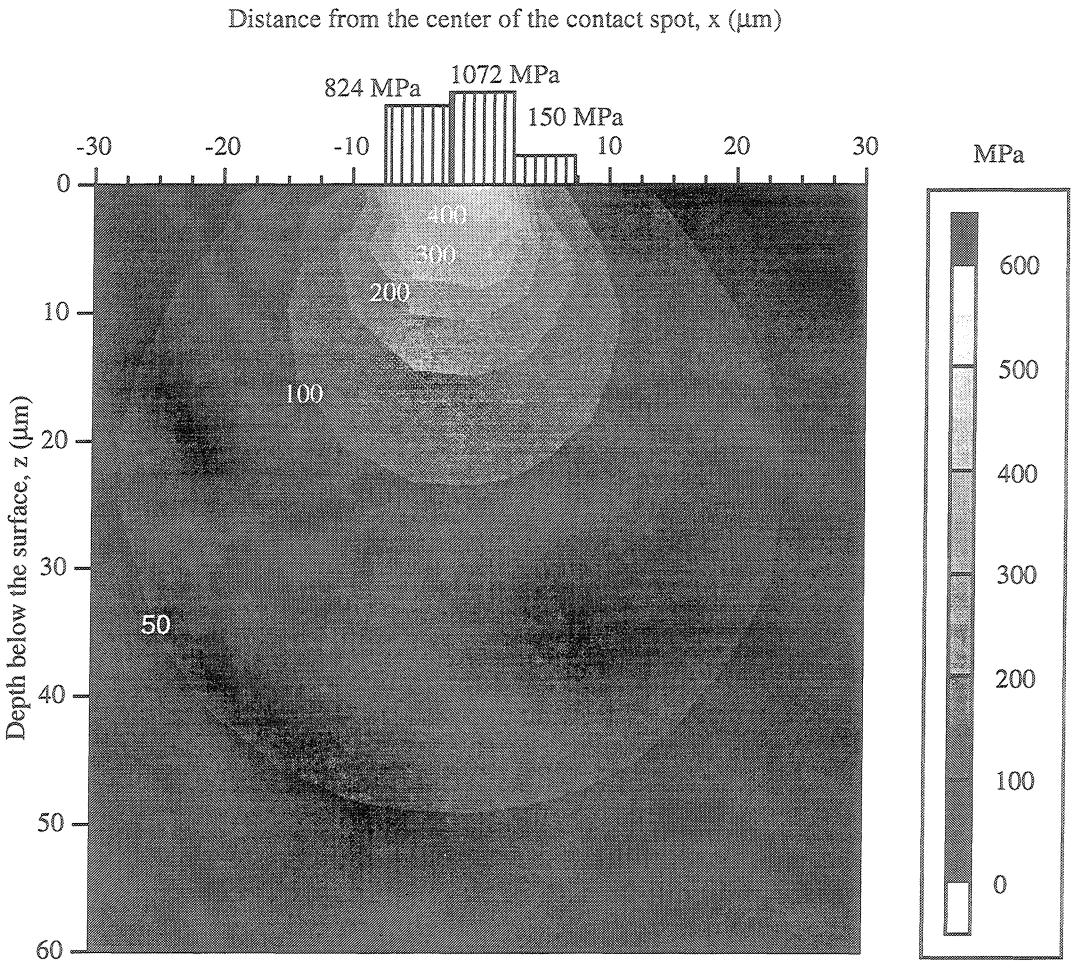

Fig. 6.2 - Distribution of the equivalent shear stresses under a contact spot
The solution corresponds to the contact spot located at $x = 4730$ μm in Fig. 5.15
$W = 222.0$ N, $P = 7.04$ MPa, $V = 0.67$ m/s, $T_0 = 30°C$, $T_b = 180°C$, $\mu = 0.3$, Material: 390-T6 Al

From the figure, it is seen that the constant stress lines can be approximated by circles intersecting the surface near the contact spot. Due to the relatively high friction coefficient, the maximum von Mises stresses occur very close to the surface. The stresses drop quickly even at small distances away from the contact. The shape of the constant stress lines also indicates that the volume of material subjected to a given range of stresses will have a maximum below the surface. This is demonstrated in Fig. 6.3 which gives the number of elements (each element is 5 μm wide) over which the equivalent stress exceeds, 50, 75, 100, 150 and 200 MPa .

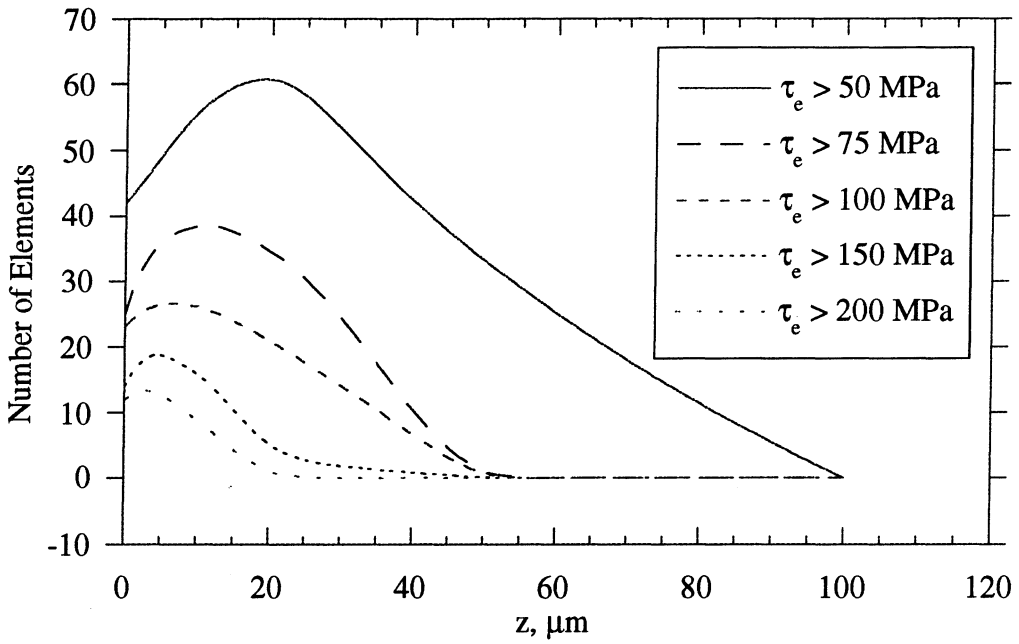

Fig. 6.3 - Number of elements in the subsurface where the equivalent shear stress exceeds a given value. The solution corresponds to the pressure distribution given in Fig. 5.15.

6.2 Subsurface Temperatures

It is generally acknowledged that the temperature distribution close to a sliding surface can be very complex. The temperature gradients may become very steep and can significantly deviate from the gradients in the deep subsurface [122]. There are three reasons for this effect. The first is the higher thermal resistance due to the constriction. The smaller the real area of contact, the higher the constriction resistance becomes. Another reason is the "skin effect", which is due to transients with very short duration. As parts of the surface constantly come in and out of contact, the local heat fluxes are impulses with high intensity and small duration. The third reason is that the thermal properties of the material close to the surface usually is different from the bulk due to chemical reactions, and mechanical modification.

As with the real area of contact, the surface and near subsurface temperatures are very difficult to obtain experimentally. Transparent bodies and Seebeck (thermal voltage) effects have been used for the purpose [73,123]. However, both of these methods have very limited applicability, as stated in Section 2.5. Hence, the estimates for the surface and subsurface temperatures have to rely on thermal models.

The most popular of the models is Block's flash temperature concept [41], which has been further developed by the theoretical work of Jaeger [124]. The model is based on the analytical solution for a point heat source acting on an infinite half-space. Results for circular and square stationary and moving heat sources have been derived. This model works very well for concentrated contacts. The reason is that the concentrated contact can be associated with a macroscopic thermal constriction resistance, which accounts for the major part of the temperature rise. The actual distribution of the real contact spots within the Hertzian contact area does not have a significant influence on the thermal resistance of the whole contact [19]. Thus, it can be assumed that the whole Hertzian contact area contributes to the conduction of heat, which avoids the solution of the problem for the actual distribution of contact spots. There is no similar approximation for the area contacts.

Another option is to solve the coupled thermo-mechanical problem of surface interactions. However, this leads to very complicated formulations. Before resorting to a coupled thermo-mechanical model, it is important to estimate the magnitude of the expected thermal effects. This can be done with simpler methods. If proven that the thermal effects are small, the mechanical and thermal parts of the problem can be decoupled and solved separately.

A simplified finite element model was developed in this study to evaluate the significance of the thermal effects. The input information necessary for the model includes:

a. Magnitude of the real area of contact

b. Average size of a contact spot

c. Average magnitude of the local heat fluxes

d. Average duration of a contact and average time lapse between successive contacts

e. Material properties.

In this study, the information for the real area of contact (A_r) and the width of the contact spot ($2a$) comes from the finite element solution described in the previous chapter. The average magnitude of the heat flux is given by:

$$\bar{q} = (\mu WV)(r_t)\frac{(2a)(2b)}{A_r} \tag{6.11}$$

where $2b$ is the average length of the contact spot and r_t is the experimentally obtained heat partitioning (Tables 3.2 and 3.3).

The average duration of the contact is assumed equal to the time necessary for the generation of a wear particle with average thickness $\bar{h}$. This time is also a function of the

experimentally determined macroscopic wear rate $\dot{h}$. After the generation of a wear particle, this part of the surface becomes unloaded. It will stay unloaded until the rest of the surface becomes sufficiently worn. Based on these assumptions, the average duration of a contact and the average time between contacts are calculated as:

$$\bar{t} = \frac{\bar{h}}{\dot{h}} \frac{A_r}{A_0} \qquad \text{and} \qquad \frac{\bar{t}_0}{\bar{t}} = \frac{A_0}{A_r} - 1 \tag{6.12}$$

The ratio of the apparent to the real contact areas A_0/A_r reflects the fact that the local wear rate must be significantly higher than the macroscopic wear rate. The calculated duration of a contact was compared to results from experimentally observed contact of a steel ball sliding on a sapphire [73]. These results suggest an estimated duration of a contact spot on the order of 25 ms. This is ten times shorter than the typical results given by Eq. (6.12), based on values of $\bar{h}$, $\dot{h}$, and A_0/A_r given in Table 6.1. It is possible that the time necessary for the generation of a wear particle is subdivided into contact periods of shorter duration. These are due to surface waviness and surface plastic deformation. These mechanisms are discussed in more detail in Chapter 8. For these reasons, the time step in the model was chosen equal to 10 μs, which allows much faster transients to be covered. Various parameters used as an input to the thermal model are given in Table 6.1.

Table 6.1 - Parameters used in the thermal model

Parameter	Symbol	Value	Source
Thickness of the transformed layer*	δ	15 μm	Fig. 4.1
Percent real area of contact*	A_r/A_0	1.1 %	Fig. 5.17
Average width of the contact spot*	$2a$	10.7 μm	Fig. 5.18
Average length of the contact spot*	$2b$	4.69 mm	Eq. (3.8)
Average width of the affected zone*	$2l$	1000 μm	$l = a(A_r/A_0)$
Heat partitioning factor*	r_t	0.126	Average of Tables 3.2 and 3.3
Average heat flux per contact spot	$\bar{q}$	0.832 W	Eq.(6.11)
Average wear rate*	$\dot{h}$	0.175 μm/s	Fig. 3.12
Average thickness of a wear particle	$\bar{h}$	≈ 4 μm	Figs. 4.1, 4.9
Average duration of a contact	$\bar{t}$	0.245 s	Eq. (6.12)
Average time between contacts	$\bar{t}_0$	22.6 s	Eq. (6.12)
*These values correspond to W = 222 N, V = 0.67 m/s, A_0 = 31.67 mm^2, μ = 0.3, T_b = 180°C			

The material properties are by far the greatest unknown. The transformed layer present on the surface (Fig. 4.1) may significantly change the thermal gradients in the subsurface. In this study, the subsurface of the pin is represented by a two-layered structure. The thermal properties of the top layer are deduced from its chemical composition (Table 4.1). Since it consists mostly of aluminum oxide, the thermal properties of flame sprayed Al_2O_3 coatings [125,126] were used in the calculations. The second layer has the thermal properties of the bulk material, 390-T6 Al. The material properties used in the thermal model are summarized in Table 6.2.

Table 6.2 - Materials properties used in the thermal model

Parameter	Symbol	Value	Source
Thermal conductivity of 390-T6 Al	k	135 W/m°K	Ref. [27]
Specific heat of 390-T6 Al	c_p	900 J/kg°K	Ref. [27]
Density of 390-T6 Al	ρ	2730 kg/m^3	Ref. [27]
Thermal conductivity of Al_2O_3	k	25.9 W/m°K	@ 180°C Ref. [126]
Specific heat of Al_2O_3	c_p	937.5 J/kg°K	@ 180°C Ref. [126]
Density of Al_2O_3	ρ	3970 kg/m^3	Ref. [126]

Since the contact spots are relatively far from each other (Fig. 5.15), it is reasonable to assume that the thermal state of the subsurface in the vicinity of a contact spot is not a function of the heat flowing through other contact spots. With these simplifications it is possible to use an "onion-skin" model for the thermal state of the subsurface. The representation of the subsurface in the model and its division into finite elements is schematically shown in Fig. 6.4.

In the model, the finite elements are bounded by isothermal surfaces, with temperatures T_s, T_1, ..T_n, ... T_∞, where T_s is the temperature of the rectangular contact patch and $T_\infty = T_b$ is the bulk temperature, just outside the affected zone. These surfaces are semi-elliptical cylinders, expressed mathematically by [19]:

$$\frac{x^2}{a^2+c^2}+\frac{y^2}{b^2}+\frac{z^2}{c^2}=1 \qquad (6.13)$$

where c is the height of the semi-ellipsoid normal to the sliding surface. At heights $c > 3a$, the ellipses become almost circular with radii c.

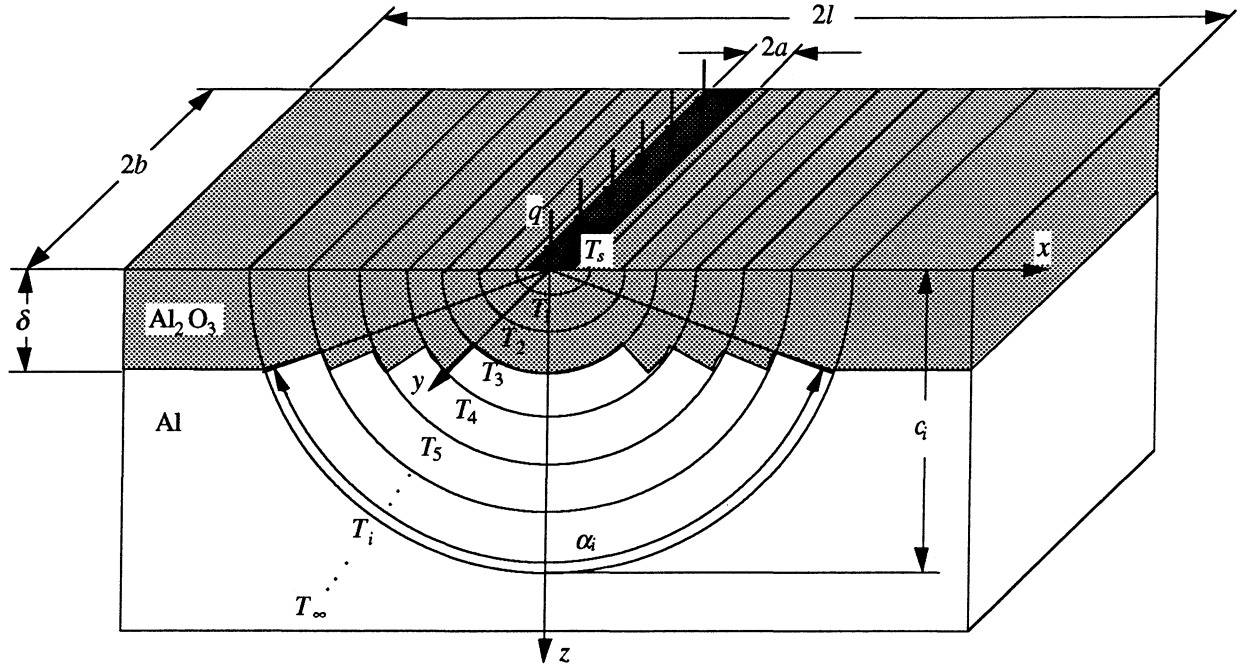

Fig. 6.4 - "Onion skin" model for the thermal state of the subsurface in the vicinity of a single contact spot

Some of the elements fall entirely within the Al_2O_3 surface layer. All of the material in them contributes to the thermal resistance of the subsurface and to the "skin effects". The larger size elements include material from both layers. Since the thermal conductivity of aluminum is much higher than the conductivity of Al_2O_3, it is assumed that all the heat flows though the sector of the element which is aluminum, while the Al_2O_3 of the element is excluded from the calculations. Each element, bounded by the ellipsoids with height c_i and c_{i+1} is characterized by a thermal resistance R_i and thermal capacitance C_t. The thermal resistance is:

$$R_i = \frac{1}{2\alpha_i k \pi b} \ln \left[\frac{\left(c_{i+1} + \sqrt{c_{i+1}^2 + a^2}\right)\left(c_i - \sqrt{c_i^2 + a^2}\right)}{\left(c_{i+1} - \sqrt{c_{i+1}^2 + a^2}\right)\left(c_i + \sqrt{c_i^2 + a^2}\right)} \right] \tag{6.14}$$

if $c < 3a$ and:

$$R_i = \frac{1}{2\pi\alpha_i k b} \ln \frac{c_{i+1}}{c_i} \tag{6.15}$$

if $c > 3a$. The angle α_i is calculated as $\alpha_i = 2\text{acos}(\delta/c_i)$. The thermal capacitance is:

$$C_i = c_p \rho V_i = 2\pi c_p \rho b[c_{i+1}(a + c_{i+1}) - c_i(a + c_i)] \tag{6.16}$$

where V_i is the volume of the material in the element. With these assumptions the subsurface can be modeled by an equivalent thermal circuit, as shown in Fig. 6.5.

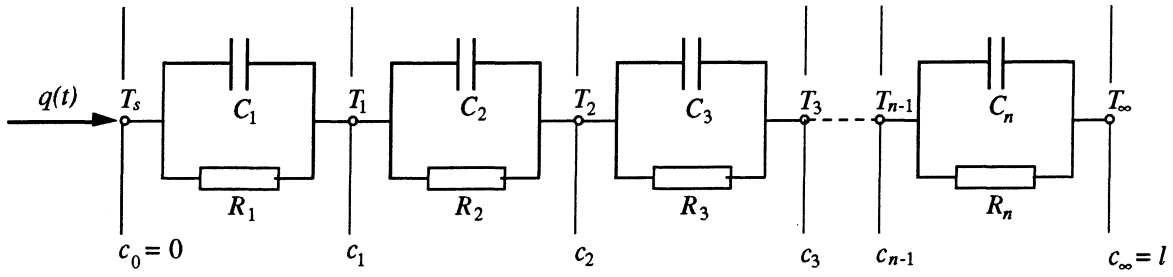

Fig. 6.5 - Equivalent thermal circuit for the "onion skin" model

The magnitude of the heat flowing into the system is the same as $\bar{q}$ from Table 6.1. Its time dependence can be varied to simulate various contact durations. In this way the time constants for the transient effects can be obtained. A typical results from these simulations is shown in Fig. 6.6. In the figure, the duration of the heat impulses is approximately five times less than the estimated duration from Table 6.1. The reason for this is to illustrate better how small the time scale of the flash temperature rise is. Even with such short heat pulses, the temperature at all depths reaches equilibrium at even shorter times. This happens on the order of 0.1 ms. Similarly, the contacts cool down very fast after the heat flux is removed. From the figure, it is also clear that the flash temperature rises for the conditions of this study are relatively small compared to the bulk temperature. Hirst and Lancaster have come to similar conclusions for the dry sliding of brass on steel [127]. The flash temperature barely exceeds 15°C compared to a bulk temperature of 180°C. The flash temperature effects at a depths between 20 and 100μm, where failure typically occurs, are in the range 5-10 °C which cannot influence the material properties significantly.

At a constant PV, the load, and consequently the real area of contact decrease with the sliding velocity. However, the total heat generated at the surface remains constant. Thus, larger local heat fluxes, and higher flash temperatures are expected when the sliding velocity is increased. This is demonstrated in Fig. 6.7, showing the flash temperature rise at 50 μm below the surface for various sliding velocities and a constant PV = 4.7 MPa m/s.

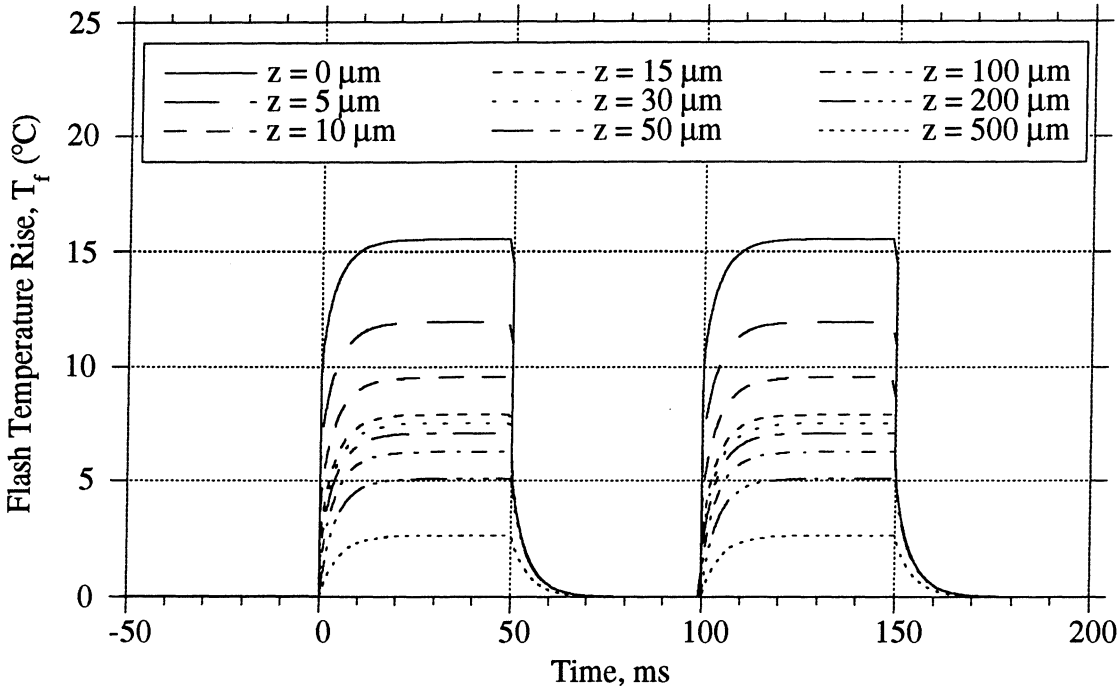

Fig. 6.6 - Flash temperature rises at various locations under the surface
$\bar{q}$ = 0.832 W, $\bar{t}$ = 0.05 s, $\bar{t}_0$ = 0.05 s, V = 0.67 m/s

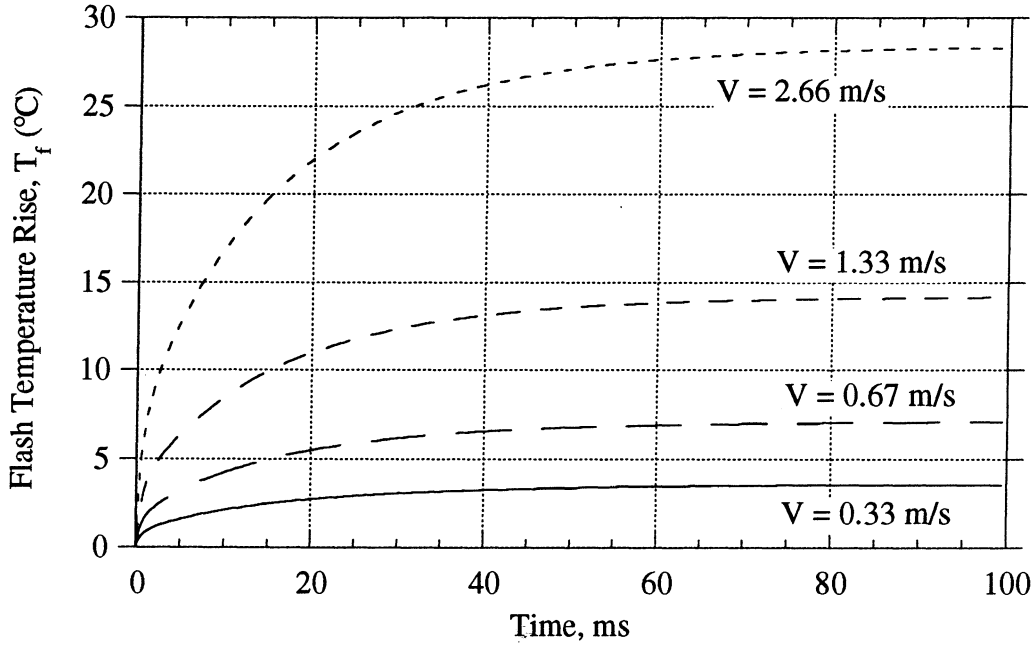

Fig. 6.7 - Effect of the sliding velocity on the flash temperature 50 μm below the surface
Constant PV = 4.7 MPa m/s

Although, the flash temperatures are not very high, the temperature gradients close to the surface are still much higher than the gradients in the bulk (Fig. 6.8). Hence, the results from the model do not contradict the established ideas about temperature distributions close to a sliding surface. However, even these high gradients do not produce significant flash temperatures.

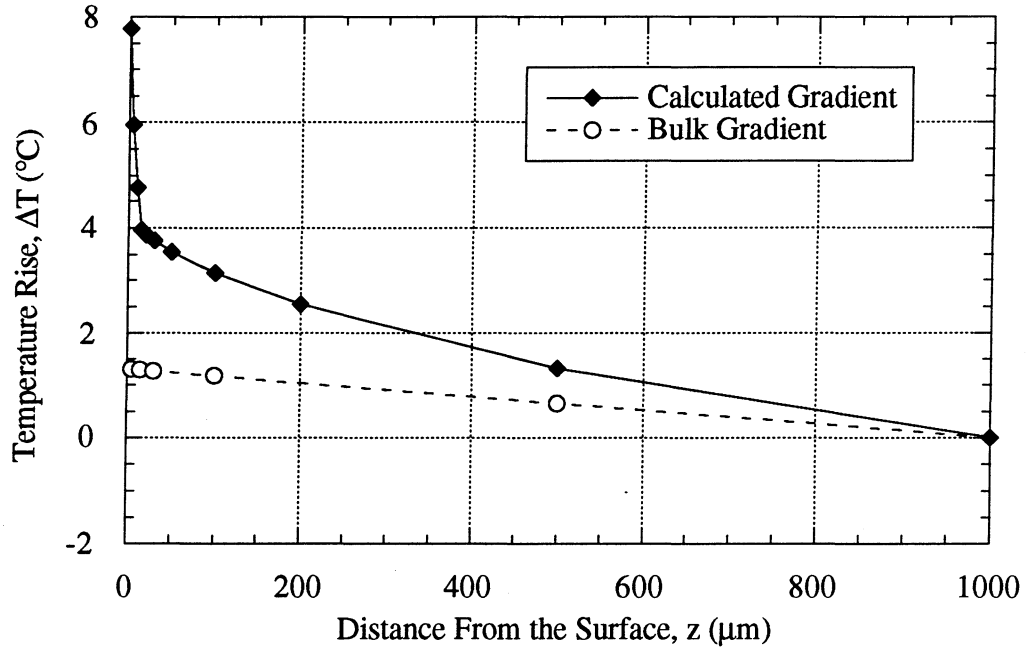

Fig. 6.8 - Comparison of the calculated and the bulk temperature gradients near the surface
The gradients correspond to the input data of Tables 6.1 and 6.2

6.3 Subsurface Strains

If the functional dependencies of strain and strain rate on stress and temperature at every particular location were known, it would be possible to obtain the subsurface strain distributions and to provide a better explanation of the experimental results. Unfortunately, there are many uncertainties associated with this process. The first is that the material properties close to the surface are very different from the bulk. The second is that little experimental data are available for the behavior of materials under the conditions found near a sliding surface.

Differences in the mechanical properties of near surface layer from the bulk are often observed under dry sliding conditions [22,128]. Data for the change of hardness with depth for aluminum-silicon alloys are given by Okabayashi [37], Sarkar et al. [33], Somi Redy et al. [39], and Perrin et al. [92]. These data show that the hardness of the material close to the surface (10

μm or less) can be 2-3 times the hardness of the bulk. Hardness measurements conducted in this study at depths of 30 μm and 5 mm also showed a 2.1 times increase in hardness for the 390-T6 Al pins, as shown in Table 6.3.

Table 6.3 - Hardness data for 390-T6 Al at room temperature
P = 12 MPa, V = 0.67 m/s, T_0 = 30°C, Environment: air

Depth below the surface	Hardness, HV	Hardness, MPa
30 μm	304	1953
5 mm	145	930

The stress and temperature conditions near the surface are very different from the typical conditions used in the mechanical testing of materials. High strain rates, strains, hydrostatic pressures, and temperatures are some of the factors influencing the materials response in a sliding system. The plastic flow is constrained by the surrounding elastic material. In addition, any accumulated residual stresses may be relieved at the elevated tests temperatures. Dynamic recrystallization may also occur [129]. Ideally, it would be desirable to know the functional relationship between stress, strain, strain rate and temperature for each particular geometrical system.

Recently, stress-strain relationships characterizing the equilibrium state of a material undergoing dry sliding have been published. Following the work by Alpas et al. [91] who obtained data for dry sliding of copper against steel, Perrin et al. [92] have constructed equilibrium stress-strain curves for two aluminum alloys. The equilibrium stress-strain curves reflect a steady-state condition of the subsurface material. They relate measured average subsurface strains to measured subsurface hardness. Both of these measurements are conducted on sections of test specimens at room temperature. The validity of the room temperature hardness measurements for the generation of these curves is questionable because the measured plastic deformation occurred at high bulk temperature when the hardness of the material was lower. However, this inaccuracy can be corrected if data about the changes of the hardness with temperature are available.

As suggested in [92], an empirical relationship which adequately describes the strain hardening behavior of aluminum is:

$$\sigma_f = \sigma_s - (\sigma_s - \sigma_0)\exp(-\chi\varepsilon^m) \tag{6.17}$$

where m and χ are constants obtained from curve fitting, σ_f is the flow stress of the material at a

given ε, σ_s is the saturation flow stress (ultimate strength) and σ_0 is the initial yield stress at the given temperature conditions. Perrin et al. [92] report that the constants m and χ are similar for various aluminum alloys. For the aluminum-silicon alloy tested in their study these constants are:

$$m = 0.65 \qquad \text{and} \qquad \chi = 0.32 \tag{6.18}$$

The same constants were used in this study to construct the stress-strain curves for 390-T6 aluminum. These curves are shown in Fig. 6.9. The values for σ_0 and σ_s at room temperature are approximated by one third of the hardnesses given in Table 6.3:

$$\sigma_0 = (1/3)H_{5mm} = 310 \text{ MPa} \quad \text{and} \quad \sigma_s = (1/3)H_{30\mu m} = 651 \text{ MPa} \tag{6.19}$$

The curves at the elevated temperatures are based on yield strength data for 390 Al from reference [27]. For these curves it is also assumed that the ratio σ_s/σ_0 does not change with temperature.

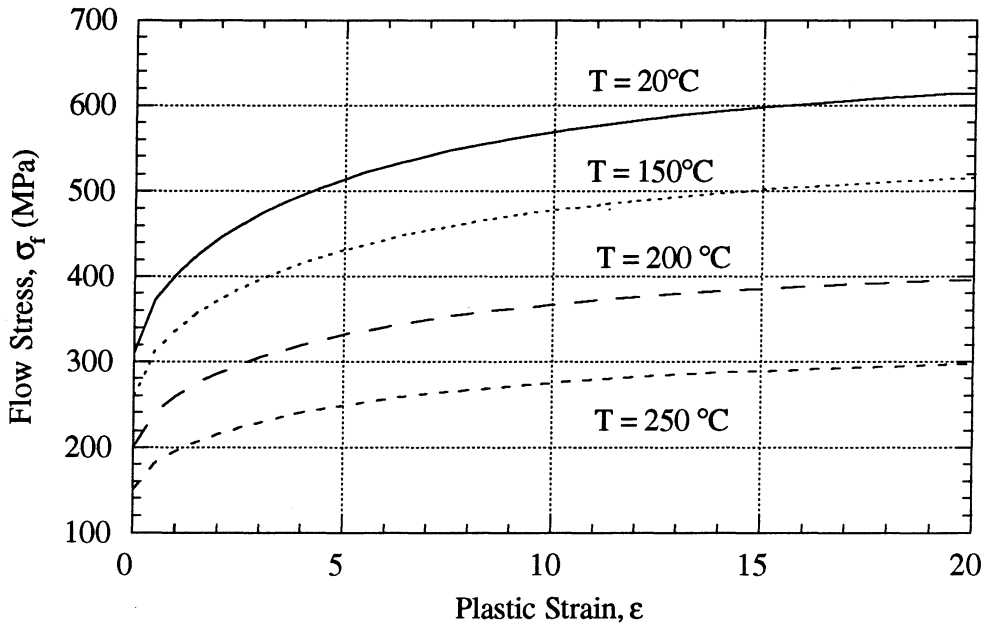

Fig. 6.9 - Stress-strain curves for 390-T6 Al at various temperatures

Unfortunately, the equilibrium curves do not provide any information about the local material response in the short duration of a contact. They cannot be used to calculate the amount of plastic deformation accumulated per loading cycle. Strain rate and frequency effects are also excluded. Hence, these curves cannot be used to explain the different response of the materials to changes in contact stress and sliding velocity.

The loading on a local basis is characterized by stress pulses of short duration and high intensity. It resembles impact loading and, therefore, the strain rate effects must be taken into account. The strain rate sensitivity of various material is often described by an empirical power law relationship [130]:

$$\frac{\sigma_f}{\sigma_0} = \left(\frac{\dot{\varepsilon}}{\dot{\varepsilon}_0}\right)^n \tag{6.20}$$

where ε_0 is the strain rate at which σ_0 was obtained. The constant n characterizes the strain rate sensitivity of the material. It is a function of the test temperature and the strain and typically increases with both. Values for this constant describing the behavior of various aluminum alloys are given in Table 6.4.

Table 6.4 - Strain rate sensitivity factors for various aluminum alloys

Material	Temperature ℃	Strain	Strain Rates, s^{-1}	Sensitivity Factor, n	Source
1100 Al	250	0.1	10^{-5} - 260	0.034	Ref. [131]
		0.2		0.041	
		0.3		0.048	
		0.4		0.055	
Al-Mg-Si Alloy	300	0.1	0.001 - 1.0	0.070	Ref. [132]
		0.2		0.078	
		0.3		0.084	
		0.4		0.086	
356 Al	232	0.07	5×10^{-5} - 1.0	0.043	Ref. [133]
3003-O Al	260	0.002	5×10^{-4} - 0.5	0.090	Ref. [134]
	425	0.002	5×10^{-3} - 0.5	0.103	
1100-O Al	200	0.2	0.095 - 212	0.054	Ref. [135]
		0.4		0.075	
		0.6		0.089	
1100 Al	250	-	-	0.064	Table 2.4
390-T6 Al	250	-	-	0.070	Table 2.4
	350	-	-	0.101	Table 2.4

The major problem with the relationship given in Eq. (6.20) is that the relative independence of the constant n on the strain rate is no longer true at high strain rates. This is demonstrated in Fig. 6.10, which shows data for the strain rate sensitivity of 1100 Al.

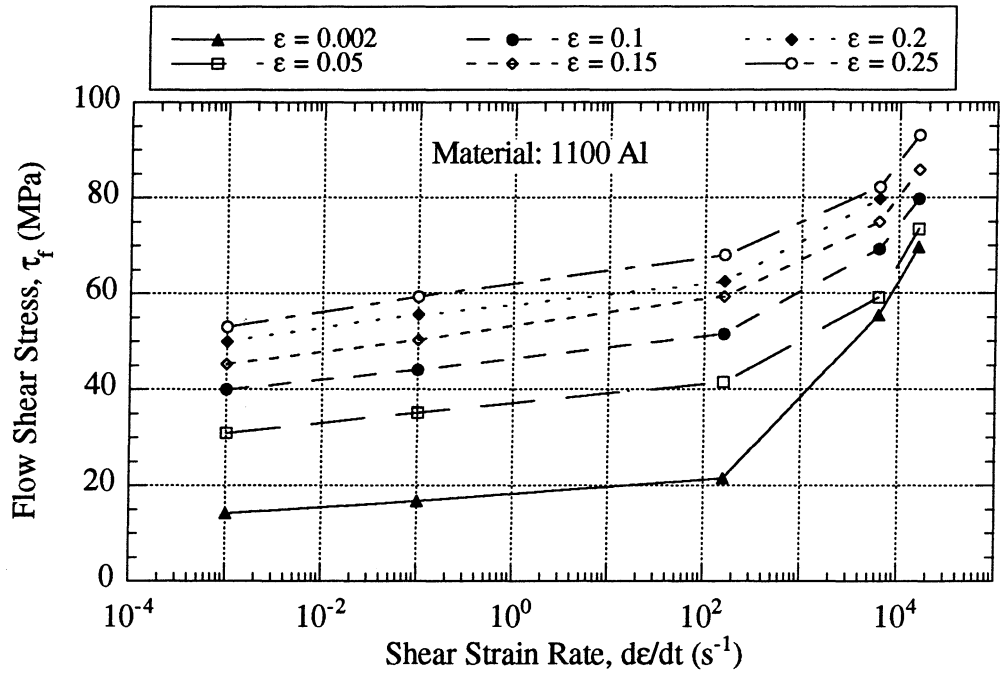

Fig. 6.10 - Strain rate sensitivity of 1100 Al at various strains (from Reference [136])

Results similar to those shown in Fig. 6.10 were obtained from dynamic testing of 1100 Al at hydrostatic pressures of 2.8 GPa [137]. In these tests, aluminum plates were shot with projectiles having various impact velocities. From the figure, it is clear that the power law relationship, Eq. (6.20), is obeyed until strain rates of about 100 s^{-1}. Most of the data from Table 6.4 also fall within this range. However, the local strain rates under dry sliding can exceed this value. At higher strains, another empirical relationship provides a better fit of the data.

$$\frac{\sigma_f}{\sigma_0} = \exp\left(\frac{\dot{\varepsilon}}{\dot{\varepsilon}_1}\right) \tag{6.21}$$

where $\dot{\varepsilon}_1$ is a parameter obtained from the curve fit.

In this study, relationships (6.20) and (6.21) were built into a numerical procedure for the calculation of subsurface strain growth with time. The procedure is essentially a finite difference

method. Based on the calculated (elastic) equivalent stress, and setting $\sigma_f = \sigma_e$, the equivalent strain rate can be calculated from formulas (6.20) and (6.21):

$$\dot{\varepsilon}_e = \dot{\varepsilon}_0(\sigma_e/\sigma_0)^{1/n} \quad \text{for} \quad \dot{\varepsilon}_e \le 100 \qquad (6.22)$$
$$\dot{\varepsilon}_e = \dot{\varepsilon}_1 \ln(\sigma_e/\sigma_0) \quad \text{for} \quad \dot{\varepsilon}_e > 100$$

As evident from Table 6.4, the value of n changes with strain. This dependence must also be incorporated in the numerical solution, because even small changes in n produce large differences in plastic strain rate. Unfortunately, the data presented in Table 6.4, especially for 390-T6 Al, are insufficient to obtain this relationship. In this study, n was assumed constant and the strain dependence was accounted for by changing the value of σ_0. In the simulation, σ_0 in Eq. (6.22) was substituted by σ_f from Eq. (6.17) This leads to an expression for the strain rate which incorporates both the dependencies on strain and equivalent stress:

$$\dot{\varepsilon}_e = \dot{\varepsilon}_0\left[\frac{\sigma_e}{\sigma_s - (\sigma_s - \sigma_0)\exp(-\chi\varepsilon^m)}\right]^{1/n} \qquad (6.23)$$

or

$$\dot{\varepsilon}_e = \dot{\varepsilon}_1 \ln\left[\frac{\sigma_e}{\sigma_s - (\sigma_s - \sigma_0)\exp(-\chi\varepsilon^m)}\right] \qquad (6.24)$$

The values of the strain rate sensitivity factor n and the constants $\dot{\varepsilon}_0$ and $\dot{\varepsilon}_1$ used in the calculation are given in Table 6.5.

Table 6.5 - Parameters used in the numerical calculations for the subsurface strains

Parameter	Symbol	Value	Source
Strain Rate Sensitivity	n	0.07	Table 6.4
Quasi-static test strain rate	$\dot{\varepsilon}_0$	1.0×10^{-5}	Ref.[131]
Curve fitting constant	$\dot{\varepsilon}_1$	3.6×10^{5}	Fig. 6.10

The shear strain rates in the direction of sliding are calculated from the equivalent strain rate as [130]:

$$\dot{\varepsilon}_{xy} = (3/2)(\dot{\varepsilon}_e/\sigma_e)\sum \sigma_{xy} \qquad (6.25)$$
$$\dot{\varepsilon}_{yz} = (3/2)(\dot{\varepsilon}_e/\sigma_e)\sum \sigma_{yz}$$

where the summation over the shear stresses reflects the influence of more than one contact spot on the surface. With the calculated shear strain rates and with a given time step, it is possible to compute the development of strains and displacements with time. These calculations are conducted with the aid of the finite difference equations:

$$\Delta\varepsilon_{xy} = (\dot{\varepsilon}_{xy})(\Delta t) \qquad (6.26)$$

$$\Delta\varepsilon_{yz} = (\dot{\varepsilon}_{yz})(\Delta t) \qquad (6.27)$$

$$u_{kl} = (1/2)\left[(u_{k-1l} + \varepsilon_{xy}\Delta x) + (u_{kl-1} + \varepsilon_{yz}\Delta z)\right] \qquad (6.28)$$

where u_{kl} is the displacement in the y direction (direction of sliding) of the node with coordinates $(k\Delta x, l\Delta z)$. The quantities Δx and Δz give the spacing of the nodes in the x and z (depth) directions. From Eq. (6.28) it can be seen that the displacement of each point in the subsurface is calculated as an increment over the displacements of its neighboring points. The calculation starts at the outer boundary of the plastically deformed zone which is mathematically described by the inequality $\sigma_e \geq \sigma_0$. Clearly, the displacement u is zero at this boundary at all times. The calculation then proceeds toward the surface over a rectangular grid of points. In this way the strains and the displacements in a single time step can be obtained. Corrections in the value of the strain rate sensitivity factor based on the accumulated strain are conducted before the next time step. The discretization used in the model is Δx = 1 μm, Δz = 1 μm, and Δt = 10 μs. A typical result from such a calculation, showing the accumulation of horizontal displacements with time at several depths, is given in Fig. 6.11. These displacements are for a vertical line directly below the contact spot shown in Fig. 6.2. These displacements are representative of the maximum plastic deformation encountered in the subsurface in a single contact period.

From the figure, it is seen that the deformation is accumulated very fast initially and then levels off as the sliding proceeds. Therefore, almost the same amount of strain will be accumulated for contact periods of various durations, provided that the time of contact is large compared to the initial time of fast strain accumulation. The time scale in Fig. 6.11 and the estimates for the

duration of a contact period, discussed earlier, indicate that this will probably be satisfied for most of the sliding conditions. The conclusion is that the amount of accumulated strain is probably a weak function of the duration of the contact period, but is a strong function of the contact stress and subsurface temperature.

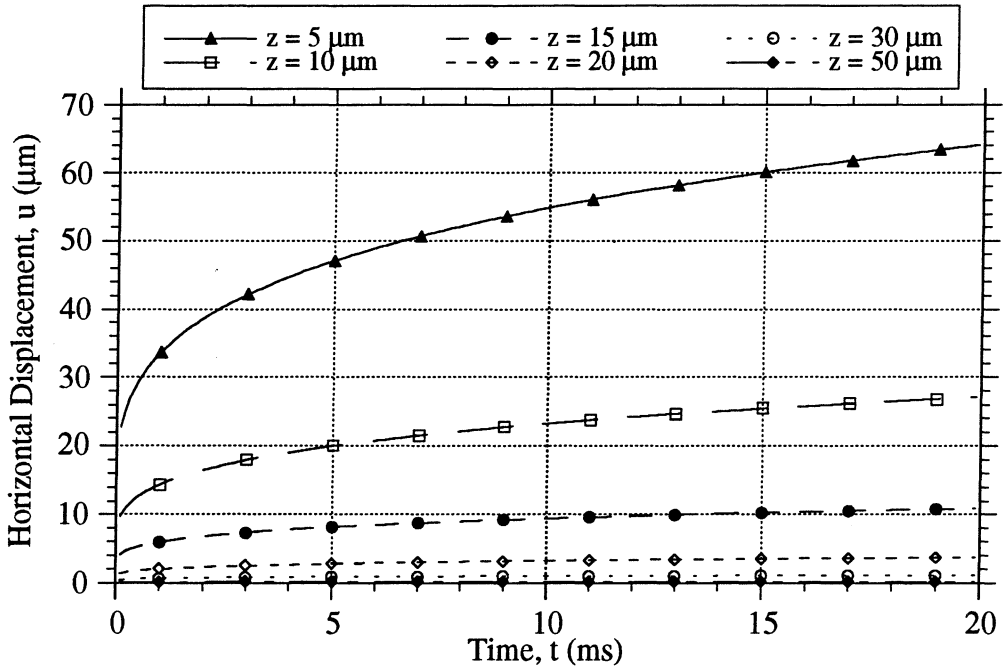

Fig. 6.11 - Accumulation of plastic deformation with time

The calculations are for points directly below the contact spot shown in Fig. 6.2

T_b = 180°C, Material: 390-T6 Al

Averaging the displacements over the whole subsurface, gives results which are more suitable for comparisons with the experimentally obtained data. The average subsurface displacements in the direction of sliding are shown in Fig. 6.12. The subsurface equivalent stresses used to obtain the deformation shown in Fig. 6.12 correspond to the contact pressures given in Fig. 5.15 and a coefficient of friction $\mu = 0.3$. Note that the average displacements are much smaller than the displacements directly under a contact spot (Fig. 6.11). This is due to the fact that most of the subsurface is only elastically deformed.

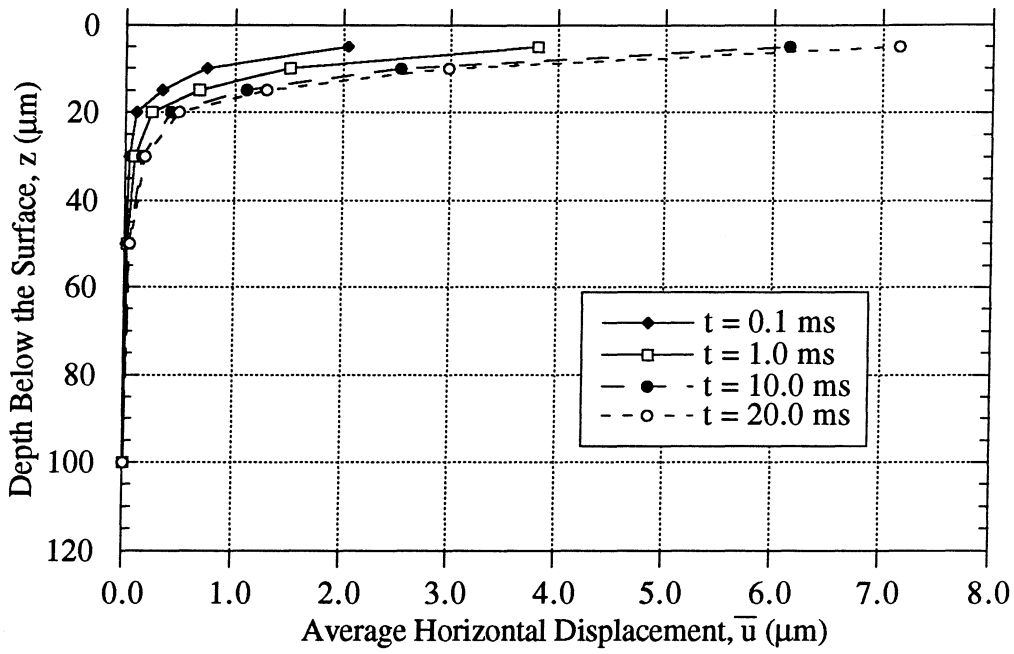

Fig. 6.12 - Accumulation of average plastic deformation with time
The subsurface equivalent stresses used to obtain the strains correspond to the surface pressures in Fig. 5.15 and $\mu = 0.3$

The displacements shown in Fig 6.12 are "snapshots" of the average displacement at several times after the initiation of sliding. The choice of times in the plot provides a logarithmic time scale. From the figure, it can be seen that the displacements roughly doubled for each ten-fold increase in time. Thus, a logarithmic relationship between the strain accumulated in a single contact period and the duration of this period is proposed:

$$(\bar{\varepsilon}/\varepsilon_0) = \log(\bar{t}/t_0) \tag{6.29}$$

where ε_0 and t_0 are normalizing parameters. This result emphasizes the high non-linearity of the strain accumulation process and provides a qualitative explanation of the relative independence of the experimentally observed average strains on the sliding velocity for a constant *PV*.

Comparing Figs. 6.12 and 4.14 it can be seen that the experimental and the theoretical results are at least qualitatively similar. The difference in the time scales for these two plots is large. In addition, Fig. 6.12 represents the deformation from a single contact period, while the results in Fig. 4.14 represent accumulation of bulk plastic strain from multiple contacts. The

generalization from a single to multiple contacts is difficult. The major uncertainty is the changes which occur in the material between contacts. The effect of strain hardening may disappear by the next contact period due to high temperature and dynamic recrystallization. Clearly, more studies on the response of the materials under sliding conditions are necessary to proceed any further with the modeling of the processes in the subsurface.

Figures 6.11 and 6.12 raise another question. If the material can undergo large deformations in the direction of sliding, it must also deform significantly in the other directions, because the shear stresses in the direction of sliding are only a fraction of the equivalent stress. The material directly under the contact may flow downwards and sideways, eventually forming bulges on the sides of the contact strip. This vertical displacement may relieve some of the pressure over the contact. This mechanism may also shorten the duration of a single contact. The shorter duration of a singe contact suggests that multiple contacts are necessary for the formation of a wear particle. Actually, this is to be expected if surface fatigue is the dominant wear mechanism.

6.4 Summary

The subsurface stresses, temperatures and strains are estimated by applying several numerical methods. The stresses are calculated on the basis of the infinite half-space approximation and information about the surface pressures and areas of contact. The latter is provided by the finite element method for the contact of runned-in surfaces. The transient subsurface temperatures are calculated with the aid of a simple finite element model. The strains are obtained from a finite difference method and by incorporating empirical relationships from literature sources. The results of these numerical solutions are summarized below:

a. For the conditions of this study, the mechanical and the thermal parts of the solution for the subsurface stresses and temperatures can be decoupled. This is due to the local effect of flash temperatures.

b. For the conditions of this study, the flash temperatures are small compared to the bulk temperature. This is due to the relatively small heat fluxes and the small constriction thermal resistances, typical for the contact geometry used.

c. The thermal gradients near the surface are higher than the gradients in the bulk. These, however, fail to produce significant temperature differences. The effect of increased flash temperature due to higher sliding velocity at the same PV is also small compared to the bulk temperature.

d. For aluminum, most of the strain accumulated in a contact period occurs early in the period. The total accumulated strain is a weak function of the period's duration. If annealing and dynamic recrystallization occur between contacts, the accumulated strain will be a stronger function of the number of contact periods.

e. The results for the strain accumulated in a single contact period cannot be generalized to account for multiple contacts due to the lack of information for the changes occurring in the material between contacts.

6.5 Contributions

With the exception of Section 6.3, most of the results presented in this chapter are based on well established methods and procedures. However, in the literature, there is very little information about the local response of the material to high stresses, temperatures, and strain rates. This process is very complex and is not well understood. On the other hand, it seems to be central to explaining the behavior of materials at scuffing. Clearly, this problem requires further investigation. The contribution of the present study to the better understanding of this phenomenon is summarized below:

a. The importance of the strain-rate dependence is revealed.

When addressing the behavior of materials under sliding conditions, most studies deal with equilibrium stress-strain curves [91,92]. These do not reveal the actual behavior of the material, which is also subjected to very high strain rates. The equilibrium stress-strain curves fail to explain the accumulation of plastic deformation on a local basis, especially close to the surface. On the other hand, the predictions of the simple model based on strain sensitivity, developed in this study, are at least qualitatively correct. Hence, the strain rate effects must be taken into account.

b. The relative independence of strain on the duration of the contact period.

The very strong non-linearity of the strain accumulation curve with time shows the weak dependence of strain on the duration of the contact period. This helps to explain the experimentally observed constant average subsurface plastic deformation along the $PV = const$ curve. It also indicates that the average strain is stronger function of the number of contacts than the duration of the contact periods.

CHAPTER 7
EVALUATION OF THE EXISTING HYPOTHESES FOR SCUFFING

It is generally accepted that, in the final stage of scuffing, metal adhesion occurs over large contact areas, unprotected by surface films. It is also commonly acknowledged that if the rate of protective films destruction exceeds the rate of films formation, the generation of such large unprotected areas is inevitable. However, there is a lot of controversy about the mechanisms for the generation and destruction of the protective films, which has resulted in numerous hypotheses for scuffing.

In most sliding systems, the surfaces of the contacting bodies are protected against scuffing by several layers which may have very different physical and chemical nature. Lubricant films generated by hydrodynamic or elastohydrodynamic lubrication may separate the surfaces completely. These, if present, represent the first line of defense against scuffing. If the severity of the sliding conditions is increased and these films cease to be effective, the protection of the surface may rely on films formed by physical or chemical reaction between the surface and the lubricant, or a chemical reaction between the surface and the environment, and other chemically active species. Finally, in the most severe case, transformed layers formed by oxidation, agglomeration of debris and extensive strain hardening may provide protection against scuffing. This is the last line of defense of the material. The destruction of the first lines of defense represents only a necessary condition for scuffing [64]. The removal of the transformed layer from large portions of the surface is the sufficient condition for scuffing.

The failure mechanism for each of the protective layers can be quite different. The variety of scuffing hypotheses is a reflection of these differences. The hypotheses for scuffing can be subdivided into two major groups. The first consists of hypotheses mainly based on the assumption that scuffing is caused by failure of lubricant films [1-3,76,79,138-139]. These hypotheses have serious limitations because the collapse of lubricant films does not always lead to scuffing [140]. Depending on the geometry and the conditions, many systems may remain operable after such collapse has occurred. In addition, these hypotheses have difficulties explaining the effect of the material, which is of primary importance for the scuffing process. Clearly , these hypotheses cannot be applied to dry sliding. For these reasons the hypotheses based on lubricant film failure are not discussed here.

The second group of hypotheses assumes that a critical condition on or under the surface of the contacting bodies is reached, which leads to surface films or bulk material failure and consequently to scuffing. Since temperature, stress, and strain describe the condition of the

material at every point on or below the surface, these are the major parameters included in the scuffing hypotheses. Hypotheses based on a critical surface or subsurface temperature are the most common [80-84]. Hypotheses based on surface and subsurface plastic deformation have also received much attention [6-9, 23]. Recently Somi Redy and coworkers introduced a hypothesis relating scuffing to a critical subsurface stress condition [16,39]. These hypotheses are considered in more detail in the following sections of this chapter.

Other hypotheses for scuffing are the critical surface energy [45], the critical contact pressure [141], and the accumulation of wear debris [14,15] hypotheses. The first of these provides a physically plausible explanation of scuffing. However, it is too general and the practical difficulties in the evaluation of the energy of engineering surfaces have limited its applicability. The critical contact pressure hypothesis contradicts most of the experimental results on scuffing. Debris can contribute to scuffing by causing lubricant starvation [15], or by forming agglomerates, which if jammed into the contact may deform plastically and eventually form cold welds [14]. On the other hand, the presence of fine debris may facilitate the formation of transformed layers. In any case, the role of debris is very system-dependent. For these reasons these hypotheses are not discussed in detail below.

7.1. Hypotheses Based on a Critical Temperature Condition

The critical surface temperature hypothesis, initially proposed by Blok [41], is probably the best known hypothesis which relates scuffing to a critical temperature condition. The major assumption of this hypothesis is that scuffing occurs when the surface temperature (T_s) of the contacting bodies reaches some critical value (T_c). The critical temperature is assumed independent of the operating conditions and contact geometry. It is a function of the materials and lubricant properties. In a simplified form, this hypothesis can be represented as:

$$T_s = \left(T_0 + C_t \mu A_0 P V + T_f\right) \geq T_c \tag{7.1}$$

where T_0 is the environmental temperature, $\left(C_t \mu A_0 P V\right)$ is the temperature rise due to frictional heating and T_f is the flash temperature. In the expression for the frictional heating, μ is the coefficient of friction A_0 is the apparent area of contact, and C_t is a constant characterizing the thermal dissipation properties of the system. The calculation of the flash temperature is based on the analytical work of Block [80] and Jaeger [123] for stationary and moving heat sources over a semi-infinite half-space. These analyses links the flash temperature to the friction coefficient, the load, the thermal properties, and the surface velocities of the bodies in contact. As discussed in

more detail in Section 6.2, the flash temperature rise is due to constriction thermal resistances, heat flux transients, and variations in the thermal properties of the materials close to the surface.

An alternative hypothesis relating scuffing to some critical thermal condition is the critical frictional power intensity hypothesis [81]. The criterion used in this hypothesis is the ratio of the generated frictional power and the Hertzian area of contact. A lot of experimental work has been done to validate these hypotheses [24,25]. The results are controversial, but it seems that most of the experimental results are in favor of the critical frictional power intensity hypothesis [15,24, 82], although both seem to produce similar results.

The experimental basis for these hypotheses is the observation that scuffing often occurs along curves described by the $PV = const$ relationship, which also approximately corresponds to a constant surface temperature condition. This relationship seems to hold for a variety of materials and contact geometries [24]. The experimental results from this study (Fig. 3.2) also show that the 1100 Al and 390-T6 Al alloys, when tested in air, scuff at a constant bulk temperature. An advantage of this hypothesis is that the effect of the environmental temperature on scuffing (Fig. 3.3) can be easily explained. Equation (7.1) predicts that the effect of increasing the environmental temperature is to decrease the PV at which scuffing occurs, which is exactly what was experimentally observed in this study (Fig. 3.3). Geometry effects can be explained on the basis of differences in the thermal dissipation constant C_t. However, a more careful examination of these results reveals that the predictions of the critical temperature hypothesis are only qualitatively correct. A quantitative analysis shows that the surface temperature at scuffing is affected by the contact geometry, the ratio of the contact pressure to the sliding velocity for a constant PV, and the test environment. Therefore, it is not a material property and cannot be used as a criterion for scuffing. Some of the most serious deviations from the constant surface temperature condition at scuffing are summarized in Table 7.1.

The first pair of data in Table 7.1 reflects the dependence of the surface temperature at scuffing on the geometry of the specimens. The tests conducted with the smaller diameter pins (geometry R44.5) were capable of withstanding almost three times higher contact pressure than the larger pins for the same sliding velocity. It was shown in Chapter 5 that the local pressure is not a strong function of the load, hence the local pressures for these two geometries are probably similar. The sliding velocities are also similar, hence, the local heat fluxes will be approximately the same. This is the reason why the flash temperature estimates for these two cases are almost the same. However, the measured bulk temperature is quite different which is a consequence of the fact that the large pins generate four times more heat for the same PV. This results in quite different surface temperatures at scuffing.

Table 7.1 - Surface temperature at scuffing for various materials and test conditions

Material	Geometry	P MPa	V m/s	PV MPam/s	T_0 °C	† $C_t\mu A_0 PV$ °C	‡ T_f °C	T_s °C
390-T6 Al	R12.7	2.81	2.66	7.47	30.0	240	62	332
	R44.5	8.43	2.79	23.5	30.0	180	59	269
DHT-3 Al	R12.7	12.25	0.33	4.04	30.0	205	4	239
	R12.7	2.99	2.67	7.98	30.0	215	62	307
1018 Steel	R12.7	15.5	0.67	10.38	30.0	320	35	385
	R12.7	5.6	2.67	14.95	30.0	460	130	620
390-T6 Al	R12.7	31.58	0.33	10.42	30.0	234	4	268
in R134a	R12.7	7.01	2.67	18.71	30.0	308	41	379
† Experimentally measured; ‡ Calculated according to the procedure described in Section 6.2								

The temperature data for DHT-3 and steel result from deviations from the $PV = const$ curve. These materials tend to fail more easily at high pressures than at high velocities. As discussed in Chapter 6, this is probably a consequence of their local stress-strain behavior. Since the flash temperature increases with the sliding velocity, the variations in the calculated surface temperatures at scuffing become larger than the measured variations in bulk temperature. In fact, a critical bulk temperature criterion seems to fit the data better. This is a consequence of the fact that scuffing is due to a subsurface rather than a surface material failure.

The last pair of data in Table 7.1 is for the tests conducted in R134a environment. Because of the large deviations from a constant PV curve (Fig. 3.7), the surface temperature at scuffing is far from being constant.

Deviations from the critical surface temperature hypothesis are not typical only for this study. Many such deviations are well documented in the literature [15,24,82,142,143]. Therefore, many attempts have been made to improve this hypothesis so that it can explain better the experimental results. A typical example are the efforts of International Research Group on Wear of Engineering Materials (IRG) [53-60]. These studies have primarily phenomenological character and have resulted in the generation of empirical relationships of the form [53]:

$$P^n V^m T^q = C = const \tag{7.2}$$

where the constants n, m, and q reflect the relative influence of the contact pressure, the sliding velocity and the surface temperature on scuffing. Unfortunately, these relationships are not applicable outside of the narrow range of conditions and geometries for which they were originally obtained.

Apart from the deviations from a constant surface temperature at scuffing, the critical temperature hypothesis has other serious problems. The major difficulty is that it is phenomenological in nature and does not provide a plausible answer to the question why should scuffing occur at a constant temperature. Desorption of protective surface layers, formed by active species is the most common explanation [4]. Unfortunately, it has quite limited application. There have been attempts to extend the desorption concept for surface films formed by chemical reactions, including oxidation [144]. The validity of this generalization is questioned by Lee and Ludema [52] who argue that all these processes are reaction rate related and therefore time-dependent. Hence, the dynamics of their formation and destruction cannot be described by a simple state equation. Metallurgical transformations due to high temperature have also been suggested as a possible mechanism [54]. These have not received convincing experimental verification. Finally, melting of the protective layers has been proposed [145]. This mechanism is also limited to specific surface compounds with low melting temperatures.

The second serious difficulty of all critical temperature condition hypotheses is their failure to explain the time dependent phenomena, typical for the scuffing process (Fig. 3.5). As "static" hypotheses they also cannot explain the observed loading history effects (Fig. 3.6).

Some of these difficulties are overcome in the competitive oxide formation and destruction hypothesis [5] and the thermoelastic instability hypothesis [146,147]. These are discussed separately in the following sections of this chapter.

7.2 Hypothesis for Scuffing Based on Competitive Oxide Formation and Removal

The competitive oxide formation/destruction hypothesis [5] states that the rates of oxide formation and destruction are functions of temperature. A critical temperature condition will be achieved if these rates become equal. If the destruction rate is higher, large areas of bare metal will be generated and scuffing will occur. Clearly, this is another hypothesis which relates scuffing to surface temperature. However, this hypothesis differs from the hypotheses discussed in the previous section by its capability to provide an explanation for the physical nature of the critical temperature condition. In addition, the difficulty with the time effects is overcome because the

kinetics of oxide formation and destruction is a time-dependent process. This hypothesis is equally suitable for dry and lubricated contacts.

In this hypothesis, the rates of oxide formation and destruction are expressed as Arrhenius-type relations:

$$R_r = v_r \exp\left(-\frac{E_r}{\Re T}\right) \tag{7.3}$$

and

$$R_f = v_f \exp\left(-\frac{E_f}{\Re T}\right) \tag{7.4}$$

where R_r and R_f are the rates of oxide removal and formation, v_r and v_f are the corresponding pre-exponential factors, E_r and E_f are the activation energies, $\Re$ is the universal gas constant and T is the absolute temperature. The scuffing criterion is expressed as:

$$R_r \geq R_f \tag{7.5}$$

In the model based on the above hypothesis, data for the rate of oxide growth are taken from static oxidation tests at temperatures in the range of 140-250°C. The rates of oxide removal are obtained from wear tests in vacuum.

As stated earlier, it is generally accepted that scuffing will occur if the rate of removal of the protective surface layers exceeds the rate of their formation. Therefore, hardly anyone will question the validity of equation (7.5). However, the determination of the rates for formation and destruction begs for criticism. It has been experimentally proven [89] that static oxidation rates cannot be used to predict the thickness of the oxide layer in a sliding contact. The results for the thickness of transformed layers observed in this study also support this view. Using static oxidation rates will predict oxide layer thickness orders of magnitude thinner than layers found in a real sliding contact. For aluminum this ratio is about 1:1000. As shown in Chapter 4, oxidation is only one of the mechanisms involved in the formation of a transformed layer. The contribution of plastic deformation and accumulation of debris is not easy to determine. The validity of equations (7.3) and (7.4) is also questionable. Sharp transitions in wear rate are typical for scuffing. These transitions are due to a large-scale subsurface failure. They cannot be correlated to wear measurements under less severe conditions, because the wear mechanisms are different. The effect of the surface temperature and the universal gas constant on wear is also unclear. It may be

possible to describe the rates of formation and destruction through curve fitting of Arrhenius-type relationships, but this is a purely phenomenological approach no better than the approach described in the previous section. Similar to Block's critical temperature postulate, the actual mechanism responsible the transition to scuffing remains unclear.

Still, the major idea behind this hypothesis remains valid. More experimental and theoretical work on the dynamics of transformed layers formation is necessary.

7.3 Hypothesis for Scuffing Based on Thermoelastic Instabilities

This hypothesis [146,147] also relates scuffing to a critical temperature condition reached at the surface. The suggested mechanism responsible for scuffing is asperity expansion. When an asperity comes into contact with the counterface it heats up and expands, which leads to a more severe loading, further heating and expansion. This sequence of events may or may not reach an equilibrium. If this process becomes unstable, which is determined by some critical surface condition, scuffing will occur.

The experimental basis of this hypothesis is the observed persistence of hot spots on the surfaces of bodies in sliding contact. In particular, these hot spots have been observed on the surfaces of railroad brakes [148]. For an elliptic contact between cylinders made of the same material, the thermoelastic stability condition is expressed as [146]:

$$W = \frac{144(R_A + R_B)}{E^2(1-\nu^2)}\left[\frac{\pi m_t^2 n_t k(1-\nu)}{\mu V m_h \alpha_t}\right]^3 \tag{7.6}$$

where W is the transition load above which scuffing will occur, V is the sliding velocity, μ is the coefficient of friction, k is the thermal conductivity of the material, E and ν are elastic constants, R_A and R_B describe the curvatures of the cylinders in the point of contact, m_t and n_t are coefficients characterizing the change of shape of the contact due to thermal loading, α_t is the coefficient of thermal expansion, and m_h is a constant which relates the load to the size of a Hertzian contact.

Equation (7.6) shows the major parameters included in the thermoelastic instability hypotheses. These are geometrical factors, factors quantifying the amount of heat flowing through the interface, elastic and thermal properties of the materials. Equation (7.6) also reveals the serious disadvantages of this hypothesis. For example, for a similar contact geometry, load, sliding velocity and coefficient of friction, Eq. (7.6) predicts the same scuffing load for all aluminum

alloys, irrespective of their composition, because all they have approximately the same elastic and thermal properties. This clearly contradicts the experimental findings. In general, any scuffing criterion which does not include the plastic behavior of the materials will fail to explain the strong dependence of scuffing on factors such as alloy composition and microstructure. This problem is addressed in the work of Yang et al. [147] who have included the ratio of the maximum Hertzian contact pressure to the yield strength of the material at the bulk temperature (P_0/σ_0) in their model. This approach is also questionable, because the strength of the material at the surface, where the events described by this hypothesis are said to occur, is very different from the strength in the bulk.

In general, the correlation between experimentally obtained scuffing data and the predictions of the thermoelastic instability hypothesis is poor [146,147]. This hypothesis is also "static" in nature and cannot explain time and loading frequency effects. Finally, it contradicts the experimental observation that scuffing is caused by subsurface failure. It seems that the thermoelastic instability hypothesis does not have any advantages over the much simpler Block's equation, while preserving the disadvantages inherent to all critical temperature condition hypotheses.

7.4 The Critical Subsurface Stress Hypothesis

The critical subsurface stress hypothesis was introduced by Somi Redy and coworkers [16,39] to describe the large-scale subsurface failure of aluminum-silicon alloys, which was observed at scuffing under dry sliding conditions. This hypothesis assumes that ductile rupture of the subsurface is the mechanism responsible for scuffing. It occurs when the shear stress (τ) at a critical depth under the surface (z_c) exceed the temperature-dependent shear strength (S_u) of the material at this depth.

$$\tau \geq S_u(T) \tag{7.7}$$

This hypothesis is a major break-through in the scientific view of scuffing. For the first time subsurface failure is suggested as the mechanism responsible for failure. The subsurface failure mechanism for scuffing is supported by the experimental observations in the original paper [16] and also by the findings of the present study. The extensive plastic deformation present at scuffing also seems to support this view. This hypothesis is also supported by the fact that the stronger aluminum alloys scuffed at higher PV's. The temperature effects can also be easily

incorporated in the hypothesis through the dependence of the shear strength on temperature (Fig. 2.4).

Unfortunately, the quantitative calculations based on the critical shear stress hypothesis do not always correlate well with the experimental data. This hypothesis was experimentally verified by conducting scratch tests, in which a steel ball is slid over an aluminum plate [16]. However, the data presented by the same authors for the results from a pin-on-disk test aren't convincing. This hypothesis seems capable of explaining the data obtained from lubricated scuffing tests of 333 Al on 52100 steel [149]. Predictions of the critical subsurface stress hypothesis were also compared to data from this study. The shear strength of 390-T6 Al at the measured bulk temperature (Fig. 2.3) was compared to the calculated subsurface equivalent shear stresses at a depth of 50 μm. This depth is approximately equal to the typical depths at which subsurface failure occurred, as shown in Figs. 4.9, 4.10, and 4.18. The shear stresses at this depth are calculated according to the procedure described in Section 6.1. The solution for the subsurface stresses is based on a surface pressure and contact areas distributions obtained from a finite element solution, as described in Section 5.9. The surface profiles used as an input to this solution were obtained from a constant load test at 95% of the scuffing *PV*. The values for the maximum and average pressures, and the real area of contact for this test were already presented in Fig. 5.17. The input data for the solution and other relevant parameters are given in Table 7.2. The results from the numerical solution are given in Fig. 7.1.

Table 7.2 - Input parameters for the verification of the critical stress hypothesis

Apparent Contact Pressure	Sliding Velocity	Measured Bulk Temperature, T_b	Ultimate Shear Strength at T_b	Shear Yield Strength at T_b
10.5 MPa	0.67 m/s	240 °C	130 MPa	60 - 70 MPa

From Fig. 7.1, it is seen that nowhere in the subsurface of the pin the equivalent stress exceeds the shear strength. However, the shear stress is higher than the shear yield strength at several locations, which indicates that plastic flow will occur. These results show that the scuffing criterion of the critical stress hypothesis is not satisfied anywhere at this depth under the surface.

An even larger discrepancy between the predictions of the critical stress hypothesis and the experimental results can be expected for the smaller size pins, because they scuff at lower bulk temperature.

Similar to the critical temperature hypotheses, the critical stress hypothesis is "static" and cannot explain the time and load-history dependencies. In fact, it can be shown that for the majority of operating conditions this hypothesis is equivalent to a critical bulk temperature condition. As shown in Fig. 5.15, the average and maximum local pressures are fairly constant at all loads. Therefore, at a constant sliding velocity, the only result from a higher load is the increase of the heat flux and, consequently, the bulk temperature. Thus the critical stress hypothesis is reduced to a critical bulk temperature condition. However, as shown in Table 7.1, the bulk temperature at scuffing is not constant and cannot be considered a material property.

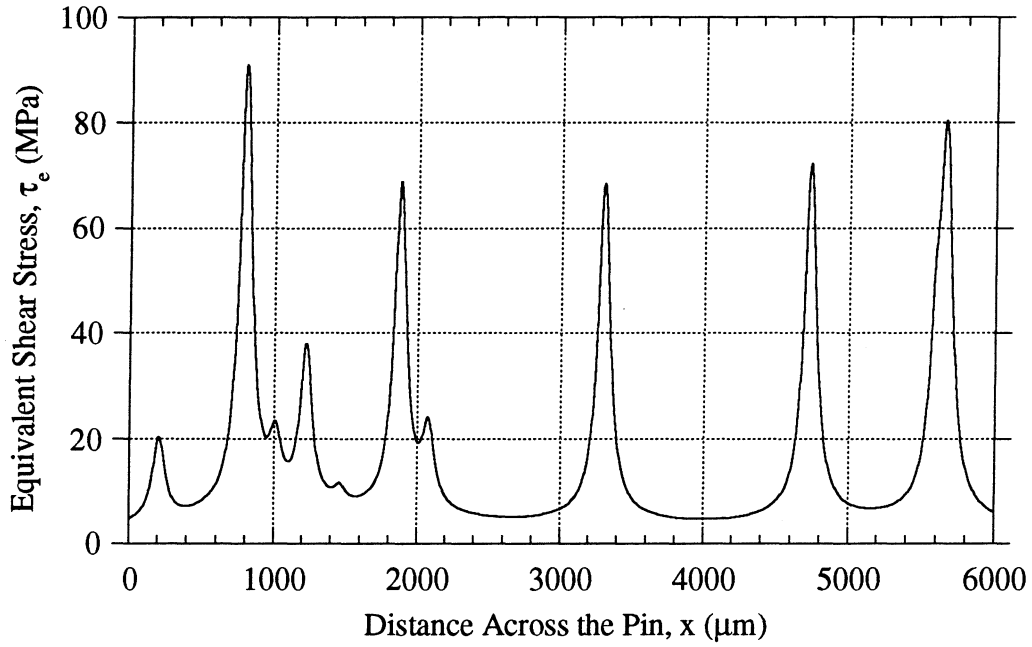

Fig. 7.1 - Equivalent shear stresses 50 μm below the surface of a 390-T6 Al pin
P = 10.5 MPa, V = 0.67 m/s, T_0 = 30 °C, T_b = 240 °C, Environment: air

7.5 Hypotheses Relating Scuffing to Surface and Subsurface Plastic Flow

It is well known that a large amount of surface and subsurface plastic flow is present at scuffing. Surface roughening is also typical. These observations are the incentive for the development of hypotheses relating scuffing to some critical amount of plastic flow.

An early attempt to relate plastic deformation to scuffing is the plasticity index criterion, originally proposed by Greenwood and Williamson [6]. According to this hypothesis, scuffing occurs when the plasticity index, given by:

$$\Psi = (E'/H)\sqrt{\sigma/R_a} \tag{7.7}$$

reaches some critical level. In this equation E' is the equivalent elastic modulus, H is the hardness of the softer material, R_a is the average asperity tip radius, and σ is the composite RMS surface roughness of the two bodies in contact. This hypothesis was experimentally verified in the work of Hirst and Hollander [7]. Park and Ludema [61] repeated the tests of Hirst and Hollander and investigated the validity of Eq. (7.7) for a large range of surface roughnesses, test conditions and material properties. Their conclusion is that the predictions of the plasticity index hypothesis deviate significantly from the experiments and cannot be used as a scuffing criterion.

Another hypothesis, proposed by Bushe and Fedorov [8], relates the dynamics of surface plastic deformation to scuffing. This hypothesis includes many parameters which are either unknown or hard to obtain experimentally. Therefore, it has not received convincing experimental verification.

Clearly, the surface and subsurface flow is a fairly complex phenomenon and cannot be described by simple relationships like Eq. (7.7). Recently, much work was done to obtain a better understanding of the plastic flow in a sliding contact [91,92,127]. Advancements in relating scuffing to plastic flow were also made. These are primarily due to the work of Ludema and coworkers [23,52,61,62,150,151]. In a series of studies they systematically evaluated the validity of various criteria for scuffing, including several critical temperature criteria, the plasticity index criterion, and the Λ-value criterion, which relates scuffing to lubricant failure. Their conclusion is that none of these criteria is valid, although they may identify conditions for very safe operation. The major reason for the inapplicability of scuffing criteria is that none of them accounts for all the controlling variables. The missing variables, according to these studies, are the time-dependent changes in surface roughness, amount of plastic deformation, and the progression of the subsurface towards fatigue failure. Unfortunately, these studies have not yet resulted in a single hypothesis where all these variables are taken into account. Instead, three separate hypotheses, emphasizing each of the above separately, have been proposed. These are discussed in more detail below.

a. Critical surface roughening hypothesis.

Surface roughening by plastic flow, whether or not there is material loss or transfer is one of the proposed criteria for scuffing [52]. However, this criterion is practically impossible to apply, because it lacks an adequate reference. Under dry sliding conditions, the surfaces loose their original surface finish in a matter of seconds. Depending on the load and the sliding velocity, the resulting surfaces may be smoother (if oxidative wear is dominant), or rougher (if fatigue wear

prevails) than the original. If the PV is gradually increased, a transition from an oxidative to fatigue wear may occur. A corresponding change in surface roughness will follow. Clearly, this transition does not indicate scuffing. The presence of surface plastic flow cannot be used as a criterion as well. Extensive plastic flow is typical for the dry sliding conditions, even at loads and sliding velocities which are far from the scuffing values (Figs. 4.12-4.16). In addition, this criterion is not practical for run-time monitoring of scuffing during the test.

b. Critical plastic deformation hypothesis

In another hypothesis, Xue and Ludema [150] have introduced the concept of a critical amount of accumulated plastic strain in the sliding track. The proposed criterion is formulated as:

$$\frac{\varepsilon_c}{\varepsilon_0} \propto \frac{\sigma_i WV}{H^2} \tag{7.8}$$

where ε_c is the critical strain, ε_0 is the ductility of the material in terms of reduction in area at fracture, and σ_i/H is the ratio of the strength of the surface films to the bulk hardness of the material. This is a very interesting hypothesis in view of the observation that scuffing failure is indeed related to the damage in the subsurface caused by extensive plastic deformation (Fig. 4.11). A major advantage of this hypothesis is its ability to explain time effects based on the concept of damage accumulation. Unfortunately, the original paper in which this hypothesis was proposed does not contain any experimental data for measured plastic deformation and, hence, proof for the validity of this concept. It is also unfortunate that this idea was not pursued any further by researchers working in this field.

It is interesting that support for the critical strain concept comes from studies in another field - the investigation of various mechanisms of wear. Following the introduction of the delamination theory of wear by Suh and coworkers [63], the attention of many researchers has shifted from the surface to the subsurface [91,92,127,152,153]. The promising concept of subsurface damage accumulation as a function of plastic strain and strain-rate was introduced [91]. Kuhlmann-Wilsdorf [153] has suggested that delamination of surface layers occurs when a critical level of shear plastic strain is reached. The proposed expression for the average shear strain in the deformed zone is:

$$\bar{\gamma} = (S/A_0)\sqrt{WN/H} \tag{7.9}$$

where S is the distance slid, A_0 is the apparent area of contact, N is the number of contact spots, W is the load and H is the hardness. It is a common assumption that the number of the contact spots is proportional to the applied load W:

$$N = \eta W \tag{7.10}$$

where η is a constant of proportionality. Substituting $S = Vt$ and $W = A_0 P$ gives:

$$\bar{\gamma} = (PV)(t)\sqrt{\eta/H} \geq \gamma_c \tag{7.11}$$

where γ_c is the critical strain. The above expression can be rearranged, resulting in the following criterion:

$$PV \geq \frac{\gamma_c}{t\sqrt{\eta/H}} \tag{7.12}$$

Although this hypothesis was intended to explain delamination wear, the same idea may be applied to the destruction of protective surface films which, depending on the severity of the conditions, may lead to scuffing.

Equation (7.12) has the PV on the left-hand side and some material properties on the right-hand side. However, this relationship cannot explain the experimentally observed $PV = const$ due to the explicit functional dependence on time. According to this expression, scuffing will always occur once conditions for subsurface plastic flow are generated. This contradicts the experimental observation that scuffing-free operation is possible in spite of the large amount of subsurface plastic deformation. This shortcoming is a consequence of the fact that Eq. 7.9 is an over-simplification of the complex process of accumulation of plastic deformation.

c. Subsurface fatigue hypothesis

A pioneering approach proposed by Kim and Ludema [62] relates scuffing to low cycle fatigue. In their study, the low cycle fatigue properties of 4340 steel are correlated to results from scuffing experiments. The approach is purely phenomenological. The mechanism relating fatigue properties to scuffing is not discussed. This is quite unfortunate, because a hypothesis based on fatigue is capable of explaining most of the experimentally observed relationships in this study, including the time and loading history dependencies. It is also supported by the presence of deep cracks in the subsurfaces of specimens undergoing scuffing. This hypothesis has difficulties in

explaining the fatigue damage in stationary bodies (the pin in the experimental setup of this study), because in this case, the concept of cycles is not well defined. No criterion based on this hypothesis has been published in the literature.

7.6 Summary

Due to the complexity of the scuffing phenomena, researchers have taken various approaches in explaining and modeling scuffing, which has resulted in a large number of hypotheses. Those applicable to sliding under dry conditions are considered in this study. The first approach relates scuffing to a critical temperature condition. The second postulates that scuffing occurs when the shear stress at a critical depth in the material exceeds the shear strength. The third relates scuffing to damage caused by extensive plastic deformation. The predictions of these hypotheses are compared to experimental observations obtained in this study and to results from models of surface interactions. Based on this comparison, the following conclusions can be made:

a. None of the existing hypotheses and criteria for scuffing can explain adequately all the experimental results and observations.

b. The hypotheses relating scuffing to subsurface plastic deformation and subsurface fatigue are the most promising. They are supported by the experimental results and by the observations of subsurfaces undergoing scuffing. These hypotheses can explain the time effects based on damage accumulation . However, none of these have been developed in enough detail to serve as a scuffing criterion. In their present state, these hypothesis do not go beyond phenomenological correlations. There is no single hypothesis which combines the effects of subsurface plastic deformation and subsurface fatigue.

c. The hypotheses relating scuffing to a critical thermal condition are phenomenological in nature and do not provide an explanation for the mechanism of scuffing. These hypotheses consider a "static" state of the material and cannot explain time and load history effects.

d. Block's flash temperature concept deviates from the experimentally observed data. The results from this study show that the surface temperature at scuffing is not a material property and cannot be used as a criterion. It is dependent on the geometry, the loading conditions, and the environment.

e. The competitive oxide formation and destruction hypothesis is also phenomenological and in its present form cannot describe adequately the complex dynamics of protective films formation and destruction. However, if this dynamics is understood, this hypothesis has a strong potential to describe the events at scuffing.

f. The thermoelastic instability hypotheses have difficulties explaining the effect of the mechanical properties of materials on scuffing. Results based on these hypotheses correlate poorly with the experimental data.

g. The critical shear stress hypothesis is a pioneering approach relating for the first time scuffing to subsurface failure. However, it cannot explain the time and load history effects. Its criterion for subsurface failure is not satisfied for the results of this study. The shear stresses at the critical depths are not high enough to cause the predicted bulk shear failure.

CHAPTER 8
PROPOSED HYPOTHESIS FOR SCUFFING

As stated in the previous chapter, none of the existing hypotheses and criteria for scuffing can explain all the experimental results and observations obtained in this study. On the other hand, the most promising concepts of critical subsurface plastic accumulation and subsurface fatigue have not been developed in enough detail to serve as a basis for a scuffing criterion. Recent advances in understanding the material behavior in sliding systems have not been incorporated into a scuffing model. Therefore, a new hypothesis for scuffing which aims at overcoming some of these problems is proposed in this study. The hypothesis is a combination and a generalization of the critical strain and the subsurface fatigue hypotheses.

A criterion for scuffing based on the proposed hypothesis is also developed as a part of this study. The criterion involves several functional relationships between the macroscopic loading parameters, the local stresses and temperatures, and the local material properties. Some of these relationships are very complicated and cannot be represented in a closed form. In the scuffing criterion, these functions are simplified to allow the representation of the criterion as a single mathematical formula.

The proposed criterion is evaluated based on its capability to explain the experimentally observed phenomena. The explanations are qualitative due to the lack of information about the behavior of the tested materials under sliding conditions. It should be emphasized that the proposed hypothesis is based on the evaluation of a few materials under dry sliding conditions. It is possible that this hypothesis may not be applicable to other materials or operating conditions.

8.1 Description of the Proposed Hypothesis for Scuffing

The hypothesis for scuffing, proposed in this study, states that the accumulation of plastic deformation and fatigue damage in the subsurface is responsible for scuffing. Although subsurface fatigue is widely recognized as one of the major wear mechanisms, the possibility that the same process could be responsible for scuffing has not been investigated in much detail. This possibility was addressed for the first time in a study by Kim and Ludema [62]. They proved that there is a good correlation between scuffing of steel/steel contacts under lubricated conditions and

low cycle fatigue. However, they did not develop this idea any further and did not provide a description of the mechanism of scuffing.

The experimental observations of the present study indicate that the mechanism responsible for scuffing may be similar to the mechanism responsible for delamination wear. Observations of subsurfaces of worn specimens and wear debris (Figs. 4.1, 4.9) show that the average thickness of wear particles generated by delamination is several times smaller than the depth of the layer affected by plastic deformation. Since damage is accumulated in the whole plastically deformed layer, cracks may initiate and propagate simultaneously at different depths. This is clearly seen in Fig. 4.9, which reveals several systems of cracks at different depths. The accumulation of damage close to the surface is responsible for wear, while the accumulation of damage further from the surface is responsible for scuffing. The possible existence of two critical depths for damage accumulation has also been demonstrated by a theoretical analysis [152].

As shown in Chapter 4, modified layers of various thicknesses and properties exist in dry sliding contact. They prevent large-scale adhesion between the surfaces. Scuffing can occur only if these protective layers are removed. In the proposed hypothesis, the removal of these layers and the subsequent formation of cold welds occurs according to the following sequence of events:

a. Accumulation of plastic deformation in the subsurface.

The contact of rough surfaces is characterized by uneven pressure distribution. Even at low loads, the local pressures may be high enough to cause plastic deformation both on and under the surface. As various parts of the surface come into contact, plastic deformation will occur in increasing number of locations, and finally the whole subsurface will be plastically deformed. The plastic deformation accumulates with time. This process is controlled by the local temperatures, stresses, and material properties, as discussed in Chapter 6.

b. Nucleation of cracks and voids.

If the amount of subsurface plastic deformation becomes large enough, cracks and/or voids will nucleate at inclusions or intersections of shear bands. The mechanism of crack nucleation at inclusions is either by decohesion, or by fracture of brittle particles. The nucleation of cracks is assumed to occur at a critical plastic strain level.

c. Propagation of cracks.

The presence of cyclic loading is a necessary condition for crack propagation. Although the macroscopic load may be constant, the load on a local scale is always cyclic. The local cyclic load is due to the discontinuous character of the wear process, the waviness of the sliding surfaces, and plastic flow at the points of contact. The combined effects of shear traction, compressive hydrostatic stress and materials properties gradient in the subsurface result in localization of the damage at one or more critical depths below the surface. Under the local cyclic loads, the cracks

grow parallel to the surface, finally resulting in the removal of the layers above them. The relative depth of the cracks below the surface determines whether this process will take the form of delamination wear or scuffing. Cracks, which propagate within the modified layer, are responsible for delamination wear. In this case, the layer is not completely destroyed, and the surface is still protected against severe adhesion. On the other hand, cracks propagating deeper than the thickness of the protective layer may cause its complete removal, resulting in the generation of macroscopically large areas of bare metal. The critical depths at which cracks propagate the fastest are determined by a combination of the loading conditions, subsurface strength gradients in the material, and the ratio of the equivalent to the hydrostatic stresses.

d. Formation of cold welds.

The exposed bare metal easily forms cold welds when it comes into contact with the counterface. The exact mechanism by which exposed areas come into contact with the counterface depends on geometrical factors. For the conditions of this study, the removal of parts of the load bearing surface by fatigue increases the load over the rest of the surface. This leads to even faster removal of the remaining parts of the load-bearing surface. This process becomes unstable, self accelerates and leads to the removal of protective films from the whole surface, which then adheres to the counterface. This is the final stage of scuffing.

8.2 Proposed Criterion for Scuffing

The criterion for scuffing based on the above hypothesis states that scuffing occurs when the damage accumulation time (t_d), necessary for initiation (t_i) and propagation (t_p) of subsurface cracks is shorter than the time (t_h) necessary for the damaged material to leave the critical zone. The limited time for damage accumulation reflects the fact that, due to wear, the damaged material changes its position relative to ta fixed reference frame and gradually leaves the zone where the conditions are the most severe. This criterion can be expresses as:

$$t_d = t_i\left(\bar{\varepsilon}, \varepsilon_c, f_p\right) + t_p\left(\Delta\bar{a}, a_c, f_c\right) \le t_h\left(\dot{h}\right) \tag{8.1}$$

The initiation time is assumed to be a function of the average local strain in the vicinity of a contact spot ($\bar{\varepsilon}$), the critical average macroscopic strain necessary for crack initiation (ε_c), and the frequency of contacts in which plastic deformation occurs (f_p). The propagation term is assumed to be a function of the average extension of the cracks per loading cycle ($\Delta\bar{a}$), a critical crack length after which unstable crack growth occurs (a_c), and the frequency of loading cycles (f_c). The critical average macroscopic strain and the critical crack length are material properties at the given

temperature. They are related to the ductility and to the fracture toughness of the material. The amount of local plastic strain is a function of the local stress, temperature, and stress-strain-strain rate relationships. Similarly, the average crack extension is a function of the local stress intensities and material properties. For given material properties, contact geometry, and surface roughness, the frequencies f_p and f_c are functions of the applied apparent contact pressure and the sliding velocity.

The above criterion does not need to be satisfied for the whole subsurface. Failure is assumed to occur if it is satisfied at a single critical depth under the surface. This assumption is based on the micrographs of subsurfaces given in Figs. 4.9-4.11, which show that most of the damage is concentrated in a relatively narrow band of material.

The proposed criterion for scuffing, as given in Eq. (8.1) is too general. The major difficulties for its application are the uncertainties associated with the functional dependencies of the parameters included in it. These functional relationships are discussed in more detail in the following sections of this chapter.

8.3 Simplifying Assumptions for the Scuffing Criterion

The simplifications necessary for the construction of a scuffing criterion involve assumptions for the interaction of rough surfaces, the distribution of subsurface pressures and temperatures, and the generation of wear particles.

a. Representation of rough surfaces.

In the simplified model, the surfaces of both bodies in contact are represented by sets of long rectangular strips, as shown in Fig. 8.1. The longer side of the strips is parallel to the direction of sliding. The strips have the same width (s) and length ($2b$), but variable height relative to a datum line. The area of each strip is $\hat{A}$. This is a good approximation of surfaces which are subjected to unidirectional sliding, as are the surfaces in this study. This representation can also be conveniently related to actual digitized surface profiles, taken perpendicular to the direction of sliding. The height of the strips corresponds to the z-coordinate of the points from a datum center line, while the sampling interval in the x-direction determines the width of the strip. Thus, every area of interest can be represented as an integer multiple of $\hat{A}$, as shown in Fig. 8.1. The real area of contact is given by $A_r = N\hat{A}$ where N is an integer number. Let the average local contact pressure over all contact spots be $\bar{p}$. Then, the contact load can be expressed as:

$$W = N\hat{A}\bar{p} \qquad \text{or} \qquad W = A_r\bar{p} \tag{8.2}$$

The actual width of the contact spots, as determined with the finite element method described in Chapter 5, is between 5 and 20 μm (Fig. 5.17) with an average of about 10 μm. Since the sampling interval used to obtain the surface profiles of the contacting surfaces was $s = 5$ μm, it is reasonable to assume that the contact spots have areas between $\hat{A}$ and $4\hat{A}$ with an average of $2\hat{A}$.

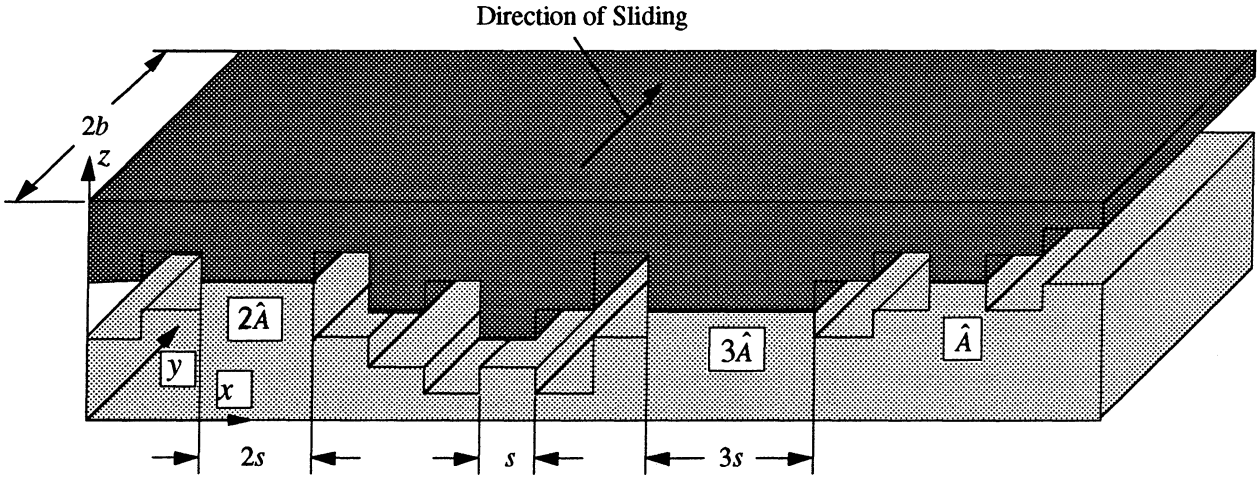

Fig. 8.1 - Representation of rough surfaces in contact

b. Idealization of the subsurface.

The subsurface is idealized by semi-elliptical regions of plastically deformed material in a large elastic matrix (Fig. 8.2). The equivalent stresses within each region are uniquely determined by the contact pressure applied on a surface strip of area $2a \times 2b$, and by a constant coefficient of friction (μ). The size and shape of the regions is determined by the equation:

$$\sigma_e(x,z) = \sigma_0(T) \tag{8.3}$$

where $\sigma_0(T)$ is the temperature-dependent yield strength of the material. The assumption for the semi-elliptical shape of the region is based on the observed stress distributions in the vicinity of a contact spot (Fig. 6.2). The state of stress in each region is assumed to be independent of the stress in other regions. This assumption is realistic, because, as shown in Fig. 5.15, the contact

spots are relatively far from each other. The equivalent stress within the region is linearly proportional to the local contact pressure p. It is further assumed that the average contact pressure over all the regions is the same and equal to $\bar{p}$.

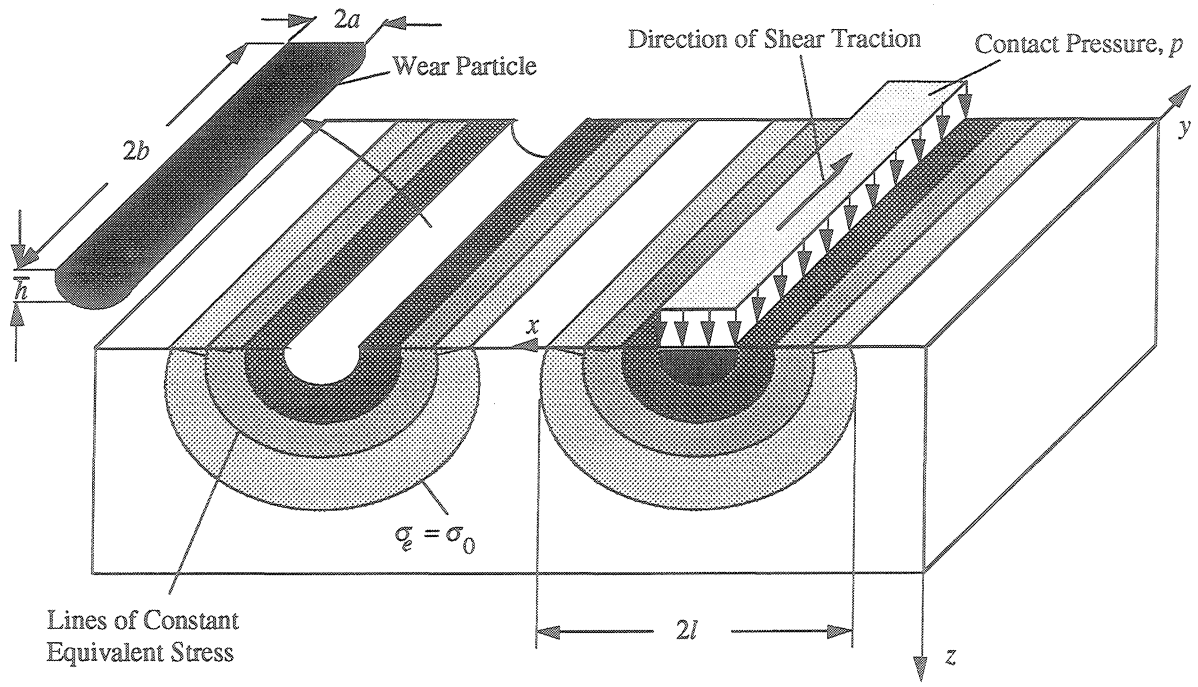

Fig. 8.2 - Idealization of the subsurface
The shaded areas represent regions where the equivalent stress exceeds the yield strength
Note that the estimates for the equivalent stresses are based on an elastic response of the material

c. Assumption for the real area of contact.

The real area of contact A_r is assumed proportional to the contact load W. This assumption is based on the results given in Fig. 5.17, which shows that this relationship is true for a broad range of loads, including the conditions immediately before scuffing. This relationship can be expressed as:

$$A_r = \beta(W/E'), \quad A_r = \beta(PA_0/E'), \quad N\hat{A} = \beta(PA_0/E'), \text{ or } \quad N = P\left(\beta A_0/E'\,\hat{A}\right) \qquad (8.4)$$

where the load is normalized by the equivalent elastic modulus E', N is the number of contact strips, and β is a constant. The elastic modulus is chosen as a normalizing factor, because the solution for the area of contact given in Fig. 5.17 is based on a fully elastic response of the

material. The deformation of the surfaces and consequently the size of the real area of contact are functions of E'. The constant β is determined by fitting a straight line through the data points for the real area of contact given in Fig. 5.17. For the conditions of this study, and for 390-T6 Al sliding on 1018 steel, the values of β and E' are:

$$\beta = 84.8 \qquad \text{and} \qquad E' = 57.8 \times 10^3 \text{ MPa.} \tag{8.5}$$

d. Assumption for the local contact pressure.

The average local contact pressure $\bar{p}$ is assumed independent of the load W. The sole effect of increasing the load W is to increase the number of contact spots. This assumption is also based on the results shown in Fig. 5.17, which indicate that both the average and the maximum local pressures are weak functions of the load.

e. Assumption for the wear mode.

The wear mode is assumed to be subsurface fatigue. This assumption is consistent with the experimental observations of this study. The wear process on a local scale is discontinuous, as shown in Fig. 8.2. Sliding proceeds for some time $\bar{t}$ before a wear particle is generated. When this happens, the load is taken by other parts of the surface, the stress within the region becomes zero, and the process of subsurface damage accumulation stops until the next loading period. It is assumed that the size of the wear particle is $2a \times 2b \times \bar{h}$, where $\bar{h}$ is the average thickness of the particle, as shown in Fig. 8.2. It is also assumed that wear obeys Archard's law, which states that the volume worn is linearly proportional to the contact load and the sliding distance and inversely proportional to the hardness of the material. The same law gives the relationship between the wear rate $\dot{h}$ and the PV as:

$$\dot{h} = (K/H)PV \tag{8.6}$$

From the wear results presented in Figs 3.11-3.13, it can be seen that this indeed is the case. On a local scale this relationship becomes:

$$\bar{h} = (K/H)\bar{p}V\bar{t} \tag{8.7}$$

or

$$\bar{h} = (K/H)(A_0/A_r)PV\bar{t} \tag{8.8}$$

f. Assumption for the subsurface temperature.

The subsurface temperature is assumed constant and equal to the measured bulk temperature. The reason for this assumption is the results from the thermal finite element model given in Section 6.2. These results show that, for the conditions of this study, the flash temperatures were small compared to the bulk temperature and could not significantly affect the mechanical properties of the material. In general, even if the flash temperature is large, its relevance to the relatively deep (50-80 μm) subsurface failure, which is the reason for scuffing, is questionable. It is expected that most of its effect will be filtered out at this depth.

8.4 Initiation of Cracks

At large plastic deformations of the matrix, voids are generated next to second-phase particles or at the intersection of shear bands. Large plastic flow also causes fracture of silicon particles in the aluminum-silicon alloys. These are the reasons for the assumption that a critical amount of plastic flow is a sufficient condition for crack initiation. This condition can be expressed as:

$$\varepsilon \geq \varepsilon_c \tag{8.9}$$

where ε is the average plastic strain at a critical depth under the surface and ε_c is a material property at the given bulk temperature. The average strain in the subsurface is the result of the contributions of the strains in the individual plastic regions shown in Fig. 8.2.

Since plastic deformation is generally dependent on the whole previous deformation history, the strain at a point in the subsurface is not uniquely determined by the state of stress at this point. As discussed in Section 6.3, the problem is further complicated by dynamic recovery and recrystallization. This makes the stress-strain-strain rate interactions in the subsurface very complicated and virtually impossible to describe with a simple equation. Simplifying assumptions have to be made.

The assumption made in this study is that dynamic recovery and recrystallization do not occur. After an initial deformation, the strain at each location remains constant until the next contact period. If the stress in the next period is higher than the stress corresponding to the already accumulated strain, further deformation will occur. In each successive contact period the deformation will be smaller until an equilibrium is reached. The experimental results given in Chapter 4 and results reported in the literature [91,92] indicate that the subsurface strain indeed reaches an equilibrium after certain period of sliding and does not increase any further. In

particular, for 390-T6 Al sliding at 80% of the scuffing *PV*, this equilibrium is reached in approximately five minutes. At 97% of the scuffing *PV*, the equilibrium is reached in less than a minute. More ductile materials may need longer times, as seen from the work of Alpas et al. [91]. There are two reasons for this equilibrium condition. The first is that the material strain hardens. The second reason is that a dynamic equilibrium is reached between the accumulation of strain and relative motion of the material toward the surface due to wear. The existence of an equilibrium and the relatively short time period in which this occurs are the reasons for the above assumption.

The strain within a plastically deformed region is non-uniform. It is a function of the position within the region. Therefore, it is convenient to work with a quantity which describes the average strain accumulated at a certain depth z over the whole plastically deformed region. This quantity is expressed as:

$$\bar{\varepsilon}_i(z) = \frac{1}{2a}\int_{-l}^{l}\left[\varepsilon_i(x,z) - \varepsilon_{i-1}(x,z)\right]dx \tag{8.10}$$

Equation (8.10) shows that the new strain accumulated in a contact period is the sum of all strain increments of all the points along the line z within the region. The integration bounds are given by the largest width of the plastically deformed region ($2l$), as shown in Fig. 8.2. The index i indicates the numbers of the contact periods. The strain $\varepsilon(x,z)$ at each point along the integration path can be obtained from Eq. (6.17), by setting $\sigma_f = \sigma_e$. The latter, in turn, is linearly proportional to the applied surface pressure $\bar{p}$. The average plastic strain accumulated over the whole subsurface for the i-th time period is:

$$\varepsilon_i = \bar{\varepsilon}_i(A_r/A_0) \tag{8.11}$$

According to the above equations, the average strain rate in the subsurface will grow with time as fresh surface strips come into contact. However, according to the assumptions made above, it will stop growing when all of the strips shown in Fig. 8.1 have been in contact once. The time (t_a) necessary for the accumulation process to stop is given as:

$$t_a = \bar{t}(A_0/A_r) \tag{8.12}$$

where $\bar{t}$ is the average time of a single contact period. If the accumulated strain in the subsurface at the end of the period t_a is smaller than ε_c, voids and/or cracks will not initiate and the sliding will continue infinitely without scuffing. However, cracks may initiate at some time t_i before the strain

hardening of the whole subsurface is completed. If cracks have not originated by the time the equilibrium condition is reached, they are not likely to form afterward, because it was assumed that there will be no further accumulation of plastic strain. The rate of strain accumulation within the time t_a is not uniform. This can be demonstrated with the aid of Fig. 8.3. Right after the initiation of sliding, the plastically deformed regions will rarely overlap due to the relatively large spacing between the individual contact spots. This is indicated by the regions with numbers 1,2, and 3 in Fig. 8.3. In this initial period of sliding, strain will accumulate fast, because the strain increments at all locations are large. As sliding proceeds, more overlaps will occur and the strain increments will decrease. It will eventually stop when the whole subsurface strain-hardens sufficiently.

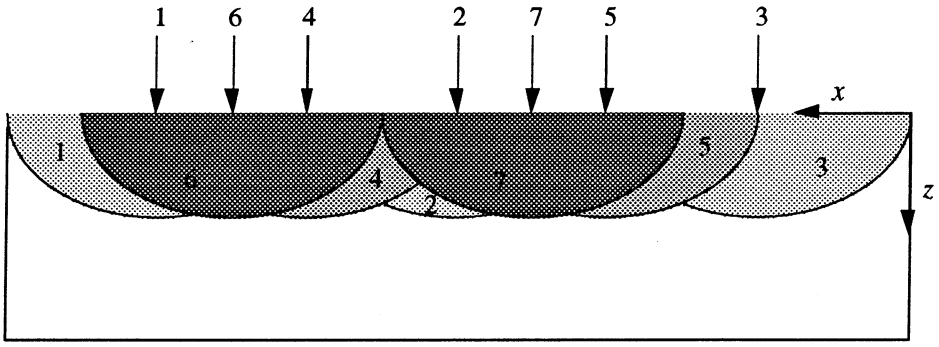

Fig. 8.3 - Overlapping of plastically deformed regions and gradual accumulation of strain in the subsurface. The numbers indicate the sequence of contact periods

With the aid of Eq. 6.17 and the results for the surface pressure distributions it is possible to illustrate the strain accumulation process. A stochastic numerical algorithm which applies contact pressures randomly on various locations on the surface was used for this purpose. The statistical distribution of the surface pressures used in the simulation was the same as the distribution given in Fig. 5.19. A typical result from this simulation is given in Fig. 8.4. The calculations are based on two depths, corresponding to a z of 25 and 35 μm. The duration of the individual contact period is taken from Table 6.1. The results in Fig. 8.4 once again indicate that accumulation of plastic deformation is a very non-linear process. The relatively small difference in the depth below the surface results in significant difference in the average subsurface strain. It should be emphasized that Fig. 8.4 is just a qualitative illustration of one possible mechanism for reaching an equilibrium in the average subsurface plastic deformation. The actual process is far more complex.

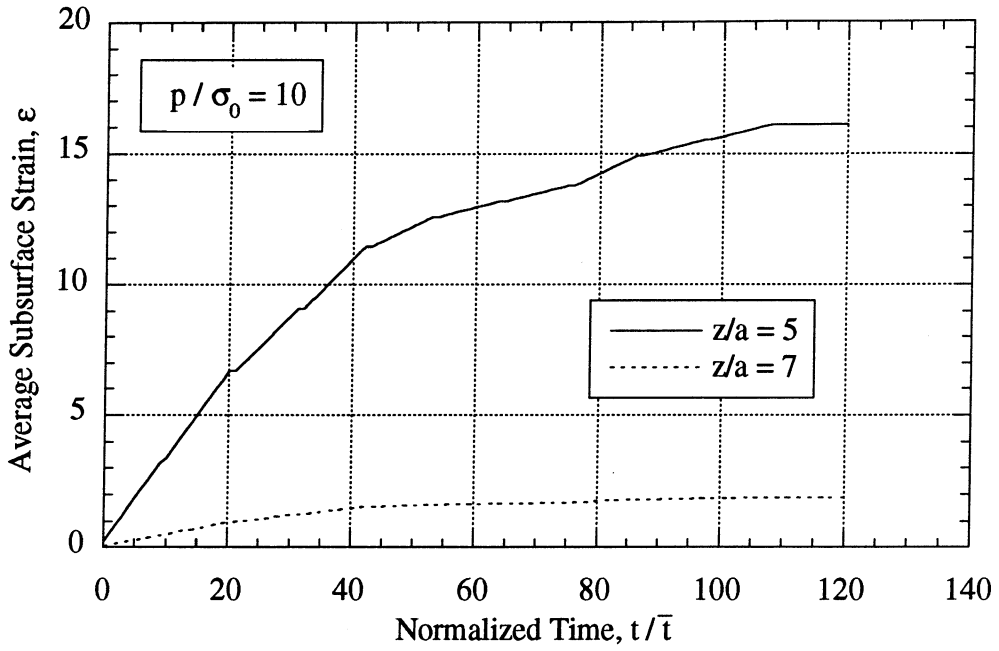

Fig. 8.4 - Accumulation of average subsurface strain with time
The average half-width of the contact spots $a \approx 5$ μm. $\bar{t} \approx 0.25$ s, $\sigma_0 \approx 150$ MPa

Generalizing Eq. (8.11) for a period of sliding with a duration t gives:

$$\varepsilon = (t/\bar{t})\sum \varepsilon_i = (t/\bar{t})(A_r/A_0)\sum \bar{\varepsilon}_i \tag{8.13}$$

If the plastic strain given by the above equation exceeds the critical strain, cracks will form. Substituting t for t_i and ε for ε_c, and solving for t_i gives the expression for the initiation time:

$$t_i = \frac{\varepsilon_c}{\sum \bar{\varepsilon}_i}\frac{A_0}{A_r}\bar{t} \tag{8.14}$$

Substituting (A_r/A_0) from Eq. (8.4) and $\bar{t}$ from Eq. (8.7) into Eq. 8.14) gives:

$$t_i = \frac{\varepsilon_c \bar{h} H E'}{K\bar{p}\beta\sum \bar{\varepsilon}_i}\frac{1}{PV} \tag{8.15}$$

8.5 Propagation of Cracks

Once initiated, cracks may propagate even if the stress is below the plastic limit. A necessary condition for crack propagation is that the stress intensity amplitude is higher than some threshold value. Another necessary condition is the presence of cyclic loading. For the test geometry chosen in this study, the loading on the aluminum pin on a macro-scale is approximately constant. Therefore, loading cycles cannot be easily identified. However, on a local scale the loading is cyclic. Two factors contribute to the cyclic load. Wear is the first. With the progression of wear, the load over a contact spot decreases and finally disappears as other parts of the surface come into contact. Conversely, when the rest of the surface is sufficiently worn out, the same contact spot will be loaded again. The second factor is the waviness of the counterface (disk) in the direction of sliding.

a. Cyclic loading due to wear.

From equation (8.7), the average time necessary for the generation of a wear particle of thickness $\bar{h}$ is:

$$\bar{t} = \bar{h}\frac{H}{K\bar{p}}\frac{1}{V} \tag{8.16}$$

During the same time interval, wear particles will be generated from all the N contact strips of the real area of contact $A_r = N\hat{A}$. Let $\bar{t}_0$ be the time between successive loading of the same contact strip. This time is equal to that necessary to reach the same wear depth $\bar{h}$ over the rest of the surface given by $A_0 - N\hat{A}$. Then, the ratio $\bar{t}_0/\bar{t}$ will be given by:

$$\frac{\bar{t}_0}{\bar{t}} = \frac{A_0 - N\hat{A}}{N\hat{A}} = \frac{A_0 - A_r}{A_r} = \frac{A_0}{A_r} - 1 \tag{8.17}$$

The total time of one loading cycle, t_c, then becomes:

$$\bar{t}_c = \bar{t}_0 + \bar{t} = (A_0/A_r)\bar{t} \tag{8.18}$$

Substituting for $\bar{t}$ from equation (8.16) gives:

$$\bar{t}_c = (A_0/A_r)\bar{t} = \left(\frac{A_0}{A_r}\right)\left(\frac{\bar{h}H}{K\bar{p}}\frac{1}{V}\right) = \left(\frac{A_0}{A_r\bar{p}}\right)\left(\frac{\bar{h}H}{K}\right) = \left(\frac{\bar{h}H}{K}\right)\frac{1}{PV} \tag{8.19}$$

Hence, the frequency of loading cycles due to wear at a given temperature will be proportional to the PV. The number of loading cycles due to wear N_w in a given period of time t is:

$$N_w = PVt\left(\frac{K}{\bar{h}H}\right) = \frac{h}{\bar{h}} = \frac{\dot{h}}{\bar{h}}t \tag{8.20}$$

Equation (8.20) provides a simple formula for the calculation of contact periods, provided the average wear rate and the average thickness of a delamination wear particle are known.

b. Cyclic loading due to surface waviness of the disk.

The surface features on worn disks and pins are strongly anisotropic. As shown in Section 5.4, the surface of the pin can be assumed to be truly one-dimensional. However, the surface of the disks, although anisotropic, is two-dimensional. The profiles taken on eight equidistant locations on the surface of the disk show variations in height, as shown in Fig. 5.3. These variations are further illustrated in Figs. 8.5 and 8.6. Figure 8.5 shows the position of the eight transverse profiles on the surface of the disk. Several concentric circles, intersecting these profiles are also shown. The vertical (z) coordinates of these intersection points are given in Fig. 8.6 which illustrates the waviness of the disk in the direction of sliding along the circles given in Fig. 8.5. These coordinates are negative because they lie below the original surface of the disk due to wear.

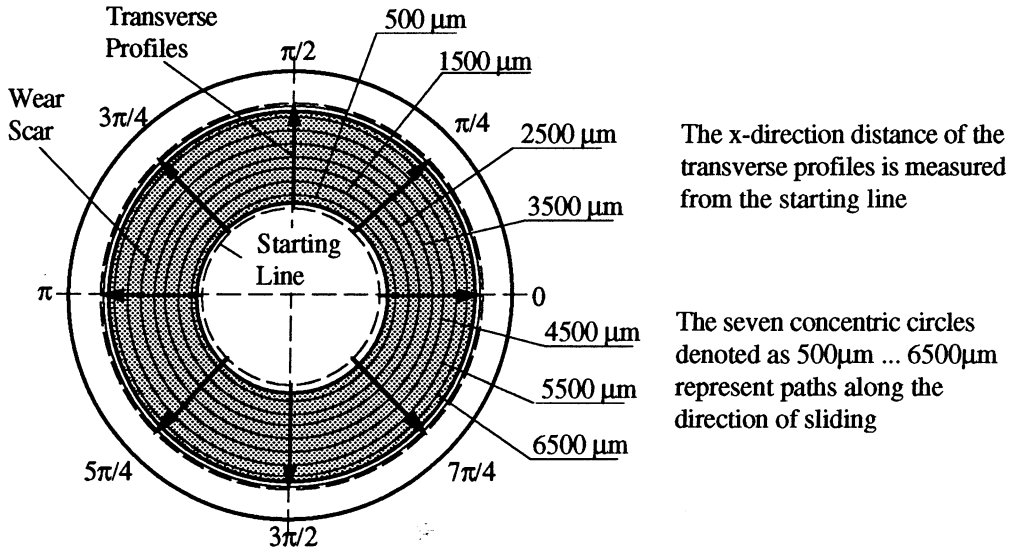

Fig. 8.5 - Schematic of transverse profiles and concentric paths along the direction of sliding on the surface of the disk

It is clear that, if the number of profiles is increased, the longitudinal representation of the disk surface will be more complete. However, even with eight data points along each line, the two-dimensional nature of the surface of the disk is clearly revealed. Variations in height along the direction of sliding produce variations in the surface and subsurface stresses. Hence, a point on or below the surface undergoes cycles of loading and unloading. The duration of these cycles is inversely proportional to the sliding velocity *V*.

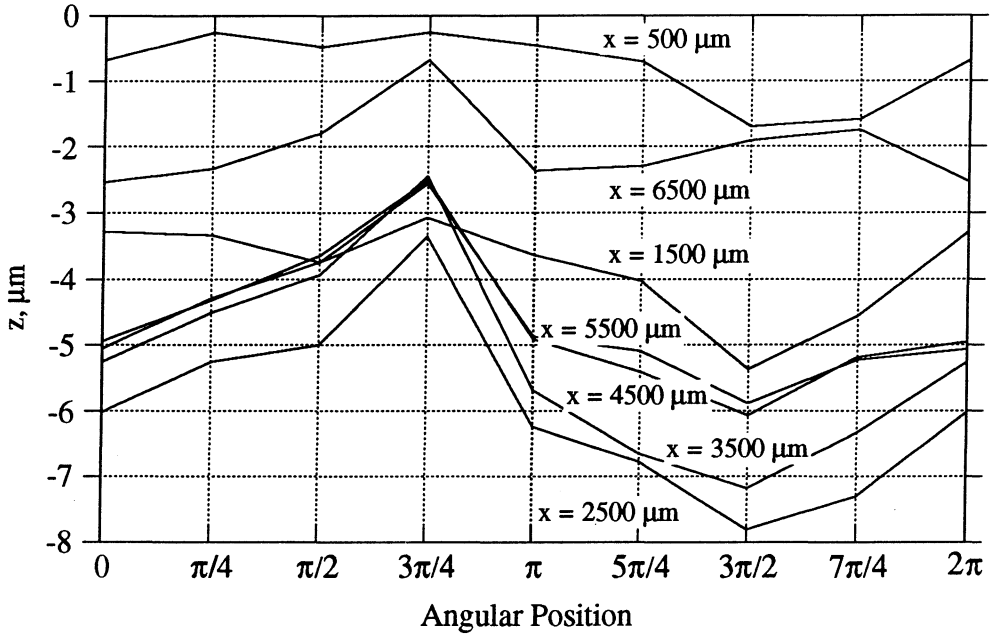

Fig. 8.6 - Longitudinal waviness of a disk along seven equally spaced concentric circles

The deviations from perpendicularity of the disk surface to the axis of rotation may also contribute to the cyclic loading of the pin surface. The duration of these cycles is inversely proportional to the RPM and, hence, to the sliding velocity *V*.

Rough estimates based on experimentally measured wear rates and wear particles thicknesses show that the duration of an average loading cycle due to wear (Table 6.1) is larger than the duration of a loading cycle due to disk waviness (t_w). According to these estimates several revolutions of the disk are necessary to produce a wear particle from a given location on the pin. The number of cycles due to disk waviness within one loading cycle due to wear is determined by the ratio $\varphi = \bar{t}/\bar{t}_w$. Both of these times are inversely proportional to *V*, hence, the number of loading cycles due to waviness (φ) within one cycle due to wear is constant. Including the effect

of the disk waviness in equation (8.20), the total number of cycles on the pin (N_c) due to both wear and waviness becomes:

$$N_c = \varphi N_w = \varphi \frac{\dot{h}}{\bar{h}} t \qquad \text{or} \qquad N_c = PVt\left(\frac{\varphi K}{\bar{h}H}\right) \tag{8.21}$$

The local cyclic loading due to wear and disk waviness is illustrated in Fig. 8.6. In the figure, the cyclic histories for two combinations of P and V for the same PV are shown. The duration of contacts for these two cases is based on the predictions of Eq. (8.7). From the figure, it is seen that the number of cycles is the same for the two combinations. The duration of the contact period is longer for the higher load. These longer cycles can be expected to cause more damage. However, as stated in Section 6.3, the process of damage accumulation is very non-linear and it is possible that approximately the same amount of damage will be caused by these two loading histories.

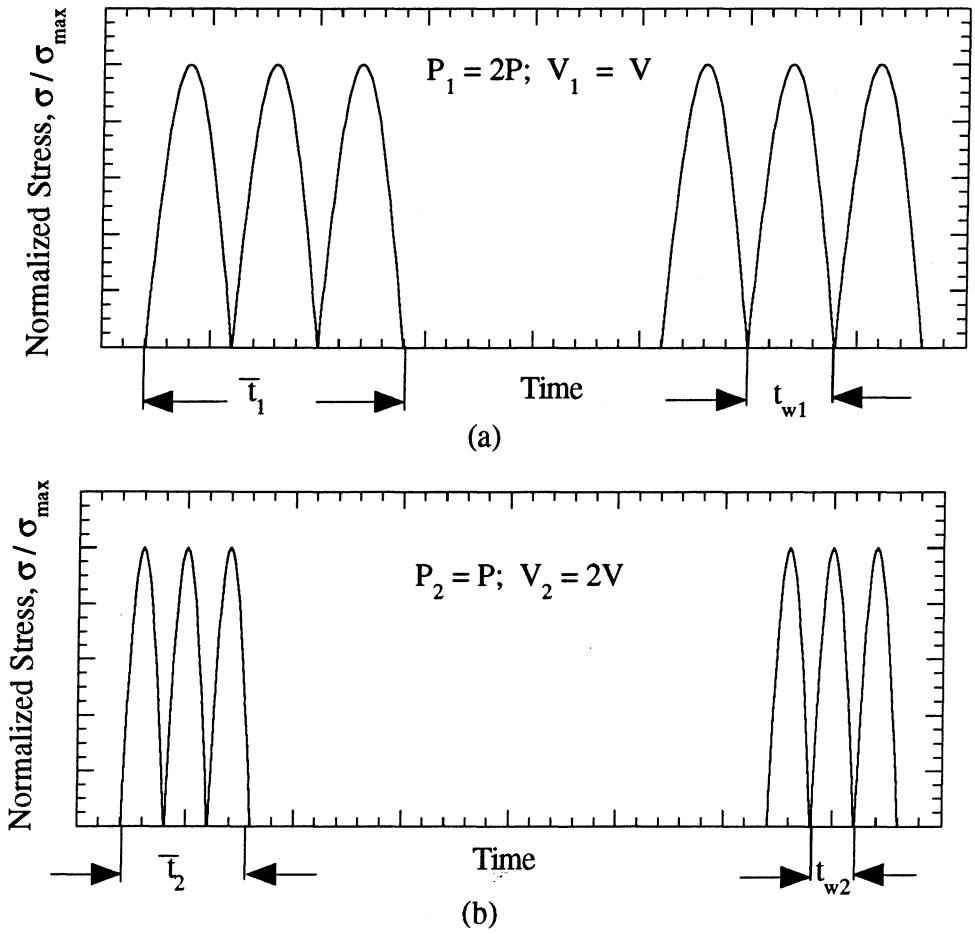

Fig. 8.7 - Schematics of a cyclic loading due to wear and disk waviness for a constant PV (a) $P_1 = 2P$; $V_1 = V$, and (b) $P_2 = P$; $V_2 = 2V$

Let $\Delta\bar{a}$ be the average extension of a crack per loading cycle, and a_c be some critical crack length after which the crack propagates unstably to failure. The subsurface cracks grow in Mode II and Mode III under combined compressive and shear stresses. Linear elastic fracture mechanics is not applicable to the present study due to the large amounts of plastic deformation in the subsurface. Therefore, it is unknown whether under these conditions, $\Delta\bar{a}$, N_c and $\bar{p}$ can be related by Paris's-type law. If a steady state crack propagation is possible, the crack length will be given by $N_c\Delta\bar{a}$. Substituting for N_c from Eq. (8.21) gives:

$$a = N_c\Delta\bar{a} = PVt\left(\frac{\varphi K\Delta\bar{a}}{\bar{h}H}\right) \tag{8.22}$$

Substituting a by a_c gives an expression for the propagation time:

$$t_p = \left(\frac{\bar{h}Ha_c}{\varphi K\Delta\bar{a}}\right)\frac{1}{PV} \tag{8.23}$$

At a given temperature, test geometry, and material properties, the parameters in the brackets are constants. Hence, the propagation time will be inversely proportional to the PV.

8.6 Critical Depth

The experimental observations of subsurfaces, given in Chapter 4, reveal that damage is not accumulated uniformly in the subsurface, but is concentrated in a relatively narrow band at some depth under the surface (Figs 4.9-4.11). This depth for 390-T6 aluminum is in the range 50-80 μm. The question is, why does the damage occur preferentially at some depth if the equivalent stress (Fig. 6.1) is the highest at or very close to the surface.

This question has been addressed in the work of several researchers [16,91,152-155]. Two approaches have been used. Rosenfield [154] has developed a fracture mechanics model in which a crack propagates in the subsurface under combined shear and compression. There is internal friction between the faces of the crack which retards its propagation. The stress intensity is expressed as:

$$K_{II} = f(\sigma_{ry} - \mu\sigma_r) \tag{8.24}$$

where σ_r is the normal compressive stress across the faces of the crack, σ_{ry} is the shear stress driving the crack, and μ is the internal coefficient of friction. For the contact geometry typical for the present study, both stresses involved decrease roughly as $1/r$ where r is the distance from the contact spot. The combination of this result with the strength gradient existing in the subsurface results in a critical depth below which the cracks will propagate faster. This simple model was originally derived for brittle materials with preexisting cracks. In two other papers [152,155] it was developed further to cover the behavior of ductile materials, which do not form cracks easily. Instead of a crack, the existence of a shear instability region where shear plastic deformation occurs preferentially was postulated.

An alternative approach was used by Alpas et al. [91] to study the damage accumulation in very ductile materials (pure copper). They based their method on the results of Rice and Tracey [156] for the enlargement of voids in triaxial stress fields. According to this analysis, the rate of voids enlargement can be described by the relationship:

$$\dot{D}(z) = \underbrace{\left[\gamma + 0.558 \sinh\left(\frac{3}{2}\frac{\sigma_m(z)}{\sigma_f(z)}\right)\right]}_{G(z)} \dot{\varepsilon}(z) D(z) \tag{8.25}$$

where $G(z)$ is the growth factor, γ is a constant between 1 and 2, $D(z)$ is the size of the void, σ_f if the flow stress of the material, σ_m is the hydrostatic component of the applied stress and $\dot{\varepsilon}$ is the strain rate. All of these are functions of the depth below the surface z. In the plastically deformed region, the applied stress at a point, σ_e, must be equal to the flow stress of the material σ_f. As stated earlier, at any given time of contact, the plastically deformed regions are far from each other, and the state of stress within each region is assumed independent of the state of stress in the rest of the subsurface. Therefore, at a point within the region, the stresses σ_e and σ_m will be both linearly proportional to the surface pressure p applied over the contact strip of width ($2a$). The ratio σ_m/σ_e is not a function of p and depends only on the relative position (x/a, z/a) of that point with respect to the center of the contact strip. A plot of the growth factor as a function of z for two positions on the surface is shown in Fig. 8.8. The values of σ_e and σ_m are calculated as:

$$\sigma_e = \frac{1}{\sqrt{2}}\sqrt{(\sigma_{xx}-\sigma_{yy})^2 + (\sigma_{yy}-\sigma_{zz})^2 + (\sigma_{zz}-\sigma_{xx})^2 + 6(\sigma_{xy}^2 + \sigma_{yz}^2 + \sigma_{zx}^2)} \tag{8.26}$$

$$\sigma_m = \frac{1}{3}(\sigma_{xx} + \sigma_{yy} + \sigma_{zz}) \tag{8.27}$$

where the stresses σ_{ii} are calculated with the aid of Eqs. (6.2)-(6.8). The plot shows that the growth factor directly under the contact, where the plastic deformation is the highest, decreases sharply close to the surface. Away from the contact this behavior is reversed - the factor increases toward the surface.

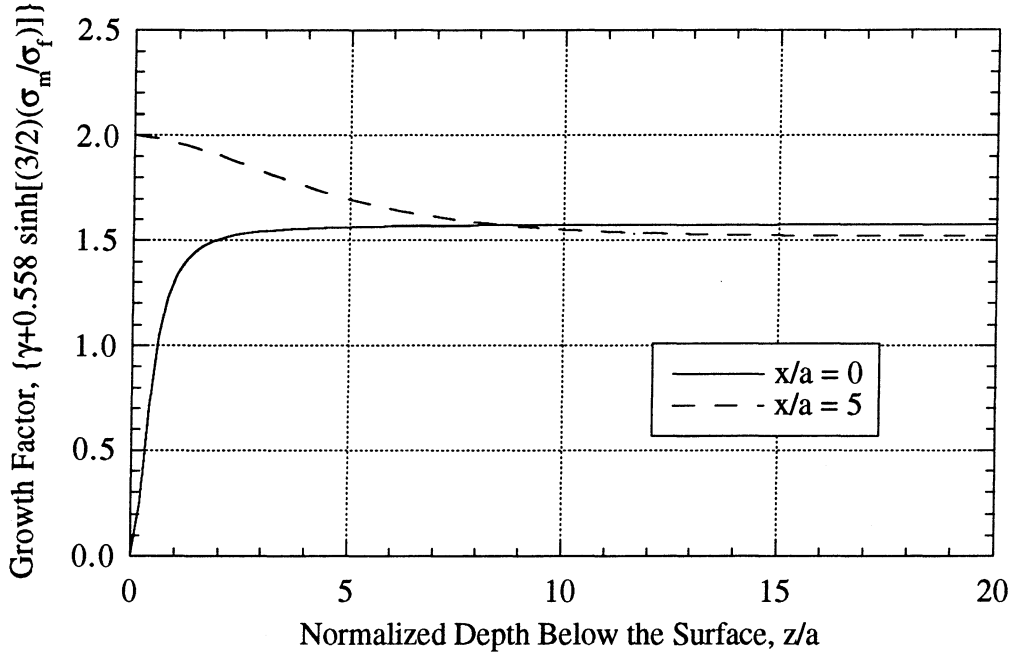

Fig. 8.8 - Damage growth factor as a function of relative depth below the surface

Equation (8.25) can be combined with Eq. (6.20) to give the void enlargement rate as a function of the applied stress. This results in the following equation:

$$\dot{D}(z) = \underbrace{\left[\gamma + 0.558\ \sinh\left(\frac{3}{2}\frac{\sigma_m(z)}{\sigma_e(z)}\right)\right]}_{G(z)} \dot{\varepsilon}_0 \left[\frac{\sigma_e(z)}{\sigma_0}\right]^{\frac{1}{n(z)}} D(z) \tag{8.28}$$

Note that the strain rate sensitivity factor n depends on the strain and, therefore, on the depth below the surface. The above relationship can be normalized with respect to the critical depth z_c where the damage is accumulated the fastest. For the same size preexisting void $D(z)$, the relative likelihood for damage accumulation as a function of depth will be given as:

$$\frac{\dot{D}(z)}{\dot{D}(z_c)} = \frac{G(z)}{G(z_c)}\left[\frac{\sigma_e(z)}{\sigma_0}\right]^{\frac{1}{n(z)}}\left[\frac{\sigma_0}{\sigma_e(z_c)}\right]^{\frac{1}{n(z_c)}} \tag{8.29}$$

As discussed in Section 6.3, there are insufficient data to obtain the functional relationship between n and ε and, consequently, between n and z. For the purpose of a qualitative illustration, similar to the approach taken in Section 6.3, this functional relationship is substituted by the depth dependence of the yield strength σ_0 on z, while n is assumed constant. The yield strength σ_0 in Eq. (8.29) is approximated by $H/3$. The functional dependence $H = H(z)$ is taken from the literature [92]. This leads to Eq. (8.30) which plot is given in Fig. 8.9.

$$\frac{\dot{D}(z)}{\dot{D}(z_c)} = \frac{G(z)}{G(z_c)}\left[\frac{\sigma_e(z)}{\sigma_e(z_c)}\frac{H(z_c)}{H(z)}\right]^{\frac{1}{n}} \tag{8.30}$$

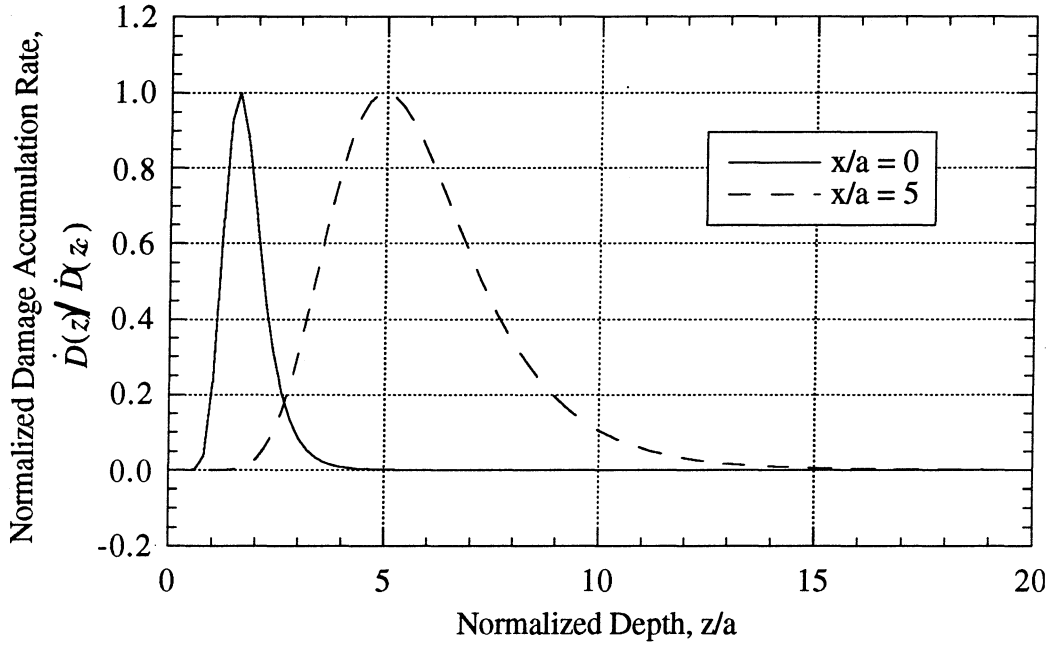

Fig. 8.9 - Likelihood of damage accumulation as a function of depth

The results in Fig. 8.9 are again a qualitative illustration. In addition, Eq. (8.25) can be applied only for very ductile materials. It is also unclear how the dynamic recrystallization will affect the enlargement of voids.

Another illustration of the damage accumulation process in the subsurface is given in Fig. 8.10. It combines the data from Fig. 8.9 with an arbitrary plot for plastic strain accumulation, resembling qualitatively the data presented in Section 4.3. These two outline the boundaries of the critical zone in which cracks are the most likely to initiate and propagate to failure. Both the critical strain at which cracks and/or voids are assumed to initiate and the values for the plastic strain at various depths are chosen arbitrarily for the purpose of a qualitative illustration. Figure 8.10 also provides an illustration of the distance h_c the material has to travel in order to leave the critical zone. The presence of a transformed layer is not taken into account in this illustration.

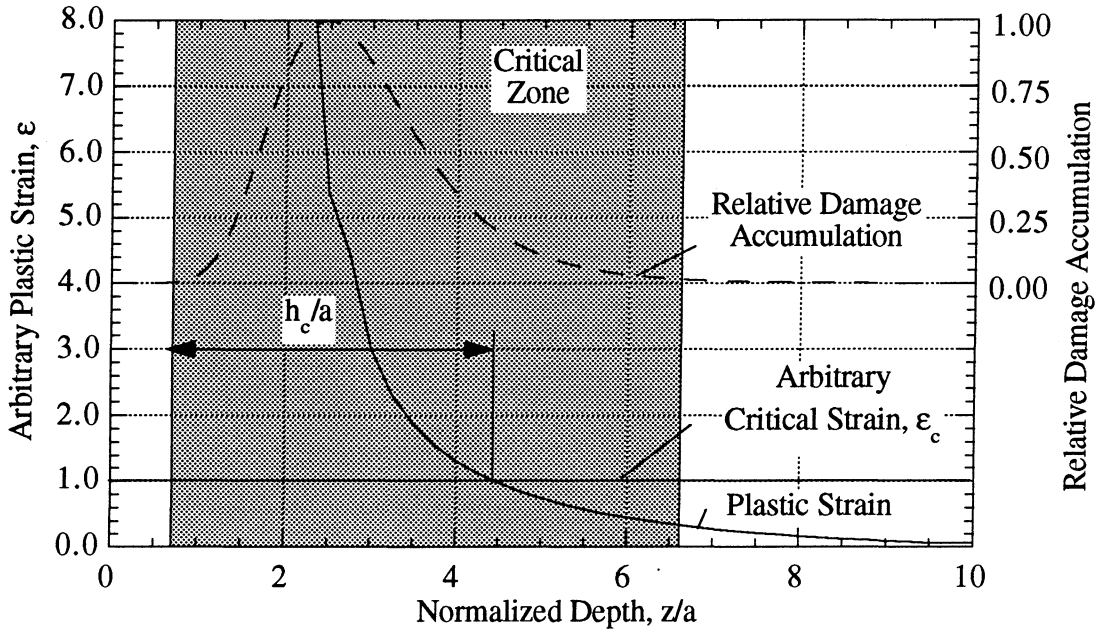

Fig. 8.10 - Illustration of the critical zone of highest damage accumulation

8.7 Total Life to Failure

Combining equations (8.15) and (8.23) gives the total time necessary to initiate and propagate a crack to failure.

$$t_d = t_i + t_p = \left(\frac{\varepsilon_c \bar{h} HE'}{K\bar{p}\beta\sum\bar{\varepsilon}_i}\right)\frac{1}{PV} + \left(\frac{\bar{h} H a_c}{\varphi K \Delta\bar{a}}\right)\frac{1}{PV} \tag{8.31}$$

For scuffing, the above sum must be larger than the time necessary for the most damaged material to leave the zone where the conditions are the most severe. Let h_c be the vertical distance, relative to the surface, which this material has to travel in order to leave the critical zone. Then the critical time will be given as $t_h = h_c/\dot{h}$. Substitution of this expression and equation (8.31) in equation (8.1) yields the final form of the simplified criterion for scuffing:

$$\left(\frac{\varepsilon_c \bar{h} HE'}{K\bar{p}\beta\sum\bar{\varepsilon}_i}\right)\frac{1}{PV} + \left(\frac{\bar{h} H a_c}{\varphi K \Delta\bar{a}}\right)\frac{1}{PV} \le \frac{h_c}{\dot{h}} \tag{8.32}$$

or

$$PV \ge \frac{H\bar{h}\dot{h}}{Kh_c}\left(\frac{\varepsilon_c E'}{\bar{p}\beta\sum\bar{\varepsilon}_i} + \frac{a_c}{\varphi\Delta\bar{a}}\right) \tag{8.33}$$

The above equation incorporates the effects of temperature, material properties, contact of rough surfaces and time. The effect of temperature is included indirectly in the values of $\sum\bar{\varepsilon}_i$ and $\Delta\bar{a}$. Note that they are both functions of $\bar{p}$, but the relationships are non-linear and quite complex.

$$\sum\bar{\varepsilon}_i = f(\bar{p}) \quad \text{and} \quad \Delta\bar{a} = f(\bar{p}) \tag{8.34}$$

When the temperature is increased $\sum\bar{\varepsilon}_i$ and $\Delta\bar{a}$ will also increase for the same value of $\bar{p}$.

The material properties are taken into account in several of the parameters given in Eq. (8.33). The critical strain ε_c and critical crack length a_c are clearly material properties. However, the relationships (8.34) are also influenced by the material properties. Parameters such as the yield strength of the material at the given temperature, the ability of the material to strain-harden, and the sensitivity to strain rate are included in Eq. (8.34). The parameters $\bar{p}$ and β characterize the contact of the surfaces. The latter are influenced by the surface roughness, presence of soft films and/or lubricant. If all the parameters on the right-hand side of Eq. (8.32) are constant this equation will produce the experimentally observed $PV = const$ curve. However, the parameters included in Eq. (8.33) are not easy to obtain experimentally. There are insufficient data to verify the predictions of Eq. (8.33) directly. Data for the critical strain, the average crack extension per

cycle and the critical crack length are not available. Clearly, further research for materials characterization is necessary.

Using Archard's law, the substitution $\dot{h} = KPV/H$ can be made. Then equation (8.33) can be further simplified to provide a relationship which can be used as a scuffing criterion at the given PV.

$$\frac{h_c}{\bar{h}} \geq \left(\frac{\varepsilon_c E'}{\bar{p}\beta \sum \bar{\varepsilon}_i} + \frac{a_c}{\varphi \Delta \bar{a}} \right) \tag{8.35}$$

8.8 Explanation of the Experimentally Observed Phenomena

The proposed criterion can explain the experimentally observed phenomena in this study. However, at the present state of our knowledge, its application must be limited to the test conditions and experimental procedures used in this study. In principle it is not limited to dry sliding, nor to aluminum/steel contacts. However, the extension of its applicability must be based on additional experimentation. The explanation of the phenomena characterizing the scuffing process is given below.

a. Effect of the material.

Material properties play a central role in the proposed criterion. They determine the rate of damage accumulation and provide the critical levels of damage that can be tolerated. The response of the material to strain hardening and high strain rates is also included.

b. $PV = const$ relationship.

Both the initiation t_i and the propagation t_p times, as a first approximation, are inversely proportional to the PV. The plastic strain accumulation is a very non-linear process. It is possible that most of the strain will be accumulated early in the contact which makes this process insensitive to the duration of the contact. On the other hand, the average strain in the subsurface is proportional to the number of contacts per unit time. This is the reason why the initiation time is often inversely proportional to the PV. The propagation time is inversely proportional to the PV because the number of loading cycles is determined by the PV. In ductile materials most of the life to failure is probably taken by the initiation process. Conversely, more brittle materials may form cracks early in the process of scuffing, while most of the time to failure is taken by crack propagation.

c. Deviations from the $PV = const$ relationship.

The PV product is proportional to the number of loading cycles. Therefore, failure at a constant PV indicates constant damage accumulation per loading cycle. The amount of damage per

cycle is determined by complex relationships between the local stresses, temperatures, and material properties and may not always be constant. In the scuffing criterion this is accounted for by the parameters $\sum \varepsilon_i$ and $\Delta \bar{a}$, which are indirectly dependent on the PV through the duration of the loading cycle and the local (flash) temperature. If this dependence is weak, failure will occur at $PV = const.$ However, if the dependence of these parameters on the PV is stronger the amount of subsurface damage per cycle will not be constant, and deviations from the $PV = const$ curve will occur.

d. Temperature dependence.

Both the amount of accumulated plastic strain and the crack extension per cycle are functions of temperature. The flow stress of the material decreases with temperature which results in increased plastic deformation. The crack growth rate also increases with temperature. The temperature dependence is indirectly included in the functional relationships between the parameters $\sum \varepsilon_i$, $\Delta \bar{a}$ and the equivalent stress σ_e .

e. Size effects.

The proposed criterion does not require constant bulk or surface temperature at scuffing. The scuffing condition is related both to the local material properties which are dependent on temperature, but also on the number of loading cycles which do not have a direct relation to temperature. Hence, this criterion does not have difficulties dealing with different size specimens because it is not associated with a critical temperature condition.

f. Time effects.

The time effects can also be explained because the proposed criterion is based on a damage accumulation model. The criterion is built by comparing the times for crack initiation t_i and propagation t_p to the time t_h the material is within a critical zone of fastest damage accumulation. Hence, the time effects are intrinsic to the criterion.

g. Effect of the loading history.

The criterion is based on damage accumulation. Hence, in principle, it can explain the loading history effects. However, a more complicated expression for the criterion involving the sum of the damage accumulated in each period must be used. A rule for damage accumulation must also be chosen. The ability of the material to withstand much higher PV's in a stepwise loading is explained through the parameters $\bar{p}$ and β, characterizing the distribution of surface pressures and contact areas. Note that these parameters will not be the same for a stepwise and immediate loading conditions because the initial low loading steps help the formation of protective films. Initial smoothening of the contact surfaces may also occur. These effects, however, may not be the primary reason for the effect of the loading history. Another factor, which is the

dynamics of the transformed layer formation, may be more important. A relatively thick transformed layer may "shield" the material below it from the high contact pressures and tangential tractions. Such a thick transformed layer can be formed during the lower load steps. The dynamics of the formation of transformed layers is not included in the scuffing criterion, which is one of its major disadvantages.

h. Effect of the environment

The presence of R134 a results in the generation of solid lubricants on the surface of the specimens. The effect of these lubricants is to reduce $\bar{p}$ and to increase β. This leads to lower subsurface strain rates. The process of strain accumulation becomes less non-linear and the supposition that most of the strain is accumulated in the beginning of the contact period is no longer true. Strain accumulation becomes dependent on the duration of the contact periods. Since the duration of the loading cycles is longer at higher pressures (Fig. 8.7), the conditions of the high pressure end of the PV curve will be more detrimental.

8.9 Summary

The existing hypotheses for scuffing cannot explain some of the phenomena observed at scuffing and contradict some of the experimental data. A new hypothesis for scuffing is proposed which overcomes some of these difficulties. The hypothesis is a generalization of the critical strain and subsurface fatigue hypotheses. The derivation involves a series of simplifications for the initiation and propagation of cracks. The proposed hypothesis for scuffing is not limited to dry sliding conditions or to aluminum/steel contacts. However, further experimentation is necessary to validate its applicability outside of the range of experimental conditions used in this study. More experimentation is also necessary for the characterization of the local material response under sliding conditions. The major results obtained in this chapter can be summarized as follows:

a. A new hypothesis for scuffing is proposed.

The new hypothesis suggests the following sequence of events leading to scuffing:

(1) Accumulation of plastic deformation in the subsurface.

(2) Nucleation of cracks and voids.

(3) Propagation of cracks.

(4) Formation of cold welds.

b. A criterion for scuffing is derived.

The criterion for scuffing is given as:

$$\underbrace{\left(\frac{\varepsilon_c \bar{h} H E'}{K \bar{p} \beta \sum \bar{\varepsilon}_i}\right)\frac{1}{PV}}_{t_i} + \underbrace{\left(\frac{\bar{h} H a_c}{\varphi K \Delta \bar{a}}\right)\frac{1}{PV}}_{t_p} \leq \underbrace{\frac{h_c}{\dot{h}}}_{t_h}$$

c. The criterion for scuffing provides a qualitative explanation of the experimental results.

The effects of the material, temperature, contact geometry, time, loading history, and type of environment can, in principle, be explained with the proposed criterion.

d. The proposed criterion needs further experimental verification.

The criterion for scuffing cannot be verified quantitatively because many of the parameters characterizing the response of the material to stress, temperature, and high strain rate under sliding conditions are not available. Further experimentation for material characterization is necessary.

e. The proposed hypothesis is not limited to dry sliding conditions and aluminum/steel contacts.

CHAPTER 9
CONCLUSIONS

Scuffing is a complex phenomenon, involving mechanical, thermal and chemical interactions between the contacting bodies, the environment, the lubricant, and other species found at the sliding interface. This is the reason why, in spite of the large number of investigations conducted in the last sixty years, this phenomenon is still poorly understood. Even the simpler case of scuffing under dry sliding conditions is very controversial. While there is an agreement that the formation of large areas of bare metal and extensive adhesion are characteristic for the final stage of the process, the exact mechanisms leading to this condition are still debated. One of the least studied and understood aspects of scuffing is the mechanism of failure of the surface and/or subsurface material, which enables the formation of large adhesive bonds. The present study concentrates primarily on this aspect of the process. A new hypothesis and its corresponding criterion for scuffing are proposed. The proposed hypothesis is based on the experimental findings of this study and on several models describing surface mechanical and thermal interactions. Although, derived from the scuffing behavior of aluminum/steel contacts under dry sliding conditions, it is possible that this hypothesis has a wider applicability.

9.1 Research Summary

The present research focuses on two major goals. The first is to obtain a more complete set of experimental data for the scuffing behavior of several aluminum alloys. The second goal is to study the physics of the scuffing phenomenon, evaluate the existing hypotheses for scuffing and explore the prospective for a theoretical description of scuffing. The work conducted in this study to attain these goals is summarized below.

a. Experimental studies.

The experiments in this study are conducted in a specially designed tribometer, which allows accurate control of the environmental conditions. An area contact (two pins-on-disk) geometry is used to study scuffing. Three combinations of pin sizes and sliding radii are tested. Five materials are used for the pins. These are commercially pure aluminum 1100, die cast hypereutectic silicon-aluminum alloy (390-T6), extruded Bi-containing eutectic silicon-aluminum alloy (DHT-3), 1018 steel, and Si-Pb brass. These materials are slid under dry sliding conditions against 1018 carburized steel disks. The environment for the tests is either air, or R134a. Most of the tests are conducted at a constant sliding velocity, while the load is increased stepwise.

The instrumentation used to identify scuffing provides run-time records for the coefficient of friction, subsurface temperature, wear, electric contact resistance, and load history. Computer control of the test rig and specially developed software provide the desired load and velocity sequences.

The mechanisms leading to scuffing under dry sliding conditions are studied by the examination of surfaces, subsurfaces and wear debris and by the quantitative measurements of the average subsurface plastic deformation and the thickness of surface layers. The surfaces of the specimens are examined by optical and electron microscopes and X-ray photoelectron spectroscopy. Microscopy is also used to study the generated wear debris and the subsurfaces of specimens undergoing scuffing. The chemical composition of the subsurfaces is studied with Auger electron spectroscopy. The subsurface plastic deformation is measured by testing specimens with brass inserts positioned perpendicular to the direction of motion. After the test, the specimens are cut parallel to the direction of sliding to reveal the deformation of the brass/aluminum interface. The results of the experimental studies can be summarized as follows:

(1) Scuffing under dry sliding conditions is due to a subsurface failure. The processes leading to scuffing seem to involve the following events:
   (a) Accumulation of plastic deformation.
   (b) Formation of voids and cracks in the subsurface.
   (c) Coalescence of voids, propagation of subsurface cracks and removal of sections of the surface.
   (d) Unstable decrease of the load bearing area.
   (e) Removal of protective layers from most of the surface.
   (f) Formation of cold welds.

(2) For the tests conducted in air, at a given environmental temperature, specified contact geometry and loading history, the contact pressure at scuffing decreases with the sliding velocity. For the 1100 and 390-T6 aluminum alloys this relationship can be expressed as $PV = const.$ This curve also represents a constant subsurface temperature condition at scuffing. The PV curves for steel and DHT-3 aluminum deviate from this hyperbolic relationship. For these materials, the PV at scuffing increases with the sliding velocity. From the three aluminum alloys tested, the 390-T6 aluminum showed the highest scuffing resistance. Steel has the highest scuffing resistance of all the materials tested

(3) The scuffing PV of 390-T6 Al decreases with the environmental temperature. The shape of the PV curve, however, remains the same. The effect of increasing the environmental temperature is to shift the curve downward.

(4) Scuffing is strongly system-dependent. Changes in the geometry of the test specimens lead to shifts of the *PV* curve.

(5) Scuffing is a time-dependent phenomenon. Above a certain critical *PV*, the time to scuffing decreases with the *PV*. This suggests that scuffing occurs when a critical amount of damage is accumulated in the material.

(6) The *PV* at which scuffing occurs depends on the previous loading history. The sudden application of the load is more detrimental than the stepwise loading.

(7) The test environment affects scuffing. The scuffing *PV* of 390-T6 aluminum tested under R134a environment deviates significantly from the $PV = const$ curve. At low sliding velocities, scuffing occurs at approximately the same *PV* as in air. At high sliding velocities scuffing occurs at considerably higher *PV*'s than in air. The reason for this behavior is a chemical reaction between aluminum and R134a, which results in the formation of aluminum fluoride and PTFE-like polymers on the surface of the specimens. These act as solid lubricants. The wear rate and the subsurface plastic deformation are lower in R134a environment than in air.

(8) The subsurfaces of specimens tested under dry sliding conditions have three characteristic regions. These are a layer of transformed material, a layer of plastically deformed material, and a layer of undisturbed material. The mechanisms for the formation of the transformed layer are oxidation, material transfer, compaction of fine wear particles, and plastic deformation.

(9) At a constant *PV*, both the thickness of the transformed layer and the amount of plastic deformation increase with time until they reach equilibrium levels. The thickness of the transformed layer and the depth of the plastically deformed region increase with the *PV*.

(10) For the tests conducted in air, the amount of accumulated plastic deformation increases with *PV*. It is constant for a wide range of *P* and *V* combinations, provided that their product remains constant. Under the same load and sliding velocity, the plastic deformation for the tests conducted in R134a environment is lower than the plastic deformation for the tests conducted in air. Under R134a the plastic deformation is not constant along the $PV = const$ curve. It is a stronger function of the contact pressure. These results are based on experiments conducted with 390-T6 Al.

b. Theoretical studies

The main goal of the theoretical studies is to evaluate the existing hypotheses for scuffing and to construct a hypothesis and a criterion which can explain most of the experimentally obtained

results. The theoretical studies are based on a model for the contact of runned-in surfaces and on several models for subsurface stresses, temperatures, and strains.

The problem of finding the local pressures and contact area distributions is solved by developing a model for the contact of runned-in surfaces. This model incorporates a finite element simulation of the contact of rough surfaces, statistical methods for the alignment of surface profiles and analytical correction factors for deviations from the infinite half-space approximation.

The local subsurface stresses, temperatures and strains are estimated by applying several numerical methods. The stresses are calculated on the basis of the infinite half-space approximation and information about the surface pressures and areas of contact. The latter is provided by the finite element method for the contact of runned-in surfaces. The transient subsurface temperatures are calculated with the aid of a simple finite element model. The strains are obtained from a finite difference method and by incorporating empirical relationships from literature sources.

With the aid of the experimental and theoretical results, several hypotheses for scuffing, applicable to sliding under dry conditions, are evaluated. These hypotheses are grouped according to their major assumptions. The first group of hypotheses relates scuffing to a critical temperature condition. The second postulates that scuffing occurs when the shear stress at a critical depth in the material exceeds the shear strength. The third relates scuffing to damage caused by extensive plastic deformation. The predictions of these hypotheses are compared to the experimental observations obtained in this study and to the results from models of surface interactions.

The most promising hypotheses are combined and generalized in the proposed new hypothesis for scuffing. With the aid of several idealizations, this hypothesis is expressed in a scuffing criterion. The proposed scuffing criterion can explain qualitatively most of the experimental results.

The major findings from the theoretical studies can be summarized as follows:

(1) For the conditions of this study, the surface pressure distributions are characterized by few high pressure spikes far apart from each other. The real area of contact increases linearly with the applied load. The maximum and the average contact pressures are weak functions of the load. The maximum pressure initially increases slightly with the load and saturates at about 60% of the scuffing load. The average contact pressure is practically constant for the whole range of test loads. The size of the contact spots increases slowly with the load. However, a sharp increase in the size of the contact spot occurs right before scuffing. Most of the spikes characteristic for the pressure distribution persist for one full revolution of the disk. However, some spikes may change magnitude, or have shorter duration. This illustrates the variability of the loading on a local basis and the presence of loading cycles.

(2) For the conditions of this study, the mechanical and the thermal parts of the solution for the subsurface stresses and temperatures can be decoupled. This is due to the small effect of flash temperatures, which are negligible compared to the bulk temperature. The low flash temperatures are the result of the relatively small heat fluxes and the small constriction thermal resistances, typical for the contact geometry used. The thermal gradients near the surface are higher than the gradients in the bulk. These, however, fail to produce significant temperature differences. The effect of increased flash temperature due to higher sliding velocity at the same PV is also small compared to the bulk temperature.

(3) For aluminum, most of the strain accumulated in a contact period occurs early in the period. The total accumulated strain is a weak function of the period's duration. If annealing and dynamic recrystallization occur between contacts, the accumulated strain is a stronger function of the number of contact periods. The results for the strain accumulated in a single contact period cannot be generalized to account for multiple contacts due to the lack of information for the changes occurring in the material between contacts.

(4) The hypotheses relating scuffing to a critical thermal condition are phenomenological in nature and do not provide an explanation for the mechanism of scuffing. These hypotheses consider a "static" state of the material and cannot explain time and load history effects. Block's flash temperature concept deviates from the experimentally observed data. The results from this study show that the surface temperature at scuffing is not a material property and cannot be used as a criterion. It is dependent on the geometry, the loading conditions, and the environment. The competitive oxide formation and destruction hypothesis is also phenomenological and in its present form cannot describe adequately the complex dynamics of protective films formation and destruction. However, if this dynamics is understood, this hypothesis has a strong potential to describe the events at scuffing. The thermoelastic instability hypotheses have difficulties explaining the effect of the mechanical properties of materials on scuffing. Its results correlate poorly with the experimental data.

(5) The critical shear stress hypothesis is a pioneering approach relating for the first time scuffing to subsurface failure. However, it cannot explain the time and load history effects. Its criterion for subsurface failure is not satisfied for the results of this study. The shear stresses at the critical depths are not high enough to cause the predicted bulk shear failure.

(6) None of the existing hypotheses and criteria for scuffing can explain adequately the experimental results and observations. The hypotheses relating scuffing to subsurface

plastic deformation and subsurface fatigue are the most promising. They are supported by the experimental results and by the observations of subsurfaces of specimens and wear debris. These hypotheses can explain the time effects based on damage accumulation. However, none of these have been developed in enough detail to serve as a scuffing criterion. In their present state, these hypothesis do not go beyond phenomenological correlations. There is no single hypothesis which combines the effects of subsurface plastic deformation and subsurface fatigue.

(7) The proposed hypothesis for scuffing can provide a qualitative explanation of the experimental results. This includes the effects of the material, temperature, contact geometry, time, loading history, and type of environment. At the present time this hypothesis cannot be verified quantitatively because many of the parameters characterizing the response of the material to stress, temperature, and high strain rate under sliding conditions are not available. Further experimentation for material characterization is necessary.

9.2 Major Accomplishments of the Present Study

Several accomplishments of this study contribute to a better understanding of the scuffing phenomenon. Contributions are made in the experimental study of scuffing, in the accumulation of phenomenological test data, and in the theoretical description of scuffing. These are discussed in more detail below.

a. Development of a new hypothesis for scuffing

The most important accomplishment of this study is the development of a new hypothesis for scuffing and its corresponding criterion. In this hypothesis, scuffing is related for the first time to the initiation and propagation of deep subsurface cracks. The observations of subsurfaces of specimens undergoing scuffing provide the proof that these cracks are present before the final adhesive phase of the scuffing process. However, they do not form at PV's lower than the scuffing PV. This suggests the existence of a strong relationship between scuffing and deep subsurface fatigue. The proposed hypothesis also provides an explanation of the existence of several stages of the scuffing process. These stages are associated with the initiation and propagation of subsurface cracks. The gradual removal of whole sections of the load-bearing surface before the final adhesive stage is also a new finding. This mechanism provides the explanation for the unstable and catastrophic growth of the areas of bare metal, leading to the final stage of scuffing.

The proposed hypothesis suggests the following sequence of events leading to scuffing:

(1) Accumulation of plastic deformation in the subsurface.

(2) Nucleation of cracks and voids

(3) Coalescence of voids and propagation of cracks.

(4) Formation of cold welds.

The criterion for scuffing is given as:

$$\underbrace{\left(\frac{\varepsilon_c \bar{h} H E'}{K \bar{p} \beta \sum \bar{\varepsilon}_i}\right)\frac{1}{PV}}_{t_i} + \underbrace{\left(\frac{\bar{h} H a_c}{\varphi K \Delta \bar{a}}\right)\frac{1}{PV}}_{t_p} \leq \underbrace{\frac{h_c}{\dot{h}}}_{t_h}$$

where t_i and t_p are the times for initiation and propagation of deep subsurface cracks and t_h is the time the material is within the critical zone of fastest damage accumulation.

The proposed hypothesis is based on the experimental data from this study. However, it may have a wider applicability. There are some indications that subsurface fatigue is the mechanism responsible for scuffing under starved lubrication conditions. At the very least, scuffing due to extensive subsurface plastic flow and fatigue is a possibility which must be considered for any sliding system where scuffing occurs.

b. Reliable reproduction and identification of scuffing under laboratory conditions.

The experimental data on scuffing reported in the literature are plagued by inconsistencies. These are partly due to the difficulties associated with the identification of scuffing under laboratory conditions. The contribution of this study to solving this problem is the development of a test setup in which the scuffing condition can be reproduced and identified reliably. This includes the development of a proper test procedure and the installation of special instrumentation. The major achievements in this respect are:

(1) Simultaneous monitoring of friction, wear, temperature and electric contact resistance.

(2) Installation of a high-accuracy contact resistance measurement circuit

c. A more complete set of experimental data for the scuffing behavior of aluminum/steel contacts.

The present study provides the most complete picture of the effect of various factors on the scuffing of aluminum. Some of these effects are investigated for the first time. In addition, data for the wear, bulk temperature, and heat partitioning at the interface are obtained. These provide a

better understanding of the conditions at scuffing. A summary of the contributions of this study to the experimental database on scuffing of aluminum is given below:

(1) The scuffing behavior of a Bi-containing aluminum alloy is studied for the first time

(2) The effect of the specimens size is studied for the first time

(3) Quantitative data for the time and loading history effects on scuffing are obtained

(4) The effect of the refrigerant environment is studied for the first time

(5) A more complete set of data for the scuffing of 390 Al is obtained

d. Development of a model for the contact of runned-in surfaces

Finite elements methods for rough surfaces interactions and methods for statistical alignments of surface profiles are both well known and described in detail in the literature. However, there are no reports for the combined use of these methods. Their simultaneous use opens the possibility to solve the problem for the contact of runned-in surfaces. Several minor improvements to the existing methods are also made. The most important among these is the simpler and better method to make corrections for edge effects.

e. Strain-rate and non-linear strain accumulation effects

The equilibrium stress-strain curves reported in the literature fail to explain the accumulation of plastic deformation on a local basis, especially close to the surface. On the other hand, the predictions of the simple model based on strain sensitivity, developed in this study, are at least qualitatively correct. This points to the importance of the strain rate effects. These have not been discussed previously in the studies related to sliding contacts.

Due to the strain rate effects, the accumulation of plastic deformation is strongly non-linear. This non-linearity results in a weak dependence of strain on the duration of the contact period. This helps to explain the experimentally observed constant average subsurface plastic deformation along the $PV = const$ curve.

9.3 Recommendations for Future Research

The present study addresses few of the problems associated with scuffing. The more general picture of this process is clearly incomplete. Three possibilities for future research in the area of scuffing of materials are discussed below.

a. Local response of materials to high stress, temperature and strain rate.

It seems that the major missing piece of information characterizing scuffing under dry sliding conditions is the response of materials under conditions of high stress, temperature, and

strain rate. This includes the development of plastic deformation on a local basis, mechanisms for crack initiation, and crack growth rates. Continuum mechanics of materials and conventional fracture mechanics may fail to provide these answers. It seems that local stress and strain concentrations and other micro-mechanical considerations must be incorporated in the future models. The question of the critical depth of damage accumulation is also a possibiility for future research.

b. Study of the dynamics of surface films formation and destruction.

All the present models for the formation of protective films on contact surfaces are based on static oxidation or other static chemical reaction rates. The effects of material transfer, debris accumulation and plastic deformation are only qualitatively recognized. There aren't any theoretical models of these processes. The experimental study of these processes is also in a very early stage. The effect of macroscopic parameters such as sliding velocity, contact pressure and temperature on the rates of formation of these films has not been studied sufficiently even on a phenomenological level. Clearly, this represents a vast area for future research.

c. Study of the more general case of scuffing under lubricated conditions.

The present study addresses the simpler problem of scuffing under dry sliding conditions. The general problem of scuffing under lubricated conditions is far more complex and less understood. The mechanisms of material failure at scuffing under lubricated conditions is a problem which has not been addressed. The effect of the lubricant on the thermal state of the surface is largely unknown. The local load-shearing mechanisms between the lubricant and the asperities and the ability of the lubricant to distribute the load more evenly over the apparent area of contact are also poorly understood. These are just a few of the problems which must be addressed in the future studies associated with the general case of scuffing under lubricated conditions.

REFERENCES

1 Cameron, A., "On a Generalized Theory of Scuffing", Proc. 12th Leeds-Lyon Symposium on Tribology, The Institut National des Sciences Appliquées, Lyon, France, 3-6 September 1985, 3-9.

2 Konishi, T., Klaus, E. E. and Duda, J. L., "Wear Characteristics of Aluminum-Silicon Alloy Under Lubricated Sliding Conditions", *Tribology Transactions*, 39 (1996), .

3 Houpert, L. G. and Hamrock, B. J., "Elastohydrodynamic Lubrication Calculations Used as a Tool to Study Scuffing", Proc. 12th Leeds-Lyon Symposium on Tribology, The Institut National des Sciences Appliquées, Lyon, France, 3-6 September 1985, 146-155.

4 Spikes, H.A. and Cameron, A., "Scuffing as a Desorption Process - an Explanation of the Borsoff Effect", *ASLE Transactions*, 17 (1974), 92-96.

5 Cuotiongco, E. C. and Chung, Y. W., "Prediction of Scuffing Failure Based on Competitive Kinetics of Oxide Formation and Removal: Application to Lubricated Sliding of AISI 52100 Steel on Steel", *STLE, Tribology Transactions*, 37:3 (1994), 622-628.

6 Greenwood, J. A. and Williamson, B.P., "Contact of Nominally Flat Surfaces", *Proc. R. Soc. London, Ser A*, 295 (1966), 300-319.

7 Hirst, W. and Hollander, A. E., "Surface Finish and Damage in Sliding", *Proc. R. Soc. London, Ser A*, 337 (1974) 379-394.

8 Bushe, N. A. and Fedorov, S. V., "State and Properties of the Frictional Contact of Metals Under Conditions of Seizure" (the translation is ours), *Trenie i Iznos*, 12 (1991) 1, 46-55.

9 McCool, J. I. and Popgoshev, D., "Effect of Asperity Interaction on Scuffing", Proc. 12th Leeds-Lyon Symposium on Tribology, The Institut National des Sciences Appliquées, Lyon, France, 3-6 September 1985, 135-145.

10 McFarlane, J.S. and Tabor, D., "Relation Between Friction and Adhesion", *Proc. R.Soc.London, Ser A*, 202 (1950), 244-253.

11 Green, A.P., "Friction Between Unlubricated Metals: A Theoretical Analysis of the Junction Model", *Proc. R. Soc. London, Series A*, 228 (1954), 191-204.

12 Edwards, C.M. and Halling, J., "Experimental Study of the Plastic Interaction of Model Surface Asperities During Sliding", *Journal of Mechanical Engineering Science*, 10 (1968) 2, 121-132.

13 Kayaba, T. and Kato, K., "Experimental Analysis of Junction Growth With a Junction Model", *Wear*, 51 (1978), 105-116.

14 Mishina, H. and Sasada, T., "Observation of Micro-Structure in Seized Portion and Mechanism of Seizure", *Transactions of the ASME, Journal of Tribology* 108 (1986) 1, 128-133.

15 Enthoven, J. and Spikes, H. A., "Infrared and Visual Study of the Mechanisms of Scuffing", *STLE Tribology Transactions*, 39 (1996) 2, 441-447.

16 Somi Reddy, A., Pramila Bai, B. N., Murthy, K. S.S., and Biswas, S. K., "Mechanism of Seizure of Aluminum-Silicon Alloys Dry Sliding Against Steel", *Wear*, 181-183, (1995), 658-667.

17 Wear Control Handbook, Peterson, and Winer editors, Glossary of Terms and Definitions in the Field of Friction, Wear and Lubrication, p. 1182.

18 Glossbrenner, E.W., "The Life and Times of an A-Spot", A Tutorial on Sliding Contacts, Proceedings of the IEEE-Holm Conference, October, 1992.

19 Holm, R., "Electric Contacts. Theory and Applications", Springer-Verlag, New York, 1967.

20 Renji, Z., Baoliang, Z., Jiajun, L., Zhouping, C., and Qi, S., "Mutual Transfer of Materials for Dry Sliding of Brass Against Stainless Steel", *Wear*, 140 (1990) 207-222.

21 Davis, F. A. and Eyre, T. S., "The Effect of Silicon Content and Morphology on the Wear of Aluminum-Silicon Alloys Under Dry and Lubricated Sliding Conditions", *Tribology International*, 27 (1994), 3, 171-181.

22 Rigney, D.A., Chen, L.H., and Naylor, G.S., "Wear Processes in Sliding Systems", *Wear*, 100 (1984), 195-219.

23 Ludema, K. C., "A Review of Scuffing and Running-in of Lubricated Surfaces, With Asperities and Oxides in Perspective", *Wear*, 100 (1984), 315-331.

24 Dyson, A., "Scuffing - a Review, Part 1", *Tribology International* 8 (1975) 4, 77-87.

25 Dyson, A., "Scuffing - a Review, Part 2", *Tribology International* 8 (1975) 6, 117-125.

26 CRC Handbook of Lubrication, Booser, E.R. editor, Vol. II Theory and Design, CRC Press Inc., Boca Raton, 1984, p.464.

27 ASM Specialty Handbook, Aluminum and Aluminum Alloys, Davis, J.R. editor, ASM International, Materials Park, Ohio, 1993.

28 Rohatgi, P. K., Liu, Y., and Ray, S., "Friction and Wear of Metal-Matrix Composites", in ASM Handbook Vol. 18, Friction, Lubrication and Wear Technology, Davis, J.R. editor, ASM International, Materials Park, Ohio, 1992.

29 Jorstad, J.L., "Aluminum Lightweight Castings - Some Cost Saving Ideas", Paper No. 770332, SAE Automotive Engineering Congress, Society of Automotive Engineers, 1977.

30 Tiwari, S. N., Pathak, J. P., and Malhotra, S. L., "Seizure Resistance of Leaded Aluminum Bearing Alloys", *Materials Science and Technology*, 1 (1985), 1040-1045.

31 Ni, X. and Cheng, H. S., "Seizure Resistance of Aluminum-Lead-Silicon Connecting Rod Bearings and Nodular Cast Iron Shafts", *STLE Tribology Transactions*, 39 (1996) 1, 121-129.

32 Ni, X. and Cheng, H. S., "Seizure Failure of Copper-Lead with Overlay and Aluminum-Tin Connecting Rod Bearings", *STLE Tribology Transactions*, 39 (1996) 1, 194-200.

33 Sarkar, A. D., "Wear of Aluminum-Silicon Alloys", *Wear*, 31 (1975), 331-343.

34 Torabian, H., Pathak, J. P. and Tiwari, S. N., "Wear Characteristics of Al-Si Alloys", *Wear*, 171 (1994), 49-58.

35 Hanna, A. H. and Shehata, F., "Friction and Wear of Al-Si Alloys", *Lubrication Engineering*, 49, (1992), 473-476.

36 Ferrante, J. and Brainard W. A., "Wear of Aluminum and Hypoeutectic Aluminum-Silicon Alloys in Boundary Lubricated Pin-on-Disk Sliding", NASA Technical Paper 1442, (1979).

37 Okabayashi, K. and Kawamoto, M., "Influences of Silicon Content and Grain Size of Primary Silicon Crystals on the Wear of High Silicon Aluminum Alloys", *Bulletin of University of Osaka Prefecture*, 19 (1968), 199-216.

38 Jasim, M. K. and Dwarakadasa, E. S., "Wear in Al-Si Alloys Under Dry Sliding Conditions", *Wear*, 119 (1987), 119-130.

39 Somi Reddy, A., Pramila Bai, B. N., Murthy, K. S.S., and Biswas, S. K., "Wear and Seizure of Binary Al-Si Alloys", *Wear*, 171 (1994), 115-127.

40 Barber, G. C., Matthews, J. J. and Jaffry, S., "Wear and Scuff Resistance of Aluminum 390", *Lubrication Engineering*, 47 (1991), 423-430.

41 Blok, H., "Theoretical Study of Temperature Rise at Syrfaces of Actual Contact Under Oiliness Conditions", *Inst. Mech. Eng. General Discussion on Lubrication*, 2 (1937), 222-235.

42 Hardy, W.B. and Doubleday, I., "Boundary Lubrication - The Paraffin Series", *Proc. Roy. Soc., London*, A 100 (1921), 550-574.

43 Hardy, W.B. and Doubleday, I., "Boundary Lubrication - The Temperature Coefficient", *Proc. Roy. Soc., London*, A 101 (1922), 487-492.

44 Bowden, F.P. and Tabor, D., "The Friction and Lubrication of Solids, Part 1", Clarendon Press, Oxford, 1950.

45 Polonskyi, Yu. Z., "On the Concept of Metal Seizure and its Applications", *Trenie i Iznos*, 12 (1991) 2, 258-266.

46 Grubin, A.N., "Fundamentals of the Hydrodynamic Theory of Lubrication of Heavily Loaded Cylindrical Surfaces", in Investigation of the Contact Machine Components, Ketova, K.F. editor, Translation of Russian Book No. 30, Central Institute for Technology and Mechanical Engineering, Moscow, 1949.

47 Dyson, A., "The Failure of Elastohydrodynamic Lubrication of Circumferentially Ground Disks", *Proc. Inst. Mech. Eng.*, 190 (1976) 1, 52-76.

48 Tallian, T., McCool, J.I., and Sibley, L.B., "Partial Elastohydrodynamic Lubrication in a Rolling Contact", *Proc. Inst. Mech. Eng.*, 180 (1965) 3B, p. 238.

49 Berthe, D., Flamand, L., Foucher, D., Hassoun, M., and Codet, M., "Theoretical and Experimental Load Division in an EHD Contact", *Proc. 4-th Leeds-Lyon Symposium on Tribology*, 1977, p. 239.

50 Cheng, H.S., "Micro-Elastohydrodynamic Lubrication", *NASA International Conference on Tribology in the 80's*, Vol. II (1984), 615-629.

51 Cheng, H.S. and Dyson, A., "Elastohydrodynamic Lubrication of Circumferentially Ground Disks", *ASLE Transactions*, 21 (1978) 1, 25-40.

52 Lee, Y. and Ludema, K. C., "The Effects of Surface Roughening and Prospective Film Formation on Scuff Initiation in Boundary Lubrication", *Transactions of the ASME, Journal of Tribology*, 113 (1991) 4, 295-302.

53 Czichos, H., "Failure Modes of Sliding Lubricated Concentrated Contacts", *Wear*, 28 (1974), 95-101.

54 Begelinger, A. and De Gee, A.W.J., "On the Mechanism of Lubricant Film Failure in Sliding Concentrated Steel Contacts", *Transactions of the ASME, Journal of Lubrication Technology*, 10 (1976), 575-579.

55 Begelinger, A. and De Gee, W. J., "Thin Film Lubrication of Sliding Point Contacts of ANSI 52100 Steel", *Wear*, 28 (1974), 103-114.

56 Salomon, G., "Failure Criteria in Thin Film Lubrication - The IRG Program", *Wear*, 36 (1976), 1-6.

57 Begelinger, A. and De Gee, A. W., "Lubrication of Sliding Point Contacts of ANSI 52100 Steel - The Influence of Curvature", *Wear* 36 (1976), 7-11.

58 Czichos, H., "Failure Criteria in Thin Film Lubrication: Investigation of the Different Stages of Film Failure", *Wear*, 36 (1976), 13-17.

59 Bollani, G., "Failure Criteria in Thin Film Lubrication With EP Additives", *Wear*, 36 (1976), 19-23.

60 Föhl, J. and Uetz, H., "Failure Criteria in Thin Film Lubrication - Influence of Temperature on Seizing, Wear and Reaction Layer Formation", *Wear*, 36 (1976), 25-32.

61 Park, K.B., and Ludema, K.C., "Evaluation of the Plasticity Index as a Scuffing Criterion", *Wear*, 175 (1994) 123-131.

62 Kim, K. and Ludema, K.C., "A Correlation Between Low Cycle Fatigue Properties and Scuffing Properties of 4340 Steel", *Transactions of the ASME, Journal of Tribology*, 117 (1995) 10, 617-621.

63 Suh, N.P., "The Delamination Theory of Wear", *Wear*, 25 (1973) 111-124.

64 Lee, S.C. and Cheng, H.S., "Correlation of Scuffing Experiments With EHL Analysis of Rough Surfaces", *Transactions of the ASME, Journal of Tribology*, 113 (1991) 4, 318-326.

65 Davis, B., Sheiretov, T.K., and Cusano, C., "Tribological Evaluation of Contacts Lubricated by Oil-Refrigerant Mixtures", 1992 International Compressor Engineering Conference at Purdue, Purdue University, W. Lafayette, IN, 1992, p. 477-487.

66 Sheiretov, T.K., VanGlabbeek, W.H., and Cusano, C., "Simulative Friction and Wear Study of Retrofitted Swash Plate and Rolling Piston Compressors", *International Journal of Refrigeration.*, 18 (1995) 5 336-342.

67 Sheiretov, T.K., VanGlabbeek, W.H., and Cusano, C., "Tribological Evaluation of Various Surface Treatments for M2 Tool Steel in a Refrigerant Environment", *1994 International Compressor Engineering Conference at Purdue*, Purdue University, W. Lafayette, IN, 103-108, July 19-22, 1994.

68 Sheiretov, T.K., VanGlabbeek, W.H., and Cusano, C., "Evaluation of the Tribological Properties of Polyimide and Poly(Amide-Imide) Polymers in a Refrigerant Environment", *Tribology Transactions* , 38 (1995) 4, 914-922.

69 Sheiretov, T.K., VanGlabbeek, W.H., and Cusano, C., "The Effect of Dissolved Water on the Tribological Properties of Polyalkylene Glycol and Polyolester Lubricants", STLE *Lubrication Engineering*. 52 (1996) 6, 463-473.

70 Yoon, H.K., Sheiretov, T.K., and Cusano, C., "Tribological Evaluation of Various Aluminum Alloys in Lubricant/Refrigerant Mixtures", 1996 International Compressor Engineering Conference at Purdue, Purdue University, W. Lafayette, IN, 1996, p. 139-144

71 Hivart, P.H., Bricout, J.P., and Oudin, J., "A New Friction-Seizure Test for Phosphate/Stearate Coatings Using Conductivity Measurement", *STLE Lubrication Engineering*, 49 (1994) 11, 833-837.

72 Leather, J.A. and MacPherson, P.B., "The Practical Use of Electrical Measurements in Lubricated Contacts", In Surface Effects in Lubrication, Dowson et al. editors, *Proceedings of the 4-th Leeds-Lyon Symposium on Tribology*, 1977.

73 Quinn, T.F.J. and Winer, W.O., "An Experimental Study of the "Hot-Spots" Occuring During the Oxidational Wear of Tool Steel on Sapphire", *Transactions of the ASME, Journal of Tribology*, 109 (1987) 4, 315-320.

74 Moffat, R.J., "The Gradient Approach to Thermocouple Circuitry", in Temperature -its Measurement and Control in Science and Industry, Reinhold, New York, 1962.

75 Durkee, D.B. and Cheng, H.S., "An Examination of a Possible Mode of Scuffing Failure in Simple Sliding", *Wear*, 59 (1980), 223-230.

76 Andersson, S. and Salas-Russo, E., "The Influence of Surface Roughness and Oil Viscosity on the Transition in Mixed Lubricated Sliding Steel Contacts", *Wear*, 174 (1994), 71-79

77 Horng, J.H., Lin, J.F,, and Li, K.Y., "Scuffing as Evaluated From the Viewpoint of Surface Roughness and Friction Energy", *Transactions of the ASME, Journal of Tribology*, 118 (1996) 7, 669-675.

Turbine Engine Oil", *Transactions of the ASME, Journal of Tribology*, 117 (1995) 7, 482-489.

79 Evans, H.P. and Snidle, R.W., "A Model for Elastohydrodynamic Film Failure in Contacts Between Rough Surfaces Having Transverse Finish", *Transactions of the ASME, Journal of Tribology*, 118 (1996) 7, 847-857.

80 Block, H, "The Flash Temperature Concept", *Wear*, 6 (1963), 483-494.

81 Matveevsky, R.M, "The Critical Temperature of Oil with Point and Line Contcat Machines", *ASME Journal of Basic Engineering*, 87 (1965), 754-760.

82. Bell, J.C., Dyson, A., and Hadley, J.W., "The Effects of Rolling and Sliding Speeds on the Scuffing of Lubricated Steel Discs", *ASLE Transactions*, 18 (1975) 1, 62-73.

83 Lee, S.C. and Cheng, H.S., "Scuffing Theory Modelling and Experimental Correlations", *Transactions of the ASME, Journal of Tribology*, 113 (1991) 4, 237-334.

84 Lee, S.C. and Chen, H., "Experimental Validation of the Critical Temperature-Pressure Theory of Scuffing", *STLE Tribology Transactions*, 38 (1995) 3, 738-742.

85 Yoon, H.K., Private Communications.

86 Barr, T.L., "SCA Studies of Naturally Passivated Metal Foils", *Journal of Vacuum Science Technology*, 14 (1977), 660-665.

87 Quinn, T.F.J., "A Review of Oxidational Wear: Part I, The Origins of Oxidational Wear", *Tribology International*, 16 (1983), 257-271.

88 Quinn, T.F.J., "A Review of Oxidational Wear: Part II: Recent Developments and Future Trends in Oxidational Wear Research", *Tribology International*, 16 (1983), 305-315.

89 Razavizadeh, K. and Eyre, T.S., "Oxidative Wear of Aluminum Alloys", *Wear*, 79 (1982), 325-333.

90 Sarkar, A.D. and Clarke, J., "Friction and Wear of Aluminum-Silicon Alloys", *Wear*, 61 (1980), 157-167.

91 Alpas, A.T., Hu, H., and Zhang, J., "Plastic Deformation and Damage Accumulation Below the Worn Surfaces", *Wear*, 162-164 (1993), 188-195.

92 Perrin, C. and Rainforth, W.M., "Work Hardening Behaviour at the Worn Surface of Al-Cu and Al-Si Alloys", *Wear*, 203-204 (1997), 171-179.

93 Bush, A.W., Gibson, R.D, and Thomas, T.R., "The Elastic Contact of a Rough Surface", *Wear*, 35 (1975), 87-111.

94 McCool, J.I. and Gassel, S.S., "The Contact of Two Surfaces Having Anisotropic Roughness Geometry", ASLE Spec. Publ. SP-7(1981), 29-38.

95 Rough Surfaces, Thomas, T. R editor, Longman, 1982.

96 Aramaki, H., Cheng, H. S., and Chung, Y.-W., "The Contact Between Rough Surfaces With Longitudinal Texture - Part I: Average Contact Pressure and Real Area of Contact", *Transactions of the ASME, Journal of Tribology*, 115:7 (1993), 419-424.

97 Nayak, P. R., "Random Process Model of Rough Surfaces in Plastic Contact", *Wear*, 26 (1973), 305-333.

98 McCool, J. I., "Comparison of Models for the Contact of Rough Surfaces", *Wear*, 107 (1986), 37-60.

99 Majumdar, A. and Bhushan, B., "Fractal Model of Elastic-Plastic Contact Between Rough Surfaces", *Transactions of the ASME, Journal of Tribology*, 113 (1991) 1, 1-11.

100 Majumdar, A. and Bhushan, B., "Role of Fractal Geometry in Roughness Characterization and Contact Mechanics of Surfaces", *Transactions of the ASME, Journal of Tribology*, 112 (1990) 4, 205-216.

101 Majumdar, A. and Tien., C. L., "Fractal Characterization and Simulation of Rough Surfaces", *Wear,* 136 (1990), 313-327.

102 Wang, S. and Komvopoulos, K., "A Fractal Theory of the Interfacial Temperature Distribution in the Slow Sliding Regime: Part I - Elastic Contact and Heat Transfer Analysis", *Transactions of the ASME, Journal of Tribology*, 116 (1994) 10, 812-823.

103 Tian, X. and Bhushan, B., "A Numerical Three-Dimensional Model for the Contact of Rough Surfaces by Variational Principle", *Transactions of the ASME, Journal of Tribology*, 118 (1996) 1, 33-42.

104 Sayles, R. S., "Computer Simulation of the Contact of Rough Surfaces", *Wear*, 49 (1978), 273-296.

105 Francis, H.A., "A Finite Surface Element Model for Plane-Strain Elastic Contact", *Wear*, 76 (1982), 221-245.

106 Ren, N., and Lee, Si. C., "Contact Simulation of Three-Dimensional Rough Surfaces Using Moving Grid Method", *Transactions of the ASME, Journal of Tribology,* 115 (1993) 10, 597-601.

107 Lee, Si. C., and Ren, N., "The Subsurface Stress Field Created by Three-Dimensionally Rough Bodies in Contact with Traction", *STLE, Tribology Transactions*, 37 (1994) 3, 615-621.

108 Lee, Si. C., and Ren, N., "The Effects of Surface Roughness and Topography on the Contact Behavior of Elastic Bodies", *Transactions of the ASME, Journal of Tribology,* 116 (1994) 10, 804-811.

109 Webster, M. N. and Sayles, R. S., "A Numerical Model for the Elastic Frictionless Contact of Real Rough Surfaces", *Transactions of the ASME, Journal of Tribology*, 108 (1986) 7, 314-320.

110 Seabra, J. and Berthe, D., "Influence of Surface Waviness and Roughness on the Normal Pressure Distribution in the Hertzian Contact", *Transactions of the ASME, Journal of Tribology,* 109 (1987) 7, 462-470.

111 Bailey, D.M. and Sayles, R. S., "Effect of Roughness and Sliding Friction on Contact Stresses", *Transactions of the ASME, Journal of Tribology*, 113 (1991) 10, 729-738.

112 Sayles, R.S., "Basic Principles of Rough Surface Contact Analysis Using Numerical Methods", *Tribology International*, 29 (1996) 8, 339-650.

113 Francis, H.A., "The Accuracy of Plane Strain Models for the Elastic Contact of Three-Dimensional Rough Surfaces", *Wear*, 85 (1983) 239-256.

114 Liang, X., Kaiyan, J., Yongquing, J., and Darong, Ch., "Variations in Contact Stress Distribution of Real Rough Surfaces During Run-in", *Transactions of the ASME, Journal of Tribology*, 115 (1993) 10, 602-606.

115 Wang, F. X., Lacey, P., Gates, R. S., and Hsu, S. M., "A Study of the Relative Surface Conformity Between Two Surfaces in Sliding Contact", *Transactions of the ASME, Journal of Tribology*, 113 (1991) 10, 755-761.

116 Sugimura, J. and Kimura, Y., "Characterization of Topographical Changes During Lubricated Wear", *Wear*, 98 (1984), 101-116.

117 Kimura, Y. and Sugimura, J., "Microgeometry of Sliding Surfaces and Wear Particles in Lubricated Contact", *Wear*, 100 (1984), 33-45.

118 Gupta, P. K. and Cook, N. H., "Statistical Analysis of Mechanical Interaction of Rough Surfaces", Transactions of the *ASME, Journal of Lubrication Technology*, 94 (1972) 1, 19-26.

119 Johnson, K. L., "Contact Mechanics", Cambridge University Press, 1985.

120 Press, W.H., Teukolsky, S.A., Vetterling, W.T., and Flannery, B.P., "Numerical Recipies in C. The Art of Scientific Computing", Second Edition, Cambridge University Press, 1991.

121 He, X. and Cheng, H.S., Private Communications.

122 Tian, X. and Kennedy, F.E., "Maximum and Average Flash Temperatures in Sliding Contacts", *Transactions of the ASME, Journal of Tribology*, 116 (1994), 167-174.

123 Ettles, C.M., Dinc, O.S., and Calabrese, S.J., "The Efffect of Frictionally Generated Heat on Lubricant Transition", *STLE, Tribology Transactions*, 37 (1994) 2, 420-424.

124 Jaeger, J.C., "Moving Sources of Heat and the Temperature of Sliding Contacts", *J. Proc. Roy. Soc. N.S.W.*, 76 (1942), 203-224.

125 CRC Practical Handbook of Materials Selection, Shackelford, J.F., Alexander, W., and Park, J.S., editors, CRC Press, Boca Raton, 1995, p.321.

126 CRC Handbook of Chemistry and Physics, Lide, D.R. editor, CRC Press Inc., Boca Raton, 1996, p.12-179

127 Hirst, W. and Lancaster, J.K., "The Influence of Speed on Metallic Wear", *Proc. Roy. Soc. London*, A259 (1961), 228-241.

128 Kuo, S.M. and Rigney, D.A., "Sliding Behavior of Aluminum", *Materials Science and Enginnering*, A157 (1992), 131-143.

129 Dautzenberg, J. H., "The Role of Dynamic Recrystallization in Dry Sliding Wear", *Wear*, 60 (1980), 404-411.

130 Slater, R.A.C., "Engineering Plasticity. Theory and Application to Metal Forming Processes", John Wiley & Sons, New York, 1977, p.150.

131 Samanta, S.K, "Relating the Flow Stress of Aluminum and Copper to Strain, Strain-Rate and Temperature", *Int. Journal of Mechanical Science*, 11 (1969), 433-453.

132 Sarkar, J., Prasad, Y.V.R.K., and Surappa, M.K., "Optimization of Hot Workability of an Al-Mg-Si Alloy Using Processing Maps", *Journal of Materials Science*, 30 (1995), 2843-2848.

133 Atlas of Stress-Strain Curves, Boyer, H.E., Ed., ASM International, Metals Park Ohio, p.423

134 Aluminum: Properties and Physical Metallurgy, Hatch, J.E., Ed., American Society for Metals, Metals Park, Ohio, 1984, p 112.

135 Puchi, E.S., "Constitutive Equations for Commercial-Purity Aluminum Deformed Under Hot-Working Conditions", *Transactions of the ASME, Journal of Engineering Materials and Technology*, 117 (1995) 1, 20-27.

136 Metals Handbook, Ninth Edition, Vol. 8, Mechanical Testing, Davis, J.R. editor, American Society for Metals, Metals Park, Ohio, 1985, p 231.

137 Metals Handbook, Ninth Edition, Vol. 8, Mechanical Testing, Davis, J.R. editor, American Society for Metals, Metals Park, Ohio, 1985, p 237.

138 Tallian, T.E., "On Competing Failure Modes in Rolling Contact", *ASLE Transactions*, 10 (1967), 418-439.

139 Johnson, K.L., Greenwood, J.A., and Poon, S.Y., "A Simple Theory of Asperity Contact in Elastohydrodynamic Lubrication", *Wear*, 19 (1972), 91-108.

140. Christensen, H., "Failure by Collapse of Hydrodynamic Oil Films", *Wear*, 22 (1972), 359-366.

141 Subramanian C., "Some Considerations Towards the Design of a Wear Resistant Aluminum Alloy", *Wear*, 155 (1992) 193-205.

140. Christensen, H., "Failure by Collapse of Hydrodynamic Oil Films", *Wear*, 22 (1972), 359-366.
141 Subramanian C., "Some Considerations Towards the Design of a Wear Resistant Aluminum Alloy", *Wear*, 155 (1992) 193-205.
142 Bailey, M.W. and Cameron, A., "The Effects of Temperature and Metal Pairs on Scuffing", *ASLE Transactions*, 16 (1973) 2, 121-131.
143 Carper, H.J. and Ku P.M., "Thermal and Scuffing Behavior of Disks in Sliding-Rolling Contact", *ASLE Transactions*, 18 (1975) 1, 39-47.
144 Buyanovskij, I. A., "Evaluation of the Upper Bounds of Applicability of Lubricants Under Conditions of Severe Boundary Lubrication by the Method of Thermal Kinetics", *Trenie i Iznos* 14 (1993) 1, 129-142.
145 Kotvis, V.P. and Tysoe, W.T., "An Investigation of Film Removal in Extreme Pressure Lubrication Using Chlorinated Hydrocarbon Additives", *Wear*, 153 (1992), 305-314.
146 Johnson, R.R., Dow, T.A., and Zhang, Y.Y., "Thermoelastic Instability in Elliptic Contact Between Two Sliding Surafces, *Transactions of the ASME, Journal of Tribology*, 110 (1988) 1, 80-86.
147 Yang, J., Cown, R.S., and Winer, W.O., Prediction of Failure Transitions in Sliding Contacts by a Thermomechanical Wear Model", *Transactions of the ASME, Journal of Tribology*, 115 (1993) 7, 432-438.
148 Barber, J.R., "The Influence of Thermal Expansion in the Friction and Wear Process", *Wear*, 10 (1967) 155-159.
149 He, X. and Cheng, H.S., Private Communications.
150 Xue, O.J. and Ludema, K.C., "Plastic Failure Effects in Scuffing of Soft Metals", *Wear of Materials* (1983) 499-506.
151 Suzuki, M. and Ludema, K. C., "The Wear Process During the "Running-In" of Steel in Lubricated Sliding", *Transactions of the ASME, Journal of Tribology*, 109 (1987) 4, 587-593.
152 Rosenfield, A.R., "A Shear Instability Model of Sliding Wear", *Wear*, 116 (1987) 319-328.
153 Kuhlmann-Wilsdorf, D., "Dislocation Concepts in Friction and Wear, in Fundamentals of Friction and Wear of Materials", Rigney, D.A. editor, American Society for Metals, Metals Park, Ohio, 1981, p 165.
154 Rosenfield, A.R., "A Fracture Mechanics Approach to Wear", *Wear*, 61 (1980), 125-132.
155 Rosenfield, A.R., "A Dislocation Theory Approach to Wear", *Wear*, 72 (1981) 97-103.
156 Rice, J.R. and Tracey, D.M., "On the Ductile Enlargement of Voids in Triaxial Stress Fields", *Journal of Mech. Phys. Solids*, 17 (1969), 201-217.